Transionospheric Signal Modelling for ePOP and SuperDARN

A Thesis Submitted to the

College of Graduate Studies and Research

in Partial Fulfillment of the Requirements

for the degree of Doctor of Philosophy

in the Department of Physics and Engineering Physics

University of Saskatchewan

Saskatoon

By

Robert Gordon Gillies

Permission to Use

In presenting this thesis in partial fulfilment of the requirements for a Postgraduate degree from the University of Saskatchewan, I agree that the Libraries of this University may make it freely available for inspection. I further agree that permission for copying of this thesis in any manner, in whole or in part, for scholarly purposes may be granted by the professor or professors who supervised my thesis work or, in their absence, by the Head of the Department or the Dean of the College in which my thesis work was done. It is understood that any copying or publication or use of this thesis or parts thereof for financial gain shall not be allowed without my written permission. It is also understood that due recognition shall be given to me and to the University of Saskatchewan in any scholarly use which may be made of any material in my thesis.

Requests for permission to copy or to make other use of material in this thesis in whole or part should be addressed to:

Head of the Department of Physics and Engineering Physics
116 Science Place
University of Saskatchewan
Saskatoon, Saskatchewan
Canada
S7N 5E2

Abstract

In 2011, the Canadian enhanced Polar Outflow Probe (ePOP) satellite will be launched. The ePOP satellite is equipped with several scientific Earth observation instruments, including a Radio Receiver Instrument (RRI) which will be used to detect High Frequency (HF) radio waves transmitted from a ground-based transmitter. The ground-based instrument will be one of the Super Dual Auroral Radar Network (SuperDARN) array of radars. A radio wave transmitted from the SuperDARN radar will propagate through the ionosphere and be detected by the RRI on ePOP. Analysis of the characteristics of the signal received by the RRI will provide information about the plasma density in the ionosphere between the transmitter and receiver. As the ePOP satellite is not yet operational, extensive ray path modelling has been performed to simulate the expected signal at the RRI for various ionospheric conditions.

The other major objective of this research was to examine the effect of the variable refractive index in the ionosphere on SuperDARN drift velocity measurements. Past comparisons between velocities measured by SuperDARN and other instruments have found that velocities measured by SuperDARN typically were about 20–30% lower. This research has shown that underestimation of drift velocities by SuperDARN is a consequence of not including the refractive index when these velocities are calculated. As refractive index measurements are not readily available, this research has involved developing and implementing various methods to estimate the refractive index in the ionosphere. These methods have demonstrated that plasma density values within the SuperDARN scattering volume are appreciably higher than background plasma densities in the ionosphere. Application of these methods, which has resulted in a much better understanding of the physics of the coherent scattering process, has resulted in agreement between velocities measured by SuperDARN and other instruments.

Acknowledgements

First, I'd like to thank my supervisor Dr. Glenn Hussey. I am extremely grateful for the opportunities he has given me to study this field of space science; from summer student work, to my Master's degree, and finally this doctoral project.

Many faculty members, researchers, and graduate students in the Institute of Space and Atmospheric Studies (ISAS) at the University of Saskatchewan and elsewhere have provided generous advice and assistance for this project. Drs. George Sofko, Kathryn McWilliams, J.-P. St.-Maurice, Sasha Koustov, Chad Bryant, and Pasha Ponomarenko have all offered very helpful and invaluable assistance and guidance. Dr. Dieter André and Engineer Jan Wiid both provided me with valuable software and equipment assistance. I would like to thank all past and current graduate students in ISAS who have assisted with my research project, including; Megan Gillies, Robyn Fiori, Donald Danskin, Bob Schwab, Gareth Perry, Joel Cooper, and Daniel Mori. I am grateful to members of the Radio and Space Plasma Physics group at the University of Leicester, UK, in particular my supervisor Dr. Darren Wright and Dr. Steve Milan, for providing me with the opportunity to study with their group for three months in 2008. Thank you also to Dr. Jackie Davies at the Rutherford Appleton Laboratory, UK and Dr. Gordon James at the Communications Research Centre, Ottawa for collaborating with me on various research projects related to my thesis.

Funding for this research was generously provided by the Canadian Space Agency (CSA) and the Natural Sciences and Engineering Research Council (NSERC) for the CASSIOPE/ePOP project and by the EU Marie Curie Early Stage Training in Space, Planetary, and Astrophysical Sciences (SPARTAN) programme. I would also like to thank the Department of Physics and Engineering Physics for providing me with financial assistance through numerous scholarships.

For my loving wife Megan and beautiful daughter Kara.

Contents

List of Figures

List of Abbreviations

ACE	Advanced Composition Explorer
AU	Astronomical Unit
B-field	Magnetic Field
CADI	Canadian Advanced Digital Ionosonde
CASSIOPE	CAScade Smallsat and IOnospheric Polar Explorer
CER	Coherent Electromagnetic Radio tomography
CHAIN	Canadian High Arctic Ionospheric Network
CPCP	Cross Polar Cap Potential
CUTLASS	Co-operative UK Twin Located Auroral Sounding System
DMSP	Defense Meteorological Satellites Program
E-field	Electric Field
EISCAT	European Incoherent SCATter radar
ePOP	enhanced Polar Outflow Probe
FAI	Fast Auroral Imager
f_oE	E-region peak
f_oF1	F1-region peak
f_oF2	F2-region peak
GAP	GPS Attitude and Positioning experiment
GPS	Global Positioning System
HF	High Frequency (3–30 MHz)
IGRF	International Geomagnetic Reference Field
IMF	Interplanetary Magnetic Field
IRI	International Reference Ionosphere
IRM	Imaging and Rapid-scanning ion Mass spectrometer
ISIS	International Satellites for Ionospheric Studies
ISR	Incoherent Scatter Radar
LT	Local Time
MGF	MaGnetic Field instrument
NMS	Neutral Mass Spectrometer
O-mode	Ordinary Mode
QL	Quasi-Longitudinal
QT	Quasi-Transverse
RIOMeter	Relative Ionospheric Opacity Meter
RRI	Radio Receiver Instrument
SEI	Suprathermal Electron Imager
SuperDARN	Super Dual Auroral Radar Network
TEC	Total Electron Content
UHF	Ultra High Frequency (300–3000 MHz)
VHF	Very High Frequency (30–300 MHz)
X-mode	Extraordinary Mode

Chapter 1

Introduction

1.1 Motivation for Research

In 2011 the Canadian designed and built CAScade, Smallsat, and IOnospheric Polar Explorer (CASSIOPE) satellite will be launched. This satellite will carry a suite of eight scientific instruments called the enhanced Polar Outflow Probe (ePOP) [*Yau et al.*, 2002; 2006]. The main objectives of the ePOP mission are to study outflows of charged particles from the polar regions of the Earth, to perform tomographic measurements of ionospheric electron densities, and to study wave particle interactions and radio wave propagation in the ionosphere. Radio wave propagation studies using the Radio Receiver Instrument (RRI) [*James*, 2003; *James and Lunscher*, 2006; *James*, 2006; *James et al.*, 2006] on ePOP are an important part of this research. The RRI will consist of two crossed dipole antennas which will be used to receive High Frequency (HF) radio waves. Radio wave signals to be detected by the RRI will primarily be provided by ground-based transmitters such as the Super Dual Auroral Radar Network (SuperDARN) HF radars [*Greenwald et al.*, 1995] and ionosondes [*MacDougall et al.*, 1995]. Analysis of the signal to be received by the RRI from these ground-based transmitters will provide information about the physics and properties of the ionosphere such as electron density distributions and radio wave absorption regions. Signal parameters such as propagation time, polarization, and relative power can all be used to determine electron density and absorption in the ionosphere between the transmitter and receiver. This experiment will introduce a new method to measure ionospheric electron densities using HF radio waves, to complement the more common Very High Frequency (VHF) and Ultra High Frequency

(UHF) tomographic experiments.

The main purpose of this research, and essentially all research in this field, is to develop a better understanding of the physics of the near-Earth space environment and the linking of the Sun-Earth system. Accurate measurements of electron density structures from the SuperDARN-ePOP experiment will aid in characterizing and modelling the ionosphere. Better predictions of electron density profiles will allow better HF communication links, in particular over the polar cap region where commercial aircraft are more frequently flying. Aircraft flying more directly over the polar region of the Earth must rely on HF radio waves to maintain communication with ground stations as VHF and higher frequency radio waves are not refracted sufficiently by the ionosphere to allow communication over large distances. Since the ionosphere is highly variable and affects the propagation and absorption of HF waves, accurate nowcasting and forecasting of ionospheric conditions is essential to ensure that these aircraft can fly on the safest and most efficient routes. Further benefits to space science research involve the increasing use of GPS (Global Positioning System) units. The accuracy and reliability of these units depends on the variability of ionospheric electron density values. Another important goal of space science is accurate forecasting of space weather conditions in near-Earth space. Solar storms are associated with energetic particles in the solar wind, which can be accelerated in the magnetosphere of the Earth. Accurate forecasting of these storms is essential to protect the electronics and inhabitants of Earth orbiting spacecraft. For a solid understanding of the behaviour of the near-Earth space environment and space weather, an understanding of the plasma processes is essential.

1.2 General plasma physics

A plasma is essentially a quasi-neutral gas of charged particles [*Baumjohann and Treumann*, 1997]. Quasi-neutrality implies that, on average, the gas has the same number of positive particles as negative particles. Small-scale regions of a plasma may have excess charge or separation of charge may happen on very fast times scales,

but quasi-neutrality ensures that on large enough time and spatial scales, there are equal numbers of positive and negative charge. If quasi-neutrality did not hold, large electric fields would develop in the plasma which would cause particle motion to cancel the fields and return the gas to quasi-neutrality. Another requirement of charged particles in a plasma is that the kinetic energy of a given particle is much higher than the potential energy due to any neighbouring particle. This criterion implies that the electrons are not bound to the atoms (making the atoms ions) and are often referred to as 'free' particles. In fact, the ions do influence the electrons due to the Debye shielding effect in a plasma and it may be more accurate to refer to the electrons as 'unbound' particles rather than 'free' particles.

An important quantity associated with a plasma is the plasma frequency f_p. The plasma frequency is the natural oscillation frequency of the charged particles in a given plasma. Given a displacement of one species of particles in a plasma from the other, the restoring Coulomb force will result in oscillations of the displaced charges at a characteristic frequency. This is analogous to oscillations in a mechanical system such as a pendulum or spring. The plasma frequency f_p is dependent on charged particle density N and mass m by the following equation:

$$f_p = \frac{1}{2\pi}\sqrt{\frac{Ne^2}{\epsilon_o m}}, \tag{1.1}$$

where e is the elementary charge (1.602×10^{-19} C) and ϵ_o is the permittivity of free space (8.85×10^{-12} F/m). Since the electrons and ions in a plasma have different masses, they also have different natural oscillation frequencies. The mass of the ions is much higher than that of the electrons, so the ion plasma frequency is much lower than the electron plasma frequency. For example, typical ionospheric electron plasma frequencies are between 1 MHz and 10 MHz, while the ion plasma frequencies are less than 100 kHz. As this research is concerned with the interaction of HF (3 MHz–30 MHz) electromagnetic waves with ionospheric plasma, the plasma frequency of interest is the electron plasma frequency. A simple relation between electron density N_e (units of m^{-3}) and plasma frequency (units of Hz) (SI units are used throughout

this thesis) is:

$$f_p = 8.98\sqrt{N_e}. \tag{1.2}$$

Conversely, if a value for plasma frequency is provided, it is easy to determine the electron density using:

$$N_e = 0.0124 f_p^2. \tag{1.3}$$

1.2.1 Particle motions

Charged particles in a plasma experience forces from both electric and magnetic fields. The equation of motion for a particle moving with velocity $\mathbf{v}$, mass m, and charge q in an electric field $\mathbf{E}$ and magnetic field $\mathbf{B}$ is:

$$m\frac{d\mathbf{v}}{dt} = q(\mathbf{E} + \mathbf{v} \times \mathbf{B}). \tag{1.4}$$

If the simple case in which the electric field is zero is considered, manipulation of Equation 1.4 will show that charged particles tend to rotate around the magnetic field with a gyro- or cyclotron frequency f_c of [e.g., *Baumjohann and Treumann*, 1997]:

$$f_c = \frac{|q|B}{2\pi m}. \tag{1.5}$$

The sense of rotation about the magnetic field is determined by the sign of the charge. The velocity parallel to the magnetic field is not affected by the field and is constant.

Next the situation in which both electric and magnetic fields are present and influence the charged particles is considered. For an electric field component that is parallel to the magnetic field $E_\parallel$, the equation of motion reduces to:

$$m\frac{dv_\parallel}{dt} = qE_\parallel. \tag{1.6}$$

This equation implies that charged particles will be accelerated along the parallel component of the electric field. In practice, for most near-Earth space plasmas, these parallel fields will accelerate the highly mobile electrons to create a canceling electric field. Therefore, there is usually no component of the electric field parallel to the magnetic field [e.g., *Baumjohann and Treumann*, 1997].

The combination of perpendicular electric and magnetic fields leads to a drift of charged particles called the 'E cross B drift'. A charged particle will be accelerated by the E-field in a direction perpendicular to the B-field. At the same time, the magnetic field is applying a force perpendicular to the velocity of the particle which causes the particle to rotate about the magnetic field. However, as the electric field is constantly applying a linear acceleration on the particle, the gyroradius of the particle (the radius of the orbit of the particle around the magnetic field lines) is smaller on one side of the orbit than the other which causes the particle to drift in a direction perpendicular to both the electric and magnetic fields. Working with the equation of motion, the drift velocity $\mathbf{V}_{E\times B}$ of charged particles can be shown to be:

$$\mathbf{V}_{E\times B} = \frac{\mathbf{E}\times\mathbf{B}}{B^2}. \tag{1.7}$$

Notice that the $E \times B$ drift motion is independent of charge so that electrons and ions drift together. The $E \times B$ drift is actually a specific case of the generalized force drift of particles in a magnetic field. A similar situation will occur when any force is applied perpendicular to a magnetic field (although, depending on the nature of the force, particles of different charge may drift in opposite directions). A non-uniform magnetic field will also create a similar drift as the gyroradius of charged particles will again be different on either side of their orbit.

1.3 Sun/Earth System

1.3.1 The Sun and solar wind

The physics of near-Earth space, including the magnetosphere and ionosphere, is largely driven by solar activity. An understanding of the solar processes involved and the linking between the Sun and Earth is essential for understanding the physics of the ionosphere, which is the primary focus of this research.

In astronomical terms, the Sun is a relatively ordinary star [e.g., *Kivelson and Russell*, 1995]. Essentially, the Sun is a ball of gas which is held together by gravitational attraction. The mass of the Sun is 1.99×10^{30} kg. The radius of the Sun is

696,000 km and the mean distance between the Sun and the Earth is 150×10^6 km (this distance is defined as one astronomical unit (AU)). The effective temperature of the surface of the Sun is ∼5800 K. Energy is produced in the core of the Sun through fusion of hydrogen atoms to form helium. This fusion process generates energy which slowly radiates outwards from the core to the surface of the Sun over a period of about 10 million years. The composition of the Sun is mostly hydrogen atoms (∼90%), helium atoms (∼10%), and small amounts of carbon, nitrogen and oxygen (∼0.1%).

The solar corona is in essence the atmosphere of the Sun and contains gas of solar origin, which is under a much higher pressure than the surrounding interstellar space. This pressure difference allows solar plasma to escape the gravitational attraction of the Sun and flow out into the solar system. It was theorized by *Parker* [1958], and later confirmed by spacecraft measurements, that the speed of the plasma in the solar wind actually increases as it flows outwards from the Sun. One instrument for measuring solar wind parameters is the Advanced Composition Explorer (ACE) spacecraft [*Stone et al.*, 1998], which is located at the Sun-Earth libration point (the location at which the gravity of the Sun and Earth balance). ACE is located outside of the magnetosphere of the Earth and regularly monitors solar wind parameters such as: flow speed, density, magnetic field strength and direction, and pressure. The solar wind near the Earth has typical flow speeds of ∼450 km/s and charged particle densities of 1–10 m^{-3}. The composition of the solar wind is mostly protons, electrons, and a small number of helium ions. It takes typically ∼4 days for solar wind plasma to flow from the Sun to the Earth so the response of the near-Earth space environment to activity observed on the Sun will be delayed by this amount of time [e.g., *Kivelson and Russell*, 1995].

The solar wind carries part of the solar magnetic field, which is known as the Interplanetary Magnetic Field (IMF), and it exists between the magnetosphere of the Earth and the Sun. The IMF is generated by currents within the Sun and travels outwards with the solar wind. The IMF has a complex structure with a magnitude of ∼5 nT. The charged particles that are moving outwards due to the high pressure

at the surface of the Sun effectively drag the IMF away from the Sun. Since the solar wind plasma is quite rarefied and very few collisions occur, the IMF is essentially 'frozen-in' to the solar wind plasma. The frozen-in condition essentially means that there is no diffusion of IMF field lines across the plasma in the time it takes the solar wind to reach the Earth [e.g., *Baumjohann and Treumann*, 1997].

1.3.2 Magnetosphere of Earth

The magnetosphere is the region of near-Earth space that contains the magnetic field of the Earth. The magnetic field of the Earth is approximately a dipole field with a northern magnetic pole near the southern geographic pole of the Earth and the southern magnetic pole near the northern geographic pole of the Earth. Although not completely understood, it is assumed that current systems in the core of the Earth create and maintain the magnetic field. Interactions between the magnetosphere and the solar wind deform the magnetosphere from the simple dipole configuration (discussed in more detail in the next section). Nonetheless, close to the surface of the Earth (e.g., in the ionosphere), modelling the field as a dipole is a good approximation. The magnetic field lines near the equator are nearly horizontal and point northwards while in the polar regions they are nearly vertical—pointing downwards in the northern hemisphere and upwards in the southern hemisphere [*Baumjohann and Treumann*, 1997].

Using the equation for a dipole field, the magnetic field of the Earth $\mathbf{B}$ may be approximated as follows:

$$\mathbf{B} = \frac{\mu_o M_E}{4\pi r^3}[(-2\sin\lambda)\hat{r} + (\cos\lambda)\hat{\lambda}], \tag{1.8}$$

where μ_o is the permeability of free space ($4\pi \times 10^{-7}$ H/m), M_E is the dipole moment of the Earth (8.05×10^{22} Am^2), r is the radial distance from the centre of the Earth (unit vector $\hat{r}$), and λ is the magnetic latitude (unit vector $\hat{\lambda}$) [e.g., *Baumjohann and Treumann*, 1997]. Using this equation, the magnitude of the magnetic field at the surface of the Earth is 3.1×10^{-5} T near the equator and 6.2×10^{-5} T at the poles. Using these numbers, the cyclotron frequency (Equation 1.5) of electrons in

the ionosphere of the Earth can be approximated to be on the order of 1 MHz. This value varies with both altitude and latitude. A model of the magnetic field of the Earth which is used for the ray path simulations discussed in this research is the International Geomagnetic Reference Field (IGRF) model [*Maus et al.*, 2005].

1.3.3 IMF–Magnetosphere interaction

In general, the solar wind and its accompanying IMF interact with the magnetosphere of the Earth and compress it on the dayside, while on the nightside the magnetosphere is extended (or 'dragged') outwards by the solar wind and IMF [e.g., *Kivelson and Russell*, 1995; *Baumjohann and Treumann*, 1997]. This interaction deforms the magnetosphere from the simple dipole approximation. The details of the interaction between the IMF and the magnetosphere of the Earth can be quite complex. Part of this complexity arises from the fact that the orientation of the IMF field lines with respect to the magnetosphere of the Earth is a constantly changing quantity.

The easiest IMF orientation to understand is the situation in which the IMF is southward pointing when it encounters the Earth. Figure 1.1 illustrates the behaviour of the magnetic field of the Earth when a southward pointing IMF encounters the magnetosphere. In this configuration, the southward IMF field lines encounter the northward pointing magnetic field lines of the Earth at some point on the sunward side or dayside of the magnetosphere (for example, the field line labelled '1' in Figure 1.1). When this occurs, magnetic field lines from the Earth connect or merge with IMF lines. The two ends of these newly merged field lines do not both close at the Earth (one end of the line is connected to one of the poles of the Earth and the other end is connected to the IMF and ultimately the Sun) and are therefore referred to as open field lines (magnetic field lines labelled '2' and '3' in the figure). These open field lines are still being dragged outwards from the Sun by the solar wind so they drape over the polar regions of the Earth and get stretched back into the nightside or tail region of the magnetosphere (field lines '4' and '5' in the figure). The tail region of the magnetosphere can be very elongated compared to the dayside

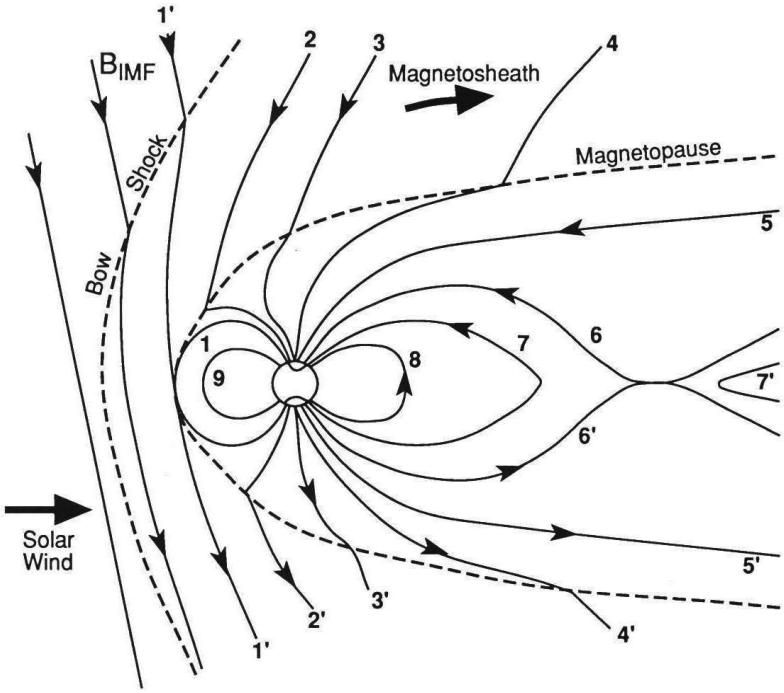

Figure 1.1: The interaction between the IMF and the magnetosphere of the Earth for a southward pointing IMF. Figure 9.11 from *Kivelson and Russell* [1995].

of the magnetosphere because of this stretching (e.g., the tail extends more than 100 Earth radii (R_E) away from the Earth, while the magnetosphere on the dayside is compressed to $\sim$10 R_E). The draped open magnetic field lines far out in the tail will be compressed by solar wind pressure and will eventually reconnect with similarly compressed open field lines from the opposite hemisphere (field line '6' in the figure). These newly reconnected (or closed) field lines are still stretched outwards in the tail of the magnetosphere, but are now connected only to the Earth and begin to return to a dipole configuration (field line '7' in the figure). As a result, they travel towards the Earth. Eventually, these reconnected field lines travel back around to the dayside of the Earth and the whole process begins all over again (field lines '8' and '9' in the figure). These processes are quite complex and merging on the dayside does not necessarily occur at the same rate as reconnection on the nightside, however over

time the number of merged field lines on the dayside must equal the number that reconnect on the nightside and an equilibrium in the magnetosphere is maintained.

Merging and transport of the newly closed magnetic field lines on the nightside of the Earth also traps the solar wind plasma associated with these newly closed field lines. This plasma is still frozen-in to the newly closed magnetic field lines on the nightside and is accelerated towards the Earth. This process results in the plasma gaining energy, and since these particles are free to move along field lines, some accelerate into the northern or southern auroral zones of the atmosphere, where the field lines to which they are attached connect to the Earth. These accelerated particles impact and excite atmospheric atoms and molecules, which create visible light known as the aurora.

Similar to the solar wind, the plasma in the F region of the ionosphere is essentially attached ('frozen-in') to the magnetic field lines of the Earth, which are being driven by solar activity in the auroral and polar regions. Figure 1.2 is a convection map generated by the SuperDARN radars and illustrates the general convection pattern for plasma in the polar cap ionosphere when the IMF is directed southward. Under these conditions, merging and transport of field lines on the dayside results in plasma convection which is antisunward over the polar region of the Earth. Reconnection of open field lines in the tail of the magnetosphere and transport back to the dayside also returns the plasma to the dayside along streamlines located at lower latitudes. In general, this behaviour results in plasma motion in the ionosphere in the form of a twin-cell convection pattern. Essentially, plasma convection in the ionosphere acts as a 'footprint' of the transport of magnetic field lines in the magnetosphere. When the IMF is not entirely southward, much more complex interactions between the magnetosphere and IMF result. The convection pattern in the ionosphere reveals details about the interaction between the magnetosphere and the IMF. Measurement of the large-scale convection patterns of plasma in the ionosphere is accomplished using instruments such as SuperDARN (discussed in detail in Section 1.5.4).

Associated with the convection of charged particles in the ionosphere is a convec-

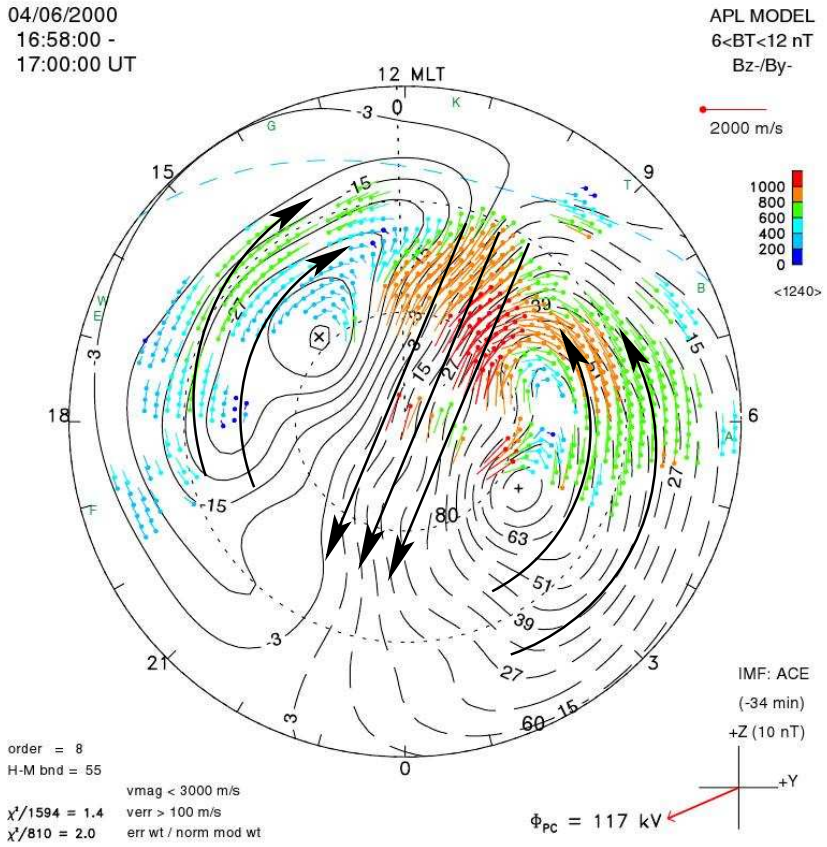

Figure 1.2: SuperDARN map of typical ionospheric convection during southward IMF conditions. Plasma flows anti-sunward over the polar cap (straight arrows) and returns to the dayside at lower latitudes (curved arrows). Figure 2b from *Chisham et al.* [2007].

tion electric field. This field is essentially a consequence the $E \times B$ drift phenomenon. In this case the solar wind driven plasma drifting at velocity $\mathbf{v}$, perpendicular to a magnetic field $\mathbf{B}$, results in an electric field $\mathbf{E}$. As the magnetic field of the Earth is relatively well-known, measuring plasma convection in the ionosphere is essentially the same as measuring electric fields in the ionosphere. Since the $E \times B$ drift direction is necessarily perpendicular to the electric field vector, the plasma particles drift along equipotential lines. In effect, a convection map of the ionosphere is also a map of equipotential field lines. In the classic twin-cell convection pattern, each convection cell centres on either a minimum or a maximum electric potential. The

difference in electric potential between these cells is called the cross-polar cap potential (CPCP) difference and is on the order of 50 kV. The SuperDARN network is one of the best instrument arrays for continuously monitoring the CPCP. The CPCP value is an important parameter for quantifying solar wind activity [*Troshichev et al.*, 1996].

1.4 The Ionosphere of the Earth

1.4.1 General

The ionosphere of the Earth is the region of the atmosphere where unbound or 'free' ions and electrons exist to form a plasma. The boundaries of the ionosphere are not well defined and the various literature sources used in the following sections, such as: *Kelley* [2009], *Hunsucker and Hargreaves* [2003], *Schunk and Nagy* [2000], *Baumjohann and Treumann* [1997], *Treumann and Baumjohann* [1997], *Kivelson and Russell* [1995] and *Hunsucker* [1991], give different values for the altitude of the bottom of the ionosphere. For example, *Baumjohann and Treumann* [1997] define 80 km altitude as the bottom of the ionosphere while *Kivelson and Russell* [1995] use 100 km. The top of the ionosphere is rarely even discussed and, in general, ionospheric science is usually only concerned with altitudes up to ∼1000 km to ∼2000 km. A clear definition of which part of the atmosphere is the ionosphere is not as important as an understanding of the overall structure and behaviour of the atmosphere in this region.

The amount of ionization in the ionosphere is actually very small compared to the neutral density. For example, at an altitude of 100 km, there is only one charged particle for every 10^8–10^9 neutral particles and at 250–300 km (the location of the highest plasma density), the charged particles represent only ∼0.1% of the atmosphere [*Hunsucker*, 1991]. The main focus for ionospheric physics is the ionized portion where the small amount of ionization largely governs the behaviour of the region, in contrast to the lower neutral atmosphere. In particular, the ionization of

the ionosphere has a consequential effect on radio waves and their propagation as will be discussed in Section 1.7.

1.4.2 Ionosphere formation

There are two main sources that produce and maintain the ionization level in the ionosphere. The first to be considered is photoionization from solar photons. Ultraviolet (UV) and extreme ultraviolet (EUV) photons (energies on the order of 10–100 eV) are the main driver of ionization in the dayside ionosphere [e.g., *Kelley*, 2009; *Hunsucker and Hargreaves*, 2003; *Schunk and Nagy*, 2000; *Baumjohann and Treumann*, 1997; *Kivelson and Russell*, 1995]. Photons of longer wavelength have energies that are too low and insufficient to allow electrons to overcome the binding energy to atmospheric atoms and molecules. The solar spectrum is less intense for energies higher than EUV and these photons are therefore not as important for ionization.

The production rate of ions in the ionosphere is governed by two factors: 1) the intensity of solar radiation of the appropriate energy, and 2) the number of neutral atmospheric particles that can be ionized. The intensity of solar radiation increases with altitude since at lower altitudes more of the radiation has been absorbed by the atmosphere above. Conversely, the neutral density of the atmosphere decreases with altitude. The competition between these two behaviours results in a peak in ion production rate between ∼150–200 km altitude [*Schunk and Nagy*, 2000]. Significantly above this altitude (>1000 km) there is sufficient solar radiation to cause ionization, however there are very few neutral particles to be ionized. Below ∼100 km, the neutral density is high, but the intensity of EUV radiation is quite low. Furthermore, at lower altitudes any particles that do happen to be ionized quickly recombine to form neutral particles due to the high atmospheric density.

The peak altitude for production of ions occurs below 200 km, which is not the altitude of peak density. The loss rate of ions by either recombination or attachment also needs to be considered. Recombination occurs when a positive ion and an electron combine to form a neutral particle. Attachment occurs when an electron

attaches to a neutral particle to form a negative ion. In an equilibrium state, the loss rate of ionization is equal to the production rate and a steady ionospheric ion or electron density results. Since there is a higher atmospheric density at lower altitudes, the loss rate will be higher at lower altitudes. This causes the altitude of the peak steady-state electron density to be above the peak production altitude. The final result is a peak electron density of typically $\sim 10^{12}$ m^{-3} or more on the dayside ionosphere at $\sim$300 km altitude. The density and altitude of this peak varies highly with latitude, time of day, time of year, and solar activity.

The second main production mechanism for ionospheric ion-electron pairs is precipitation of highly energetic magnetospheric particles at high magnetic latitudes [e.g., *Baumjohann and Treumann*, 1997; *Kivelson and Russell*, 1995]. Magnetospheric particles can be accelerated along field lines after reconnection in the tail region occurs as discussed in Section 1.3.3. This acceleration can result in particles with energies in the keV range striking the atmosphere. It requires only 13.6 eV to ionize oxygen atoms, so a single precipitating electron can collide with, and ionize, a great number of atmospheric neutrals. Furthermore the newly ionized particles may have enough energy to excite secondary ions [*Sofko et al.*, 2007].

When electrons excited by precipitating particles fall back into their ground states they often emit visible light. This visible light in the northern hemisphere is called the Aurora Borealis (Aurora Australis in the southern hemisphere) or more commonly the northern lights (or southern lights in the southern hemisphere). The precipitating particles follow the nearly vertical magnetic field lines as they stream into the atmosphere and the bands of light they produce are along these lines. Aurora are often visible at roughly 70° magnetic latitude (the auroral zone), although the location of auroral displays can be quite variable as it depends on complicated processes in the magnetosphere. The auroral green line of atomic oxygen produces green aurora at a wavelength of 557.7 nm and at altitudes between 100–200 km. Less prominent are red line emissions of atomic oxygen at a wavelength of 630.0 nm above 200 km. Nitrogen emissions provide even fainter violet and blue light which is not observable by the human eye.

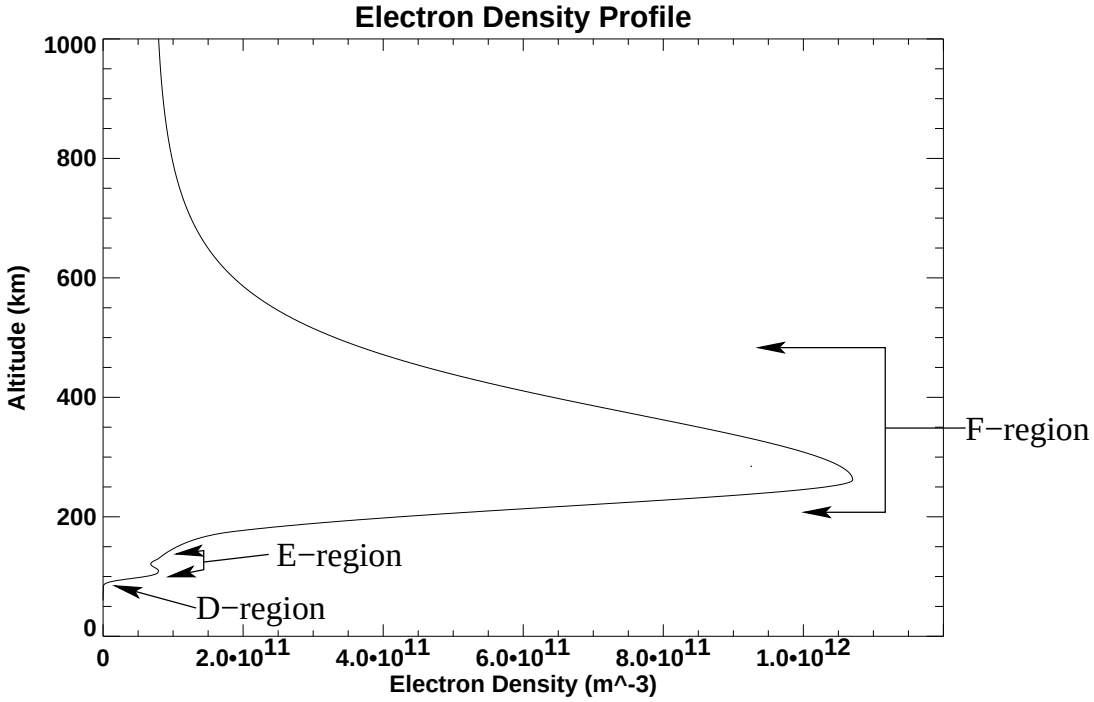

Figure 1.3: Typical ionospheric electron density profile generated using the International Reference Ionosphere (IRI) model [*Bilitza*, 2001].

1.4.3 Ionosphere regions

Due to the different atmospheric constituents and amount of ionizing radiation and precipitation at various altitudes, the ionosphere is split into different altitude regions. The D region is the lowest and exists below ∼90 km. The E region exists between ∼90 km and ∼150 km. Finally, the F region, where the most ionization occurs, exists between ∼150 km and the 'top' of the ionosphere. A diagram of a typical ionospheric electron density profile and the three different regions is presented as Figure 1.3.

D region

The lowest region of the ionosphere is termed the D region. This layer exists below altitudes of ∼90 km. The D region has electron density values that are actually too low to be considered a plasma [*Baumjohann and Treumann*, 1997]. The electron

density is usually less than $\sim 10^9$–10^{10} m^{-3}, which results in a plasma frequency f_p of ∼300–900 kHz. The cyclotron frequency of electrons in the D region is smaller than or comparable to the collision frequency of electrons with other particles. This implies that electrons orbiting in the magnetic field do not even complete one revolution before colliding with another particle. In effect the electrons in the D region are governed by the motion of neutral particles and can be considered unmagnetized. Of the ions that are created in the D region, the most abundant are NO^+ and O_2^+ [*Kelley*, 2009]. As these ions are much heavier than electrons, they have even lower gyrofrequencies and higher collision frequencies and are also considered unmagnetized. Essentially, neutral chemistry and dynamics governs the D region.

Modelling of the D region becomes important when absorption of radio waves is considered. At these altitudes, the high neutral density results in a very high collision rate between any unbound electrons that do exist and neutral particles. Absorption of HF waves is dependent on both collision frequency and electron density. Under disturbed conditions the electron density of the D region can be increased by high energy ionization sources, such as energetic particle precipitation or X-rays from the Sun, which penetrate to relatively low altitudes. Under these conditions, HF radio waves can be completely absorbed in the D region and lower E region [*Hunsucker and Hargreaves*, 2003].

E region

The E region is the ionospheric layer between ∼90 km and 150 km. Historically, this layer was the first to reflect ground-based radio transmissions and it was therefore termed the 'electric' or 'E' layer. The naming conventions for the lower 'D' region and higher 'F' region follow from the E region. Unlike the D region, the E region is defined by a peak in electron density, which exists near 110 km altitude. This electron density peak has a typical daytime density of 10^{11} m^{-3} resulting in a plasma frequency of ∼3 MHz. As with the D region, the ions in the E region are mostly NO^+ and O_2^+.

Unlike in the D region where the collision and gyro frequencies are similar, the

electron collision frequency is much lower than the electron gyrofrequency in the E region. This condition results in magnetized electrons, which are governed by electric and magnetic forces instead of neutral dynamics. Conversely, below ∼130 km, the more massive ions in the E region have a very low gyrofrequency and a high collision frequency and are unmagnetized as in the D region. These conditions result in the ions moving with the electric field, while the electrons undergo $E \times B$ drift. Since the movements of positive and negative charges are in different directions, separation of charge and large currents can develop in the E region. Since this behaviour essentially represents a conversion between kinetic energy and electrical energy, the E layer has also been termed the dynamo layer [*Baumjohann and Treumann*, 1997].

One interesting feature of the E region is an anomaly called the sporadic-E layer [*Hunsucker and Hargreaves*, 2003]. A sporadic-E layer is an intense increase of electron density of more than an order of magnitude in a very thin layer (∼1 km). These sporadic-E layers can have electron densities that are higher than 10^{12} m^{-3} and may reflect radar signals that are intended to study the higher F region.

F region

The uppermost region of the ionosphere is termed the F region. The F region exists from ∼150 km to the top of the ionosphere and has an electron density peak between typically 250 km and 300 km altitude. The F region and its peak contain the highest plasma density in the near-Earth space environment. Although the value of the peak density can vary by more than an order of magnitude, depending on location, season, time of day, and solar cycle period (discussed in detail in the next section), the typical peak density in the F region is 10^{12} m^{-3}, corresponding to a plasma frequency of 9 MHz [e.g., *Kivelson and Russell*, 1995]. The F-region ions consist mostly of atomic oxygen ions.

The F region is further classified by the F1 and F2 peaks, which occur at slightly different altitudes. The F1 layer has a lower density than the F2 layer and forms at ∼200 km altitude. The F1 layer is a dayside and summer phenomenon and disappears in winter and nightside conditions [*Hunsucker and Hargreaves*, 2003]. The F2 peak

occurs at ∼300 km and has the highest electron density in the F region. The two peaks exist because of the different atmospheric constituents and solar radiation at different altitudes.

The electron collision frequency in the F region is even lower than in the E region, so electrons are fully magnetized and follow the $E \times B$ drift motion. Unlike the lower E region, the ions in the F region also have collision frequencies that are much lower than their gyrofrequency. The ions are also magnetized and follow the $E \times B$ drift. Since there is no charge dependence on the $E \times B$ drift velocity, to a first approximation the ions and electrons in the F region drift together.

1.4.4 Electron density variability

The ionosphere is formed mainly by photoionization by solar EUV radiation on the dayside of the Earth and energetic particle precipitation on the nightside. Since both processes depend on both location and solar activity, the resulting electron density of the ionosphere is highly variable. As will be discussed in later sections, the propagation characteristics of HF radio waves are highly dependent on the electron density of the ionosphere (especially around the peak density of the F region [*Gillies et al.*, 2007]). It is therefore important to have a solid understanding of the variability of the electron density in the ionosphere with latitude, solar cycle period, and local time.

Latitudinal dependence on electron density

The ionization rate of the ionosphere due to solar radiation is very similar to the heating of the atmosphere of the Earth. If the Sun shines on the ionosphere more directly, more ion/electron pairs will be created. The general relationship between solar zenith angle χ (the angle the Sun makes with the zenith, which is related to geographic latitude) and electron density N_e is [*Baumjohann and Treumann*, 1997]

$$N_e \propto \sqrt{\cos \chi}. \tag{1.9}$$

It is expected, therefore, that the equatorial and middle latitudes will have higher electron densities than auroral and polar latitudes. In general this is the case; however, various localized processes and structures can complicate the situation.

One would expect that, in terms of latitude, the F-region ionosphere above the equator would contain the highest electron density; however, this is not what is observed. A trough of lower electron densities occurs near the equator, while the peak in density occurs at roughly $\pm 10°$–$20°$ in latitude away from the equator. This phenomenon is called the F-region equatorial anomaly [*Bhuyan et al.*, 2003]. At the equator during daytime there is an eastward pointing electric field and the mainly horizontal magnetic field of the Earth is directed northward. Plasma near the equator drifts upwards through the $E \times B$ motion creating a 'fountain effect'. The plasma lifts up from the F region at the equator and falls down to Earth along magnetic field lines north and south of the equator. The result of this motion is a lower electron density near the equator and peaks north and south of the equator. The electron density across the equatorial anomaly can be observed in Figure 1.4, in which the International Reference Ionosphere (IRI) [*Bilitza*, 2001] estimates of electron density at 300 km altitude is plotted as a function of latitude for March 21, 2000 at 12 LT (Local Time).

Another well defined structure that exists at middle to auroral latitudes is the mid-latitude or main ionospheric trough. The main trough is primarily a nightside phenomenon between latitudes of 55° and 75° on the equatorward edge of the auroral zone [*Moffett and Quegan*, 1983]. The trough can range in width from 1° to 10° in latitude [e.g., *Kersley et al.*, 1997; *Moffett and Quegan*, 1983]. The electron density in the trough is often an order of magnitude less than outside the trough. The edges of the trough, in particular the poleward edge, can have very large electron density gradients. On the poleward side of the trough, particle precipitation ionizes the ionosphere to create higher electron densities. It is speculated that creation of the main trough is primarily due to different convection patterns near the trough [*Moffet and Quegan*, 1983]. Essentially, this theory states that some convection paths in the ionosphere do not encounter regions with any ion-electron production mechanisms

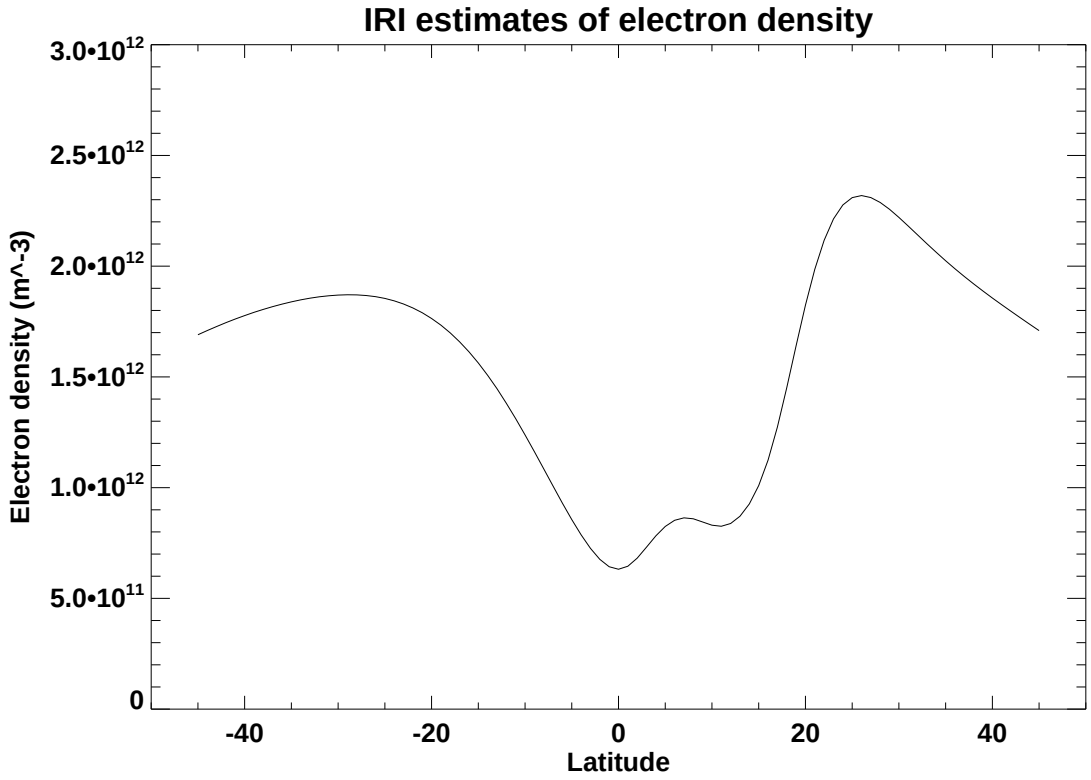

Figure 1.4: Electron density values near the equator estimated from IRI for March 21, 2000, 12 LT, at 300 km altitude.

for several hours. The plasma density in these regions decays over this time due to recombination and creates the main trough. Another possible mechanism for the generation of the main trough is a higher recombination rate due to heating in regions in which the relative speed between ions and neutral particles is large [*Rodger et al.*, 1992].

The magnetic field lines of the Earth in the polar cap and poleward auroral regions of the ionosphere are generally connected directly to the IMF because of merging on the dayside of the magnetosphere, as discussed in Section 1.3.3. On the dayside of the ionosphere the IMF lines that merge in the magnetosphere map down to high latitudes to what is termed the 'polar cusp' [e.g., *Hunsucker and Hargreaves*, 2003]. In this region there is an increase of electron density due to solar wind particles precipitating down magnetic field lines. Similarly, on the nightside of the ionosphere

there exists a region in which highly energetic particles which have been accelerated in the tail of the magnetosphere precipitate down field lines and increase the electron density. Each energetic particle can excite several neutral atmospheric atoms and molecules to both create light known as the aurora and increase the electron density. Between the polar cusp on the dayside and the precipitation region on the nightside, the polar cap is a region with lower electron densities.

The behaviour of the electron density in the F region at middle latitudes has a strong seasonal dependence. Electron densities are lower in the winter than summer during nighttime hours, as expected. However, during the daytime at middle latitudes, a seasonal anomaly exists. Electron densities at middle latitudes during daytime in winter months are much higher than daytime electron densities during summer months. This behaviour is referred to as the seasonal anomaly and is caused by the seasonal variation of atmospheric constituents with altitude in the ionosphere [*Davies*, 1966].

Solar cycle dependence on electron density

As the Sun is the driver of ionization in the ionosphere, it is not surprising that there is a strong solar cycle dependence on electron density values. The eleven year solar activity cycle is characterized by maximum and minimum periods of both sunspot number (a factor that controls solar wind activity) and the intensity of EUV and X-ray radiation. There was a solar maximum in 2002 which was followed by an uncharacteristically deep and long solar minimum which was only showing weak signs of an end in 2009–2010.

The production rate of electron-ion pairs in the ionosphere from either solar photoionization or precipitation of solar wind particles is dependent on the solar cycle. In general, lower electron densities occur during solar minimum conditions and higher electron densities occur during solar maximum conditions. The solar wind in particular can become quite weak during solar minimum conditions [e.g., *Kivelson and Russell*, 1995]. The electron density in the high latitude ionosphere, which is formed largely by precipitating solar wind particles, is highly dependent on

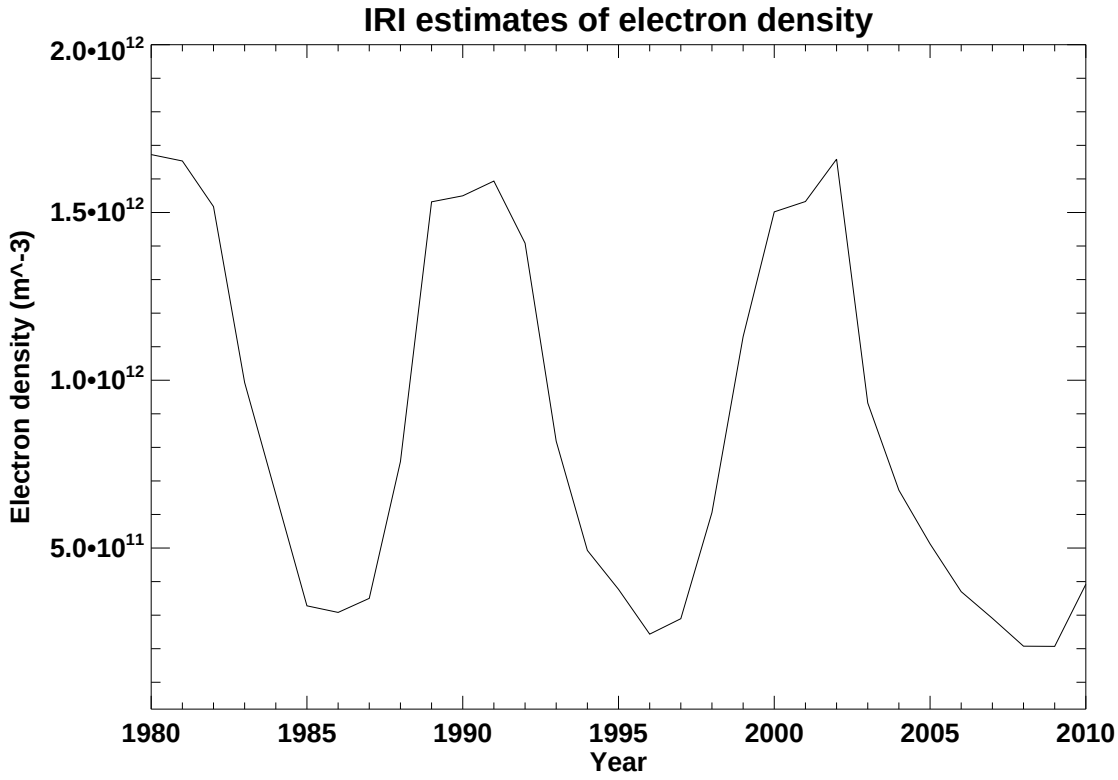

Figure 1.5: IRI estimates of electron density at 300 km altitude as a function of solar cycle.

solar cycle. At lower latitudes there is some dependence of electron density on solar cycle, but not to the same extent as at higher latitudes. Figure 1.5 demonstrates the effect of solar cycle on noontime electron density estimates provided by IRI at an altitude of 300 km over Saskatoon from 1980 to 2010.

Local time dependence on electron density

Once again, as the Sun is the main driver of ion-electron pair production, there is an associated strong diurnal variation of electron density in the ionosphere. The electron density in the dayside F-region ionosphere can be an order of magnitude higher than on the nightside. The variation of electron density with local time depends on other factors such as time of year and latitude. At higher latitudes, auroral precipitation can increase the electron density at nighttime compared to

the daytime. In particular, during winter months when the polar region may not be exposed to any photoionization, it would be expected that auroral precipitation would dominate the production of electron-ion pairs.

Convection of the ionospheric plasma over the polar region of the ionosphere can result in plasma from photoionization on the dayside travelling over the polar region to the nightside. This behaviour results in a so-called 'tongue' of ionization, which stretches from the sunlit dayside ionosphere into the polar cap region [*Foster et al.*, 2005]. This plasma convecting over the polar cap can break up into smaller polar cap patches. Polar cap patches can also be created from fast variations of solar wind flow speed or changes in the IMF on the dayside [*Sojka et al.*, 1993; *Anderson et al.*, 1988]. These patches are between 200 km and 1000 km in size and contain electron density values that are up to ten times that of the background ionosphere. Also, the gradients on the edges of these patches are quite sharp. It is expected that as these patches travel over the polar cap, they would tend to cascade into smaller structures [*Hosokawa et al.*, 2009]. The high gradients at the edges of these patches provide ideal circumstances for the generation of wave-like irregularities which can scatter coherent radar signals (discussed in further detail in Sections 1.4.5 and 1.5.4).

1.4.5 Gradient Drift Instability

Various processes in a plasma can produce regions in which the plasma density becomes irregular and non-uniform. When the processes involved in creating these irregularities have positive feedback loops, the irregularities are unstable and grow in magnitude. Wave-like irregularities in the ionosphere are very important for the operation of many ionospheric radars because if the irregularity has an appropriate wave vector, coherent scatter of the probing radar wave can occur through Bragg-like scattering. This section will briefly describe the gradient drift instability which is one of the most common instabilities that occurs in the F-region ionosphere.

As the name implies, the gradient drift instability [*Simon*, 1963] is a result of gradients in the background electron density. Also of importance is the orientation of the gradient to the electric and magnetic fields in the ionosphere. In the F region,

when a gradient in the background electron density exists perpendicular to both the background electric and magnetic fields, an enhancement of any existing wave-like irregularities in the plasma results. As presented in Figure 1.6, one plasma configuration that allows for the growth of an irregularity through the gradient drift instability is as follows: in the diagram the magnetic field is into the page, the electric field is to the right, the background electron density has a gradient ∇N_e pointing upwards, and a wave-like perturbation develops in the plasma (represented in the figure as an enhancement in density on the left and a depletion in density on the right). The main motion of the plasma is upwards due to the $E \times B$ drift, however some charge separation occurs due to collisions. Collisions cause the ions to have a drift component parallel to the background electric field which causes a build up of positive charge on the rightward edge of the density enhancement. This charge separation results in a secondary electric field δE directed to the left in the enhancement. In the density depletion, the opposite occurs and a similar secondary electric is directed to the right. The $E \times B$ motion from these secondary electric fields drives plasma in the enhancement downwards (into a region with lower background density) and plasma in the depletion upwards (into a region with higher background density). Essentially, compared to the local background density, both the enhancement and depletion appear more severe and the irregularity grows. On the edges of the irregularity, smaller-scale gradient drift waves can also develop. As the process proceeds, large scale structures, such as polar cap patches, can cascade down to form $\sim$10-m scale irregularities which are detected by HF radars.

1.5 Ground-based Ionospheric Radio Experiments

Ground-based instruments have been used to study the ionosphere since 1901 when it was first found that radio waves could be affected by a conducting layer in the atmosphere. In 1901 a radio transmission travelled from the British Isles to Newfoundland, which would be impossible with straight line-of-sight transmissions. It was therefore realized that in order to propagate around the curvature of the Earth,

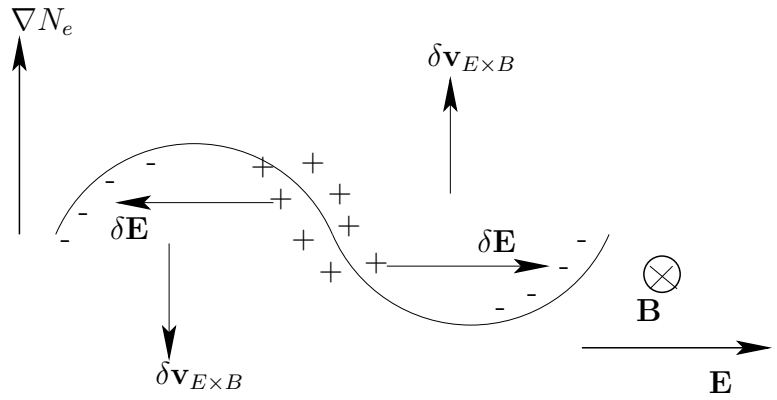

Figure 1.6: Geometry required to produce gradient drift instabilities in the F region.

the radio waves must have bounced off of an ionized and reflective layer in the atmosphere [*Hunsucker and Hargreaves*, 2003]. Study of the ionosphere is difficult by direct methods, atmospheric measuring balloons are not able to reach sufficient altitudes [*Pfotzer*, 1972] and atmospheric drag results in satellite orbits that must be above the lower portion of the ionosphere (orbits below ∼300 km will decay very rapidly [*Montenbruck and Gill*, 2000]). Remote sensing of ionospheric parameters can be accomplished relatively easily and inexpensively by radio instruments deployed on the ground. Many different ground-based instruments have been and are employed around the Earth to study various properties of the ionosphere and, by extension, the magnetosphere and solar wind. This section will briefly list and explain the most widely used ground-based radio instruments such as: ionosondes, riometers, incoherent scatter radars, and coherent scatter radars. As it is one of the focuses of this research, the global network of coherent HF radars known as SuperDARN will be explained in detail.

1.5.1 Ionosondes

An ionosonde is a device that transmits and receives radio wave pulses at various frequencies [*Bibl and Reinisch*, 1978]. As will be discussed in more detail in Section 1.7, a radio wave that propagates through a plasma will be reflected if the local plasma

frequency (given by Equation 1.1) is equal to, or larger than, the propagating radio wave frequency. This reflection criteria can be used by ground-based ionosondes to measure the electron density profile in the ionosphere up to the F-region peak density or to measure the line-of-sight velocity of plasma in the ionosphere [*Reinisch et al.*, 1998].

An ionosonde transmits a pulse at a given frequency and measures the time it takes for the pulse to propagate from the transmitter to the layer in the ionosphere with a plasma frequency equal to the pulse frequency and back to the (typically) co-located receiver. This travel time is used to roughly determine the altitude of the plasma layer that reflected the pulse. Actually, since the electron density in the ionosphere increases gradually, a pulse propagating through the ionosphere will slow down as it approaches the reflecting layer, which results in an overestimation of the height of the layer. For this reason the height recorded by an ionosonde is termed the 'virtual height' and is higher than the actual height of the reflecting layer. When mapping the electron density in the ionosphere, an ionosonde systematically transmits and receives pulses at a range of frequencies between ∼0.5 MHz and 20–30 MHz. An idealized example of a plot of ionosonde pulse frequency versus virtual height, called an 'ionogram', is presented in Figure 1.7. As the labels indicate, the ionogram in Figure 1.7 shows the altitude and peak plasma frequency of the E region, the F1 peak, and the F2 peak. The actual electron density profile for a given ionogram can be determined using a recursive algorithm to convert the virtual height to real height [e.g., *Titheridge*, 1985]. An ionogram such as the one presented in Figure 1.7 can be produced in just a few seconds (depending on the required resolution). Ground-based ionosondes are scattered about the entire Earth and continuously provide enormous amounts of information about the electron density distribution in the ionosphere. Data from these ionosondes represents an important contribution to empirical models used by the International Reference Ionosphere (IRI) model to predict F-region electron densities below the f_oF2 peak [*Bilitza*, 2001].

One limitation of a ground-based ionosonde is that it does not provide any information about the ionosphere above the F-region peak density. Any ionosonde pulse

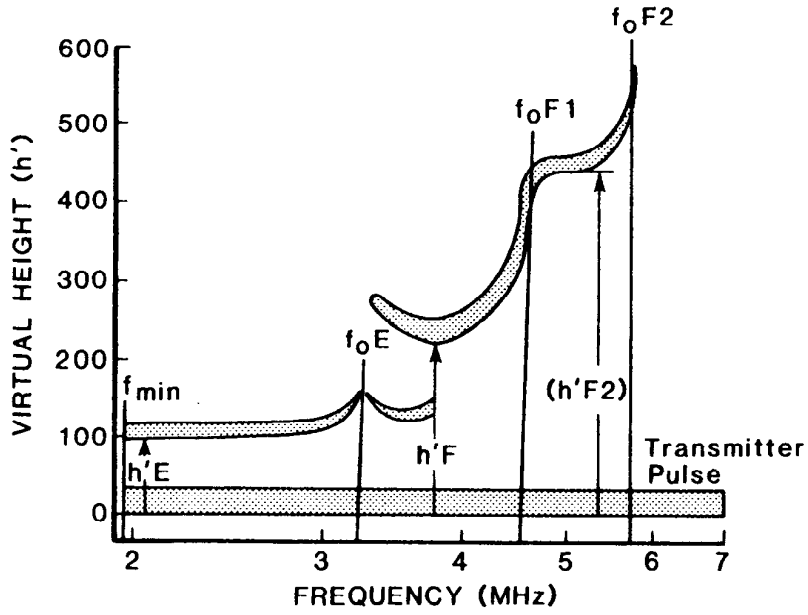

Figure 1.7: An example of an idealized ionogram. The figure shows the virtual heights of the E region $h'E$, the bottom of the F1-layer $h'F$, and the bottom of the F2-layer $h'F2$. Also labelled are the peak plasma frequencies of the E region f_oE, F1-peak f_oF1, and F2-peak f_oF2. Figure 4.3 from *Hunsucker and Hargreaves* [2003].

with a high enough frequency to propagate through the F-region peak will not be reflected back to the receiver. Since the majority of the electron density in the ionosphere is above the f_oF2 peak, this can be a limitation for assisting with radio wave experiments and communications with satellites above the peak. Placement of an ionosonde on an orbiting satellite, termed a topside sounder, allows electron density profiles of the upper region of the ionosphere to be made. Topside sounders will be discussed in more detail in Section 1.6. One area of the ionosphere that can not be measured by ionosondes is the trough-like region of the ionosphere between the E-region peak and the bottom of the F region. Radio signals launched from ground-based ionosondes will be reflected by the E-region peak density before they reach this trough while signals transmitted from space-based ionosondes will be reflected by the F-region peak.

A collection of ionosonde stations located in Canada make up the Canadian Advanced Digital Ionosonde (CADI) network [*MacDougall et al.*, 1995]. A CADI ionosonde consists of a transmitter and four receivers spread out to allow interferometry measurements to be performed. In addition to performing swept-frequency scans for monitoring ionospheric electron density profiles, the CADI ionosondes can also be run in a fixed frequency mode which allows Doppler drift velocities of ionospheric plasma to be measured [*Grant et al.*, 1995]. Measurements of drift motion are performed by transmitting pulses at a fixed frequency that is less than the peak plasma frequency in the F region. The fixed frequency pulse is reflected in the ionosphere and the returned signal is detected by the four separate receivers on the ground. These receivers are spaced so that interferometry measurements can be performed to determine the direction-of-arrival of the returned pulse. The Doppler shift of the returned pulse is also measured to determine ionospheric drift velocity. These Doppler shift measurements are made with 30-s resolution. At present there are six operational CADI ionosondes which contribute to the Canadian High Arctic Ionospheric Network (CHAIN) [*Jayachandran et al.*, 2009]. The CHAIN group of instruments also includes several ground-based GPS receivers, which measure the Total Electron Content (TEC) along a line between the receiver and a GPS satellite in space.

1.5.2 Riometers

During strong solar activity, particles precipitating in the auroral zone can penetrate to relatively low altitudes. These particles can ionize the usually neutral D region and cause HF radio signals to be completely absorbed [*Hargreaves and Sharp*, 1965]. This phenomenon was first observed by ionosondes which tended to not receive signal during high solar activity. This blacking out of ionosonde signals can be used as a measurement of ionospheric radio absorption; however, as each ionosonde has a different sensitivity, this technique is limited. A more quantitative measurement of radio absorption in the D and lower E regions of the ionosphere is obtained by using a device called a riometer [*Little and Leinbach*, 1959].

A riometer (Relative Ionospheric Opacity Meter) is essentially just a passive radio receiver which measures the absorption of a fixed-frequency signal travelling through the ionosphere. Typical riometers measure the intensity of cosmic-radio noise at ∼30 MHz, which is a high enough frequency to ensure that signal will not be reflected by the dense plasma in the F region of the ionosphere. Since the cosmic-radio noise is constant, absorption can be measured by taking the difference between the received signal intensity and the intensity during a quiet day. Riometers typically provide a value for the amount of absorption that would be expected to occur to a radio wave at a frequency of 30 MHz. Since the absorption of a radio wave in a plasma is proportional to the square of the frequency, a simple conversion can be performed to determine the amount of absorption at any frequency given the level of absorption at 30 MHz.

Several riometer stations spread throughout the auroral zone map the level of absorption as a function of location [*Rostoker et al.*, 1993]. These maps are used to determine if ground-based radio instruments and commercial communication devices will function properly or if transmitted signals will be absorbed in the D region.

1.5.3 Incoherent scatter radars

For decades after the discovery of the ionized portion of the Earth's atmosphere, ionosondes were the primary radio instruments used for study of the ionosphere. One limitation of ground-based ionosondes is the inability to study the ionosphere above the F-region peak altitude and, when the E-region peak is very dense, between the E and F regions. An incoherent scatter radar (ISR) [*Gordon*, 1958; *Bowles*, 1958] uses much higher frequency waves and does not rely on total reflection to obtain a signal and, as such, does not have the limitations of an ionosonde.

Incoherent scatter radars are able to provide information about a variety of ionospheric parameters. As will be discussed in more detail below, the line-of-sight velocity of the plasma, the electron and ion temperature, and the plasma density are all quantities that an ISR can measure at a variety of ranges along the radar beam. An incoherent radar transmits a short VHF or UHF pulse into the ionosphere (all

current ISRs operate at frequencies of ∼50 MHz or higher [*Kelley*, 2009]). At these high frequencies, the radar signal is mostly unaffected by the ionosphere; however, a small amount of energy is scattered by the electrons along the radar beam. When the wave pulse encounters an electron, the oscillating electric field of the wave causes acceleration and oscillation of the electron. The oscillating electron behaves as a small dipole antenna and re-radiates an electromagnetic wave at nearly the same frequency as the radar wave. Some of this scattered energy travels back to the (typically) co-located radio receiver on the ground. Each electron that the transmitted wave encounters will radiate some energy back to the receiver but, due to the random nature of the electrons, the signals are out of phase (the reason for naming the radars 'incoherent'). The relative amount of energy that is scattered back to the radar by ionospheric electrons is very small so ISRs must transmit using very high power.

After a pulse is transmitted, the radar continuously receives signal. Range is determined by assuming speed of light propagation in a vacuum and halving the delay time for a return signal. Different ranges can be examined by analyzing the signal at various appropriate delay times. An example of the Doppler spectrum from an idealized incoherent scatter echo is presented in Figure 1.8. At a given range, each electron encountered by the wave pulse will scatter a small amount of signal back to the receiver. As the number of electrons at a given range increases, the power of the returned signal increases. Therefore, the total echo power received at a particular range (represented by the area under the curve in Figure 1.8) provides a measure of electron density at that range. Since the returned echo power naturally decreases with range, normalization of the signal must be performed to determine the overall electron density profile. An ISR will often have an ionosonde station nearby which can be used to calibrate the electron density profiles by providing an accurate measurement of the F-region peak density.

The electrons that scatter the incoherent radar wave pulse are not stationary. The electrons have random thermal motions and may also have a bulk drift motion along the radar beam direction. The thermal motion of the electrons results in a broadening of the received spectrum because the motion of each electron will cause a

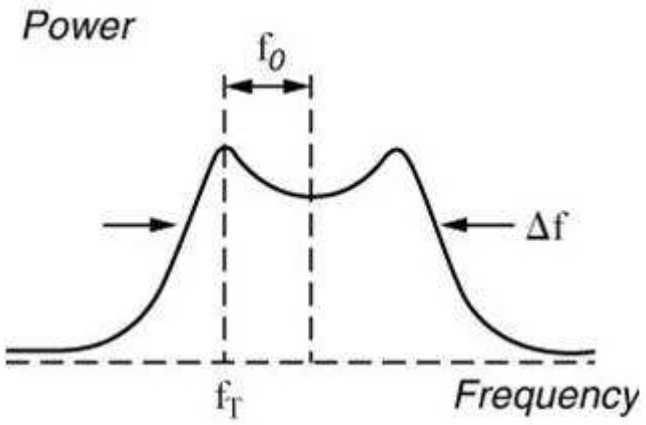

Figure 1.8: An example of an idealized incoherent radar Doppler spectrum. The figure presents the received power as a function of frequency. f_T represents the transmitted frequency and f_o is the Doppler shift (from which the line-of-sight velocity is determined). The spectral width Δf is a measure of the ion temperature. The area under the curve represents the received power and can be used to measure the electron density. Figure A.1 from *Kelley* [2009].

different Doppler shift to the returned wave. If there is more thermal motion, there will be more spread of frequencies that return to the receiver. Since the electrons are linked to the ions, the width of the returned echo, represented by Δf in Figure 1.8, is actually a measure of the ion temperature [*Bowles*, 1958]. The electron temperature can also be measured by an incoherent radar by analyzing the shape of the Doppler spectrum. The bulk motion of the electrons and ions in the ionosphere along the line-of-sight of an ISR can be determined by measuring the overall Doppler shift of the entire spectrum (represented by the frequency offset f_o in Figure 1.8).

The first dedicated incoherent scatter radar was built at Arecibo, Puerto Rico [e.g., *Tepley*, 1997] in 1959. This famous radio instrument is the largest in the world and is located at geographic latitude 18.3°N. Although famous for radio astronomy studies, Arecibo was originally built to study the ionosphere of the Earth. Several incoherent scatter radars now operate at equatorial, middle, and high latitudes. An ISR operates on Canadian soil near Resolute Bay, Nunavit [*Bahcivan et al.*, 2010]. This new ISR is located deep in the polar cap region (geographic coordinates: 75.0°N, 95.0°E).

EISCAT

Line-of-sight ion velocity and electron density data from one particular ISR, the European Incoherent SCATter (EISCAT) radar [*Rishbeth and van Eyken*, 1993], has been used for the research in this thesis. The transmitter for the EISCAT system operates at 931 MHz and is located in Tromsø, Norway (geographic coordinates: 69.6°N, 19.2°E). The EISCAT radar system also consists of two passive receiving stations located in Kiruna, Sweden (geographic coordinates: 67.9°N, 20.4°E) and Sodankyla, Finland (geographic coordinates: 67.4°N, 26.6°E). Use of these two passive receivers, along with the Tromsø receiver, allows three independent measurements of line-of-sight drift velocities to be made at a set location in the ionosphere. Analysis of these tristatic velocity values allows the full ionospheric velocity vector to be determined. A comparison of Hankasalmi SuperDARN data to EISCAT tristatic velocity values from 1995-1999 is the primary focus of Chapter 5 of this thesis.

1.5.4 Coherent scatter radars

Plasma irregularities in the ionosphere, such as the gradient drift instability discussed in Section 1.4.5, can become intense enough to scatter probing radio signals. When the wavelength of these irregularities is equal to one-half the radar wavelength, coherent Bragg-like scattering can occur. The wave reflected by each irregularity wave-front is in phase with the wave reflected by subsequent wave fronts and a strong signal is received by the radar system. Unlike an incoherent scatter radar, the frequency spectrum recorded by the receiver measures the properties of the wave-like irregularity, not the individual electrons. Therefore, coherent radar systems are not able to directly measure electron density and plasma temperatures, but they can measure the coherency and line-of-sight velocity of the ionospheric irregularities. In the F region, it has been demonstrated that the plasma irregularities drift at the same velocity as the background plasma [*Villain et al.*, 1985] so coherent radars effectively measure the bulk drift of the ionospheric plasma.

One benefit of coherent scatter radar systems over incoherent radars is that, be-

cause of the coherent nature of the returned echo, much less transmitted power is required to provide meaningful backscatter signal. Due to this low power requirement, coherent radar systems are much less expensive and less complex to build than incoherent radar systems. ISR stations can also detect coherent scatter from ionospheric irregularities and, due to the much higher initial transmitter power, these result in saturation of the receivers unless the signal is significantly attenuated.

Aside from the lack of information about electron density and temperature, the main drawback to coherent radar use is that measurements can only be made when the radar wave vector is parallel to the plasma irregularity wave vector. Since most irregularities develop parallel to the magnetic field lines of the Earth, this typically requires the radar wave vector to be perpendicular to the magnetic field lines. At VHF and higher radar frequencies, for which there is no refraction of the wave, this aspect sensitivity requirement limits the range of locations at which measurements can be made. At equatorial latitudes, the magnetic field of the Earth is nearly horizontal, so coherent radar measurements of ionospheric irregularities may only be made when the radar beam is roughly vertical. At higher latitudes, VHF radar beams must be nearly horizontal to scatter from irregularities which are aligned along the nearly vertical magnetic field lines. This requirement limits VHF coherent radar observations to the E region at higher latitudes [*Fejer and Kelley*, 1980; *Kelley*, 2009].

Coherent scatter radars that use HF (3–30 MHz) instead of VHF or UHF operating frequencies have been developed to overcome the aspect sensitivity limitation for high latitude studies. Since the usual plasma frequency in the ionosphere is between ∼1–10 MHz, radio wave frequencies between ∼10–20 MHz are able to propagate, however, they are significantly refracted by the ionospheric plasma. Waves transmitted at frequencies higher than, but comparable to, the plasma frequency in the ionosphere tend to refract downwards resulting in some waves propagating in an essentially horizontal direction (over-the-horizon). The refraction to roughly horizontal allows wave propagation that is perpendicular to the magnetic field lines in the F region of the high latitude ionosphere. Using this refractive effect, high latitude HF

radars can obtain coherent scatter, and corresponding ionospheric drift velocities, throughout the auroral and polar ionosphere of the Earth. The magnetoionic and wave propagation theory which describes this refractive effect will be discussed in Section 1.7.

Although the combination of HF radar frequency and the plasma frequency of the ionosphere allow for significant refraction, and therefore an increased field-of-view, *Gillies et al.* [2009] has shown that this combination can also result in systematic underestimation of the coherent HF radar velocity measurements. All radars determine the velocity of a scattering object v_s by measuring the Doppler shift of the returned radar echo and applying the following equation:

$$v_s = \frac{\Delta f_D v_p}{2f} = \frac{\Delta f_D}{2f}\frac{c}{n_s}, \tag{1.10}$$

where, Δf_D is the Doppler shift, v_p is the phase speed of the radar wave at the scattering location, f is the radar frequency, c is the speed of light in a vacuum, and n_s is the refractive index at the scattering location. As will be demonstrated in Section 1.7, the refractive index for HF radio waves in a magnetoionic medium, such as the ionosphere, is less than unity. Since there has been no method to measure refractive index in the scattering volume, and it is a highly variable quantity which depends on the electron density, analysis of HF coherent radar data has always been performed by assuming a refractive index of 1.0. In actuality, the refractive index at the location of scatter for a coherent HF radar wave is typically $\sim$0.7–0.8 [*Gillies et al.*, 2010a]. This indicates that all coherent HF radar measurements that assume the refractive index is 1.0 actually underestimate Doppler velocities by 20–30%.

SuperDARN

The largest array of HF coherent scatter ionospheric radars is the Super Dual Auroral Radar Network (SuperDARN) [*Greenwald et al.*, 1995; *Chisham et al.*, 2007]. This global array of HF radars has been built over the last two decades to include more than 20 radars spread throughout the northern and southern hemispheres. It is typical to have two SuperDARN radars measure the line-of-sight component of

the plasma drift velocity in the same region of the ionosphere, but from different directions (hence the term 'Dual' in SuperDARN). The combination of the two line-of-sight velocity vectors can provide the component of the full velocity vector in the plane perpendicular to the magnetic field of the Earth.

A SuperDARN radar consists of 16 antennas which are phased to transmit radio waves along one of 16 different beam directions. The beams directions are separated by 3.24°, providing a total azimuthal coverage of 52°. Each beam typically samples 75 range gates, each with a range resolution of 45 km. In normal operation each beam is sampled for 3 or 7 s, and a full scan of all 16 beams is accomplished in one or two minutes, respectively. The velocity, backscatter power, and spectral width are recorded for each range gate, that receives backscatter, on every radar, every one or two minutes. Along with the main array of 16 antennas, several SuperDARN radars are equipped with an interferometry array of four antennas placed ∼100 m from the main array. The phase difference between the signal received by the interferometry array and the main array is used to provide a measure of the elevation angle at which an echo is received [*André et al.*, 1998; *Milan et al.*, 1997].

The ∼20 SuperDARN radars spread throughout the northern and southern hemispheres operate continuously to provide ionospheric convection velocities in hundreds of range cells every one or two minutes. Ionospheric models are used to fit the line-of-sight velocity data to create large-scale ionospheric convection maps in both hemispheres. As the F-region plasma irregularities follow the $E \times B$ drift motion and the magnetic field is relatively constant, these velocity maps can be used to infer ionospheric electric fields [*Ruohoniemi and Baker*, 1998]. Measurement of ionospheric electric fields allows creation of high latitude electric potential contour maps which are used to determine the cross polar cap potential (CPCP) (discussed in Section 1.3.3).

A further capability of some of the SuperDARN radars is to operate in a *Stereo* mode in which two receiving channels can be sampled simultaneously [*Lester et al.*, 2004]. The Co-operative UK Twin Located Auroral Sounding System (CUTLASS) radars are the set of two SuperDARN radars located in Hankasalmi and Pykkvibaer.

The CUTLASS radars were the first to develop the Stereo mode capability and now two southern hemisphere radars also have this capability (Syowa South and TIGER Unwin) [*Chisham et al.*, 2007]. The Stereo mode allows a radar to run two different modes simultaneously. For example, a radar could transmit and receive signal at two different frequencies which can be very useful for providing better coverage and measuring electron density at the scattering location [*Gillies et al.*, 2010a].

Over the years of SuperDARN operation several studies have been performed to confirm that velocities measured by SuperDARN are representative of the actual plasma drift. These studies compared line-of-sight velocities measured by various SuperDARN radars and other ionospheric instruments. As mentioned previously, *Villain et al.* [1985] confirmed that the irregularities which coherent radars detect do indeed drift at the same velocity as the background electron density. Comparisons between SuperDARN velocities and the EISCAT incoherent radar were performed by *Eglitis et al.* [1998] and *Davies et al.* [1999]. These studies found that velocities measured by both SuperDARN and EISCAT were comparable, but velocities measured by SuperDARN were systematically slower than velocities measured by EISCAT, especially in the *Davies et al.* [1999] study. Similar results were reported by *Xu et al.* [2001] and *Xu* [2003] in studies which compared SuperDARN velocities to velocities measured by the Sondrestrom incoherent scatter radar. Comparisons between line-of-sight velocities measured by various SuperDARN radars and drift velocities measured by DMSP (Defense Meteorological Satellites Program) satellites were performed by *Drayton et al.* [2005] and *Drayton* [2006]. Like the SuperDARN-ISR comparisons, these studies found that SuperDARN measured similar, but slightly lower, velocities compared to the DMSP satellites. One of the main focuses of this thesis research was to re-examine the comparisons by *Davies et al.* [1999] and *Drayton et al.* [2005] with the inclusion of an estimate of refractive index.

1.6 Ionospheric Satellites

1.6.1 Canadian topside sounders

The Canadian Alouette 1 satellite was launched in 1962 [e.g., *Hartz*, 1964]. The Alouette 1 spacecraft measured the local magnetic field strength and performed topside electron density soundings of the ionosphere. A topside sounder is essentially an ionosonde attached to an orbiting satellite and is used to measure the electron density in the ionosphere from the altitude of the satellite down to the F-region peak (the 'topside' of the ionosphere) [*Knecht et al.*, 1961]. Alouette 1 was designed to operate for one year, however it actually provided data for ten years. The Alouette 2 satellite was nearly identical to Alouette 1 and was launched in 1965. The topside soundings from the the Alouette satellites are the primary data used in predicting (modelling) the topside ionospheric electron density in the International Reference Ionosphere (IRI) model [*Bilitza*, 2001].

A new class of Canadian satellites called the International Satellites for Ionospheric Studies (ISIS) was developed after the success of the Alouette program [*Franklin and Maclean*, 1969; *Daniels*, 1971]. ISIS 1 was launched in 1969 and ISIS 2 was launched in 1971. Each satellite was again equipped with a sounder to measure the electron density distribution of the topside of the ionosphere. Additionally, ISIS 1 and 2 contained instruments to measure ion and electron temperatures, ion masses, and magnetic field strength. The ISIS 2 satellite was equipped with cameras to record some of the first optical images of the auroral oval from space. The topside sounding instruments on both satellites were also used as passive receivers of ground-based radio waves. Dedicated ground stations transmitted HF radio waves through the ionosphere and these radio waves were received by the ISIS satellites. Analysis of the signal received by ISIS 2 from a ground transmitter located in Ottawa in 1978 is the topic of Chapter 2. The ISIS 2 satellite operated until 1990.

1.6.2 The CASSIOPE Satellite

In 2011, the Canadian designed and built CAScade, Smallsat, and Ionospheric Polar Explorer (CASSIOPE) satellite will be launched [*Yau et al.*, 2002; *Yau et al.*, 2006]. CASSIOPE will be one of the first Earth observation space science satellite entirely built by Canada since ISIS 2 in 1971. The CASSIOPE satellite bus is divided into two payloads. A commercial communications payload, called Cascade, is a proof-of-concept data transferring system. Cascade will be used as a large data storage and delivery system for commercial purposes (e.g., data transferring from remote locations such as oil and gas mines). The scientific payload is the enhanced Polar Outflow Probe (ePOP) which consists of eight space science instruments.

- The Imaging and Rapid-scanning ion Mass spectrometer (IRM) instrument will measure the velocity distribution and composition of ions of eV energies near the satellite. This instrument will provide *in situ* plasma density measurements.

- The Suprathermal Electron Imager (SEI) instrument will measure the energy distribution and pitch angle of electrons of energies 1–100 eV *in situ*.

- The Neutral Mass Spectrometer (NMS) will measure the velocity and composition of neutral particles *in situ*.

- The MaGnetic Field instrument (MGF) will measure the local magnetic field.

- The Fast Auroral Imager (FAI) will measure optical auroral emissions in a range of wavelengths from 650–1100 nm.

- The GPS Attitude and Positioning experiment (GAP) will provide data on satellite position and attitude. GAP will also perform ionospheric tomography measurements with GPS satellites.

- The Coherent Electromagnetic Radio tomography (CER) instrument will transmit beacon signals at 150 MHz, 400 MHz, and 1067 MHz. These signals will be

detected by a chain of ground receivers to provide tomography measurements of ionospheric electron densities.

- The Radio Receiver Instrument (RRI) will receive HF waves from dedicated ground transmitters in the frequency range of 10 Hz to 18 MHz.

There are three main scientific objectives to be studied with the ePOP mission. The first is the study of ion outflows from the polar regions of the Earth. In addition to providing paths for particle precipitation of charged particles to enter the ionosphere from the magnetosphere, the nearly vertical magnetic field lines in the polar regions also allow transport of ionospheric ions up into the magnetosphere [*Chappell et al.*, 1987]. The second area of study for the ePOP mission is ionospheric tomography [e.g., *Bernhardt et al.*, 1998]. The CER instrument will transmit VHF and UHF signals to various ground receivers and the phase of the signal received at each ground transmitter will give a measure of the electron density between the ePOP satellite and the ground receiver. The electron density information provided by each ground receiver can be combined to provide a tomographic map of the ionosphere. The GAP instrument will perform a similar experiment, although it will receive UHF signals from various GPS satellites. Again, the phase of the wave received by GAP will give a measure of the electron density in the ionosphere. The third scientific goal of the ePOP mission is the study of wave-particle interactions and radio wave propagation in the ionosphere. The RRI instrument on ePOP will receive HF waves from various dedicated ground transmitters. The characteristics of the signal received by the RRI will give information about the ionosphere between the ground transmitter and satellite. This third objective will be discussed in more detail in the next section.

1.6.3 RRI-SuperDARN experiment

The RRI instrument on the ePOP satellite will be used to measure radio wave signals between 10 Hz and 18 MHz. The RRI will consist of four 3-m monopole antennas which will be oriented to create effectively two 6-m orthogonal dipole antennas. The

Canadian SuperDARN radars (only the Saskatoon radar at this time) will transmit HF waves which will propagate through the high-latitude ionosphere and be detected by the RRI.

When the ePOP satellite orbits over a SuperDARN radar, it can be oriented so that the crossed dipole antennas will be able to measure the full polarization of the received transionospheric wave. Direction-of-arrival measurements may be made by the RRI because each monopole antenna will have a separate receiving channel [*James*, 2003]. Knowledge of the direction-of-arrival of the received waves will be useful to fully determine the propagation paths of HF waves. The simultaneous measurement of direction-of-arrival by RRI and elevation angle by SuperDARN will allow for the determination of the location of coherent scatter.

Measurement of various signal parameters by the RRI as it orbits over a SuperDARN radar will provide information about electron density structures and absorption in the ionosphere. The electron density in the ionosphere is highly variable and often consists of enhancements and depletions of scale sizes from several meters to hundreds of kilometers. A wave propagating through the ionosphere will be affected by these electron density structures. Modelling has been performed by *Wang et al.* [2004] to determine the effect these structures have on signal characteristics such as: power, delay time, and direction-of-arrival. The effect of ionospheric electron density structures on the specifics of wave polarization has been modelled by *James* [2006], *James et al.* [2006], *Gillies et al.* [2007], and *Gillies et al.* [2010b]. These studies modelled the Faraday rotation, differential mode delay time, and relative propagation mode power which will be received by the RRI for various propagation conditions. Using these studies as a basis, interpretation of the signal received by the RRI when the experiment is operational will allow for detection, measurement, and better understanding of ionospheric structures.

1.7 Magnetoionic Theory

1.7.1 Wave Polarization

One of the primary signal characteristics that will be measured by the RRI on ePOP is wave polarization. As the RRI is able to measure the full polarization state of a received HF wave, the variables that define the polarization of a propagating electromagnetic wave are presented. The variables and coordinate system used in this thesis are based on *Budden* [1961]. The polarization of a wave is defined by the shape that the end point of the electric field vector of the wave traces as the wave propagates. The general polarization state of a wave is elliptical. An example of a polarization ellipse is presented in Figure 1.9. The polarization ellipse can be fully defined by the semi-major and semi-minor axes a and b respectively, and the orientation angle ψ, as shown. The ellipticity angle χ (not shown) defines the shape of the polarization ellipse and can be determined from the semi-major and semi-minor axes by:

$$\chi = \pm \arctan(b/a). \tag{1.11}$$

The polarization ellipse can range from linear (ellipticity of 0°) to circular (ellipticity of ±45°). Figure 1.9 also presents the orientation of the coordinate system when the wave propagates in a region with an external magnetic field $\vec{B}$ (such as the ionosphere of the Earth). By convention, the wave propagation direction is defined to be along the z-axis and the external magnetic field $\vec{B}$ is placed in the x-z-plane. The angle between the propagation direction and the magnetic field is the aspect angle θ.

1.7.2 Radio waves in a magnetized plasma

When a radio wave propagates in a magnetized plasma, such as the ionosphere, it decomposes into two different modes of propagation which have different refractive indices and different polarizations. The two modes of propagation are termed the Ordinary (O) and Extraordinary (X) modes and are affected differently by the external magnetic field. The Appleton-Hartree equation [*Appleton and Builder*, 1933;

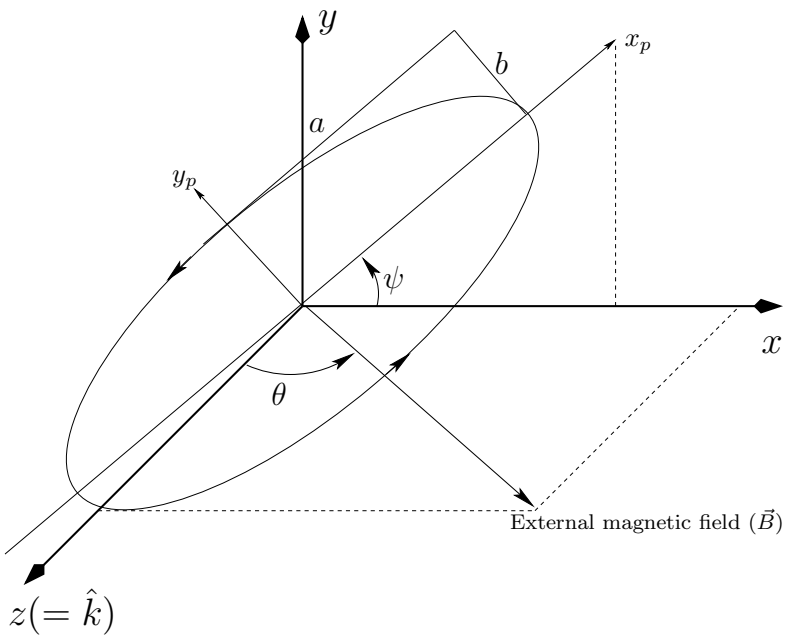

Figure 1.9: General polarization state ellipse.

Hartree, 1929] can be used to determine the index of refraction for each of these two modes of propagation when collisions between charged and neutral particles are not considered:

$$n^2 = 1 - \frac{X}{1 - \frac{Y^2 \sin^2\theta}{2(1-X)} \pm \sqrt{\frac{Y^4 \sin^4\theta}{4(1-X)^2} + Y^2 \cos^2\theta}}, \tag{1.12}$$

where X is the squared ratio of plasma frequency to radio wave frequency(f_p^2/f^2), Y is the ratio of gyrofrequency to radio wave frequency (f_c/f), and θ is the aspect angle of the wave. Note that the variable 'X' (in italics) in Equation 1.12 represents the squared ratio of plasma frequency to radar frequency and should not be confused with the 'X'-mode ('X' in normal script) of propagation. The refractive index for the O-mode of propagation is determined by using the positive sign in the denominator of Equation 1.12 and the refractive index for the X-mode of propagation is determined from the negative sign. Inspection of Equation 1.12 reveals that the refractive index of the X-mode will be smaller than the O-mode (the X-mode is affected by the plasma to a greater extent than the O-mode).

In the ionosphere, the magnetic field is roughly constant and the electron density

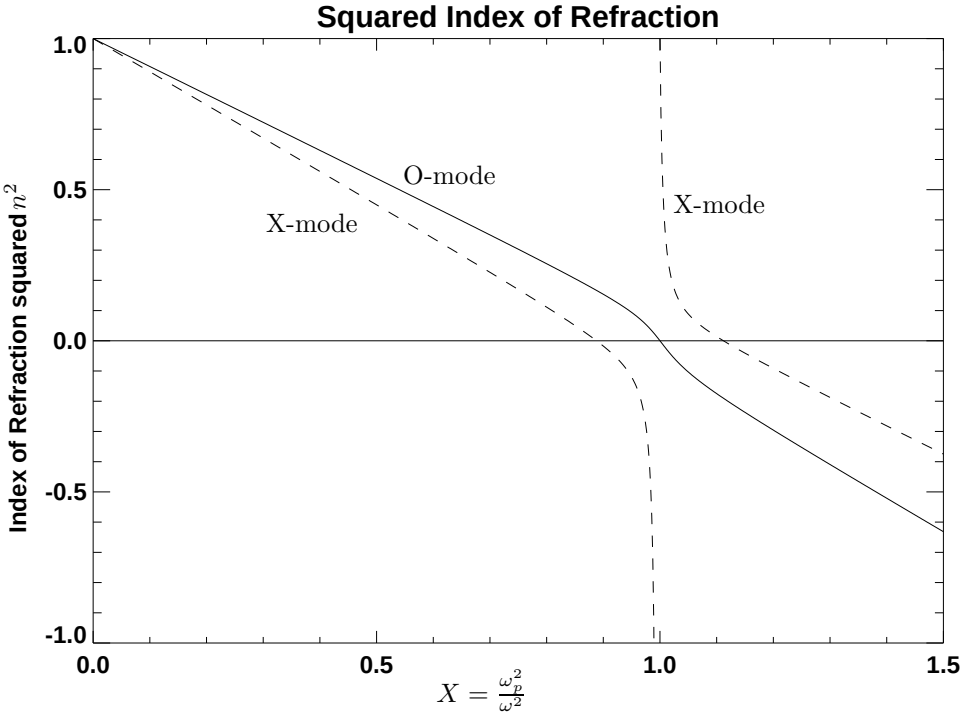

Figure 1.10: Squared refractive index values for the O-mode (solid curve) and the X-mode (dashed curve) as a function of X. The refractive index values were calculated using a constant aspect angle of 40°, a magnetic field strength of 6.0×10^{-5} T, and a radio wave frequency of 15.0 MHz.

is quite variable, so usually the variable of interest in Equation 1.12 is the ratio of plasma frequency to wave frequency X. A plot of the behaviour of refractive index as the ratio X is increased is presented in Figure 1.10. As the electron density increases, the refractive index for both modes decreases and the separation between the O-mode and the X-mode increases. When the plasma frequency is equal to the wave frequency, the refractive index of the O-mode goes to zero and the wave is reflected. This reflection criterion is the principle behind the operation of ionosondes.

The polarization of a propagating wave is found by using the wave polarization ratio ρ [*Budden*, 1961]:

$$\rho = \frac{\mathbf{E}_y}{\mathbf{E}_x}. \tag{1.13}$$

$\mathbf{E}_y$ and $\mathbf{E}_x$ represent the phasor electric fields of the propagating wave along the y- and x-axes, respectively. The polarization ratio for a given set of propagation

conditions is calculated using the following equation:

$$\rho = i\frac{(Y\sin\theta)^2}{2Y\cos\theta(1-X)} \pm i\sqrt{\frac{(Y\sin\theta)^4}{4(Y\cos\theta)^2(1-X)^2}+1}. \tag{1.14}$$

Equation 1.14 provides two values for the polarization ratio which correspond to the two modes of propagation. The sign and magnitude of ρ determine the sense of rotation and the shape of the polarization ellipse, respectively. In the absence of collisions, the semi-major axis of the O-mode wave is oriented parallel to the x-axis (or parallel to the magnetic field in the plane of polarization) and the semi-major axis of the X-mode wave is oriented parallel to the y-axis (or perpendicular to the magnetic field in the plane of polarization). The solution for Equation 1.14 giving an absolute value for ρ that is less than one corresponds to the O-mode (the magnitude $\mathbf{E}_x$ is larger than $\mathbf{E}_y$) and the solution for Equation 1.14 giving an absolute value for ρ that is greater than one corresponds to the X-mode (the magnitude $\mathbf{E}_y$ is larger than $\mathbf{E}_x$). The total polarization of a propagating wave will be the superposition of the polarizations of the O-mode and X-mode.

Inspection of Equation 1.14 reveals that the polarization of a wave is dependent on the propagation direction with respect to the external magnetic field. When a wave is propagating mostly parallel or anti-parallel to the external magnetic field lines (the aspect angle θ is $\sim 0^\circ$ or $\sim 180^\circ$), it is termed Quasi-Longitudinal (QL) propagation. At the other extreme, when the wave propagation direction is mostly perpendicular to the external magnetic field lines (θ is close to 90°), it is termed Quasi-Transverse (QT) propagation.

Under QL propagation conditions, Equation 1.14 gives values of $\rho = \pm i$ which indicates that the polarization ellipses of the two modes of propagation are circular with opposite senses of rotation. If the relative magnitude of the two modes is equal, the superposition of the two circular waves of opposite sense of rotation will create a linear wave. Recall that the two modes of propagation have different indices of refraction (Equation 1.12) and, therefore, the phase speed or rotation rate of the two circular waves will be different. This difference in rotation rate will cause a change in the orientation angle of the resultant linear wave as it propagates. In essence,

when a linear wave propagates along the magnetic field lines in a plasma, the plane of polarization will rotate. This is called Faraday rotation [*Budden*, 1985]. Faraday rotation will only occur when the wave is propagating in the QL regime and the magnitudes of O- and X-mode circular states are close to equal.

When the wave propagation direction is perpendicular to the external magnetic field lines, QT propagation results. Under these conditions, when $\theta = 90°$, Equation 1.14 gives values of zero for the O-mode and infinity for the X-mode. Axis ratios of zero and infinity represent orthogonal linear waves oriented parallel and perpendicular to the external magnetic field, respectively. As with QL propagation, the two modes in QT propagation have different indices of refraction and a phase difference develops between the modes as they propagate. Assuming the linear polarizations of the individual modes are nearly equal, this phase difference will cause the ellipticity of the resultant wave to oscillate between circular, elliptical, and linear polarization states.

In between the extremes of QL and QT propagation, the polarization of the two propagating modes becomes elliptical. The net polarization of the propagating wave will include both the ellipticity oscillation from the QT regime and the Faraday rotation from the QL regime (in general, the orientation angle and ellipticity of the polarization ellipse will change as the wave propagates). The situation is further complicated when the relative amplitude or power of the two modes of propagation is not equal, as is often the case. A thorough analysis of wave polarization and the relative power of the O- and X-modes is presented in Chapter 3.

1.7.3 Ray path modelling

The ray path modelling or ray tracing performed in this thesis involves the calculation of the path a radio wave travels as it propagates through the magnetized ionosphere. A ray tracing program has been developed at the University of Saskatchewan to calculate the path of an HF radio wave given a wave frequency, electron density profile, and initial propagation direction. The refractive index at each point along the ray path is calculated using Equation 1.12 and Hamiltonian ray path equations

developed by *Haselgrove* [1963] are used to calculate the path that either the O- or X-mode follows as they propagate through the ionosphere.

The ray tracing program can calculate wave paths through either one-dimensional electron density profiles (the profile varies with altitude only) or two-dimensional electron density profiles (the profile varies with both altitude and latitude). Typically the electron density profiles used in the ray tracing for this thesis were generated using the IRI model, although a user supplied profile from any source may be used. The magnetic field information for the ray tracing program is supplied by the IGRF model [*Maus et al.*, 2005]. Modifications of the original program to allow convergence of ray paths at a specific location in the ionosphere (for example, the location of the ePOP satellite) was performed by *Gillies* [2006].

As discussed in Section 1.5.4, HF waves propagating through the ionosphere are refracted downwards towards the horizontal direction. Waves that propagate into the ionosphere at low elevation angles experience more refraction than waves propagating at higher elevation angles. The ray tracing program can be used to simulate this refraction. An example of the propagation of O-mode waves at 15 MHz from the Saskatoon SuperDARN for various elevation angles calculated by the ray tracing program is presented in Figure 1.11. A horizontally stratified IRI electron density profile with a peak density of 10^{12} m^{-3} was used in the calculation of ray paths in Figure 1.11. Notice that waves with elevation angles below $\sim$35° are totally internally reflected by the ionosphere. Waves launched at high elevation angles ($>\sim$60°) propagate through the ionosphere with little deviation.

1.8 Outline of Thesis

This thesis has been written in the manuscript style. Chapters 2 through 5 each consist of a paper published in either *Annales Geophysicae* or the *Journal of Geophysical Research*. Chapter 6 consists of a paper manuscript which has been accepted by the *Journal of Geophysical Research*. Each of Chapters 2 through 6 also contains a short section explaining the significance of the paper and the relation to the rest of the

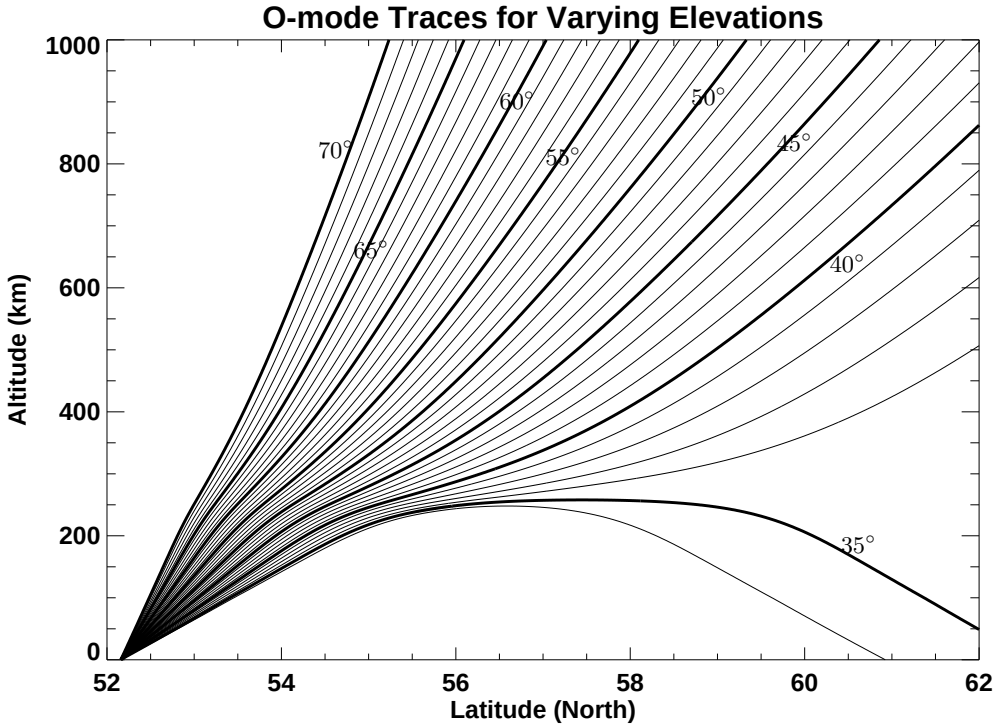

Figure 1.11: Radio wave propagation paths for the O-mode at 15 MHz though a one-dimensional electron density profile with a peak of 10^{12} m^{-3}. The labels on the various ray paths are the elevation angles of the wave at SuperDARN.

thesis.

Chapters 2 and 3 deal with wave simulations performed in preparation for the RRI-SuperDARN experiment. The study described in Chapter 2 covers an analysis of transionospheric HF signal data received by the ISIS 2 satellite in 1978. Various features of the signal were analyzed and ray path modelling was performed. Chapter 3 presents a study of the polarization specifics of the SuperDARN radars and the relative power of the two modes of propagation that will be detected by the RRI. The relative power of the two propagation modes were simulated for various ionospheric conditions. This analysis and modelling of the signal characteristics will be used as the basis for interpreting transionospheric data provided by the RRI instrument on ePOP when it is operational.

Chapters 4 through 6 discuss the underestimation of ionospheric drift velocities

measured by SuperDARN. This underestimation in velocities is due to the neglect of the refractive index in the scattering volume. Chapter 4 presents the effect of refractive index on Doppler velocity calculations made by HF radars. A proxy of the refractive index in the scattering volume was based on using elevation angle measurements made by SuperDARN. It was developed and tested using ray tracing simulations. A comparison between SuperDARN and DMSP measurements of velocity was also performed. Chapter 5 continues the analysis of the elevation angle proxy for refractive index and compares SuperDARN measurements of velocity to EISCAT measurements of velocity. Chapter 6 deals with the development of a new method to directly measure refractive index in the SuperDARN scattering volume using radar frequency shifts.

Finally, Chapter 7 will summarize the main findings of each chapter and discuss the overall conclusions of this work. Possibilities for future work in this area of research are also discussed.

Chapter 2

Transionospheric propagation results from ISIS II

2.1 Introduction

The research presented in this chapter is based on the following publication:

- Gillies, R. G., G. C. Hussey, H. G. James, G. J. Sofko, and D. André, Modelling and observation of transionospheric propagation results from ISIS II in preparation for ePOP, *Ann. Geophys.*, 25, 87–97, 2007.

This research deals with analysis and modelling of transionospheric HF radio wave propagation for the ISIS 2 and ePOP satellites. The results of this study will be used as a basis for interpretation of the results from the RRI-SuperDARN experiment discussed in Section 1.6.3.

2.2 Results

The ePOP satellite will be launched in 2011. The RRI instrument on ePOP will receive HF radio waves transmitted from ground-based instruments such as SuperDARN. Figure 2.1 illustrates some of the possible experiments that will be performed with the RRI-SuperDARN mission. For example, some of the wave energy from the transmitter on the ground may be coherently scattered by F-region irregularities (the ray path labelled 'b' in the figure) and the rest will forward scatter to the receiver on ePOP. The combination of data from the returned signal at SuperDARN (elevation

angle, spectral width, velocity, and backscatter power) and the signal received by the RRI (propagation delay time, polarization, angle of arrival, etc.) will provide information about the propagation path of the wave, the location of the scattering volume in the ionosphere, and the characteristics of the scattering irregularities. Another possible scattering mechanism is demonstrated by ray path 'd' in the figure. In this case, the wave propagation direction is not perpendicular to the magnetic field and Bragg scattering will cause the wave energy to be scattered away from SuperDARN. This indirect scatter will be detected by the RRI instrument and these measurements of the irregularity may be compared to direct measurements made by SuperDARN. Each of these items will broaden the understanding of HF radio wave propagation in the ionosphere and the coherent scattering process for radars such as SuperDARN.

In preparation for the RRI-SuperDARN mission, it was imperative to model the expected signal that will be received by the RRI under various ionospheric conditions. This goal was partly accomplished by analyzing data from a similar experiment performed in 1978 by the ISIS 2 satellite and a HF ground-based transmitter located in Ottawa, Canada, and this work is presented in this chapter as the publication *Gillies et al.* [2007].

The transmitter/receiver on ISIS 2 interlaced the routine topside soundings of the ionosphere with reception of the transionospheric 9.3 MHz pulses sent from the transmitter in Ottawa. Characteristics of signal recorded by the ISIS 2 receiver included splitting of pulses due to the different propagation characteristics of the O- and X-modes and periodic fading of signal intensity resulting from Faraday rotation of the transmitted linear wave. Ray path modelling was performed to simulate the rate of periodic Faraday fading and differential mode delay time as functions of latitude. Good agreement was found between the periodic fade rates and differential mode delays calculated by the model and experimental values measured by the ISIS 2 receiver. When the RRI on ePOP is operational and receiving signal from SuperDARN radars, measurement of the signal parameters discussed in this study will allow estimates to be made of ionospheric electron densities.

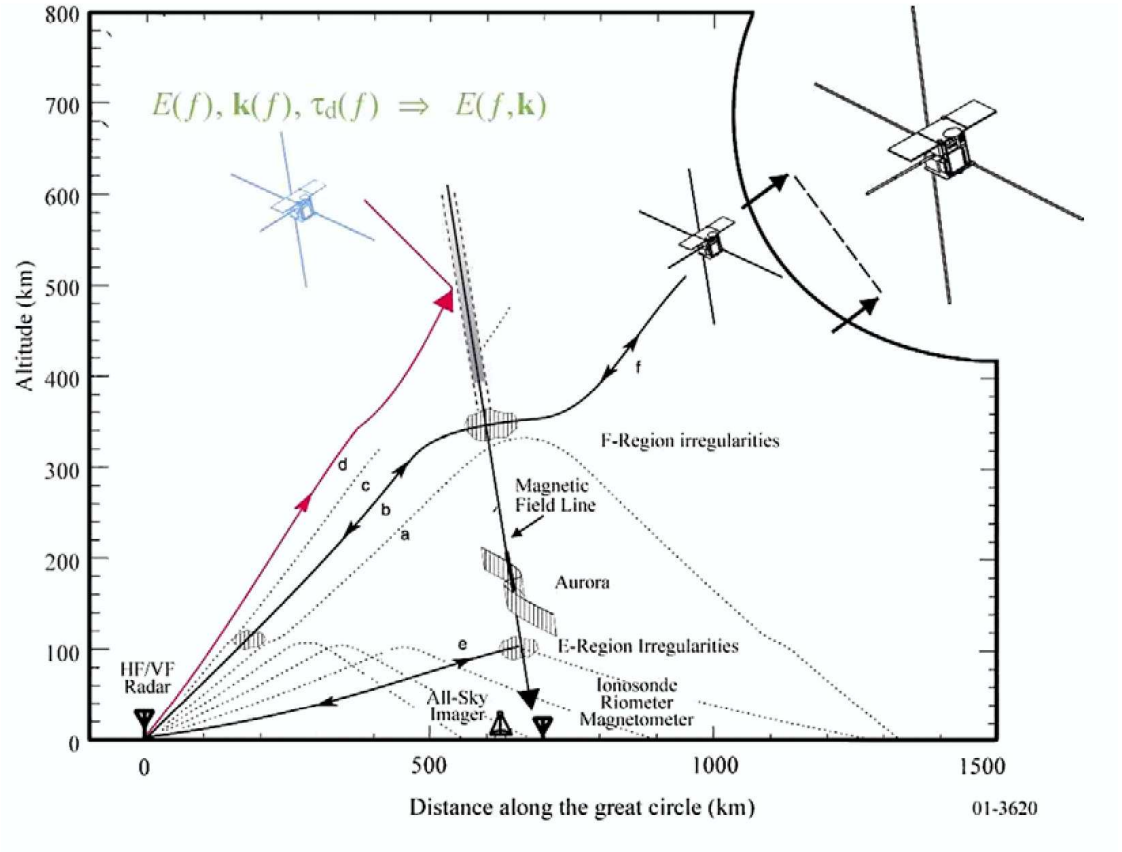

Figure 2.1: Some of the possible RRI-SuperDARN experiments that will be performed. Figure 2 from *Yau et al.* [2006].

One intriguing finding of this study was the fact that periodic Faraday fading only occurred when the ISIS 2 satellite was south of the Ottawa transmitter. It was not possible to completely determine the reason for this behaviour because the ISIS 2 satellite was equipped with only a single dipole antenna and full polarization measurements were not possible. The most probable explanation for the lack of periodic Faraday fading north of the transmitter was that the geometry with respect to the magnetic field of the Earth caused the relative power of one mode of propagation to be much higher than the other. If the two modes did not propagate with near equal power, there could not be Faraday rotation of the wave and no Faraday fading would be apparent. Verification of this theory will be made when the ePOP-SuperDARN experiment occurs. The RRI on ePOP will be equipped with two orthogonal dipole

antennas and will have the ability to perform full polarization measurements of the incoming HF signal. Preparation for analyzing the polarization characteristics of the signal received by the RRI by calculating the amount of power delivered to either mode of propagation by SuperDARN is the topic of the next chapter.

2.3 Published paper

The analysis and modelling of ISIS 2 transionospheric data discussed in this chapter was published in *Annales Geophysicae* in 2007. Presented immediately below is the paper in the journal format:

- Gillies, R. G., G. C. Hussey, H. G. James, G. J. Sofko, and D. André, Modelling and observation of transionospheric propagation results from ISIS II in preparation for ePOP, *Ann. Geophys.*, 25, 87–97, 2007.

Ann. Geophys., 25, 87–97, 2007
www.ann-geophys.net/25/87/2007/

Annales Geophysicae

Modelling and observation of transionospheric propagation results from ISIS II in preparation for ePOP

R. G. Gillies[1], G. C. Hussey[1], H. G. James[2], G. J. Sofko[1], and D. André[1]

[1]Institute for Space and Atmospheric Studies, University of Saskatchewan, Saskatoon, Saskatchewan, Canada
[2]Communications Research Centre, Ottawa, Ontario, Canada

Received: 11 September 2006 – Revised: 4 January 2007 – Accepted: 16 January 2007 – Published: 1 February 2007

Abstract. The enhanced Polar Outflow Probe (ePOP) is scheduled to be launched as part of the Cascade Demonstrator Small-Sat and Ionospheric Polar Explorer (CASSIOPE) satellite in early 2008. A Radio Receiver Instrument (RRI) on ePOP will receive HF transmissions from various ground-based transmitters. In preparation for the ePOP mission, data from a similar transionospheric experiment performed by the International Satellites for Ionospheric Studies (ISIS) II satellite has been studied. Prominent features in the received 9.303-MHz signal were periodic Faraday fading of signal intensity at rates up to 13 Hz and a time of arrival delay between the O- and X-modes of up to 0.8 ms. Both features occurred when the satellite was above or south of the Ottawa transmitter. Ionospheric models for ray tracing were constructed using both International Reference Ionosphere (IRI) profiles and local peak electron density values from ISIS ionograms. Values for fade rate and differential mode delay were computed and compared to the values observed in the ISIS II data. The computed values showed very good agreement to the observed values of both received signal parameters when the topside sounding *fo*F2 values were used to scale IRI profiles, but not when strictly modelled IRI profiles were used. It was determined that the primary modifier of the received signal parameters was the *fo*F2 density and not the shape of the profile. This dependence was due to refraction, at the 9.303-MHz signal frequency, causing the rays to travel larger distances near the peak density where essentially all the mode splitting occurred. This study should assist in interpretation of ePOP RRI data when they are available.

Keywords. Radio science (Ionospheric physics; Radio wave propagation) – Space plasma physics (Numerical simulation studies)

Correspondence to: R. G. Gillies
(rgg646@mail.usask.ca)

1 Introduction

In early 2008, the Cascade Demonstrator Small-Sat and Ionospheric Polar Explorer (CASSIOPE) small satellite is scheduled to be launched (Yau et al., 2002, 2006). The satellite bus, as well as many of the instruments, are Canadian designed and built. The satellite will consist of two payloads, a commercial prototype data storage and forward system called Cascade and a scientific package of instruments called the enhanced Polar Outflow Probe (ePOP). The main scientific goals of ePOP are to study ion outflows from the polar region, radio wave propagation, and ionospheric tomography (Yau et al., 2006). The main instruments used for the radio wave propagation experiment will be ground-based transmitters, such as Super Dual Auroral Radar Network (SuperDARN) HF radars (Greenwald et al., 1995) and Canadian Advanced Digital Ionosondes (CADI) (MacDougall et al., 1995), and the Radio Receiver Instrument (RRI) (James, 2003, 2006a, b; James et al., 2006; Wang et al., 2004) on the ePOP payload.

The RRI consists only of a radio receiver (i.e., a passive system) and four 3-m antennas. Each antenna has an independent receiving channel, but the monopoles will often be operated as two perpendicular 6-m dipole antennas. The ground-based transmitters will radiate HF radio waves. These will propagate through the ionosphere, and the RRI instrument will have the ability to observe various parameters of these arriving waves including their polarization state.

Along the wave propagation path ionospheric electron density enhancements and/or depletions (blobs, patches, troughs, etc.) are expected to modify the received signal parameters. As a result, it is expected that the signal recorded by the RRI will have a complex structure. As an initial step toward interpretation of the signal received by the RRI when it is flown the influence of various ionospheric structures along the propagation path must be assessed. This paper deals with preliminary modelling research which has been performed to achieve this goal. Once the effects of

Published by Copernicus GmbH on behalf of the European Geosciences Union.

ionospheric properties upon the signal are understood it is envisioned that the received signal can be used to measure or at least detect these ionospheric structures.

At this point, no data exist for the SuperDARN-RRI experiment and thus only modelling predictions can be studied. Therefore, it was of interest to examine past transionospheric experiments to provide a first step to deal with SuperDARN-RRI simulations. Examples of such experiments are the transionospheric portions of the International Satellites for Ionospheric Studies (ISIS) satellite missions from the 1970s (Franklin and Maclean, 1969). To this end, data from the ISIS II mission during 1978 have been studied in detail.

2 The ISIS II transionospheric experiment

2.1 Background

The ISIS II satellite (Daniels, 1971) was launched in 1971 into an essentially polar orbit (89° inclination) at 1400 km altitude. The primary instrument on the satellite was a radio sounder consisting of 18-m and 73-m dipole antennas and an HF transmitter and receiver. This instrument was mainly configured for topside soundings of the ionosphere, but for special experiments it was configured to receive signals from ground-based transmitters. For several ISIS II passes over a transmitter located in Ottawa, Canada (Geographic coordinates: 45.42° N, 75.70° W; Geomagnetic coordinates: 56.36° N, 0.53° E), the topside sounder alternated between a swept-frequency ionosonde mode and a fixed-frequency receiver mode. In the ionosonde mode, the satellite would perform a sweep for ∼20 s. Then the sweep would turn off and the signal from a fixed-frequency ground-based transmitter would be received for ∼25 s. This switching occurred throughout a pass over a given transmitter. At the altitude of the satellite, this resulted in a topside scan for approximately 1.2° latitude of satellite travel and then transionospheric data for approximately 1.3° latitude of satellite travel.

The Ottawa transmitter used in this experiment radiated a power of 1 kW at (usually) 9.303 MHz. Other frequencies were used but are not examined in this study. The antennas of the transmitter consisted of two perpendicular dipoles oriented horizontal to the Earth. The transmitting sequence consisted of square wave pulses sent at a repetition frequency of 180 Hz.

For the ISIS II observations presented in this study, passes were selected based on three criteria. First, orbital data of ISIS II had to be available for a particular pass. Second, it was necessary for the data from a pass to have been digitized (Bilitza et al., 2004). The digitized data from these passes were made available by the Alouette-ISIS Data Restoration project of the U.S. National Space Science Data Center (NSSDC, 2004). Finally, a pass was only examined if ground transmitted signal had been received for a significant portion of the pass. The most probable reason for a pass not meeting the third criterion was that the *fo*F2 frequency was higher than or comparable to the transmitted frequency of 9.303 MHz, with the result that the ground-based transmitted waves were reflected back to the Earth. On this basis, a detailed examination was made of eighteen passes from June and July 1978. All of these passes occurred between either ∼01:00–04:00 UT (∼20:00–23:00 LT (local evening)) or ∼13:00–16:00 UT (∼08:00–11:00 LT (local morning)). Finally, it should be noted that all the data were from quiet or slightly disturbed geomagnetic conditions (typical K_p values were between two and three or less). Therefore it was not unreasonable to assume, and the analysis to be presented supports this, that the ionosphere was relatively stable and smoothly varied in both altitude and latitude under these conditions. This is especially true for the ISIS II study wherein the analyzed data was predominantly from directly above or to the south of the Ottawa transmitter. Of course, the ePOP mission is focused on the polar (and auroral) region(s) where the ionosphere can be very active and disturbed geomagnetically. However, the results from the slightly disturbed events presented in this paper will serve as a reference with which to compare the dynamic variations expected during more disturbed periods.

2.2 General signal characteristics

In general, the signal received by ISIS II behaved as expected. The signal was weaker and noisier at satellite locations closest to the Ottawa-transmitter horizon. Directly above the transmitter, the signal was strongest. When the satellite was north of the transmitter, periodic fading of signal intensity at a rate of 0.1 Hz was observed. This fading was caused by the spacecraft spin at a rate of 3 rpm. In the southern portions of the pass, faster periodic fading of signal intensity was observed due to Faraday rotation of the wave as will be discussed in Sect. 2.4. Satellite spin fading should be observed south of the transmitter as well because the dipole receiving antenna was rotating with respect to an incoming linear wave. However, this spin fading was not detectable. The reason is that the Faraday rotation effect and the spinning of the dipole antenna both contribute to the observed fade rate. Since the Faraday fading was typically much higher than 0.1 Hz, it has been assumed that the observed fade rate is effectively only due to Faraday rotation of the wave and the satellite spin has been neglected in the southern portions of the pass. Due to this coupling of satellite spin and the Faraday rotation effect, 0.1 Hz should be added to or subtracted from the measured Faraday fade values, but since it is unknown which way the satellite was spinning relative to the Faraday rotation and 0.1 Hz is quite small compared to the typical fade rates, this error has been neglected. Also apparent in southern portions of the passes was a time delay between the arrival of the two modes of propagation at the satellite. This differential mode delay is discussed in the next section.

2.3 Differential mode delay

When an electromagnetic wave propagates in a magnetoionic medium there exist two modes of propagation, the ordinary mode (O-mode) and the extraordinary mode (X-mode) (Budden, 1961). These modes propagate with different indices of refraction and thus different propagation paths and group speeds result. The different propagation properties of the two modes caused the received signal pulses at ISIS II to be split into separate mode components. This splitting is evidenced as a time delay between the arrival of the O-mode and X-mode at the receiver. An example of differential mode delay is in plot a) in Fig. 1. Differential mode delay is observed at the beginning (O-mode only band above the combined (and dominant) O- and X-mode band) and end (X-mode only band below the combined (and dominant) O- and X-mode band) of each pulse as shown in the top plot in Fig. 1.

The locations and magnitudes of differential mode delay instances were determined directly from observations of the received signal data. The resolution of the available data resulted in an error of ± 0.1 ms in all differential mode delay values. There was measurable differential mode delay in fifteen of the eighteen studied passes and it was mostly observed when the satellite was to the south of the Ottawa transmitter. The magnitude of differential mode delay ranged from 0.1 ms to 0.8 ms. The magnitude was, in general, larger for latitudes farther from the transmitter.

It should be noted that there is some differential mode attenuation due to collisions in the D- and E-regions as discussed with reference to Fig. 10 from James et al. (2006), which showed that the differential absorption between the modes at 90 km is $\sim$0.15 dB/km and drops to less than 0.02 dB/km at 100 km. It was therefore expected that the differential attenuation between the modes would have been on the order of one dB at most. A disturbed ionosphere may induce more collisions at these altitudes, but since all the passes examined here were for quiet conditions, the effect of absorption on the received signal parameters was not considered significant and is not considered in the present study.

2.4 Periodic Faraday fading

The second regularly observed feature of the transionospheric propagation in the ISIS II data was periodic fading of signal intensity. Periodic fading of a single mode (signal intensity of only either the O-mode or X-mode wave periodically varies) is illustrated in Fig. 1 as cross-section c) for the O-mode only band. The single mode fading is difficult to discern in the top plot, but clearly discernable in cross-section line plot c). Single mode fades are believed to be the result of focusing and defocusing of single mode waves by ionospheric enhancements and depletions acting like lenses. Discussion of single mode fades can be found in James et al. (2006) and is not further considered here.

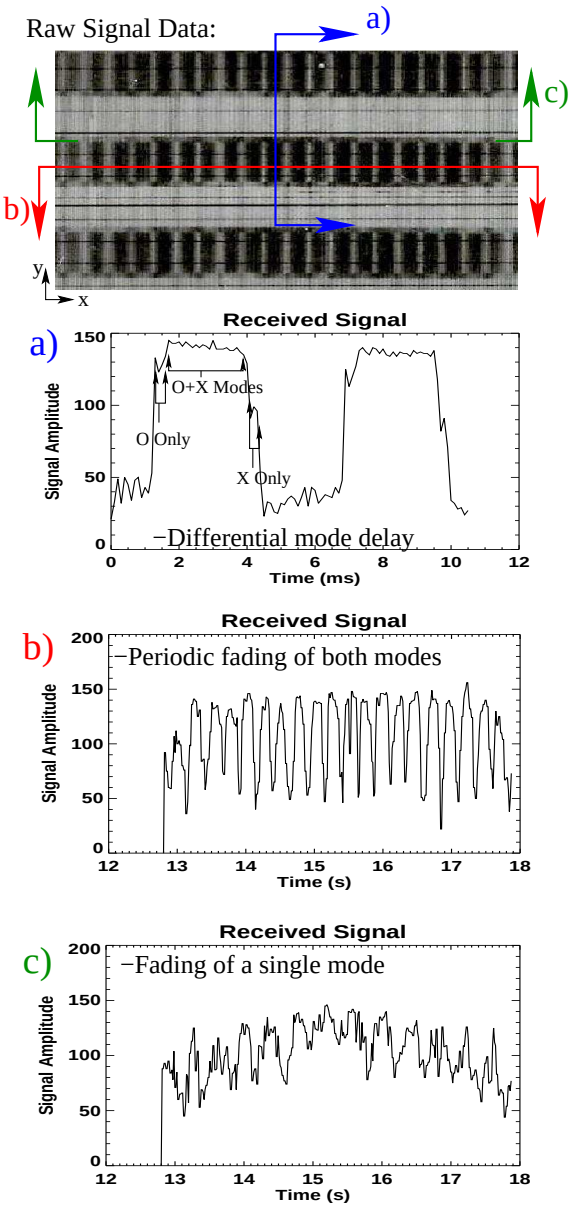

Fig. 1. A six second example of signal received by the ISIS II satellite at 13:59:12 UT, 3 July 1978. Dark on the grey-scale data plot at the top represents received signal amplitude on the dipole antenna. Individual amplitude scans are plotted as a function of time in the −y-direction. The grey-scale plot results from the juxtaposition of many successive amplitude scans in the +x-direction. Individual 180-Hz pulses are seen as three dark horizontal bands. This pattern is maintained over several seconds of time in the x-direction. Examples of: **(a)** Differential mode delay is observable at the beginning and end of each pulse. **(b)** Periodic Faraday fading occurs in portions of signal with both modes at a rate of 4.0 Hz. **(c)** Single mode fades are also present. Note, the y-axis for plots (a), (b), and (c) has arbitrary relative amplitude units.

An example of periodic fading of signal intensity when both modes were received at the same time is illustrated in cross-section b). These fading instances occurred for up to several tens of seconds at a time. A likely explanation for this periodic fading is the Faraday rotation of the linearly polarized total electric field of the transmitted wave. Since the antenna is a linear dipole, strong signal was received when the electric field was nearly aligned with the dipole axis. As the satellite moved along its orbit the incoming linear wave would Faraday rotate out of alignment with the dipole axis. Weakest signal occurred when the antenna dipole and electric field were closest to perpendicular. This continuous changing of the electric field orientation led to a periodic fading of signal intensity as the satellite travelled through space.

The periodic fading of both modes was observed in eight of the eighteen studied passes. Periodic fading was analyzed by performing a Fourier analysis on the sections of data where signal was received by ISIS II from the Ottawa ground transmitter. The fading rates ranged from 0.5 Hz to 13 Hz. As with differential mode delay, periodic fading was observed only south of the transmitter and the fade rate frequency was observed to increase in magnitude at locations more equatorward of the transmitter.

3 Transionospheric modelling

3.1 3-D ray tracing program

The Appleton-Hartree equation for the index of refraction of a radio wave in a magnetoionic medium was used to derive computational ray tracing equations based on the ray formalism of Haselgrove (1963). Applied to the magnetoionic refractive index, the Haselgrove (1963) equations provide both the group velocity and rate of change in wave vector (in three dimensions) given the wave-vector direction and wave frequency and a set of propagation conditions such as magnetic field strength and direction, and electron density. The authors have applied these equations in a computer program for full three-dimensional ray tracing. The program calculates the path, at a given frequency, that either the O- or X-mode travels from a fixed transmitter to a satellite position. The program uses the International Geomagnetic Reference Field (IGRF) model (Maus et al., 2005) for determining the magnetic field and takes a user supplied one- or two-dimensional electron density profile. Using a Newton iteration method (James, 2006a), the ray trace converges to intersect with the location of the satellite within 10 m in typically a few iterations. It should be pointed out that the 10-m convergence criterion, in practice, applies to a line perpendicular to the propagation path at the satellite and corresponds to an error along the ray path of at most 10 cm. Hence, this corresponds to a very small phase-path difference between the modes at HF frequencies (Gillies, 2006).

3.2 Ray trace modelling for ISIS II

As discussed in Sect. 2.2, eighteen passes of the ISIS II satellite over the Ottawa transmitter were examined in detail. These passes produced Faraday fading and differential mode delay in the received signal. Ray tracing computations have been performed for these passes. Comparisons between the Faraday fading and differential mode delay values obtained from the ray tracing computations and the actual observed data were then made. In order to predict values for Faraday fade rates and differential mode delays, the ray tracing program found a ray path for every 0.1° latitude of the satellite orbit over the transmitter. Initially, the International Reference Ionosphere (IRI) model (Bilitza, 2001) was utilized to obtain electron density profiles. The resulting Faraday fade rates and differential mode delay values that were obtained by using the IRI model did not show good agreement with the observed values, although overall gross trends were exhibited. This is illustrated in Fig. 2 for Faraday fade rate and Fig. 3 for differential mode delay. These figures present the observed ISIS II values of the two quantities (as dashed lines with diamonds indicating data points) and the predicted values using the IRI generated profile (as dash-dotted lines) for the afternoon pass on 8 July. Notice that the observed data are at latitudes south of the Ottawa (45.4° N) transmitter while the ray tracing results demonstrate that Faraday fading and differential mode delay should be observed north of the transmitter as well. This discrepancy will be discussed in Sect. 4.1. Both observed and predicted values of fade rate and differential mode delay show an increase with increasing distance from the transmitter, but the predicted values increase at a much faster rate than the observed values.

Recall that the ISIS II satellite performed a topside ionogram scan roughly once every 2.5° in latitude. Therefore, it was decided to utilize the *fo*F2 values that the satellite sounder had determined to develop more realistic two-dimensional electron density profiles. These simulated profiles utilized the *fo*F2 values taken directly from the topside scans while relying on the IRI model for the shape of the profiles (i.e., the *fo*F2 values were used to scale IRI profiles). It should be noted that this scaling option did not simply multiply the entire profile by the scaling factor. In the IRI model the various altitude regions use different ionospheric models to determine electron density so a change (scaling) of the *fo*F2 value, for example, only affects electron densities near it. Figure 4 shows the *fo*F2 density values that were obtained from both the IRI and the topside soundings. On this day the IRI overestimates the peak values by typically ∼30%. Scaling to the *fo*F2 values led to a significant improvement in agreement between the computed and observed values. There are some limitations to how accurately the profiles represented the actual ionospheric conditions. First, the sounder performed a scan only every 2.5° latitude or roughly every 350 km. This separation of measurements was insufficient to resolve small scale ionospheric structures. Secondly,

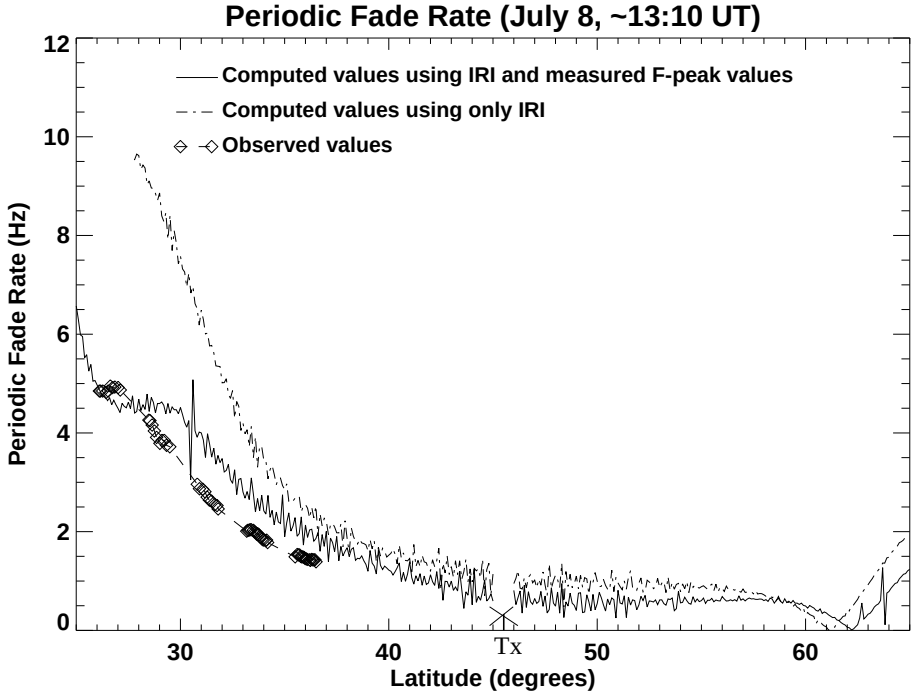

Fig. 2. An example comparison between simulated and observed Faraday fade rates. This pass occurred on 8 July 1978, 13:10 UT. The two computed curves were obtained using two different electron density profiles, one generated using only the IRI model and the other using the model scaled to the topside sounding *fo*F2 values.

the determination of an accurate *fo*F2 value was not always possible due to noise and/or weak signal near the cut-off frequency in some of the ionograms. At times this resulted in ambiguity in the peak plasma frequency by up to 1 MHz. Finally, there was error introduced from the fact that only the F-region peak was used to adjust the IRI profile. This meant that the shape of the profile was not the same as the actual profile during the experiment. However, as will be shown in Sect. 4.3, the shape of the profile mattered little provided the peak density was reasonably accurate.

Using the *fo*F2 value to scale the IRI model electron density profiles resulted in much better agreement between actual data and the computed fade rates and differential mode delays, as shown in Figs. 2 and 3. It can be seen that the computed results using the topside ionogram peaks are much closer to the observed values than the computed values using only the IRI. This comparison demonstrates the necessity of reliable *fo*F2 values for the ray tracing.

4 Discussion

4.1 ISIS II transionospheric analysis

Examination of ISIS II data has revealed two prominent features in the observed signal received during the transionospheric experiment. The first is a measurable time delay between the arrival at the satellite receiver of the two modes of propagation. The second is periodic fading in the received signal, explained as Faraday fading arising when a linearly polarized wave electric field is incident on a dipole receiving antenna.

The differential mode delay values ranged from 0.1 to 0.8 ms and were observed at latitudes to the south of the Ottawa transmitter. The transmitted frequency was 9.303 MHz for the ISIS experiment considered here. For future experiments of this type, such as SuperDARN-ePOP collaborations, the transmitter will be able to operate at frequencies from about 8 MHz to 20 MHz. Hence, depending on the operating frequency, the ePOP RRI should observe differential mode delay values comparable to the ISIS receiver. The most likely reason for greater differential mode delay observed to the south of the transmitter is that the overall ionospheric electron density increases due to the increase in photoionization with decreasing latitude. This has the effect of bringing the transmitted wave frequency closer to the cutoff frequencies of the modes. The consequence is that the X-mode, which is closer in frequency to its cutoff frequency than the O-mode, experiences more dispersion and greater signal delay.

Periodic Faraday fading of the two modes occurred at rates up to 13 Hz and, as with mode delay, was observed only south of the transmitter. An explanation for this is slightly

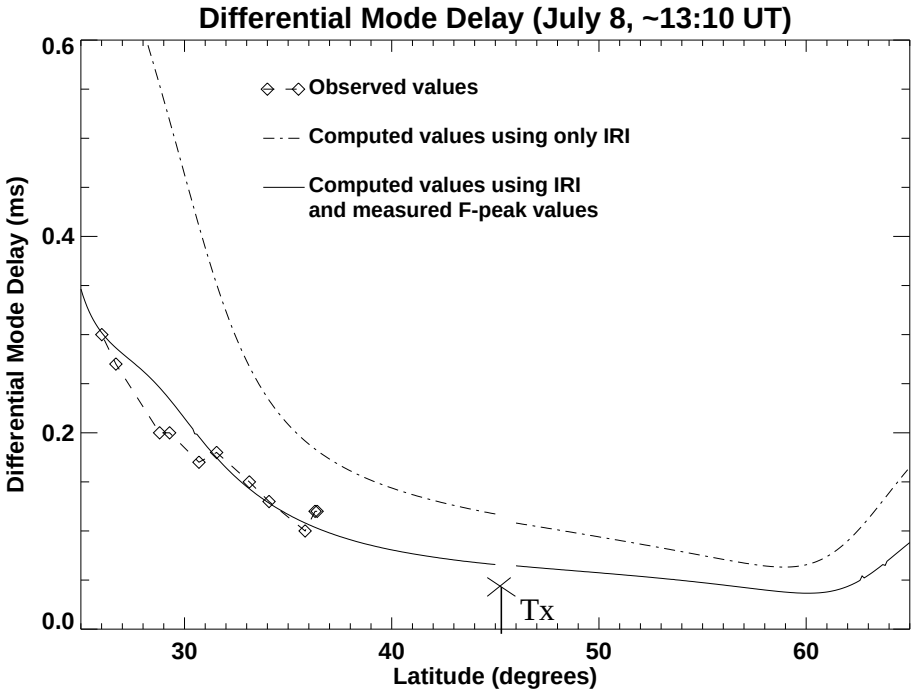

Fig. 3. An example comparison between simulated and observed differential mode delay times. This pass occurred on 8 July 1978, 13:10 UT. The two simulated curves represent two different electron density profiles, one generated using only the IRI model and the other using the model scaled to the topside sounding *fo*F2 values.

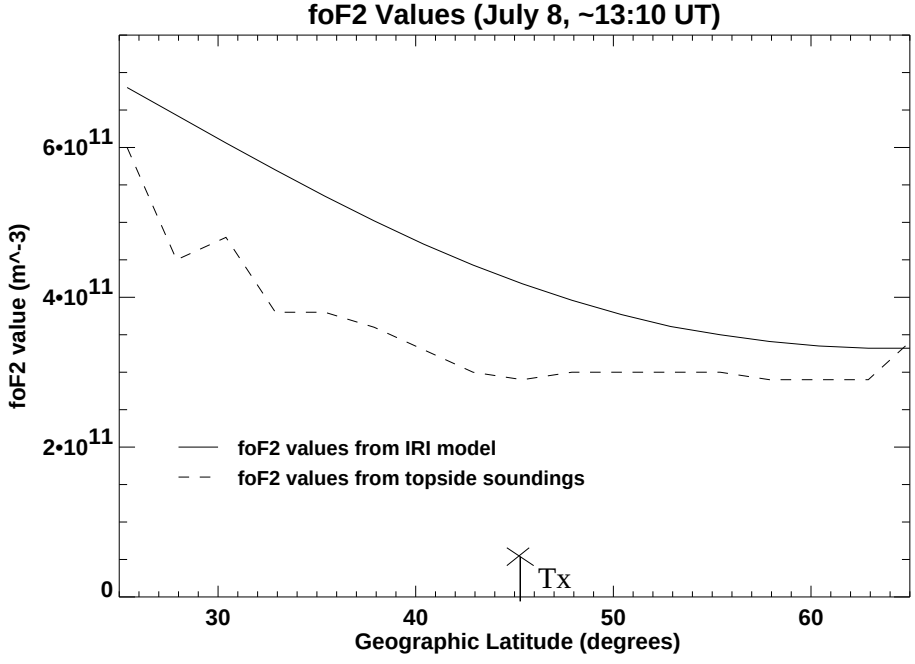

Fig. 4. The *fo*F2 values obtained from both the IRI model and the ISIS II topside soundings for the pass on 8 July 1978, 13:10 UT.

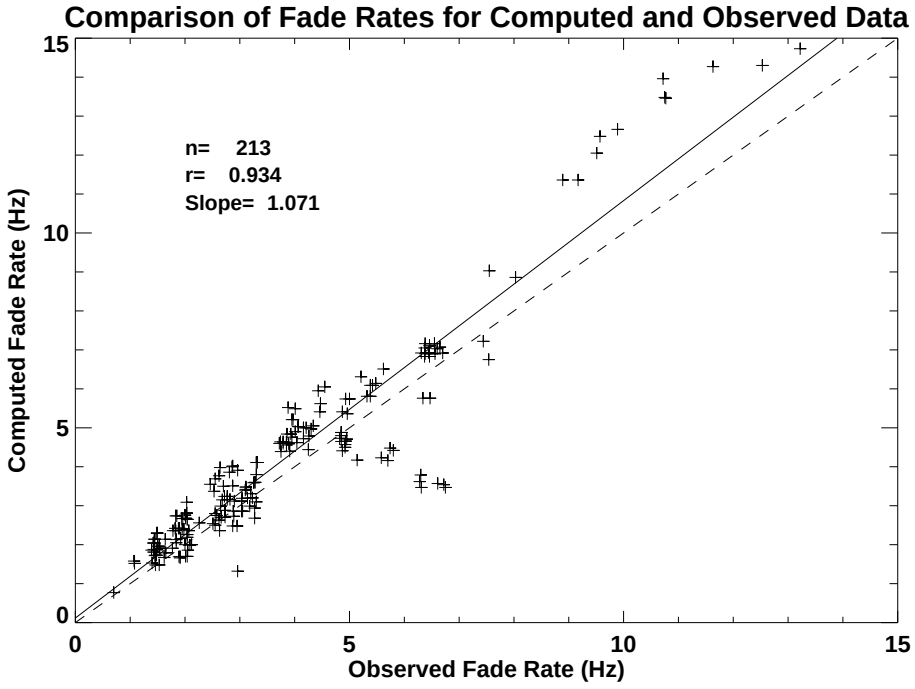

Fig. 5. A linear regression comparison of all computed and observed Faraday fade rates for the ISIS II experiment. The dashed line is the ideal fit and the solid line is the best fit. The regression analysis used 213 points and gave a regression coefficient of 0.934 and a slope of 1.07.

more complex than that for differential mode delay. The most probable reason for the lack of observable Faraday fading north of the transmitter was a disparity between the received power of the O- and X-modes. As presented by James (2006a) and James et al. (2006), in several instances the X-mode was at least 10 dB stronger than the O-mode. This amplitude disparity was clearly not due to absorption in the E-region because the X-mode is absorbed more than the O-mode. This disparity was possibly due to the distribution of power between the O- and X-modes when the wave propagated in a northward direction. This is currently under investigation.

This 10-dB disparity had the effect of preventing Faraday rotation (which requires circularly polarized modes of roughly equal amplitude) during portions of a pass. Instead, this disparity in mode amplitude would have caused the combined wave to not be strictly linearly polarized and thus the received signal polarization state would have been complex. This complexity could not be properly analyzed with only a single dipole antenna. The RRI on ePOP will be a useful instrument for analyzing the polarization state of the signal received poleward of the transmitter as the antenna will consist of two crossed dipoles.

Another minor factor that would not be supportive of Faraday rotation occurring north of the transmitter was the angle between the propagation vector and magnetic field direction (the aspect angle) becoming close to perpendicular (i.e., the propagation conditions are not as favourable for the Faraday rotation effect). However, Fig. 8 of James et al. (2006), which takes this factor into account, indicates that deep Faraday fades are expected throughout a pass, and clearly this is not observed in the ISIS II data.

4.2 Observed and modelled ISIS II signal comparisons

Comparisons between observed and simulated differential mode delay and periodic fading values have been performed for each simulated pass. Figures 2 and 3 demonstrated that the IRI model alone cannot develop electron density profiles that are sufficiently realistic to reproduce these received signal parameters. However, given a relatively quiet ionosphere (K_p less than four for this data set), the use of measured *fo*F2 densities to scale IRI profiles produces better agreement between the ray tracings and the observations. A disturbed ionosphere would probably have many smaller scale structures that topside soundings taken every 2.5° in latitude would not resolve and this might significantly lower the agreement. Also, a disturbed ionosphere would result in higher collision frequencies and differential absorption in the D- and E-region portion of the transionospheric wave path.

In order to quantify the comparisons of all the passes, a linear regression analysis was performed comparing the simulated quantities to the observed quantities for both Faraday fading and differential mode delay. This analysis is shown

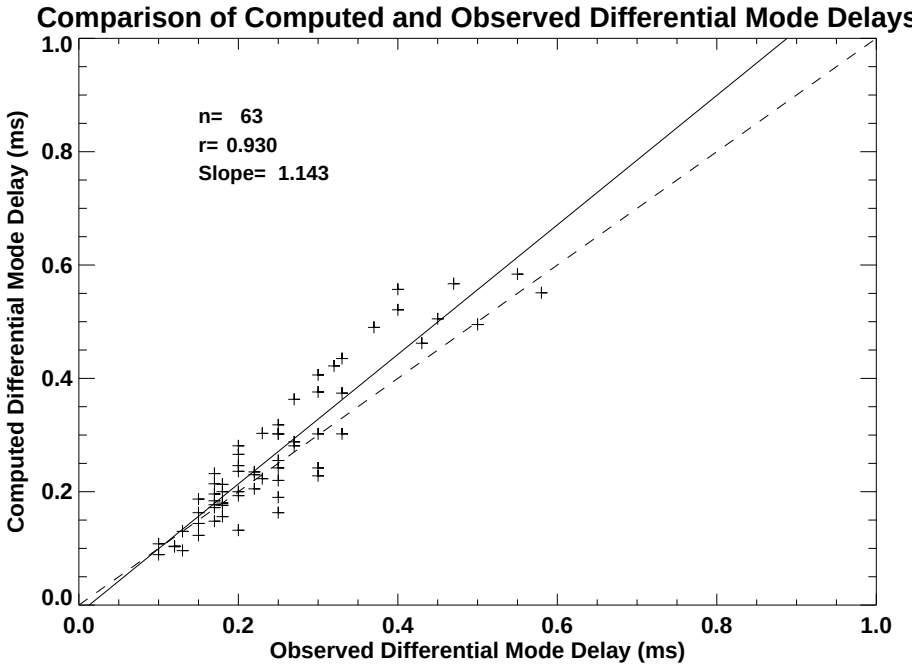

Fig. 6. A linear regression comparison of all simulated and observed differential mode delays for the ISIS II experiment. The dashed line is the ideal fit and the solid line is the best fit. The regression analysis used 63 points and gave a regression coefficient of 0.930 and a slope of 1.14.

as Fig. 5 for Faraday fading and Fig. 6 for differential mode delay. Plotted are the observed values of either quantity for all passes on the horizontal axis and the corresponding simulated values on the vertical axis. A best fit line is plotted in both cases. For Faraday fading 213 data points were compared, resulting in a best fit slope of 1.07 and a regression coefficient of 0.934. For mode delay 63 points were compared with a best fit slope of 1.14 and a regression coefficient of 0.930. Notice that the only group of points that show very poor agreement between observed and computed values is a small cluster of points in Fig. 5. This cluster had an observed fade rate of nearly 7 Hz, but the simulation value was ∼3 Hz. The probable reason for this poor agreement is that the 2.5° latitude spacing between topside soundings was too large spatially in this case as a large change in the ionospheric electron density was observed between the two soundings. Other than this, the comparisons were quite good despite the limitation of not having actual electron density profiles for the ray tracing predictions.

4.3 Electron density profile considerations

One of the most interesting features that this study illustrated was that the *fo*F2 peak density is very important in describing the propagation path and characteristics of a transionospheric HF wave. It is not surprising that this is important because the phase difference that accumulates between the O- and X-modes is directly dependent on electron density. Since both differential mode delay and Faraday fade rate depend on the integrated phase difference between the modes, it was expected that accurately simulating the electron density profile was necessary. The interesting point of this study is that it appears that the IRI model was useful provided the maximum was scaled to the correct *fo*F2 value. Therefore, it appears that the shape of the profiles is of secondary importance. To examine whether this hypothesis is correct a simple test was performed to compare the effects of the profile shapes versus the effects of the *fo*F2 values on simulated wave parameters. A model IRI profile for 1 July 1978, 14:00, at Ottawa, scaled to a peak density of 5.1×10^{11} m^{-3}, was used as a base case. Further IRI profiles of different shapes were used for a variety of ionospheric conditions, with the model constrained to keep the same peak density (5.1×10^{11} m^{-3}) in each case. Profiles were created for three latitudes (0°, 45°, and 80°) for both winter (1 January) and summer (1 July) and day (14:00 LT) and night (02:00 LT). This ensured that the profiles would be quite different in shape, but still retained the same peak electron density. Finally, the one base profile was scaled up slightly to create a profile with the same shape as the base profile, but with a peak density of 6.0×10^{11} m^{-3}. The various profiles that were created for this test are listed in Table 1.

Since the goal of this test was to determine which profile parameter, profile shape or *fo*F2 value, is dominant for the ray tracing calculations, a measure of profile shape was

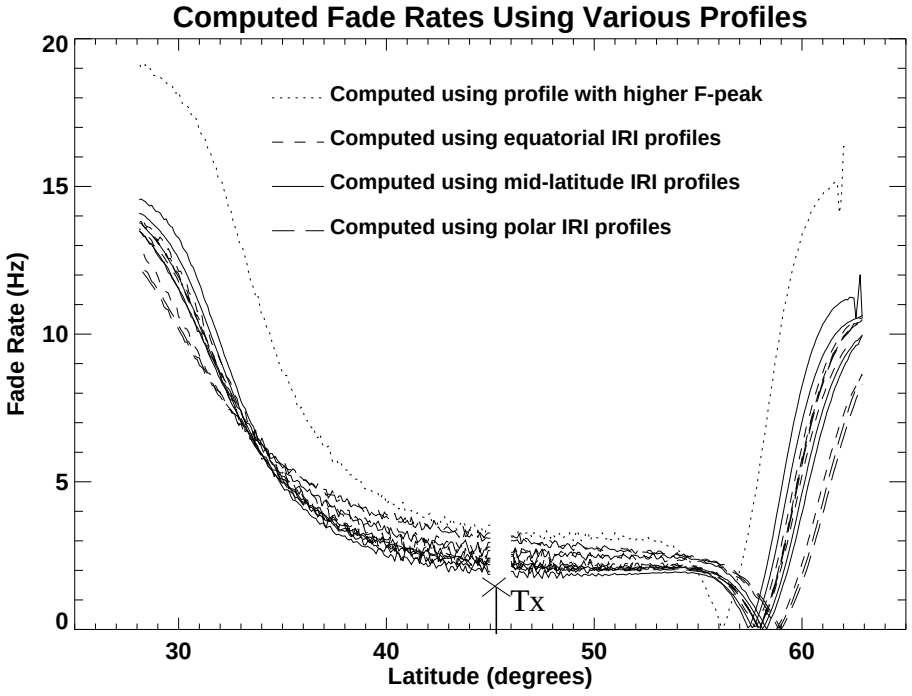

Fig. 7. The simulated Faraday fade rate as a function of satellite latitude using each electron density profile listed in Table 1. All the results for profiles with the same *fo*F2 value essentially coincide with one another and as such are essentially indistinguishable in the plot. Results show slightly higher fade rate values for profiles with higher TEC above the transmitter. Away from the transmitter, profiles with the same *fo*F2 peak produce similar values, but the profile with a higher peak results in much higher fade rates. Also, notice that the Faraday fade rate values drop to zero around 55° to 60° latitude. This is a consequence of the Faraday rotation the satellite observes at this location changing rotation directions. As a result the Faraday fade rate drops to zero as the polarization state switches from rotating in one direction to the other.

required. It was decided to incorporate the Total Electron Content (TEC) value of the various profiles to provide a numerical measure of profile shape. In this study, the TEC value is taken as the integrated electron density from the ground to 1400 km in units of $10^{16}\,\mathrm{m}^{-2}$. There are other measures of profile shape that could have been used, such as *fo*F2 height and width, E-region density, electron density at the satellite location, etc.; however, TEC is a good overall measure of a given profile. Listed in Table 1 is the TEC value for each profile. The TEC value for the scaled up base profile was $22.63\times10^{16}\,\mathrm{m}^{-3}$ (or 22.63 TEC units). Notice that the profiles in Table 1 have TEC values that range from 14.59 to 27.30 TEC units. Therefore, the profile with a higher *fo*F2 value has a TEC value that falls within the range of the TEC values of the profiles with a lower *fo*F2 value. This allows a study of the effect of *fo*F2 on the ray tracing results to be relatively independent of TEC (or shape) of the profiles.

Each profile was used to predict the signal that would be received by a satellite flying at 1400 km over a 9.303-MHz transmitter located in Ottawa. The Faraday fade rate and differential mode delay were calculated every 0.1° latitude. The results of these calculations are presented as Fig. 7 for Faraday fade rate and Fig. 8 for differential mode delay.

At latitudes away from the transmitter, quantities computed for profiles with the same *fo*F2 value showed similar values. Conversely, the profile with a slightly higher *fo*F2 value resulted in much higher fade rate and mode delay values. This indicates that the two received signal parameters are mostly independent of TEC but highly dependent on F-region peak values at ranges far from the transmitter. Overhead of the transmitter, the two values are observed to be dependent more on TEC than on peak density. The reason for this behaviour is that above the transmitter a radio wave travels essentially straight up and the TEC of a profile dominates the determination of the phase difference that develops between the two modes. When the satellite is north or south of the transmitter, the ray is refractively bent by the highly dense F-region and spends a proportionately longer time in the region in and around the peak density, and the two modes split significantly in this region. This significant splitting accounts for the majority of the accumulated phase difference between the two modes. For example, directly above the transmitter (satellite at 45° latitude), ∼60% of the total mode delay occurs within ±100 km in altitude of the *fo*F2 peak, while south of the transmitter with the satellite at 35° latitude, more than 90% of the total differential mode delay

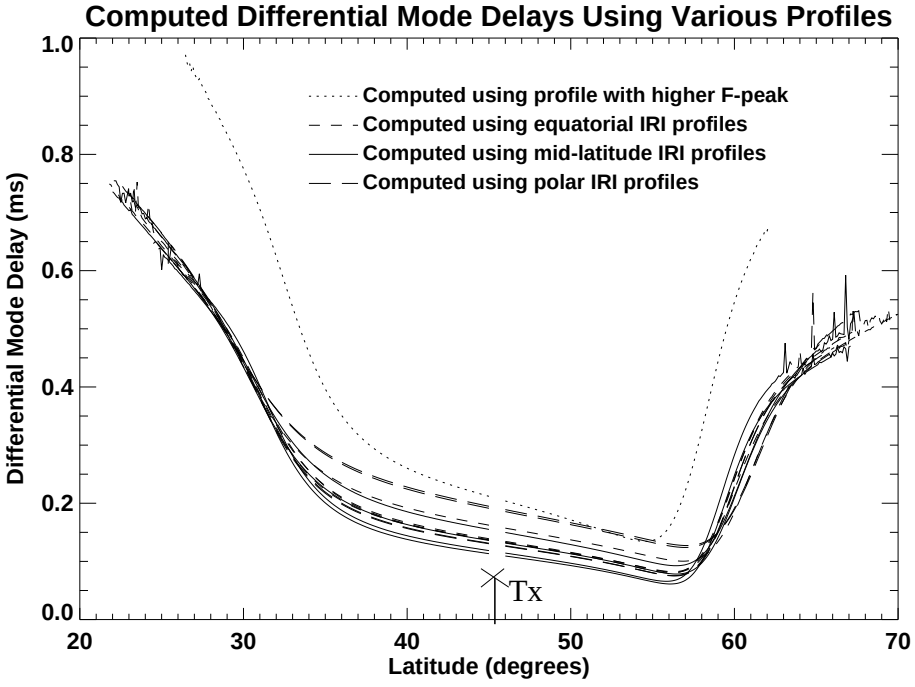

Fig. 8. The simulated differential mode delay at various satellite latitudes using each electron density profile listed in Table 1. Results show higher differential mode delay values for profiles with higher TEC above the transmitter. Away from the transmitter, profiles with the same *fo*F2 peak produce similar values, but the profile with a higher peak results in much higher differential mode delay values.

Table 1. Various IRI generated electron density profiles. All profiles are generated at 75.7° W longitude (Ottawa).

Date (1978)	Time (LT)	Latitude (° N)	TEC ($\times 10^{16}$ m^{-2})	*fo*F2 ($\times 10^{11}$ m^{-3})
1 Jan	02:00	0.0	18.23	5.1
1 Jan	14:00	0.0	19.01	5.1
1 Jan	02:00	45.0	14.59	5.1
1 Jan	14:00	45.0	14.75	5.1
1 Jan	02:00	80.0	17.76	5.1
1 Jan	14:00	80.0	17.70	5.1
1 July	02:00	0.0	18.65	5.1
1 July	14:00	0.0	22.28	5.1
1 July	02:00	45.0	18.24	5.1
1 July	14:00	45.0	19.78	5.1
1 July	02:00	80.0	26.72	5.1
1 July	14:00	80.0	27.30	5.1
1 July	14:00	45.0	22.63	6.0

occurs within this altitude region. Therefore, this is the reason that, at the frequency of 9.303 MHz, the *fo*F2 value and not the shape (or TEC) of the electron density profile is critical in obtaining reasonable ray tracing results for the experiment presented in this study.

5 Conclusions

Data from the ISIS II satellite mission has been analyzed in preparation for the upcoming ePOP mission. The received signal data from the ISIS II satellite mission showed two prominent features: differential mode delay and periodic Faraday fading. Both features were observed to the south of the transmitter where nearly equal O- and X-mode amplitudes allowed clear Faraday fading and higher electron densities resulted in larger mode splitting. The rate of measured periodic fading varied up to 13 Hz and the magnitude of differential mode delay was as high as 0.8 ms. Ray tracing predicted the observed fade rates and differential mode delays using electron densities derived from measured *fo*F2 values and IRI profiles. The simulated and observed data showed very similar trends for each of the examined passes. This good agreement was dependent on having a representative electron density profile for the ray tracing analysis. The two parameters which were used to characterize an electron density profile were the profile shape (examined using TEC values) and the peak electron density (*fo*F2). The comparison between the ISIS II measurements and the computations indicated that the *fo*F2 parameter, and not the TEC parameter, essentially determined the outcome of the simulations. This behaviour is a consequence of refraction causing the wave to travel longer near the peak density where larger splitting of the modes due to the higher electron densities in this

region occurs. This was clearly the case for the transmitter frequency of 9.303 MHz, which was a few MHz above *fo*F2. Of course, the use of higher transmitter frequencies would cause the wave to be refracted less and the *fo*F2 value would likely not dominate the received signal parameters to such an extent.

This paper has demonstrated that ray tracing computations can reasonably reproduce transionospheric propagation characteristics under quiet geomagnetic conditions and at mid-latitudes (i.e., south of the Ottawa transmitter in this study). No evidence of Faraday fading or differential mode delay was observable north of the Ottawa transmitter for the ISIS II study. As discussed, previous results (James et al., 2006; James, 2005) indicated that the X-mode to O-mode ratio was on the order of 10 dB in this region and thus Faraday rotation and clear mode splitting were not expected. Instead of a simple linear wave, the resulting polarization state would be much more complex under these conditions. The RRI instrument on the ePOP satellite will be much more sensitive and consist of two crossed dipoles; therefore, it may be possible to interpret these complex signals.

Acknowledgements. We acknowledge the support of the Canadian Space Agency and the Natural Sciences and Engineering Research Council (NSERC) to the CASSIOPE/ePOP project for our research. International Reference Ionosphere (IRI) electron density profiles have been provided by the Space Physics Data Facility (SPDF). Digitized online ISIS II data has been supplied by R. F. Benson at the National Aeronautics and Space Administration (NASA) Goddard Space Flight Center (GSFC) and Coordinated Data Analysis Web (CDAWeb).

Topical Editor M. Pinnock thanks W. Bristow and A. Stocker for their help in evaluating this paper.

References

Bilitza, D., Huang, X., Reinisch, B. W., Benson, R. F., Hills, H. K., and Schar, W. B.: Topside Ionogram Scaler With True Height Algorithm (TOPIST): Automated processing of ISIS topside ionograms, Radio Sci., 39, RS1S27, doi:10.1029/2002RS002840, 2004.

Bilitza, D.: International Reference Ionosphere 2000, Radio Sci., 36, 261–275, 2001.

Budden, K. G.: Radio Waves in the Ionosphere, Cambridge University Press, 1961.

Daniels, F.: ISIS-II Spacecraft, CRC Report No. 1218, Communications Research Centre, Ottawa, 1971.

Franklin, C. A. and Maclean, M. A.: The Design of Swept-Frequency Topside Sounders, Proceeding of the IEEE, 57(6), 897–929, 1969.

Gillies, R. G.: Modelling of Transionospheric HF Radio Wave Propagation for the ISIS II and ePOP Satellites, M.Sc. Thesis, Institute of Space and Atmospheric Studies, University of Saskatchewan, 2006.

Greenwald, R. A., Baker, K. B., Dudeney, J. R., Pinnock, M., Jones, T. B., Thomas, E. C., Villain, J.-P., Cerisier, J. C., Senior, C., Hanuise, C., Hunsucker, R. D., Sofko, G., Koehler, J., Nielsen, E., Pellinen, R., Walker, A. D. M., Sato, N., and Yamagishi, H.: DARN/SuperDARN: A Global View of the Dynamics of High-Latitude Convection, Space Sci. Rev., 71, 761–796, 1995.

Haselgrove, J.: The Hamiltonian ray path equations, J. Atmos. Terr. Phys., 25, 397–399, 1963.

James, H. G.: Effects on transionospheric HF propagation observed by ISIS at middle and auroral latitudes, Adv. Space Res., 38(11), 2303–2312, 2006a.

James, H. G.: A digital radio receiver for ionospheric research, NATO Specialist Meeting IST-056, "Characterizing the Ionosphere", Paper 23, Fairbanks, AK, USA, 12–16 June 2006b.

James, H. G.: High-frequency direction finding in space, Review of Scientific Instruments, 74(7), 3478–3486, 2003.

James, H. G., Gillies, R. G., Hussey, G. C., and Prikryl, P.: HF fades caused by multiple wave fronts detected by a dipole antenna in the ionosphere, Radio Sci., 41, RS4018, doi:10.1029/2005RS003385, 2006.

Maus, S., Macmillan, S., Chernova, T., Choi, S., Dater, D., Golovkov, V., Lesur, V., F. Lowes, Luhr, H., Mai, W., McLean, S., Olsen, N., Rother, M., Sabaka, T., Thomson, A., and Zvereva, T.: The 10th generation international geomagnetic reference field, Physics of the Earth and Planetary Interiors, 151, 320–322, 2005.

MacDougall, J. W., Grant, I. F., and Shen, X.: The Canadian Advanced Digital Ionosonde: Design and Results, Rep. UAG-104, Ionosondes and Ionosonde Networks, 21–27, World Data Center A, Boulder, 1995.

NSSDC: ISIS/Alouette topside sounder data restoration project, available from: http://nssdc.nasa.gov/space/isis/isis-status.html, 2004.

Wang, L., MacDougall, J. W., and James, H. G.: Ionospheric structure effects on HF radio wave propagation for the Enhanced Polar Outflow Probe (e-POP) satellite mission, Radio Sci., 39, RS2019, doi:10.1029/2003RS002975, 2004.

Yau, A. W, James, H. G., and Lui, W.: The Canadian Enhanced Polar Outflow Probe (ePOP) mission in ILWS, Adv. Space Res., 38(8), 1870–1877, 2006.

Yau, A. W., Cogger, L. L., King, E. P., Knudsen, D. J., Murphree, J. S., Trondsen, T. S., Tsuruda, K., James, H. G., and Walkty, I.: The Polar Outflow Probe (POP): Science Objectives and Instrument Development, Canadian Aeronautics and Space Journal, 48(1), 39–49, 2002.

Chapter 3

Relative O- and X-mode transmitted power from SuperDARN

3.1 Introduction

The research presented in this chapter is based on the following publication:

- Gillies, R. G., G. C. Hussey, G. J. Sofko, and H. G. James, Relative O- and X-mode transmitted power from SuperDARN as it relates to the RRI instrument on ePOP, *Ann. Geophys.*, 28, 861–871, 2010c.

This study involved the calculation of the relative power delivered to the O- and X-modes of propagation from the SuperDARN radars. The expected relative mode power to be detected by the RRI on ePOP was also calculated for various ionospheric conditions.

3.2 Results

The HF radio waves transmitted from SuperDARN radars (any HF radar) are split into two modes of propagation in the magnetized ionosphere. The two modes propagate at different speeds and along different paths and will therefore arrive at the RRI at slightly different times. Since the RRI has two crossed dipole antennas, full polarization measurements of received HF waves can be made and the two modes of propagation can be distinguished. The analysis of ISIS 2 data in the previous chapter revealed that knowledge of the relative power of the two modes is essential

to fully analyze the received signal. The effect of Faraday rotation on the propagating wave was evidenced by periodic fading of signal intensity when the satellite was located above and southwards of the transmitter. Further analysis was required to determine the reason for the lack of Faraday rotation when the wave propagated northwards from the transmitter. As discussed in Section 1.7, two conditions are required for Faraday rotation to occur. The wave must propagate in the QL regime and the relative amplitude or power of the two propagation modes must be mostly equal. Wave propagation in a northward direction from the transmitter located in Ottawa would result in QT propagation. In addition, depending on the initial polarization of the wave, the relative power distribution of the O- and X-modes can be quite different. Unlike the RRI on ePOP, the ISIS 2 satellite was only equipped with a single dipole antenna and could not make full polarization measurements of the received signal. Due to this limitation, a complete understanding of the propagation and polarization of the wave was not possible. Accurate modelling of the polarization and relative power delivered to the O- and X-modes with the resulting expected power to be received at the RRI is essential for interpretation of the experimental transionospheric results when they are available. The study presented in this chapter deals with modelling the relative power of the X-mode compared to the O-mode under various ionospheric conditions.

This research determined that the polarization of the waves transmitted by the SuperDARN radars resembles the X-mode of propagation when the wave propagation direction is roughly perpendicular to the external magnetic field lines. That is, the X-mode dominates the transmitted signal when a wave propagates northwards. Coherent scatter from field aligned ionospheric irregularities occurs only when the propagating wave is perpendicular to the magnetic field lines. As such, this implies that the waves that are coherently scattered and measured by SuperDARN are dominated by the X-mode of propagation. Since the X-mode of propagation has an index of refraction that is lower than unity (as does the O-mode, but to a lesser extent), it was realized that the refractive index in the SuperDARN scattering volume is not unity as has been previously assumed. Since the refractive index is less than unity,

and is not accounted for, SuperDARN line-of-sight Doppler velocities are underestimated. In fact, several previous studies, such as *Davies et al.* [1999], *Xu et al.* [2001], and *Drayton et al.* [2005], have noted that velocities measured by SuperDARN were statistically lower than those measured by other instruments; however, explanations for these statistical findings were not sufficient. The development and testing of a technique to estimate the refractive index in the SuperDARN scattering volume will be the topic of the next chapter.

3.3 Published paper

The modelling of relative mode power discussed in this chapter was published in *Annales Geophysicae* in 2010. Presented immediately below is the paper in the journal format:

- Gillies, R. G., G. C. Hussey, G. J. Sofko, and H. G. James, Relative O- and X-mode transmitted power from SuperDARN as it relates to the RRI instrument on ePOP, *Ann. Geophys.*, 28, 861–871, 2010c.

Ann. Geophys., 28, 861–871, 2010
www.ann-geophys.net/28/861/2010/

Annales Geophysicae

Relative O- and X-mode transmitted power from SuperDARN as it relates to the RRI instrument on ePOP

R. G. Gillies[1], **G. C. Hussey**[1], **G. J. Sofko**[1], **and H. G. James**[2]

[1]Institute for Space and Atmospheric Studies, University of Saskatchewan, Saskatoon, Saskatchewan, Canada
[2]Communication Research Centre Canada, Ottawa, Ontario, Canada

Received: 27 October 2009 – Revised: 15 March 2010 – Accepted: 16 March 2010 – Published: 24 March 2010

Abstract. The Cascade Demonstrator Small-Sat and Ionospheric Polar Explorer (CASSIOPE) satellite is scheduled to be launched in 2010. On board this satellite will be a suite of eight scientific instruments comprising the enhanced Polar Outflow Probe (ePOP). One instrument is the Radio Receiver Instrument (RRI) which will be used to receive HF transmissions from various ground transmitters such as the Super Dual Auroral Radar Network (SuperDARN) array. Magnetoionic polarization and propagation theory have been used to model the relative power that SuperDARN delivers to the Ordinary (O) and Extraordinary (X) modes of propagation. These calculations have been performed for various frequencies in the SuperDARN transmitting band and for all five Canadian based SuperDARN radars. The geometry of the radars with respect to the background magnetic field results in the X-mode dominating the transmitted signal when the modelled wave propagates northward and is nearly perpendicular to the magnetic field lines. Other propagation directions (i.e., above or southwards of the radar) results in propagation which is anti-parallel to the magnetic field lines and an equal splitting of transmitted power between the O- and X-modes occurs. The modelling analysis shows that for either high transmitting frequencies or low ionospheric electron densities, the range of latitudes that signal will be received is quite large (up to ∼90° of latitude). Also for these conditions, the range of elevations where the X-mode signal strongly dominates the O-mode signal will be apparent in the received signal. Conversely, for lower transmitting frequencies or higher ionospheric electron densities, the latitudinal range that signal will be received over is smaller. Here the X-mode-only band is not apparent in the received signal as both modes will be received with roughly equal power. These relative mode power calculations can be used to characterize the average electron density content in the ionosphere or provide a measure of relative absorption in the D- and E-regions when the satellite passes through the field-of-view of a SuperDARN radar.

Keywords. Radio science (Radio wave propagation; Instruments and techniques)

1 Introduction

The Canadian designed and built Cascade Demonstrator Small-Sat and Ionospheric Polar Explorer (CASSIOPE) small satellite will be launched in 2010 (Yau et al., 2006). The satellite bus will consist of two payloads, a commercial data storage and forward system called Cascade and a scientific group of instruments called the enhanced Polar Outflow Probe (ePOP). ePOP will consist of various particle detectors, active and passive radio experiments, an auroral imager, a magnetic field detector, and a GPS system. The scientific goals of ePOP are to study outflows of particles from the polar regions, radio wave propagation, and ionospheric tomography (Yau et al., 2006). Some radio experiments will use the Radio Receiver Instrument (RRI) on ePOP (James, 2003, 2006; James and Lunscher, 2006; James et al., 2006). The RRI is a radio receiver that is fed by four 3-m dipole antennas. Each antenna can operate as a separate monopole, or in pairs as two crossed (perpendicular) 6-m dipoles. The RRI will measure electric fields between 10 Hz and 18 MHz. One RRI experiment to be undertaken will include various ground-based HF transmitters such as the Super Dual Auroral Radar Network (SuperDARN) radars (Greenwald et al., 1995), which will transmit HF waves to be detected by the RRI as ePOP orbits overhead.

One objective of the SuperDARN-RRI experiment is the detection of various ionospheric structures through interpretation of the signal received by the RRI. The background

Correspondence to: R. G. Gillies
(rob.gillies@usask.ca)

Published by Copernicus Publications on behalf of the European Geosciences Union.

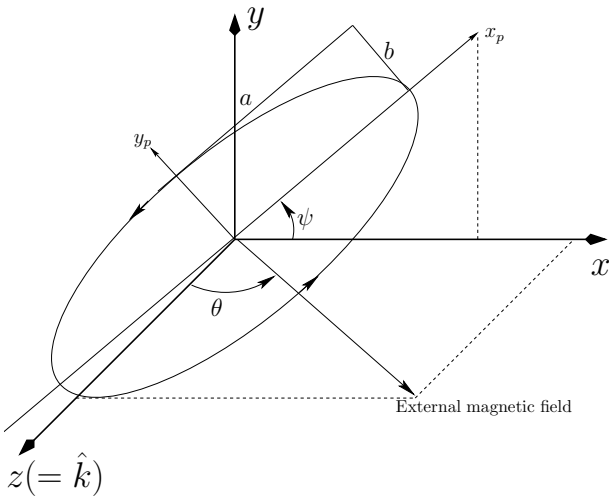

Fig. 1. The coordinate system and a general polarization ellipse. The orientation angle is represented by ψ, a represents the semi-major axis, b represents the semi-minor axis, and θ is the aspect angle. The propagation direction of the wave $\hat{\boldsymbol{k}}$ is in the z-direction and the polarization of interest is in the x-y-plane.

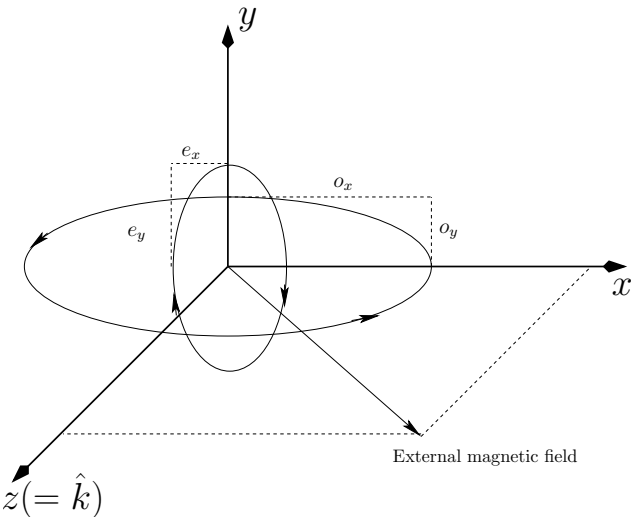

Fig. 2. The two magnetoionic modes predicted by Budden (1961) which exist from the decomposition of the wave in Fig. 1. The propagation direction of the modes $\hat{\boldsymbol{k}}$ is in the z-direction and the polarization of interest is in the x-y-plane.

electron density of the ionosphere is often perturbed by enhancements and depletions ranging in scale sizes from several meters to several hundred kilometers. Various modelling efforts have been undertaken to determine the effect of these structures on the received signal. For example, Wang et al. (2003) studied the signature of ionospheric structures on the received power, signal delay, and direction of arrival. Thorough studies of data and modelling from a previous HF transionospheric experiment performed by the ISIS II satellite have also been performed by James (2006), James et al. (2006), Gillies (2006), and Gillies et al. (2007). In these studies, the experimentally measured Faraday rotation and differential signal delay of radio waves was compared to the same parameters as determined by computational models.

In the present paper, the polarization state of the SuperDARN radars is examined and more specifically the relative amount of transmitted power that will be distributed between each of the two magnetoionic modes of propagation is modelled. The relative power of each mode received by the RRI was thoroughly investigated for various transmitter frequencies and ionospheric electron density profiles. This knowledge of the relative power of the two propagation modes will greatly assist in interpretion of the RRI instrument observations. This research is also of interest for general SuperDARN science as it details the propagation environment. The Doppler velocity that SuperDARN detects is directly related to the index of refraction at the scattering location (Gillies et al., 2009). Since the two modes of propagation have different indices of refraction, knowledge of which mode is involved in the scattering process is of significance when interpreting line-of-sight velocity values derived from coherent SuperDARN scatter.

2 Determination of relative mode power

This section has two objectives; namely, to define a general elliptical polarization state of a propagating magnetoionic wave (Fig. 1) at any point in the ionosphere using notation given by Budden (1961) and then to resolve this general polarization state into the two allowed magnetoionic propagation modes at that ionospheric location (Fig. 2). This decomposition will provide an expression for the amount of power that is injected into the X-mode relative to the O-mode, given an initial polarization state. This calculation is of use for the upcoming RRI experiment, as the RRI on ePOP will, at times, receive pulses from the two modes separately (the received pulses may overlap or be completely separate depending on factors such as: the pulse length, the transmitted frequency, and the ionospheric electron density).

The coordinate system used for this derivation is described by Budden (1961) and illustrated in Fig. 1. In this system, the z-axis is oriented parallel to the wave propagation vector ($\hat{\boldsymbol{k}}$). The x-axis is determined because the external magnetic field is taken to be in the x-z-plane at an angle θ to the z-axis. The y-axis follows from the definitions for the x- and z-axes. In this geometry, Budden (1961) has shown that, when collisions are negligible, the two magnetoionic propagation modes are orthogonal elliptical polarization states in the x-y plane and have principal axes along the $\hat{x}$ and $\hat{y}$ directions as demonstrated in Fig. 2.

A three-dimensional rotation is performed to transform the horizontally polarized SuperDARN wave in a local radar coordinate system into the Budden (1961) axes. This rotation allows the wave polarization state to be completely described

in this axis system and determines the value for the orientation angle ψ so that decomposition of the wave into the two allowed propagation modes can be performed.

The polarization ellipse of the wave in the principal axis frame has major and minor axes given by a and b, respectively. In the principal axis frame (see Fig. 1), this initial polarization state (i.e., the polarization leaving the radar antennas) ($\overrightarrow{E_\mathrm{r}}$) can be expressed as:

$$\overrightarrow{E_\mathrm{r}} = (ae^{i\phi_\mathrm{x}}\hat{\mathrm{x}_\mathrm{p}} + be^{i\phi_\mathrm{y}}\hat{\mathrm{y}_\mathrm{p}})e^{i(\omega t - kz)} \quad (1)$$

where ϕ_x and ϕ_y are the phases of the oscillation in the $\hat{\mathrm{x}_\mathrm{p}}$ and $\hat{\mathrm{y}_\mathrm{p}}$ directions, respectively, and $\phi_\mathrm{y} - \phi_\mathrm{x} = \pm\pi/2$, where the $(\pm)$ describes the sense of rotation of the polarization ellipse. Therefore, the polarization can be re-written as:

$$\overrightarrow{E_\mathrm{r}} = (a\hat{\mathrm{x}_\mathrm{p}} + (\pm i)b\hat{\mathrm{y}_\mathrm{p}})e^{i(\omega t - kz + \phi_x)}. \quad (2)$$

A rotation of this ellipse must be performed to describe the polarization state in the Budden (1961) coordinate system which is defined using the propagation direction of the wave and the magnetic field orientation. Given a value for ψ using coordinate transforms mentioned previously, the polarization can be described as:

$$\overrightarrow{E_\mathrm{r}} = [(a\cos\psi - (\pm i)b\sin\psi)\hat{x} + (a\sin\psi + (\pm i)b\cos\psi)\hat{y}]e^{i(\omega t - kz + \phi_x)}. \quad (3)$$

Equation (3) completely describes the polarization ellipse of Fig. 1.

The next step is to describe the polarization states of the two magnetoionic modes of propagation. This is accomplished using the wave-polarization ratio:

$$\rho = \frac{\boldsymbol{E}_\mathrm{y}}{\boldsymbol{E}_\mathrm{x}} \quad (4)$$

Where $\boldsymbol{E}_\mathrm{x}$ and $\boldsymbol{E}_\mathrm{y}$ are the phasor representations of the electric field along the x- and y-axes, respectively. In the absence of collisions, ρ is given by the following equation:

$$\rho = i\frac{Y_\mathrm{T}^2}{2Y_\mathrm{L}(1-X)} \pm i\sqrt{\frac{Y_\mathrm{T}^4}{4Y_\mathrm{L}^2(1-X)^2} + 1} \quad (5)$$

or

$$\rho = i\frac{(Y\sin\theta)^2}{2Y\cos\theta(1-X)} \pm i\sqrt{\frac{(Y\sin\theta)^4}{4(Y\cos\theta)^2(1-X)^2} + 1}, \quad (6)$$

where $X = (\omega_p/\omega)^2$, $Y = \omega_c/\omega$, $Y_\mathrm{L} = (\omega_c/\omega)\cos\theta$, and $Y_\mathrm{T} = (\omega_c/\omega)\sin\theta$ (note that X represents the ratio of ω_p^2 to ω^2, not the X-mode of propagation). Further: ω_c is the cyclotron frequency, ω_p is the plasma frequency, ω is the radio wave frequency, and θ is the aspect angle. The major axis of the O-mode is oriented along the x-axis (i.e., the O-mode major axis is always parallel to the component of the external B-field that is perpendicular to $\hat{\boldsymbol{k}}$) and the major axis of the X-mode is oriented along the y-axis (this behaviour is illustrated in Fig. 2). This condition indicates that, with respect to Eq. (4), the absolute value of ρ for the O-mode is always less than one and the absolute value of ρ for the X-mode is always greater than one. Both values for ρ are purely imaginary, indicating that the electric field oscillations along the x- and y-axes are 90° out of phase for either mode.

When a radar wave is propagating nearly (or exactly) parallel or anti-parallel to the magnetic field lines (the aspect angle θ is near 0° or 180°), the two polarization modes become circularly polarized waves with opposite sense. In the other extreme, when the radar wave propagates nearly (or exactly) perpendicular to the magnetic field, the polarization state of a mode is linear, each orthogonal to the other, assuming there are no collisions. In between these two propagation regimes, each mode takes on an elliptical polarization state which, if there are no collisions, is orthogonal to the other mode.

The polarizations of the two modes of propagation ($\overrightarrow{E_\mathrm{o}}$ for the O-mode and $\overrightarrow{E_\mathrm{e}}$ for the X-mode) are described by:

$$\overrightarrow{E_\mathrm{o}} = (o_\mathrm{x}e^{i\phi_{o\mathrm{x}}}\hat{x} + o_\mathrm{y}e^{i\phi_{o\mathrm{y}}}\hat{y})e^{i(\omega t - kz)} \quad (7)$$

and

$$\overrightarrow{E_\mathrm{e}} = (e_\mathrm{x}e^{i\phi_{e\mathrm{x}}}\hat{x} + e_\mathrm{y}e^{i\phi_{e\mathrm{y}}}\hat{y})e^{i(\omega t - kz)} \quad (8)$$

o_x and o_y represent the major and minor axes of the O-mode ellipse and similarly, e_x and e_y represent the major and minor axes of the X-mode ellipse (note that e_x and e_y represent the axes of the X-mode ellipse should not be confused with the base of the natural logarithm e). Equation (4) gives the relation between the phasor representations of the oscillations along the x- and y-axes for each mode:

$$\rho_\mathrm{oc} = \frac{o_\mathrm{y}e^{i\phi_{o\mathrm{y}}}}{o_\mathrm{x}e^{i\phi_{o\mathrm{x}}}} \quad (9)$$

and

$$\rho_\mathrm{ec} = \frac{e_\mathrm{y}e^{i\phi_{e\mathrm{y}}}}{e_\mathrm{x}e^{i\phi_{e\mathrm{x}}}}, \quad (10)$$

where ρ_oc and ρ_ec are the axis ratios for the O- and X-modes from Eq. (6), respectively. Substitution gives,

$$\overrightarrow{E_\mathrm{o}} = o_\mathrm{x}e^{i\phi_{o\mathrm{x}}}(\hat{x} + \rho_\mathrm{oc}\hat{y})e^{i(\omega t - kz)} \quad (11)$$

and

$$\overrightarrow{E_\mathrm{e}} = e_\mathrm{x}e^{i\phi_{e\mathrm{x}}}(\hat{x} + \rho_\mathrm{ec}\hat{y})e^{i(\omega t - kz)}. \quad (12)$$

Recall that, because collisions have been neglected, ρ_oc and ρ_ec are imaginary numbers and have opposite signs to represent the opposite sense of rotation of the two modes. For simplicity, the imaginary portion of the two wave-polarization ratios should be explicitly written, so two new variables will be defined as $i\rho_\mathrm{o} = \rho_\mathrm{oc}$ and $i\rho_\mathrm{e} = \rho_\mathrm{ec}$ where the values for ρ_o and ρ_e are purely real. Also, for simplicity, the phases ϕ_{o_x} and ϕ_{e_x} will be written as ϕ_o and ϕ_e. The polarizations of the two modes become:

$$\overrightarrow{E_\mathrm{o}} = o_\mathrm{x}e^{i\phi_\mathrm{o}}(\hat{x} + i\rho_\mathrm{o}\hat{y})e^{i(\omega t - kz)} \quad (13)$$

and

$$\overrightarrow{E_{\mathrm{e}}} = e_{\mathrm{x}} e^{i\phi_{\mathrm{e}}} (\hat{x} + i\rho_{\mathrm{e}}\hat{y}) e^{i(\omega t - kz)} \tag{14}$$

The sense of rotation of the modes is opposite, indicating that ρ_{o} and ρ_{e} must have opposite signs, which Eq. (6) assures.

Now the initial polarization (Eq. 3) can be equated to the polarizations of the two modes of propagation:

$$\overrightarrow{E_{\mathrm{r}}} = \overrightarrow{E_{\mathrm{o}}} + \overrightarrow{E_{\mathrm{e}}}. \tag{15}$$

Equating the real and imaginary components of both the x- and y-axis values in Eq. (15) gives:

$$a\cos\psi = o_{\mathrm{x}}\cos\phi_{\mathrm{o}} + e_{\mathrm{x}}\cos\phi_{\mathrm{e}}, \tag{16}$$

$$-(\pm)b\sin\psi = o_{\mathrm{x}}\sin\phi_{\mathrm{o}} + e_{\mathrm{x}}\sin\phi_{\mathrm{e}}, \tag{17}$$

$$a\sin\psi = -\rho_o o_{\mathrm{x}}\sin\phi_{\mathrm{o}} - \rho_e e_{\mathrm{x}}\sin\phi_{\mathrm{e}}, \tag{18}$$

$$(\pm)b\cos\psi = \rho_{\mathrm{o}} o_{\mathrm{x}}\cos\phi_{\mathrm{o}} + \rho_{\mathrm{e}} e_{\mathrm{x}}\cos\phi_{\mathrm{e}}. \tag{19}$$

The knowns in these equations are a, b, $(\pm)$, and ψ, which define the initial conditions for the wave, (for example, for the initial SuperDARN polarization, a =1.0, b =0.0, the $(\pm)$ does not matter, and ψ is calculated through the coordinate transform mentioned previously). Also known from the local magnetoionic conditions are ρ_{o} and ρ_{e} (from Eq. 6). The unknowns, which need to be solved to determine the relative power delivered to X-mode, are o_{x}, e_{x}, ϕ_{o}, and ϕ_{e}. The solutions to these equations are:

$$\phi_{\mathrm{o}} = \arctan\left[\tan\psi\left(\frac{(\pm)b\rho_{\mathrm{e}} - a}{(\pm)b - a\rho_{\mathrm{e}}}\right)\right], \tag{20}$$

$$o_{\mathrm{x}} = \frac{\sin\psi((\pm)b\rho_{\mathrm{e}} - a)}{\sin\phi_{\mathrm{o}}(\rho_{\mathrm{o}} - \rho_{\mathrm{e}})}, \tag{21}$$

$$\phi_{\mathrm{e}} = \arctan\left[\tan\psi\left(\frac{(\pm)b\rho_{\mathrm{o}} - a}{(\pm)b - a\rho_{\mathrm{o}}}\right)\right], \tag{22}$$

$$e_{\mathrm{x}} = \frac{\sin\psi((\pm)b\rho_{\mathrm{o}} - a)}{\sin\phi_{\mathrm{e}}(\rho_{\mathrm{e}} - \rho_{\mathrm{o}})}. \tag{23}$$

The values for o_{y} and e_{y} are found using:

$$o_{\mathrm{y}} = |\rho_{\mathrm{o}}| o_{\mathrm{x}} \tag{24}$$

$$e_{\mathrm{y}} = |\rho_{\mathrm{e}}| e_{\mathrm{x}}. \tag{25}$$

Finally, the relative power that is delivered to the X-mode compared to the O-mode (R_{e}), which is the quantity that is discussed in the following sections, in units of dB is:

$$R_{\mathrm{e}} = 10\log_{10}\left[\frac{e_{\mathrm{x}}^2 + e_{\mathrm{y}}^2}{o_{\mathrm{x}}^2 + o_{\mathrm{y}}^2}\right]. \tag{26}$$

3 The SuperDARN radar system

High-latitude ionospheric convection is continuously monitored by the Super Dual Auroral Radar Network (SuperDARN) set of radars. A SuperDARN radar consists of sixteen transmitting antennas which produce, at any given time, a single beam of dwell time 7 s (normal scan) or 3 s (fast scan). By means of a phasing matrix, the beam is progressively shifted by 3.25° through 16 successive beam positions, thereby covering an azimuth range of 52° during a single complete scan. The frequency range of the radars is 8–20 MHz (Greenwald et al., 1995).

The antenna beam pattern of a SuperDARN array is designed for poleward viewing at elevation angles less than ∼45°. In practice, power is radiated from the horizontal antennas through all elevation angles from 0–180° (e.g., Arnold et al., 2003). This is beneficial for the ePOP mission as the RRI can therefore receive transmitted signal throughout a pass over a given SuperDARN radar. The electric field polarization of the SuperDARN antennas is linear and oriented horizontal to the Earth. Since the geomagnetic field lines are nearly vertical at higher latitudes, the SuperDARN transmitted linear horizontal polarization is roughly perpendicular to the magnetic field lines. According to the magnetoionic theory, for propagation perpendicular to the magnetic field lines, the horizontal waves transmitted northward are predominantly extraordinary mode (X-mode) signals before entering the ionosphere.

3.1 SuperDARN mode power distribution

The equations for relative mode power derived in Sect. 2 were used to determine the power that a SuperDARN radar distributes to either mode of propagation. Inspection of Eq. (6) indicates that the polarization state with which the two modes propagate is dependent on electron density N_{e} ($\omega_{\mathrm{p}} = \sqrt{e^2 N_{\mathrm{e}}/\epsilon_{\mathrm{o}} m}$), radar frequency ω, and propagation direction θ. As the radars are ground-based, the initial electron density and collision frequency were taken as zero and the polarization ratios of the modes depended only on θ and ω. Equations (20) through (26), along with the polarization ratio (Eq. 6), were used to determine the relative mode power. The power distribution for the Saskatoon SuperDARN (geographic coordinates: 52.16° N, 106.53° E, magnetic coordinates: 61.34° N, 45.26° W) at various frequencies has been modelled. Figure 3 illustrates the relative X-mode power $\left(10\log_{10}\left[\frac{e_{\mathrm{x}}^2+e_{\mathrm{y}}^2}{o_{\mathrm{x}}^2+o_{\mathrm{y}}^2}\right]\right)$ for 12.5 MHz propagation at different elevation and azimuth angles. The directions of geographic north, west, south, and east are represented by "N", "W", "S", and "E", respectively. The edge of the large circle represents 0° elevation angle, while the centre of the circle represents 90° elevation angle or directly vertical. The solid and dashed arrows illustrate the direction to magnetic north and the boresight of the radar, respectively. An X-mode relative

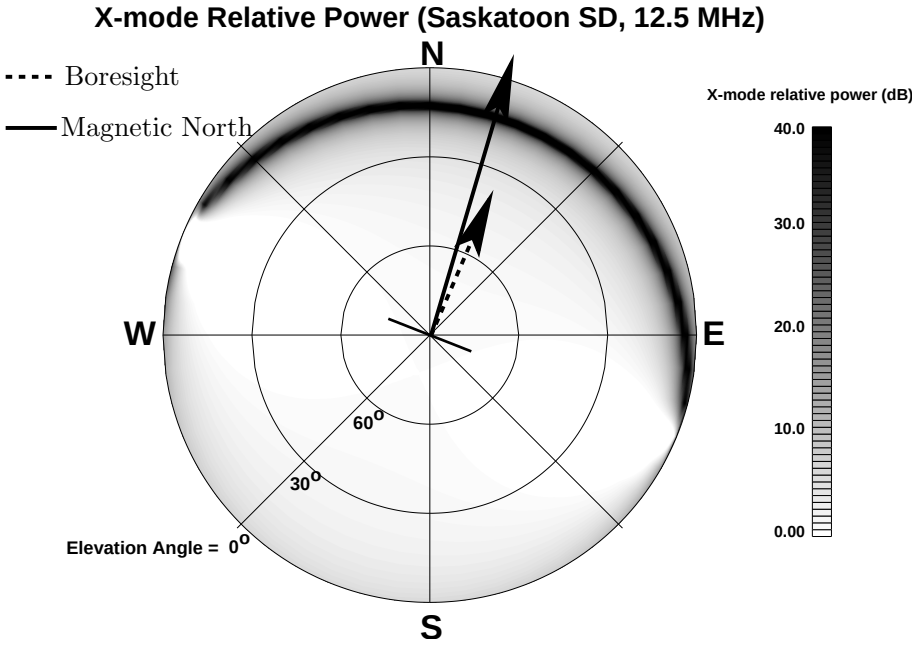

Fig. 3. Relative power delivered to the X-mode (Eq. 26) at 12.5 MHz from the Saskatoon SuperDARN as a function of elevation and azimuth angles.

Table 1. Locations of Canadian SuperDARN radars.

Radar	Latitude (° N) (Geographic)	Longitude (° W) (Geographic)	Latitude (° N) (Geomagnetic)	Longitude (° W) (Geomagnetic)
Saskatoon	52.16	106.53	61.34	45.26
Kapuskasing	49.39	82.32	60.06	9.22
Prince George	53.98	122.59	59.88	65.67
Rankin Inlet	62.82	92.11	72.96	28.17
Inuvik	61.41	133.80	71.15	86.5

power of 0.0 dB (white on the contour plot) would correspond to equal splitting between the two propagation modes. The elevation and azimuth angles which show darker shades on the plot indicate higher relative X-mode power is transmitted in these directions by SuperDARN.

From this figure, it is immediately apparent that there is a band of elevation angles north of the transmitter where the transmission is dominated by the X-mode. Meanwhile, above and south of the radar, the two transmission modes are roughly equal in power. It should also be noted that, near 0° elevation angle and at azimuths that are nearly perpendicular to the boresight, there are two small regions in the plot in which the signal is dominated by the O-mode. This is due to the special geometry that exists in this location between the external magentic field, the propagation vector, and the initial wave polarization. However, since very little signal is transmitted in the direction parallel to the antenna, this region is of little importance. Modelling has also been performed for the other SuperDARN radars in Canada which are listed in Table 1. In general the results are quite similar to the Saskatoon radar modelling. The X-mode relative power maximum is roughly centred on geomagnetic north and decreases in elevation for an increase in geomagnetic latitude. This behaviour is demonstrated in Figs. 4 and 5 which illustrate the relative X-mode power at 12.5 MHz for the Prince George (which is at a different longitude than the Saskatoon radar) and Rankin Inlet (which is at a high latitude) radars, respectively. It is clearly evident for the Prince George radar that the X-mode maximum power band is oriented to centre on magnetic north. Meanwhile the Rankin Inlet radar, which is the closest to the geomagnetic pole, shows an X-mode maximum band very close to the horizon.

Also noted (though not shown) was the effect of frequency on the mode power distributions. Transmitter frequencies of

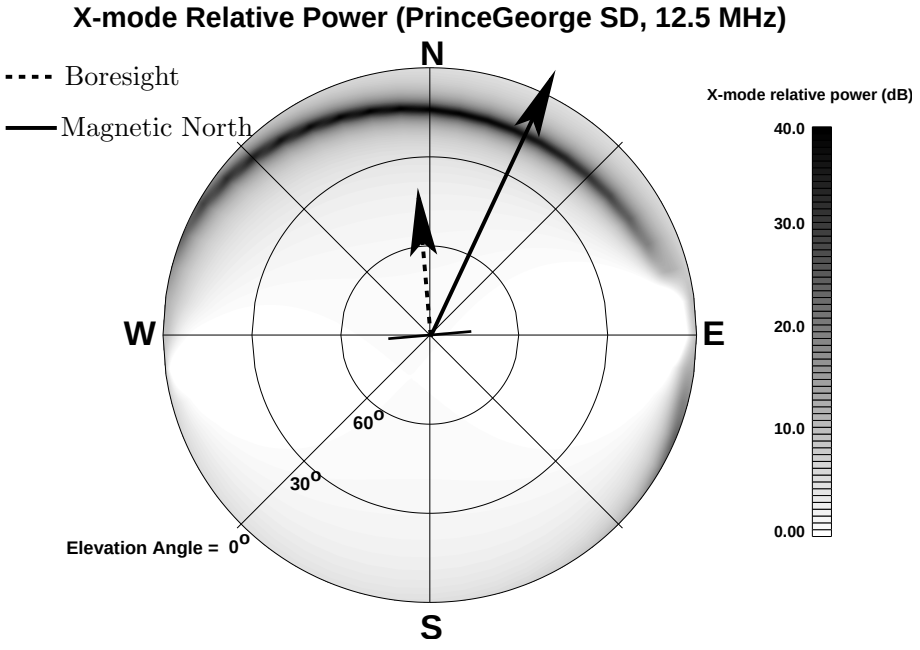

Fig. 4. Relative power delivered to the X-mode (Eq. 26) at 12.5 MHz from the Prince George SuperDARN as a function of elevation and azimuth angles.

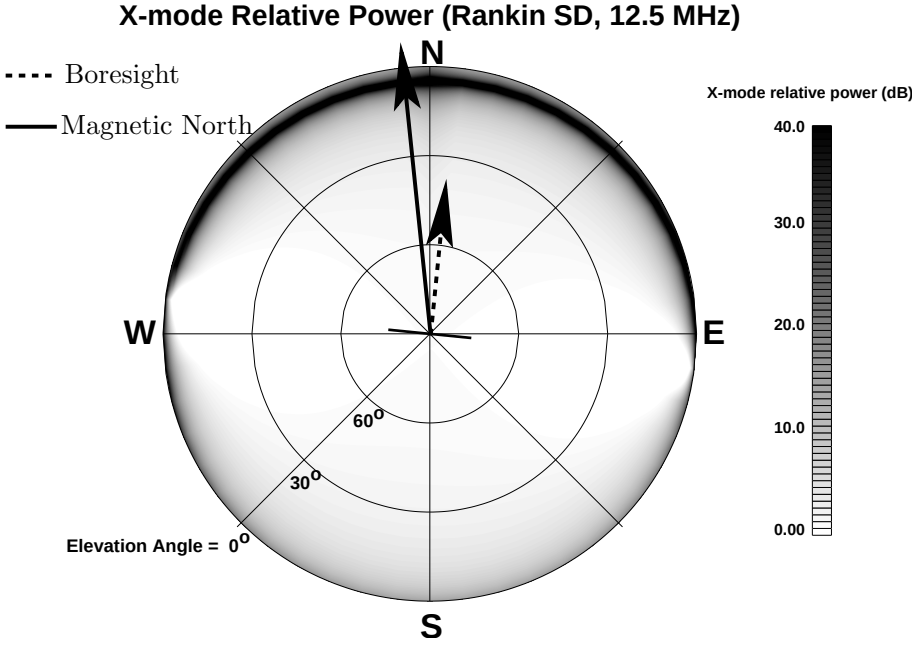

Fig. 5. Relative power delivered to the X-mode (Eq. 26) at 12.5 MHz from the Rankin Inlet SuperDARN as a function of elevation and azimuth angles.

9.5 MHz, 12.5 MHz, and 14.5 MHz were used in the mode power simulations. The main effect of frequency upon the distributions was a slight narrowing of the X-mode maximum band at higher frequencies, which will be discussed in more detail in Sect. 5.

It should be stressed that the power distributions in Figs. 3 through 5 illustrate only the relative power between the two modes and not the absolute transmitted power. The SuperDARN radars have complex antenna patterns and the absolute power of a transmitted signal will vary with launch

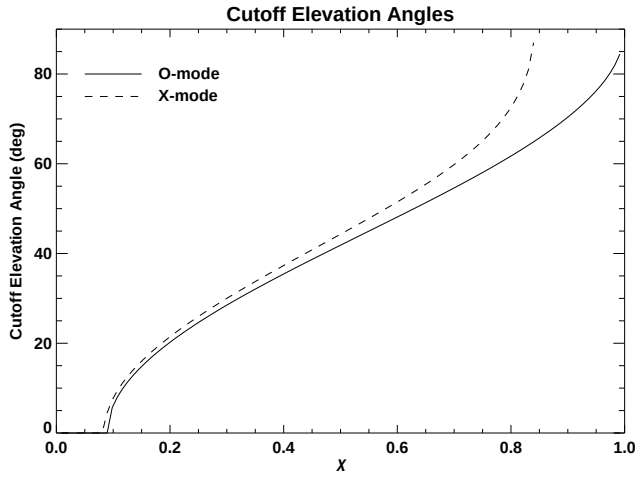

Fig. 6. Cutoff elevation angles as a function of the ratio X ($=\omega_p^2/\omega^2$) at the location of the peak electron density for the O-mode (lower curve) and X-mode (upper curve). Waves launched from the Saskatoon SuperDARN at lower elevation angles than these will be refracted back to Earth and not detected by the RRI on ePOP.

elevation and azimuth angles; however, the relative power between the modes as presented in Figs. 3 to 5 is still correct.

4 Power distributions to be detected by RRI

The preceeding section dealt with the power distributions of the O- and X-modes from a SuperDARN perspective. In order to focus this discussion on the ePOP/RRI experiment, the behaviour of the transmitted waves from SuperDARN as they propagate through the ionosphere to the orbiting RRI receiver was examined.

4.1 Cutoff elevation angles

The main finding of the modelling of the relative power, for either mode received by the RRI, was that waves launched at lower elevation angles will not escape the ionosphere. These waves will be internally reflected by the highly dense F-region peak and thus will not be detected by the orbiting RRI receiver. The peak ionospheric electron density at SuperDARN latitudes can range from below $10^{11}\,\mathrm{m}^{-3}$ to above $10^{12}\,\mathrm{m}^{-3}$ (e.g., Hunsucker and Hargreaves, 2003). With this range of possible densities, the cutoff elevation angle (the minimum elevation angle for which a wave of a given frequency can propagate through the F-peak and reach the satellite) can vary substantially.

For a horizontally stratified ionosphere, the cutoff elevation angle may be found using Snell's Law in spherical coordinates (Bouguer's Law) (Born and Wolf, 1959):

$$n_o R_o \cos\phi_o = n_p R_p \cos\phi_p \tag{27}$$

where n_o, R_o, and ϕ_o are the refractive index, radius (from the centre of the Earth), and elevation angle of the wave at the antenna location, respectively, and n_p, R_p, ϕ_p have similar meanings at the location of the peak electron density in the ionosphere. For the SuperDARN radar, the initial index of refraction n_o on the ground can be taken as unity, and R_o is the radius of the Earth R_E. When the signal at the cutoff elevation angle is totally internally reflected its propagation direction will be horizontal, indicating that ϕ_p is 90°. Radar waves at higher elevation angles will escape the ionosphere and reach the satellite. The peak electron density occurs at roughly $h_{scat} = 300\,\mathrm{km}$ so $R_p = R_E + h_{scat}$. The index of refraction in the ionosphere as given by the Appleton-Hartree equation (Budden, 1961) is

$$n^2 = 1 - \frac{X}{1 - \frac{Y_T^2}{2(1-X)} \pm \sqrt{\frac{Y_T^4}{4(1-X)^2} + Y_L^2}}. \tag{28}$$

The variables X, Y_T, and Y_L are as defined in Sect. 2. The positive sign in Eq. (28) corresponds to the O-mode of propagation and the negative sign to the X-mode of propagation. In Fig. 6, Eqs. (27) and (28) are used to plot the cutoff elevation angle ϕ_o for both modes of propagation versus the ratio X ($=\omega_p^2/\omega^2$), given a constant magnetic field strength of 5×10^{-5} T and an aspect angle $\theta = 80°$. These values are representative of the Saskatoon SuperDARN radar wave propagation conditions. The top curve represents the X-mode cutoff elevation angle and the bottom curve represents the O-mode cutoff elevation angle. Only waves launched at elevation angles higher than those plotted in the figure for a given value of X will escape the ionosphere and reach the RRI on ePOP. As such, the X-mode-only band near 12° elevation angle that is evident in Fig. 3 will only be observable by the RRI when the value for the ratio X at the location of peak F-region electron density is lower than ∼0.1 (the figure indicates that waves launched at elevation angles higher than ∼10° will escape the ionosphere). It should be noted that this cutoff angle calculation has assumed a horizontally stratified ionosphere. In reality, the F-region peak density will vary with latitude north and south of the radar.

Further affecting the transmitted signal as it propagates through the ionosphere is relative absorption of the modes in the lower ionosphere. Depending on the local time and the state of the ionosphere, this absorption can range from essentially zero to complete absorption. For quiet conditions ($K_p < 2$ or 3), it is expected that the amount of absorption for either mode at SuperDARN frequencies will be less than 1 dB. For slightly disturbed conditions ($3 < K_p < 5$), the absorption will be no more than ∼2 dB for the O-mode and ∼4 dB for the X-mode (James et al., 2006; Gillies et al., 2007). Finally, for very disturbed conditions ($K_p > 5$ or 6), both modes will be almost completely absorbed in the D- and E-regions and no signal will reach the RRI receiver.

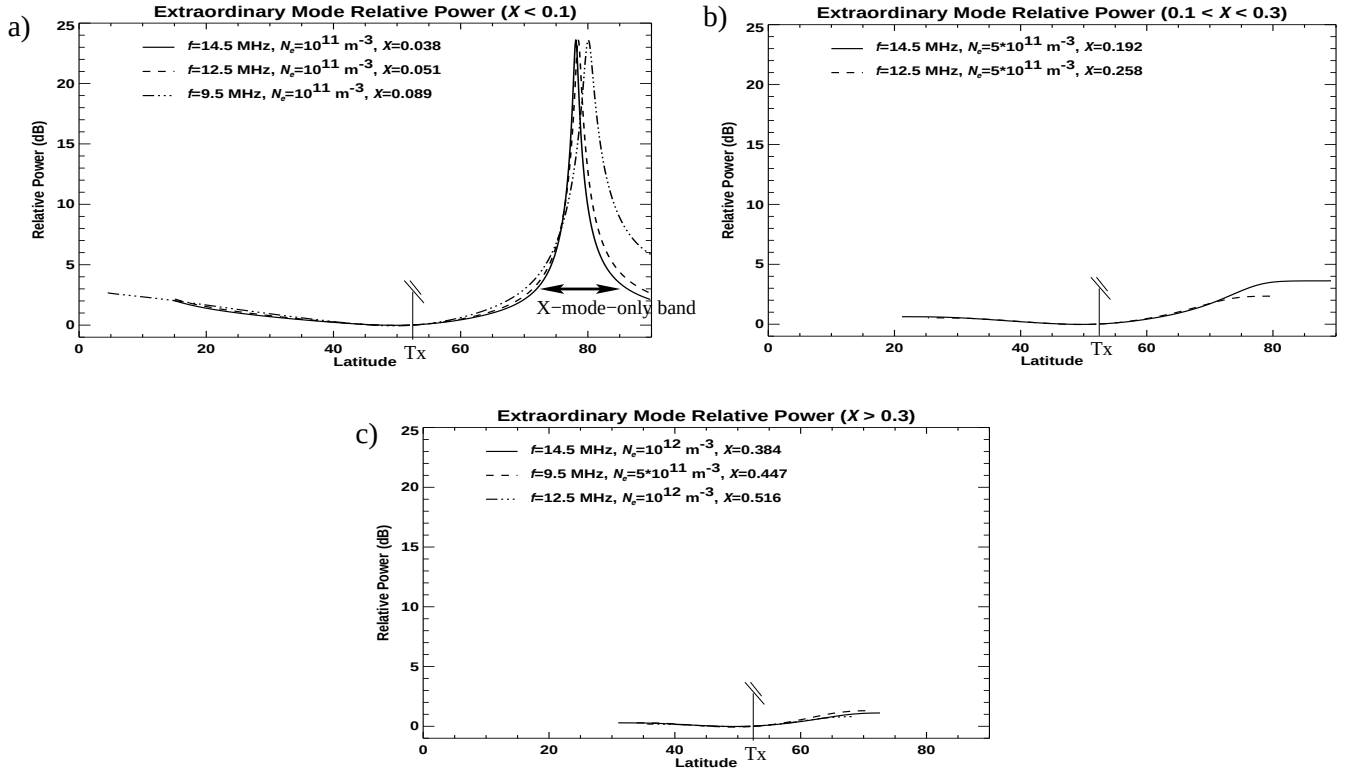

Fig. 7. Modelled X-mode relative power that will be received by the RRI on ePOP. Panels **(a)**, **(b)**, and **(c)** illustrate transmitter frequency and ionospheric peak density combinations which correspond to; $X < 0.1$, $0.1 < X < 0.3$, and $0.3 < X$, respectively. The modelling assumes a north-south satellite orbit at 1500 km directly over the Saskatoon SuperDARN radar (latitude – 52.16° N).

4.2 Raypath modelling of signal received by RRI

The relative mode power that is to be received by the RRI on ePOP as it orbits over the Saskatoon SuperDARN radar has been modelled. A ray tracing program based on the ray equations from Haselgrove (1963) iteratively determined the path a wave would take from the transmitter on the ground to a given location of the satellite orbit. The program took as input the frequency to be transmitted, the starting (antenna) location, and an electron density profile. The electron density profiles for this study were determined from the International Reference Ionosphere (IRI) model (Bilitza, 2001). The magnetic field data for the ray trace program were obtained from the International Geomagnetic Reference Field (IGRF) model (Maus et al., 2005). For this study, the electron density distributions were horizontally stratified so they varied in altitude only. The iteration process was used to study a total of eight passes of the satellite over the transmitter at an orbital altitude of 1500 km, the approximate apogee of the ePOP satellite. The N_e profile and transmitter frequency were varied for each pass. For both the O- and X-modes, rays which propagated from the SuperDARN radar location to the orbiting RRI receiver were calculated for 0.1° latitude increments. Once these connecting rays were determined, the equations developed in Sect. 2 were used to model the relative mode power the RRI would observe in a pass over the transmitter.

Figure 7 illustrates the modelled relative power of the X-mode to that of the O-mode that would be detected by the RRI as a function of satellite latitude as it passes over the Saskatoon SuperDARN for a variety of electron density and frequency combinations. Absorption in the D- and E-regions has been taken into account; however, the electron density profiles were obtained for quiet conditions, so there was very little effect. It should be noted that Fig. 7 predicts equal splitting of power between the O- and X-modes for the majority of the ePOP orbit, however when ionospheric conditions are appropriate for preferential absorption of the X-mode, the O-mode signal that will be detected by the RRI will be higher than that of the X-mode in these locations. A further effect, which has not been considered, is focusing and defocusing of the waves as they propagate through the ionosphere (Hunsucker, 1991). It is possible that skip-distance focusing could preferentially favour the O-mode over the X-mode, which may result in the O-mode being received with a higher power than the X-mode in some instances. Future studies considering the amount of absorption for different levels of ionospheric activity and the effect of focusing and defocusing of the waves are being planned.

In Fig. 7, different transmitter frequency and peak electron density combinations were modelled and are presented by the different curves in the three panels. The panels (a), (b), and (c) in the figure correspond to frequency–peak density combinations which result in; $X < 0.1$, $0.1 < X < 0.3$, and $X > 0.3$, respectively. The peak ionospheric electron density used to produce the values for X in panel (a) was 10^{11} m^{-3} which is a reasonable value to expect in the nighttime ionosphere at SuperDARN observation latitudes. For these low values of X (<0.1), the range of latitudes over which signal was detected was quite large and the X-mode-only band of signal was clearly observable. The curves in panel (b) in Fig. 7 were calculated using a peak electron density of 5×10^{11} m^{-3}, which is a reasonable estimate of peak N_e during evening or morning hours. At these moderate X values ($0.1 < X < 0.3$), the traced waves reached the satellite for a large range of latitudes, and the power was more evenly distributed between the O- and X-modes. Finally, the curves in panel (c) were generated primarily using a profile with a peak N_e of 10^{12} m^{-3} which is representative of electron densities during the daytime. For the higher X values (>0.3), the range of latitudes over which the the signal was observed was much narrower. It should be noted that the given values of X in Fig. 7 are not only dependent on local time as discussed, but also vary with time of year and location. Also, it was assumed in the generation of the profiles used in Fig. 7 that there was little auroral activity. Further, the SuperDARN transmitting frequency is chosen to provide the widest range of ionospheric scatter so that the more extreme values for X may not often occur.

5 Discussion

5.1 Relative mode power distribution of SuperDARN

The plots of relative X-mode power as a function of propagation direction in Figs. 3 to 5 illustrate the X-mode-only band. The middle of the band occurs in the direction where both propagation direction and the wave polarization electric field are perpendicular to the field lines. This behaviour is evident in Figs. 3, 4, and 5 which present the relative power delivered to the X-mode as a function of propagation direction for the Saskatoon, Rankin Inlet and Prince George radars, respectively. The reason that the X-mode-only band is centered on geomagnetic north relates to the geometry of the radar boresight with respect to the background magnetic field. Northward propagation of the waves places them nearly perpendicular to the field lines. Recall that in this regime, the two modes have orthogonal linear polarization states. The O-mode polarization is oriented along the component of the magnetic field in the polarization plane, while the X-mode is oriented perpendicular to this component. Since the initial polarization of SuperDARN is linear and oriented horizontal to the surface of the Earth (or perpendicular to the nearly vertical magnetic field lines), it is basically an X-mode wave when leaving the antenna array. Therefore, it is not unexpected that the X-mode would dominate the transmitted signal in this region. Conversely, above the transmitter and slightly southward, the wave propagates nearly along the magnetic field lines. In this regime, the two modes propagate as orthogonal circular polarization states. The summation of two circular waves of opposite sense will only produce the initial linear wave if they are of equal amplitude. Therefore, for propagation directions that are not perpendicular to the magnetic field lines, the two modes are of roughly equal power.

The effect of frequency on the mode power distributions was also noted (though not presented). An increase in transmitter frequency caused the X-mode-only band to narrow slightly. This was caused by the fact that, at higher frequencies, the band of aspect angles over which the modes take on nearly linear polarizations is much smaller.

It should also be noted that the index of refraction directly affects the Doppler velocity that is measured by SuperDARN (Gillies et al., 2009) and since the indices of refraction for the O- and X-modes are different, identifying which mode participates in coherent scatter is important. Since coherent scatter occurs due to field aligned irregularities, the SuperDARN wave must be perpendicular to the magnetic field lines to receive scatter. Therefore, scatter is received from elevation angles typically below $\sim30^\circ$. Inspection of Figs. 3 through 5 indicates that it is primarily the X-mode which participates in ionospheric scatter. The refractive index of the X-mode is slightly lower than that of the O-mode, so it is important to use the correct value for refractive index when modifications are made to SuperDARN velocity estimates to account for this effect.

5.2 Relative mode power detected by the RRI

Figure 7 demonstrates the relative X-mode power that is expected to be received by the RRI on ePOP as a function of latitude for various ionospheric conditions. For low values of X (<0.1), the signal is expected to be observed over a large latitudinal range and there is a clear region of X-mode-only signal. This behaviour occurs because the computed waves are not bent substantially by the ionosphere and even low elevation angle waves reach the satellite (as could be predicted from Fig. 6). For slightly higher values of X, the signal is observed over a large range of latitudes, but the X-mode-only band is not apparent. In this range, the cutoff elevation angle is higher than the X-mode-only band observed in Fig. 3 so this band does not appear. Near the cutoff elevation angle, however, the traced waves are bent substantially by the ionosphere and this is the reason signal is predicted for a relatively large range of latitudes. When the values for X are even higher (>0.3) the signal is observed over a very short latitudinal range. In these cases, the cutoff elevation angles are quite large and the traced waves are not able to travel far

north or south of the transmitter without being reflected back to Earth before reaching ePOP satellite altitudes.

It is apparent from Fig. 7 that the relative mode power received at RRI will be highly dependent on both frequency and electron density. As the transmitting frequency is known, an analysis of the relative mode power pattern as a function of latitude with reference to Fig. 7 will reveal the variations of the peak ionospheric electron density. If signal is received only over a narrow range of latitudes and the O- and X-modes are of equal power throughout the pass, a high X value at the peak will be inferred. For example, a peak X value of 0.3 or higher will correspond to a peak N_e value above $\sim 6\times10^{11}\,m^{-3}$ if the transmitter frequency is 12.5 MHz. However, if signal is received for a wide range of latitudes and there is a clear X-mode-only band present, then the peak X value and thus the peak electron density will be low. For example, a peak X value of less than 0.1 will only occur when the peak N_e value is below $\sim 2\times10^{11}\,m^{-3}$ for a transmitter frequency of 12.5 MHz.

Another benefit of the measurement of mode power will be the insight that it brings into the relative absorption of the two modes. For example, in the calculations for Fig. 7 it was assumed that there was a quiet ionosphere and thus little absorption of the signal in the D- and E-regions. However, if the X-mode is received with considerably less power than the O-mode at latitudes where the modelling indicated the modes should have roughly equal power, a measure of the amount of relative absorption that occurred can be obtained.

6 Conclusions

The polarization along the paths followed by SuperDARN rays has been studied in preparation for the upcoming ePOP satellite mission. The relative power of the two modes of propagation as a function of propagation direction and frequency has been calculated for each of the Canadian radars. It has been determined that the horizontal linearly polarized wave that is transmitted by the radars resembles the X-mode for propagation north of a transmitter. Therefore, there is a band of azimuths where the X-mode dominates the transmitted signal. This band of "X-mode-only" signal is oriented towards magnetic north and is at an elevation angle equal to the dip angle of the magnetic field lines at the radar. The width of this band narrows with increasing frequency. Meanwhile, above and south of the radars, the transmitted signal is split roughly equally between the O- and X-modes. This is because the modes are circularly polarized states of roughly equal power resulting from the initial linear wave.

Ray tracing of a wave from the Saskatoon SuperDARN to the ePOP RRI receiver was performed for various frequencies and electron density profiles. The relative mode power that will be received as a function of satellite latitude was determined for various F-region peak X (ω_p^2/ω^2) values. It was found that, with an increase in X, the satellite observes signal over a narrower latitude range above the transmitter. Also, the X-mode-only band is only apparent for low peak X values. These calculations of relative mode power as a function of both satellite latitude and electron density will help characterize the ionospheric density profiles and provide a measure of relative absorption of the two propagation modes when the RRI receives signal from the SuperDARN ground transmitters.

It has also been found that for the northward propagation directions from SuperDARN which are most appropriate for ionospheric scatter, the X-mode dominates the transmitted signal. Since the index of refraction is an important factor for interpretation of the measured SuperDARN velocities (Gillies et al., 2009), the fact that the X-mode dominates the coherent scatter is an important result. Attempts to account for refractive index to improve the SuperDARN line-of-sight velocities must recognize that it is the refractive index for the X-mode and not the O-mode which must be applied to the measured velocities.

Acknowledgements. During this work RGG was supported by the Canadian Space Agency and the Natural Sciences and Engineering Research Council (NSERC) to the Canadian component of the SuperDARN ground based radar system and the CASSIOPE/ePOP project. International Reference Ionosphere (IRI) electron density profiles have been provided by the Space Physics Data Facility (SPDF).

Topical Editor K. Kauristie thanks P. Dyson and M. Uspensky for their help in evaluating this paper.

References

Arnold, N. F., Robinson, T. R., Lester, M., Byrne, P. B., and Chapman, P. J.: Super Dual Auroral Radar Network observations of fluctuations in the spectral distribution of near range meteor echoes in the upper mesosphere and lower thermosphere, Ann. Geophys., 19, 425–434, 2001, http://www.ann-geophys.net/19/425/2001/.

Bilitza, D.: International Reference Ionosphere 2000, Radio Sci., 36, 261–275, 2001.

Budden, K. G.: Radio Waves in the Ionosphere, Cambridge University Press, 1961.

Gillies, R. G., Hussey, G. C., Sofko, G. J., McWilliams, K. A., Fiori, R. A. D., Ponomarenko, P., and St.-Maurice, J.-P.: Improvement of SuperDARN velocity measurements by estimating the index of refraction in the scattering region using interferometry, J. Geophys. Res., 114, A07305, doi:10.1029/2008JA013967, 2009.

Gillies, R. G., Hussey, G. C., James, H. G., Sofko, G. J., and André, D.: Modelling and observation of transionospheric propagation results from ISIS II in preparation for ePOP, Ann. Geophys., 25, 87–97, 2007, http://www.ann-geophys.net/25/87/2007/.

Gillies, R. G.: Modelling of Transionospheric HF Radio Wave Propagation for the ISIS II and ePOP Satellites, M.Sc. Thesis, Institute of Space and Atmospheric Studies, University of Saskatchewan, 2006.

Greenwald, R. A., Baker, K. B., Dudeney, J. R., Pinnock, M., Jones, T. B., Thomas, E. C., Villain, J.-P., Cerisier, J. C., Senior, C.,

Hanuise, C., Hunsucker, R. D., Sofko, G., Koehler, J., Nielsen, E., Pellinen, R., Walker, A. D. M., Sato, N., and Yamagishi, H.: DARN/SuperDARN: A Global View of the Dynamics of High-Latitude Convection, Space Sci. Rev., 71, 761–796, 1995.

Haselgrove, J.: The Hamiltonian ray path equations, J. Atmos. Terr. Phys., 25, 397–399, 1963.

Hunsucker, R. D.: Radio Techniques for Probing the Terrestrial Ionosphere, Springer-Verlag Berlin Heidelberg, 1991.

Hunsucker, R. D. and Hargreaves, J. K.: The High-Latitude Ionosphere and its Effects on Radio Propagation, Cambridge University Press, 2003.

James, H. G.: Effects on transionospheric HF propagation observed by ISIS at middle and auroral latitudes, Adv. Space Res., 38(11), 2303–2312, 2006.

James, H. G.: High-frequency direction finding in space, Review of Scientific Instruments, 74(7), 3478–3486, 2003.

James, H. G., Gillies, R. G., Hussey, G. C., and Prikryl, P.: HF fades caused by multiple wave fronts detected by a dipole antenna in the ionosphere, Radio Sci., 41, RS4018, doi:10.1029/2005RS003385, 2006.

James, H. G. and Lunscher, W. H. H. J.: A digital radio receiver for ionospheric research, NATO Specialist Meeting IST-056, "Characterizing the Ionosphere", Paper 23, Fairbanks, AK, USA, 12–16 June 2006.

Maus, S., Macmillan, S., Chernova, T., Choi, S., Dater, D., Golovkov, V., Lesur, V., F. Lowes, Luhr, H., Mai, W., McLean, S., Olsen, N., Rother, M., Sabaka, T., Thomson, A., and Zvereva, T.: The 10th generation international geomagnetic reference field, Phys. Earth Planet. Int., 151, 320–322, 2005.

Wang, L., MacDougall, J. W., and James, H. G.: Ionospheric structure effects on HF radio wave propagation for the Enhanced Polar Outflow Probe (e-POP) satellite mission, Radio Sci., 39, RS2019, doi:10.1029/2003RS002975, 2004.

Yau, A. W, James, H. G., and Lui, W.: The Canadian Enhanced Polar Outflow Probe (ePOP) mission in ILWS, Adv. Space Res., 38(8), 1870–1877, 2006.

Chapter 4

Refractive index estimates from interferometry

4.1 Introduction

The research presented in this chapter is based on the following publication:

- Gillies, R. G., G. C. Hussey, G. J. Sofko, K. A. McWilliams, R. A. D. Fiori, P. V. Ponomarenko, and J.-P. St.-Maurice, Improvement of SuperDARN velocity measurements by estimating the index of refraction in the scattering region using interferometry, *J. Geophys. Res.*, 114, A07305, doi:10.1029/2008JA013967, 2009.

This study examined the systematic underestimation of velocities measured by the SuperDARN radars due to the neglect of the effect of the refractive index in the SuperDARN scattering volume. A method to estimate refractive index was developed, which used elevation angle measurements made by SuperDARN as a proxy.

4.2 Results

High-latitude, HF coherent scatter radars rely on refraction to bend the propagating waves to be perpendicular to the nearly vertical magnetic field lines. Therefore, the refractive index along the path and in the SuperDARN scattering volume is less than one. Until recently, there has been no simple direct method to measure the refractive index in the scattering volume so Doppler velocity calculations made by

SuperDARN have assumed that the refractive index was unity (that of free space). This assumption results in an underestimation of line-of-sight velocities made by SuperDARN by a factor equal to the refractive index at the scatter location. Previous studies by *Davies et al.* [1999], *Xu et al.* [2001], and *Drayton et al.* [2005] have compared velocities measured by SuperDARN to velocities measured by satellites (DMSP) and incoherent scatter radars (EISCAT and Sondrestrom). Each of these studies found, statistically, SuperDARN velocities were 20–30% lower than velocities measured by the other instruments. For example, a comparison between DMSP measurements of velocity and SuperDARN measurements of velocity is presented in Figure 4.1. The linear regression analysis presented in the figure demonstrates that there is very good correlation between the two data sets ($r = 0.92$); however, velocities measured by SuperDARN tend to be statistically lower than velocities measured by DMSP (the slope of the best fit line is only 0.82). It is reasonable to assume that one primary reason for the underestimation of velocities by SuperDARN is due to the neglect of the refractive index in the scattering volume.

As discussed in Section 1.5.4, the SuperDARN array of radars is an essential tool for ionospheric and general space science research. In order to provide the best possible measurements, it is important to determine the refractive index in the scattering volume of SuperDARN so that the amount of underestimation of velocities can be determined. Instruments that measure electron density such as: incoherent scatter radars, ionosondes, and certain satellites, can give an estimate of refractive index within the field-of-view of a SuperDARN radar. Unfortunately, these instruments are not widespread enough to provide electron density values throughout the very large field-of-view associated with all SuperDARN radars. Furthermore, a SuperDARN range cell is 45 km in range, $\sim$50 km in width and may extend for $>$100 km in altitude. The actual location at which scatter occurs is unknown and may only occur in a very small volume of the large range cell. Therefore, one goal of this thesis was to develop methods by which data from SuperDARN itself could be used to predict the refractive index in the scattering volume. This chapter deals with the development and testing of a method that uses elevation angle measurements

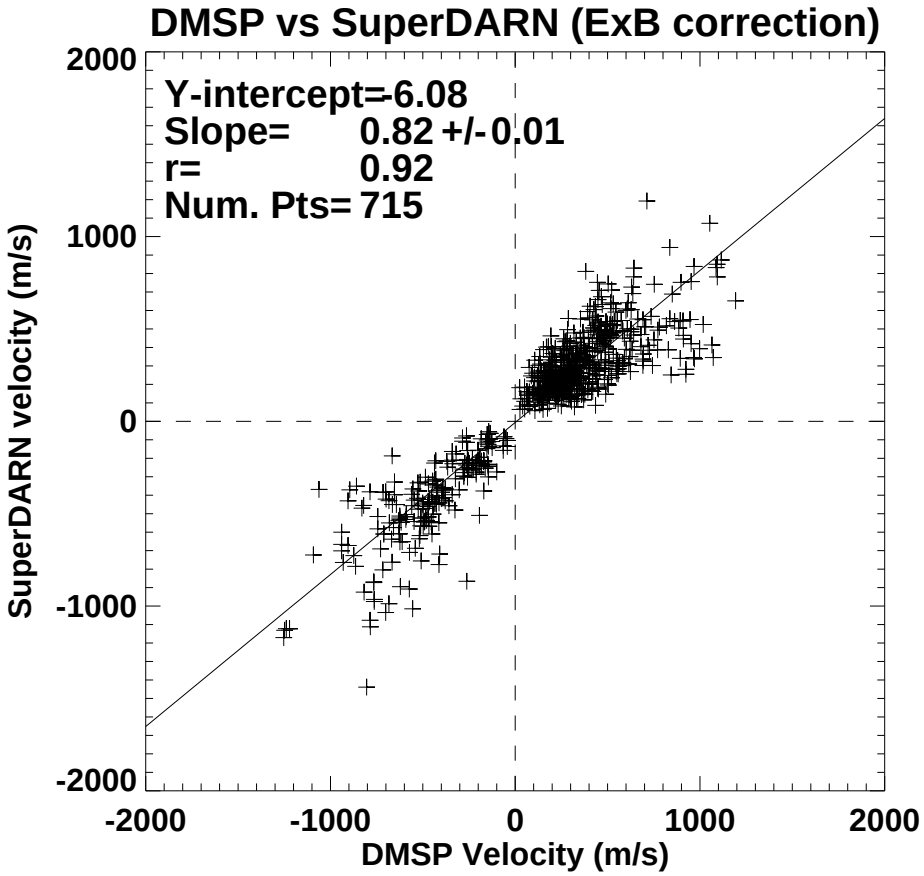

Figure 4.1: Velocities measured by the DMSP satellites and corresponding velocities measured by the SuperDARN radars. Figure 14 from *Ponomarenko et al.* [2009].

from SuperDARN as a proxy for the refractive index in the scattering volume.

Two issues that affect the usefulness of the elevation angle proxy for refractive index are the occasional lack of elevation angle data from some SuperDARN radars and the assumption of a spherically stratified ionosphere. Other estimates of refractive index can be made given a value for electron density in the scattering volume from, for example, incoherent scatter radars. Although, the use of incoherent scatter measurements to determine electron density and refractive index in the scattering volume of SuperDARN is limited, it was beneficial to compare velocities and refractive index values obtained by both radar systems. A comparison between EISCAT

incoherent scatter data and Hankasalmi SuperDARN data, which used electron density measurements from EISCAT, elevation angle measurements from Hankasalmi, and electron density predictions from IRI to determine refractive index, is the focus of the next chapter and the follow-through of this one.

4.3 Published paper

The effect of the refractive index in the SuperDARN scattering volume and the development of the elevation angle proxy discussed in this chapter was published in the *Journal of Geophysical Research* in 2009. Presented immediately below is the paper in the journal format reproduced by permission of American Geophysical Union:

- Gillies, R. G., G. C. Hussey, G. J. Sofko, K. A. McWilliams, R. A. D. Fiori, P. V. Ponomarenko, and J.-P. St.-Maurice, Improvement of SuperDARN velocity measurements by estimating the index of refraction in the scattering region using interferometry, *J. Geophys. Res.*, 114, A07305, doi:10.1029/2008JA013967, 2009.

JOURNAL OF GEOPHYSICAL RESEARCH, VOL. 114, A07305, doi:10.1029/2008JA013967, 2009

Improvement of SuperDARN velocity measurements by estimating the index of refraction in the scattering region using interferometry

R. G. Gillies,[1] G. C. Hussey,[1] G. J. Sofko,[1] K. A. McWilliams,[1] R. A. D. Fiori,[1,2] P. Ponomarenko,[3] and J.-P. St.-Maurice[1]

Received 5 December 2008; revised 27 April 2009; accepted 5 May 2009; published 10 July 2009.

[1] In past calculations of convective velocities from Super Dual Auroral Radar Network (SuperDARN) HF radar observations, the refractive index in the scattering region has not been taken into account, and therefore the inferred ionospheric velocities may be underestimated. In light of the significant contribution by SuperDARN to ionospheric and magnetospheric research, it is important to refine the velocity determination. The refractive index in the ionosphere at SuperDARN observation *F* region altitudes has typical values between 0.8 and close to unity. In the scattering region, where conditions are more extreme, the index of refraction may be much lower. A simple application of Snell's law in spherical coordinates (Bouguer's law) suggests that a proxy for the index of refraction at the scattering location can be determined by measuring the elevation angle of the returned ionospheric radar signal. Using this approximation for refractive index, the Doppler velocity calculation can be refined for each SuperDARN ionospheric echo, using the elevation angles obtained from the SuperDARN interferometer data. A velocity comparison of DMSP and SuperDARN observations has revealed that the SuperDARN speeds were systematically lower than the DMSP speeds. A linear regression analysis of the velocity comparisons found a best fit slope of 0.74. When the elevation angle data were used to estimate refractive index, the best fit slope rose 12% to 0.83. As most SuperDARN radars employ an interferometer antenna array for elevation angle measurements, the improvement in velocity estimates can be done routinely using the method outlined in this paper.

Citation: Gillies, R. G., G. C. Hussey, G. J. Sofko, K. A. McWilliams, R. A. D. Fiori, P. Ponomarenko, and J.-P. St.-Maurice (2009), Improvement of SuperDARN velocity measurements by estimating the index of refraction in the scattering region using interferometry, *J. Geophys. Res.*, *114*, A07305, doi:10.1029/2008JA013967.

1. Introduction

[2] The global network of Super Dual Auroral Radar Network (SuperDARN) [*Greenwald et al.*, 1995] radars measure ionospheric convection in the auroral and polar regions. These HF radars rely on ionospheric refraction to bend the transmitted waves until they are perpendicular to the magnetic field lines. When this occurs, field-aligned ionospheric irregularities can coherently scatter the wave back to the radar. The Doppler shift of the returned wave is used to determine the line-of-sight velocity of the plasma in the scattering region. If it is assumed that the scattering region has a refractive index of unity, the apparent line-of-sight velocity of the scatterer, $v_{s,a}$ is

$$v_{s,a} = \frac{\Delta\omega_D c}{2\omega} \tag{1}$$

where $\Delta\omega_D$ is the Doppler shift of the received wave, ω is the frequency of the radar wave, and c is the speed of light in a vacuum [*Baker et al.*, 1995]. However, the speed of the radar wave in a scattering region of refractive index n_s is c/n_s, so the scatterer velocity $v_{s,c}$ accounting for the refractive index is given as [*Ginzburg*, 1964]

$$v_{s,c} = \frac{\Delta\omega_D c}{2\omega}\frac{1}{n_s} \tag{2}$$

The index of refraction in the *F* region ionosphere, where the HF radar waves are backscattered, is typically less than unity. Because the current SuperDARN Doppler velocity calculation does not account for the index of refraction effect, the ionospheric convection velocity will be underestimated if the index of refraction differs significantly from

[1]Institute of Space and Atmospheric Studies, University of Saskatchewan, Saskatoon, Saskatchewan, Canada.
[2]Natural Resources Canada, Geomagnetic Laboratory, Ottawa, Ontario, Canada.
[3]Space Physics Group, University of Newcastle, Callaghan, New South Wales, Australia.

0148-0227/09/2008JA013967$09.00

unity. Previous velocity comparisons have revealed that SuperDARN speeds are consistently less than speeds obtained by other instruments, such as DMSP [*Drayton et al.*, 2005; *Drayton*, 2006], the European Incoherent SCATter radar (EISCAT) [*Davies et al.*, 1999], and the Canadian Advanced Digital Ionosonde (CADI) [*Xu et al.*, 2001; *Xu*, 2003]. Including the index of refraction term, as required by equation (2), in the SuperDARN determination of velocity is not possible unless there is a reliable n_s estimation for a given observation. It is important to include refractive index effects in the velocity determinations since SuperDARN is an important instrument for ionospheric and magnetospheric studies. SuperDARN produces large-scale convection maps and associated cross polar cap potential difference values every 1 or 2 min. The data products that are based on the SuperDARN observations may therefore also be not as accurate as they could be. In addition to radar studies of the ionosphere, SuperDARN provides important content to a number of multi-instrument collaborations, such as CLUSTER [*Balogh et al.*, 2001] and THEMIS [*Angelopoulos*, 2008] studies, so it is prudent to find a method to estimate n_s.

[3] The parameters which determine the index of refraction in an ionized magnetic medium are given in the Appleton-Hartree equation [*Budden*, 1961]; mainly, the electron concentration (number density) N_e, the magnetic field vector, and the radar wave frequency. In the F region ionosphere the controlling parameters are N_e and the radar wave frequency. The peak electron concentration in the F region ionosphere ranges typically from 10^{11} m^{-3} to 10^{12} m^{-3} [e.g., *Hunsucker and Hargreaves*, 2003]. With this range of possible number densities, and for SuperDARN HF frequencies in the range 9–18 MHz, n_s can vary from ~0.0 to 1.0, but, as will be shown below, typical values appear to be between 0.8 and 1.0.

2. Ray Path Modeling

[4] Ray tracing equations as derived by *Haselgrove* [1963], and based on the Appleton-Hartree equation for the index of refraction, have been modeled in a computer program. The model has been used to calculate the path an HF radar wave will travel through a magnetized plasma, such as the ionosphere. Magnetic field information for the ray tracing model is supplied by the International Geomagnetic Reference Field (IGRF) model [*Maus et al.*, 2005]. An electron density profile is user supplied and can be one- or two-dimensional. The 1-D profiles vary with altitude only and thus maintain the same profile at all horizontal (or latitudinal) distances. The 2-D profiles vary with latitude, as well as with altitude.

2.1. Refraction in a Spherical Coordinate System

[5] If the ionosphere is assumed to be a collection of spherical shells concentric with the center of the Earth, one can utilize Bouguer's law [*Born and Wolf*, 1959], which is Snell's law applied to a spherical coordinate system, to obtain an expression relating the index of refraction at the scattering volume to the angle of arrival or the elevation angle of a backscattered radar wave

$$nR\cos\phi = n_o R_o \cos\phi_o. \tag{3}$$

The variables n_o, R_o, and ϕ_o are the initial refractive index, radius (from the center of the Earth), and elevation angle of the ray, respectively, and n, R, ϕ have similar meaning except at some arbitrary point along the raypath. In the case of scatter from field-aligned irregularities using SuperDARN, these quantities are all relatively well known. First, replace the arbitrary n value with n_s to represent the index of refraction at the scattering location. The initial radius, R_o, is the radius of the Earth. The final radius R is the radius of the Earth plus the scattering altitude (h_s). The angle of arrival ϕ_o is known from interferometry measurements performed by SuperDARN [*Milan et al.*, 1997; *André et al.*, 1998]. The final elevation angle ϕ is 90° minus the magnetic dip angle ψ for scattering from field-aligned irregularities. Rearranging equation (3) to determine n_s in the scattering region gives

$$n_s = \frac{R_E}{(R_E + h_s)} \frac{\cos\phi_o}{\sin\psi}. \tag{4}$$

Equation (4) is independent of any vertical gradients in electron concentration N_e (or consequently the index of refraction n) along the raypath. Both ψ and h_s in equation (4) have some variability; however, as will be demonstrated in section 3.1, any variation of ψ between 80° and 90° or h_s between 150 km and 400 km (which are appropriate values for high-latitude F region coherent backscatter) will have a limited effect on the value of n_s. Therefore, the only piece of information that is needed to determine n_s (and thus determine a refined measured Doppler velocity) is the elevation angle of the returned radar wave. It must be noted, however, that horizontal gradients in N_e were not taken into account in the derivation of equation (4). In order to determine the effect of horizontal gradients on n_s, raypath modeling has been performed.

2.2. Electron Density Profile Selection

[6] To cover the range of possible propagation conditions, a total of 43 different electron number density profiles have been used for the raypath modeling in this study. Of these profiles, twenty were horizontally stratified with N_e only varying in altitude. These 1-D profiles were generated using the International Reference Ionosphere (IRI) model [*Bilitza*, 2001] for both day and night conditions with peak electron concentrations ranging from 10^{11} m^{-3} to 10^{12} m^{-3}. In addition to this, 23 2-D profiles were also created with N_e varying with latitude and altitude (only latitudinal horizontal gradients were considered in the present study). These 2-D profiles were categorized as follows: (1) eight were based on ISIS II topside sounding measurements [*Bilitza et al.*, 2004]; (2) three were directly generated from the IRI model; (3) eight were based on midlatitude trough measurements [*Kersley et al.*, 1997; *Moffett and Quegan*, 1983]; (4) four were artificial profiles with exceptionally large horizontal gradients. An example of one of the 2-D profiles is presented as Figure 1. This N_e profile was generated using both the IRI model and ISIS II topside sounding measurements from 27 June 1978.

[7] The objective for creating these 2-D profiles was to simulate a variety of expected profiles based on observed data as well as some profiles with extreme horizontal gradients which would not be normally expected. The

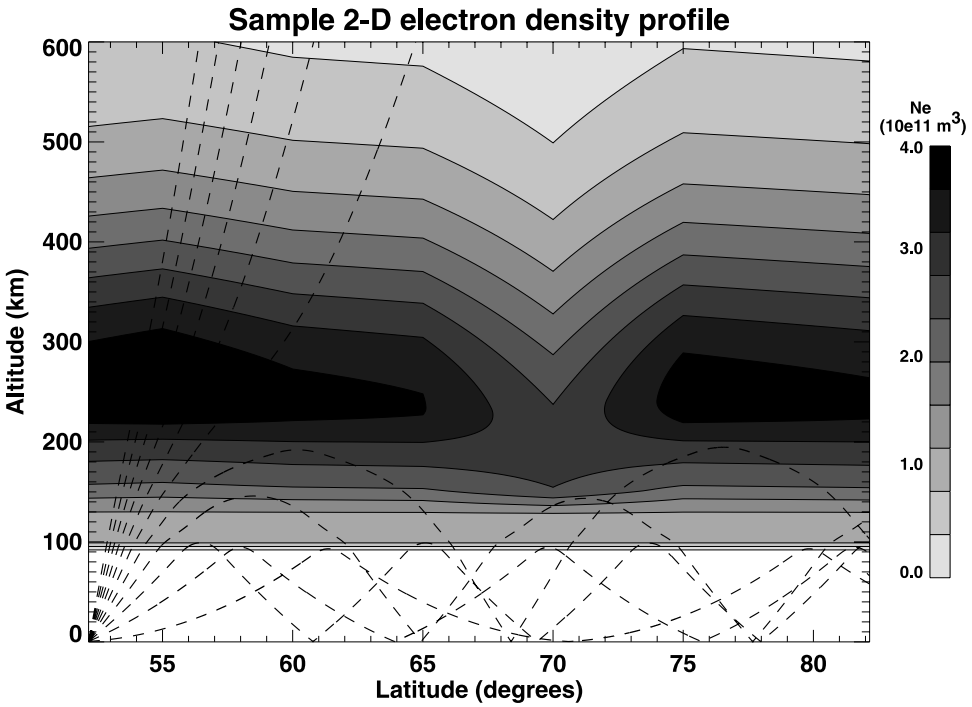

Figure 1. A sample of an electron density profile that was used in this study. The electron density profile was determined using both ISIS II topside soundings of the f_oF_2 peak on 27 June 1978 and the IRI model. The dashed lines on the plot represent a sampling of raypaths from the Saskatoon SuperDARN at a transmitter frequency of 12.5 MHz for varying elevation angles.

profiles constructed to have extreme horizontal gradients had peak electron density gradients of 0.5×10^{11} m^{-3}/°lat over 20° latitude, which is larger than the expected gradient over this latitudinal range from the change in solar zenith angle. In the trough modeled profiles, the peak latitudinal electron density gradient reached 2×10^{11} m^{-3}/°lat, although the horizontal gradient was more localized in latitude. Smaller-scale horizontal gradients, such as the strong gradients associated with precipitation events were not considered.

3. Results

3.1. Elevation Angle Dependence

[8] The ray tracing program was used to calculate the path that a radar wave at a given elevation angle would travel through modeled N_e profiles. Radar wave paths for integer values of elevation angles from 1° to 90° were simulated at three frequencies (9.5 MHz, 12.5 MHz, and 14.5 MHz) for each of the 43 profiles discussed in section 2.2. The points on the raypaths where the ray was within 1° of perpendicularity to the magnetic field lines were selected as scattering locations and recorded, along with the refractive index and elevation angle, subject to the restriction that only scattering heights above an altitude of 150 km were appropriate for F region scatter.

[9] According to equation (4), there should be a clear relationship between the received elevation angle and the refractive index for a spherically stratified ionosphere. The primary objective of the ray tracing simulations was to determine the effect of horizontal gradients on this relationship. Scatter plots of ϕ_o versus n_s (elevation angle versus index of refraction at the scattering location) derived from the simulations are presented as Figure 2. Also included in each plot, as two thick dashed lines, are the conceptual curves from equation (4) for both $h_s = 150$ km, $\psi = 80°$ and $h_s = 400$ km, $\psi = 90°$. Note that these extremes in assumed magnetic dip angle and scatter altitude only change the analytical curve to a minimal degree. The scatter points are split into two groups, those obtained using 1-D electron density profiles (Figure 2a) and those using 2-D electron density profiles (Figure 2b). The points from the 1-D profiles follow the conceptual curves closely as is expected, while the points from the 2-D profiles deviate slightly from the curves.

[10] Figure 2 clearly illustrates the relationship between angle of arrival and refractive index. There is some deviation from the Bouguer's law due to the profiles with the simulated extreme horizontal gradients, but the points generally follow the expected curve. From these plots it is apparent that the measured angle of arrival ϕ_o of a SuperDARN echo leads to a reasonable estimate of the local index of refraction n_s in the scattering region. This allows for the inclusion of n_s in the measured Doppler velocity calculation to be made.

[11] A SuperDARN radar measures elevation angle by using a receiving-only interferometry array of 4 antennas positioned behind or in front of the main array by ~100 m. The cross-correlation between the signal received by the interferometry array and the main array is used to determine the phase difference and elevation angle of the returned echo [*Milan et al.*, 1997; *André et al.*, 1998]. A point of consideration, however, is that the SuperDARN interferometer array can only unambiguously measure elevation angles

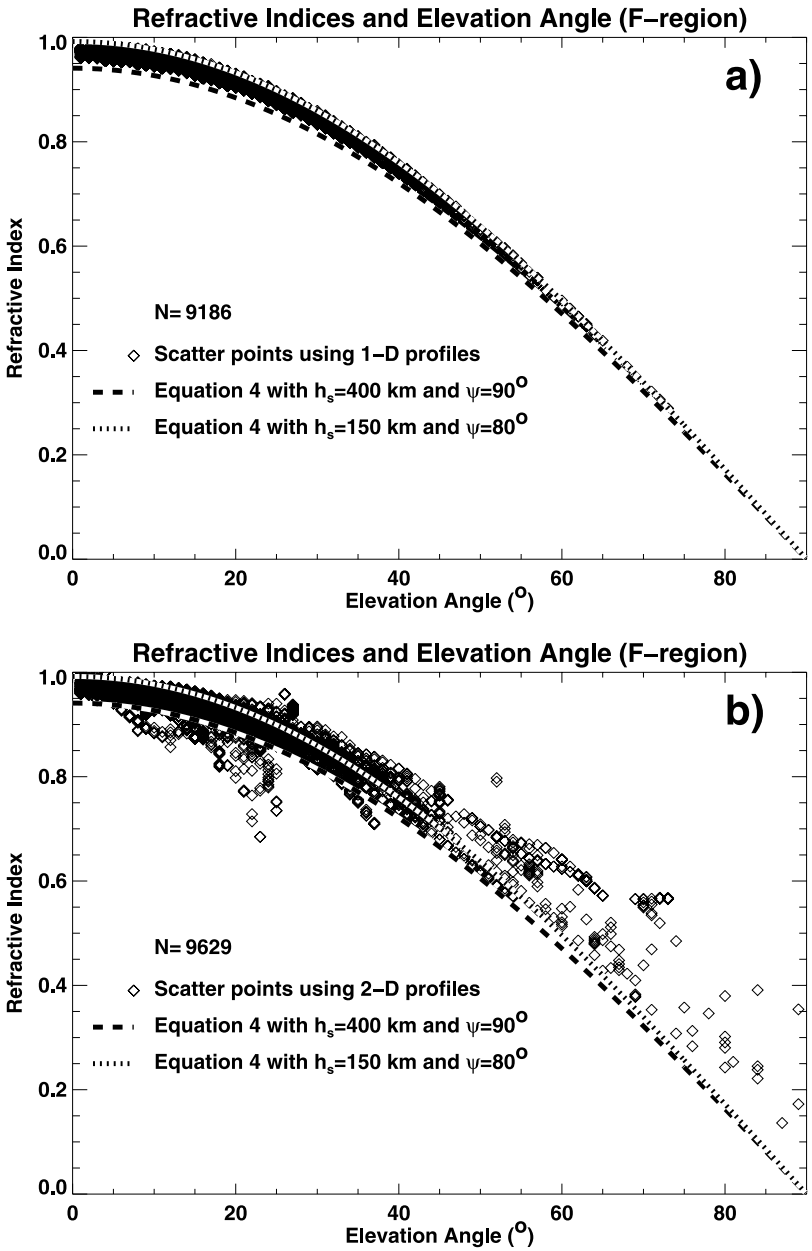

Figure 2. Indices of refraction and elevation angles from ray trace modeling in the *F* region. Each point represents a point on a ray that was within 1° of perfect aspect and was above 150 km altitude. (a) Scatter points found using 1-D N_e profiles and (b) scatter points found using 2-D N_e profiles. The two conceptual curves in each plot are found using equation (4) for two different values of scattering altitude and magnetic dip angle.

if they are less than $\phi_{lim} \sim 40°$, the exact angle being dependent on frequency. This is because the phase difference between the main array and the interferometry array can only be measured up to modulo 2π. Any echoes that occur at elevation angles greater than ϕ_{lim} will be recorded as lower elevation angles. However, as shown in section 3.2, very few modeled scattering points have elevation angles above this value and this restriction should therefore typically not be a concern.

3.2. Scattering Statistics

[12] Although the points presented in Figure 2 are all the result of computational modeling, it is of interest to examine the statistical variation of the refractive index. It should be noted that the actual N_e profiles are not known accurately along the SuperDARN raypaths. The profiles used were chosen to examine the range of possible combinations that might occur. Neither ionosonde observations nor TEC profiles, such as those from GPS receiver arrays, can provide sufficient resolution and detail. An RRI (Radio Receiver Instrument) experiment in which actual SuperDARN transmissions are received every ~20 μs along the ePOP satellite trajectory may provide more detailed N_e profiles [*Yau et al.*, 2006]. The occurrence of index of refraction in the simulated scattering region above 150 km are presented in Figure 3. From Figure 3 it is apparent that,

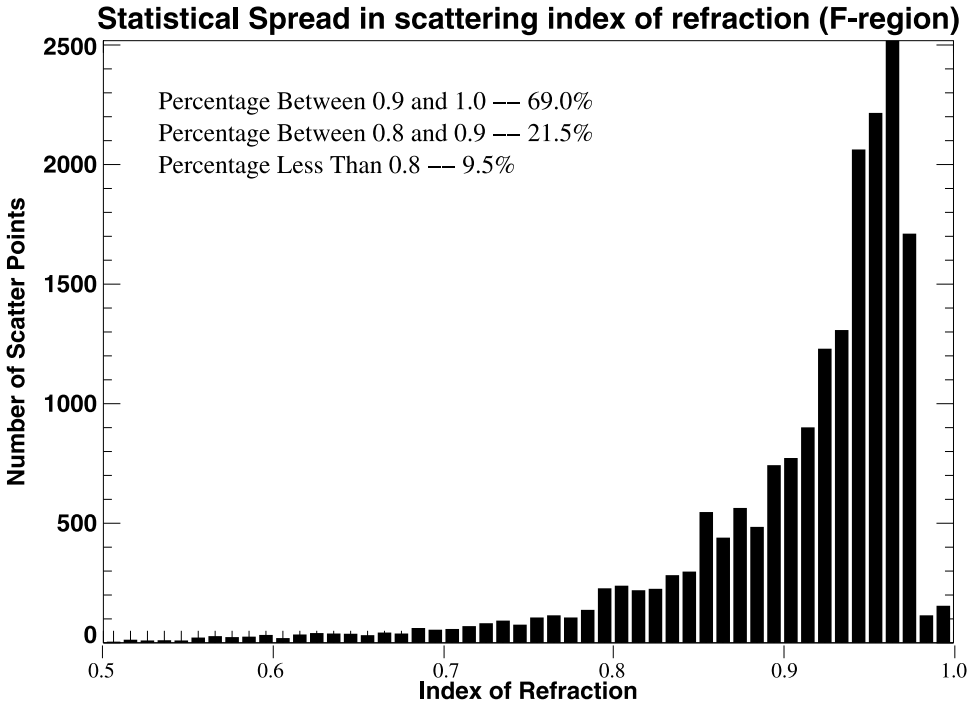

Figure 3. Statistical variation of index of refraction derived from the simulations in the scattering region for scattering altitudes above 150 km.

for the profiles simulated in this study, the majority (~70%) of refractive index values in the scattering region are >0.9. Only about 20% of the echoes have a refractive index between 0.8 and 0.9, and less than 10% have an index of refraction <0.8. The weighted mean value for n_s is 0.91. This suggests that even if the refractive index cannot be estimated using angle-of-arrival measurements (e.g., owing to lack of interferometry measurements), the SuperDARN measured Doppler velocity for a given ionospheric echo is typically around 10% too low.

3.3. DMSP/SuperDARN Velocity Comparison

[13] There have been a number of previous comparisons of *F* region velocity measurements between SuperDARN and a variety of other instruments. For example, *Davies et al.* [1999] compared SuperDARN velocities with velocities from the EISCAT incoherent scatter radar, *Xu et al.* [2001] compared SuperDARN velocities with velocities from the Sondrestrom incoherent scatter radar, and *Xu* [2003] compared SuperDARN velocities with velocities obtained from ionosondes, incoherent scatter radars, and DMSP satellites. *Drayton* [2006] and *Drayton et al.* [2005] performed an extensive comparison between SuperDARN and DMSP velocities. Data over a 4 year period (1999–2002) were compared when the satellite and radar velocity components were within 5°. A least squares fit of the velocity measurements between SuperDARN and DMSP gave a slope of 0.84 in the *Drayton* [2006] study.

[14] As a test to see if including the refractive index correction at the scattering region in the SuperDARN velocity calculations eliminates, or at least reduces, the apparent underestimation of SuperDARN velocity measurements, another SuperDARN-DMSP comparison was performed for this paper (other comparisons are in progress). The *Drayton* [2006] study was used as a basis for applying the n_s refinement to SuperDARN Doppler velocity calculations. In this present comparison, the proxy method to obtain an estimate of the refractive index at the scattering region by using the angle of arrival or elevation angle of the returned echo (equation (4)), was employed. The refractive index term has been omitted from the SuperDARN velocity calculation in the past because the value was unknown. Unfortunately, some of the radars in the *Drayton* [2006] study did not have elevation angle data available. Therefore, the inclusion of the n_s term to the entire data set was not possible and ~80% of the data points which they employed had to be discarded, leaving 159 individual velocity comparisons to consider.

[15] The possibility of including SuperDARN scatter from the *E* region of the ionosphere, where the drift velocity is not expected to be equivalent to the ExB velocity was taken into consideration. As an initial check, trigonometry was employed, including multiple hop scenarios, using the measured elevation angle of an echo and the slant range to estimate the altitude of the ionospheric scatter. It was found that only ten of the 159 measurements which were considered in this study had the slightest possibility of being from an altitude appropriate for *E* region scatter. As a final check, these possible *E* region echoes were found not to have significantly lower SuperDARN velocity values than the corresponding DMSP measurements. Therefore, there was no *E* region contamination.

[16] The selection criteria for DMSP and SuperDARN velocity values to compare was covered in detail by *Drayton et al.* [2005]; however, a brief summary is presented in this paper. SuperDARN line-of-sight data collected in the standard mode of operation with 1 or 2 min scan times was considered. In these modes each of

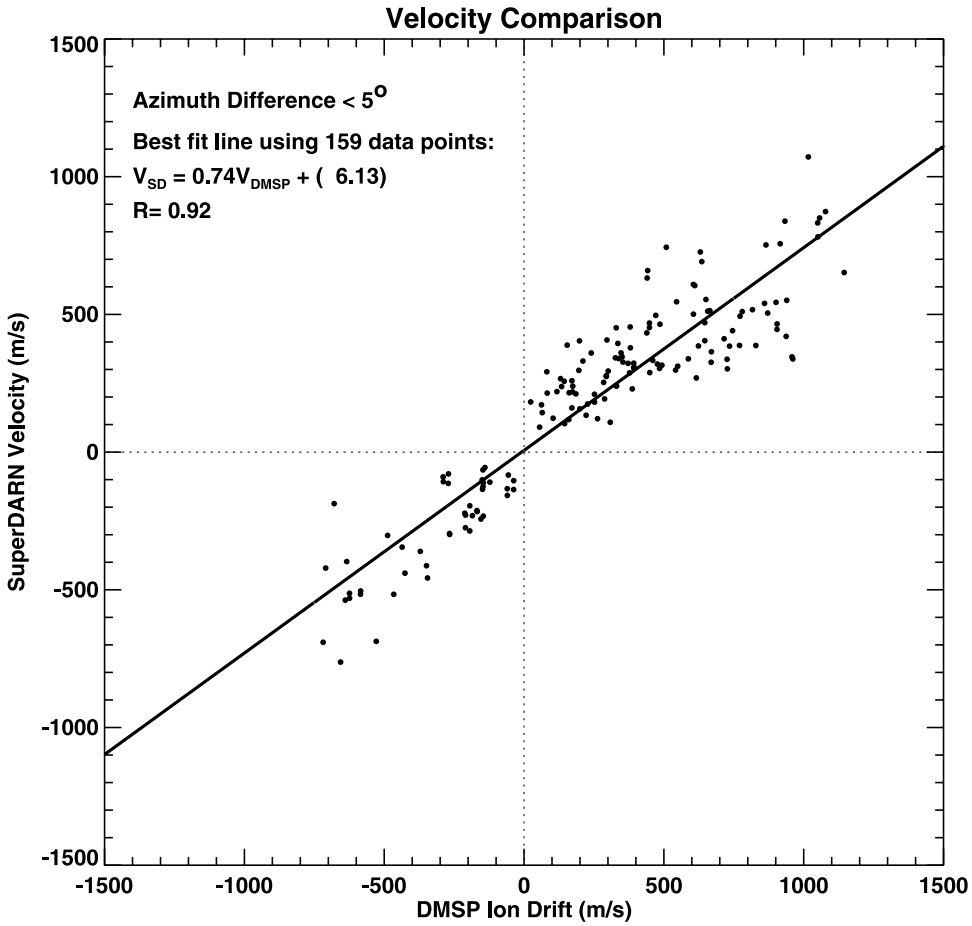

Figure 4. SuperDARN and DMSP velocity comparison. The data have been corrected for the field mapping between 840 km (DMSP altitude) and 250 km (SuperDARN scatter altitude). The solid line represents the least squares best fit.

the 16 beams of a given radar was scanned for either 3 or 7 s (1 min or 2 min scans, respectively). The beam width was 3.24°, corresponding to a cell width of ~110 km at a range of 2000 km, which was the average range. The velocity measurements were binned into 45-km range gates beginning at 180 km. Only SuperDARN velocities with echo power of more than 3 dB and a spectral width of less than 500 m/s were considered.

[17] The DMSP data consisted of 4-s averaged cross-track ion drift measurements. Measurements with a poor quality flag were not considered. Satellite passes over a given radar were considered if the angle between the cross-track ion drift measurement of the satellite and the line-of-sight measurement of the radar in the horizontal plane were within 5°. All 4-s DMSP measurements which were within 45 km of the center of the SuperDARN cell of interest were averaged. Usually three DMSP measurements met this criteria for a given SuperDARN range cell. This averaging resulted in a DMSP measurement over about 90 km along the satellite track compared to the ~45 × 110-km SuperDARN cell. The DMSP velocity measurement at ~840 km was then mapped down to the SuperDARN measurement altitude of ~250 km. Measurements of DMSP were recorded if they met the previous criteria and occurred within the 1 or 2 min scan time of the given SuperDARN radar. Therefore, measurement times may have been separated by up to 2 min; however, the actual integration time by each instrument was comparable (~12 s for DMSP and 3 or 7 s by SuperDARN).

[18] The comparison between DMSP and SuperDARN velocities when elevation angle information was available is presented as Figure 4. A linear regression analysis of the data found that the slope of the best fit line was 0.74 and the regression coefficient was 0.92. This comparison includes an altitude ExB correction along dipole field lines. A dipole field-mapping correction to velocities accounts for the difference in measurement altitude of ~840 km altitude for DMSP and an assumed scattering altitude of 250 km for SuperDARN. This altitude difference results in the higher-altitude measurements being ~16% larger before being mapped down to SuperDARN scattering altitudes [*Drayton*, 2006]. Again, the comparison shows that SuperDARN velocities were on average lower than DMSP values, and, in fact, even lower than the *Drayton* [2006] study where the slope of the best fit line was 0.84. The discrepancy between these two data sets is addressed in section 3.3.1.

[19] The index of refraction proxy using elevation angle was used to improve the velocity measurements for SuperDARN. In Figure 5, the comparison data is presented with the SuperDARN velocity calculations improved using the

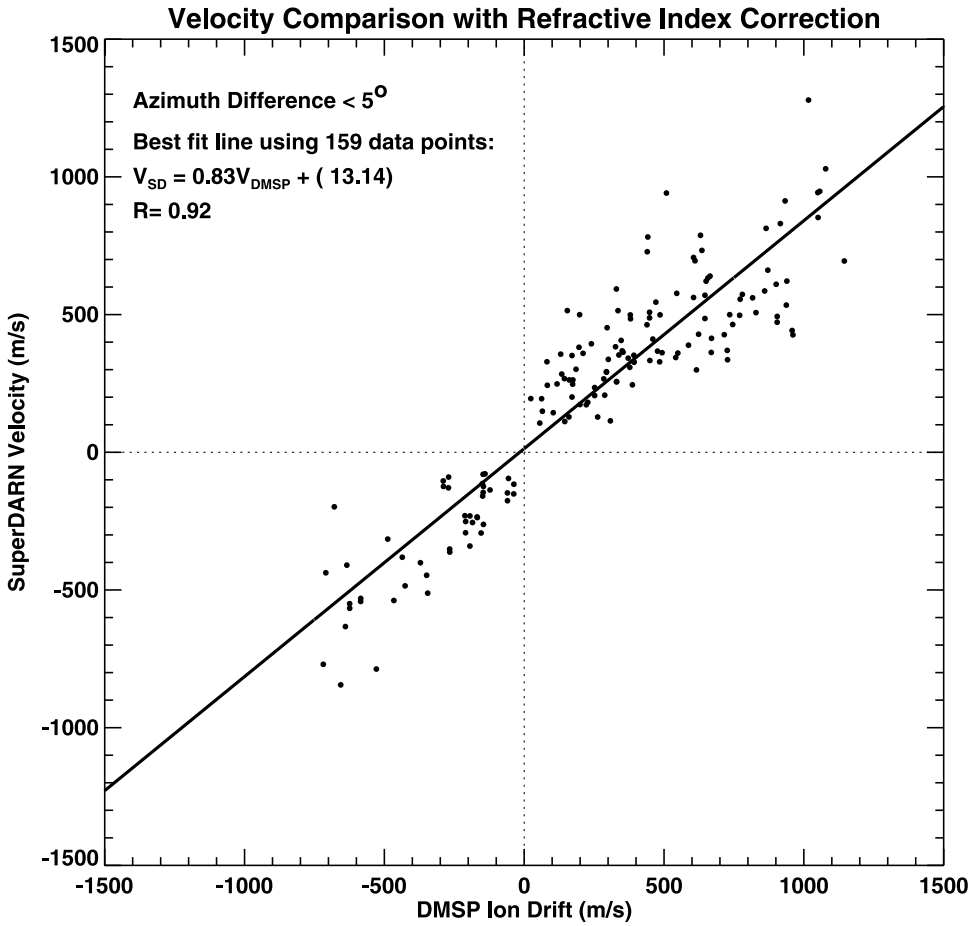

Figure 5. SuperDARN and DMSP velocity comparison. The data have been corrected for both the field mapping between 840 km (DMSP altitude) and 250 km (SuperDARN scatter altitude) and the index of refraction using equation (4) with SuperDARN angle-of-arrival data. The solid line represents the least squares best fit.

elevation angle as a proxy to provide an index of refraction estimate from equation (4). For this estimate of n_s, the scattering altitude was assumed to be h_s = 250 km and ψ was found using a dipole estimate for the magnetic field of the Earth (note that ψ was always between 80° and 90° and therefore was essentially constant). There is better agreement between the velocity measurements of the two instruments, with the slope of the best fit line increasing from 0.74 to 0.83.

3.3.1. Examination of Slope Difference

[20] The difference in slope between the *Drayton* [2006] study (0.84) and the subset of the data used in this study (0.74) is quite large. The discrepancy between the data sets is a systematic effect because repeatedly randomly sampling 20% of the points from the *Drayton* [2006] study could not produce a slope as low as 0.74.

[21] A probable explanation for the lower slope velocity comparison value in the present study compared to the slope in the *Drayton* [2006] study is that the radars which provided the elevation angle data in this study had relatively more data points within the auroral oval than the *Drayton* [2006] study. Table 1 lists the radars used in both studies, the number of data points used for each, and the slope values obtained.

[22] The number of data points inside and outside the auroral oval were determined using DMSP particle spectra to estimate the location of the auroral oval. It was found that for the *Drayton* [2006] study, 244 out of 715 points were within the oval (∼34%), while for the subset of points in which elevation angle data was available for this study, 101 out of 159 points were within the oval (∼64%). A linear regression analysis of the points within the auroral oval results in a best fit slope of 0.71, while the same analysis of points outside the auroral oval results in a best fit slope of

Table 1. SuperDARN Radars Used for Velocity Comparisons

	Drayton [2006]		Present Study	
Radar	Number of Points	Best Fit Slope	Number of Points	Best Fit Slope
Halley	159	0.58	0	–
Hankasalmi	43	0.74	27	0.81
Kodiak	111	0.87	37	0.82
Pykkvibaer	60	0.71	51	0.72
Sanae	80	0.56	0	–
Saskatoon	59	0.68	43	0.70
Stokkseyri	49	0.87	1	–
Syowa East	86	0.99	0	–
Syowa South	68	0.90	0	–

0.86. Clearly, the points within the auroral oval (which the subset used in this study is biased toward) had a tendency to have a lower best fit slope value than the points outside the auroral oval.

[23] One possible explanation for this difference is that higher electron densities within the auroral oval produce a lower index of refraction, on average. Higher electron densities in the auroral zone are expected for a number of reasons. Within the auroral oval, processes such as particle precipitation, field aligned currents, and higher photoionization could all cause the electron density to increase, particularly in the scattering regions where highly structured and large N_e spatial gradients are expected in the neighborhood of small-scale, intense FACs whose primary precipitating electrons produce large numbers of secondary electrons. This would reduce the index of refraction. If this reduction is neglected, the result is lower SuperDARN velocity measurements and a lower slope when compared with DMSP measurements. It is also likely that the greatest contributions to the radar scattering are the areas where the electron densities and their gradients are the most extreme.

[24] In contrast, in the polar cap region where there is less photoionization and the plasma density becomes depleted because of the polar wind and diffusion on open flux tubes, the electron densities are expected to be lower, on average. Therefore the index of refraction is expected to be closer to unity, so the measured SuperDARN velocities there should be closer to the values obtained from DMSP.

4. Discussion

[25] SuperDARN velocity measurements are routinely calculated using equation (1), which does not account for the refractive index in the scattering region. To account for n_s, equation (2) should be employed; however, a measured estimate of n_s was not available until now. The use of equation (4) and the interferometry measured elevation angle is able to give a proxy for an estimate of n_s which allows the use of equation (2) for a better velocity estimate by SuperDARN. As equation (4) was derived under spherically symmetric conditions, horizontal gradients were not taken into account. Section 3 was concerned with accessing the significance of these horizontal gradients in using equation (4) as a proxy estimate of n_s. This analytical proxy showed that the presence of horizontal gradients caused some deviation from equation (4), as would be expected; however, use of equation (4) is an excellent zeroth-order estimate for n_s, the index of refraction in the scattering region.

[26] Figure 5 illustrates that SuperDARN velocity measurements appear to be systematically underestimated when compared to DMSP even after taking into consideration n_s using the elevation angle proxy. One possible reason for this discrepancy may arise from temporal and spatial disagreement between measurements. In both this and the *Drayton* [2006] studies, although both the integration time and spatial extent of measurements were comparable, they may have occurred up to 2 min apart and the refractive nature of SuperDARN HF wave propagation could also have caused a small uncertainty in determination of the scattering location. On a statistical basis, however, these sources of disagreement should tend to cancel out (i.e., SuperDARN should both overestimate and underestimate some velocities). This does not appear to be the case here and would also not explain previous comparisons with other instruments in which SuperDARN velocities were always statistically lower.

[27] The modeling in this study has been focused on large-scale effects of horizontal gradients on the elevation angle proxy for estimating n_s, and did not consider the much smaller scale, but potentially high gradients, expected to be present (and required) for scattering. Such gradients would be expected to be present as there is auroral precipitation in this region which would cause gradient structures as small as hundreds of meters or even less to develop [e.g., *Noël et al.*, 2000, 2005; *Sofko et al.*, 2007]. Furthermore, medium-scale structures, such as polar patches would also cause deviation from the analytical curve. In fact, it may be that ionospheric scatter occurs predominantly in the presence of such density gradients. One of the main sources of ionospheric irregularities that cause coherent scatter is the gradient drift instability, which requires gradients in electron density. As scattering is assumed to occur predominantly in the presence of such structures, then the few points clustered below the analytical curve in Figure 2 (which were the result of raypath modeling using high electron density gradients) may occur more often than the modeling suggests. Inclusion of these potentially important effects requires further study.

5. Conclusions

[28] The index of refraction in the SuperDARN scattering region has been neglected in velocity estimations until now as it was not typically available. This has resulted in underestimation of measured Doppler velocities by SuperDARN. As these measurements can be an integral part of studies in ionospheric and magnetospheric science any improvements in their accuracy is beneficial.

[29] This paper presents a method to obtain a refinement to SuperDARN velocities by using angle-of-arrival or elevation angle measurements of the returned radar echoes as a proxy for the index of refraction in the scattering volume. Evidence supporting the proposed relation between angle of arrival and index of refraction was provided by raypath modeling. Ray tracing simulations through a variety of 1-D and 2-D ionospheric electron density profiles have indicated that the index of refraction in the scattering region is usually between 0.8 and 1.0 for ~90% of cases. To further test the proxy, a velocity comparison between DMSP and SuperDARN measurements has also been performed. This study found that the comparison between SuperDARN and DMSP measured velocities was improved by inclusion of the index of refraction using elevation angle data; however, SuperDARN measured velocities were still lower on average. Nevertheless, the elevation angle method to determine a proxy for index of refraction is a simple, but effective, first step toward improving SuperDARN velocity measurements.

[30] **Acknowledgments.** We acknowledge the support of the Canadian Space Agency and the Natural Sciences and Engineering Research Council (NSERC) to the Canadian component of the SuperDARN ground-based radar system and the CASSIOPE/ePOP project for our research. International Reference Ionosphere (IRI) electron density profiles have been

provided by the Space Physics Data Facility (SPDF). Digitized online ISIS II data have been supplied by R. F. Benson at the National Aeronautics and Space Administration (NASA) Goddard Space Flight Center (GSFC) and Coordinated Data Analysis Web (CDAWeb). We gratefully acknowledge the Center for Space Sciences at the University of Texas at Dallas and the U.S. Air Force for providing the DMSP thermal plasma data.

[31] Zuyin Pu thanks Ray Greenwald and Darren Wright for their assistance in evaluating this paper.

References

André, D., G. Sofko, K. Baker, and J. MacDougall (1998), SuperDARN interferometry: Meteor echoes and electron densities from groundscatter, *J. Geophys. Res.*, *103*, 7003–7015.

Angelopoulos, V. (2008), The THEMIS Mission, *Space Sci. Rev.*, *141*, 5–34.

Baker, K. B., J. R. Dudeney, R. A. Greenwald, M. Pinnick, P. T. Newell, A. S. Rodger, N. Mattin, and C.-I. Meng (1995), HF radar signatures of the cusp and low-latitude boundary layer, *J. Geophys. Res.*, *100*, 7671–7695.

Balogh, A., et al. (2001), The Cluster Magnetic Field Investigation: Overview of in-flight performance and initial results, *Ann. Geophys.*, *19*, 1207–1217.

Bilitza, D. (2001), International Reference Ionosphere 2000, *Radio Sci.*, *36*, 261–275.

Bilitza, D., X. Huang, B. W. Reinisch, R. F. Benson, H. K. Hills, and W. B. Schar (2004), Topside Ionogram Scaler With True Height Algorithm (TOPIST): Automated processing of ISIS topside ionograms, *Radio Sci.*, *39*, RS1S27, doi:10.1029/2002RS002840.

Born, M., and E. Wolf (1959), *Principles of Optics: Electromagnetic Theory of Propagation, Interference and Diffraction of Light*, Pergamon, New York.

Budden, K. G. (1961), *Radio Waves in the Ionosphere*, Cambridge Univ. Press, Cambridge, U. K.

Davies, J. A., M. Lester, S. E. Milan, and T. K. Yeoman (1999), A comparison of velocity measurements from the CUTLASS Finland radar and the EISCAT UHF system, *Ann. Geophys.*, *17*, 892–903.

Drayton, R. A. (2006), Study of SAPS-like flows with the King Salmon SuperDARN radar, M.Sc. thesis, Univ. of Saskatchewan, Saskatoon, Saskatchewan, Canada.

Drayton, R. A., A. V. Koustov, M. R. Hairston, and J.-P. Villian (2005), Comparison of DMSP cross-track ion drifts and SuperDARN line-of-sight velocities, *Ann. Geophys.*, *23*, 2479–2489.

Ginzburg, V. L. (1964), *The Propagation of Electromagnetic Waves in Plasmas*, Pergamon, New York.

Greenwald, R. A., et al. (1995), DARN/SuperDARN: A global view of the dynamics of high-latitude convection, *Space Sci. Rev.*, *71*, 761–796.

Haselgrove, J. (1963), The Hamiltonian ray path equations, *J. Atmos. Terr. Phys.*, *25*, 397–399.

Hunsucker, R. D., and J. K. Hargreaves (2003), The High-Latitude Ionosphere and Its Effects on Radio Propagation, Cambridge Univ. Press, Cambridge, U. K.

Kersley, L., S. E. Pryse, I. K. Walker, J. A. T. Heaton, C. N. Mitchell, M. J. Williams, and C. A. Willson (1997), Imaging of electron density troughs by tomographic techniques, *Radio Sci.*, *32*(4), 1607–1621.

Maus, S., et al. (2005), The 10th generation international geomagnetic reference field, *Phys. Earth Planet. Inter.*, *151*, 320–322.

Milan, S. E., T. B. Jones, T. R. Robinson, E. C. Thomas, and T. K. Yeoman (1997), Interferometric evidence for the observation of ground backscatter originating behind the CUTLASS coherent radars, *Ann. Geophys.*, *15*, 29–39.

Moffett, R. J., and S. Quegan (1983), The mid-latitude trough in the electron concentration of the ionospheric F-layer: A review of observations and modelling, *J. Atmos. Terr. Phys.*, *45*(5), 315–343.

Noël, J.-M. A., J.-P. St.-Maurice, and P.-L. Blelly (2000), Nonlinear model of short-scale electrodynamics in the auroral ionosphere, *Ann. Geophys.*, *18*, 1128–1144.

Noël, J.-M. A., J.-P. St.-Maurice, and P.-L. Blelly (2005), The effect of E-region wave heating on electrodynamical structures, *Ann. Geophys.*, *23*, 2081–2094.

Sofko, G., R. Schwab, M. Watanabe, C. Huang, J. Foster, and K. McWilliams (2007), Auroral post-secondary ions from the nightside ionosphere in the inner magnetosphere, *J. Atmos. Sol. Terr. Phys.*, *69*, 1213–1232.

Xu, L. (2003), SuperDARN-derived plasma convection comparison with other data and application to field-aligned current measurements, Ph.D. thesis, Univ. of Saskatchewan, Saskatoon, Saskatchewan, Canada.

Xu, L., A. V. Koustov, J. Thayer, and M. A. McCready (2001), SuperDARN convection and Sondrestrom plasma drift, *Ann. Geophys.*, *19*, 749–759.

Yau, A. W., H. G. James, and W. Lui (2006), The Canadian Enhanced Polar Outflow Probe (e-POP) mission in IWS, *Adv. Space Res.*, *38*(8), 1870–1877.

R. A. D. Fiori, R. G. Gillies, G. C. Hussey, K. A. McWilliams, G. J. Sofko, and J.-P. St.-Maurice, Institute of Space and Atmospheric Science, University of Saskatchewan, 116 Science Place, Saskatoon, SK S7N 5E2, Canada. (rob.gillies@usask.ca)

P. Ponomarenko, Space Physics Group, University of Newcastle, University Drive, Callaghan, NSW 2308, Australia.

Chapter 5

EISCAT-SuperDARN velocity comparisons

5.1 Introduction

The research presented in this chapter is based on the following publication:

- Gillies, R. G., G. C. Hussey, G. J. Sofko, D. M. Wright, and J. A. Davies. A comparison of EISCAT and SuperDARN F-region measurements with consideration of the refractive index in the scattering volume, *J. Geophys. Res.*, 115, A06319, doi:10.1029/2009JA014694, 2010b.

This study involves a comparison between velocities measured by the SuperDARN radar in Hankasalmi, Finland and coincident velocities measured by the EISCAT incoherent scatter radar. Several different estimates of refractive index are applied to improve the velocities measured by SuperDARN.

5.2 Results

A comparison between measurements of velocity made by the EISCAT incoherent scatter radar and the Hankasalmi SuperDARN radar from 1995–1997 was performed by *Davies et al.* [1999]. As with the DMSP-SuperDARN comparison discussed in the previous chapter, this comparison found good correlation between the velocities measured by the two instruments however, again, velocities measured by SuperDARN were statistically lower. The study discussed in this chapter expands the comparison to include velocities measured in 1998 and 1999 and improves the measurements of velocity made by SuperDARN by accounting for refractive index in the SuperDARN

scattering volume.

Three different estimates of refractive index values in the SuperDARN scattering volume were made to improve the velocities measured by SuperDARN. Measurements of electron density from EISCAT, estimates of electron density from the IRI model, and elevation angle measurements from SuperDARN were all used to provide values for refractive index. Each of these methods provided a large-scale or background estimate of refractive index, and did not account for any small-scale structures, which may be only a few kilometers in extent, within the SuperDARN range cell. The EISCAT measurements were from a fixed location within the SuperDARN cell and, on average, would have provided electron density values that were representative of the background ionosphere. IRI provides smoothed estimates of electron density and does not account for small-scale ionospheric structures. Finally, since the elevation angle proxy depends on the total refraction between the SuperDARN antenna and the scattering volume, it only provides a rough measure of electron density in the ionosphere.

The main conclusion of the *Gillies et al.* [2010b] EISCAT-SuperDARN comparison was that the different large-scale estimates of refractive index did not account for the entire underestimation of SuperDARN velocities, although they improved them. It was proposed that one possible reason for the discrepancy was that SuperDARN scatter tends to occur in the most disturbed regions of the ionosphere where the electron density is the highest. It is reasonable to assume that most SuperDARN scatter occurs in regions within a range cell with the highest electron density because the scattering cross-section increases with electron density. Also, small-scale structures with high electron densities (and gradients) are ideal for the generation of gradient drift instabilities which are necessary for coherent scatter to occur. In fact, *Hosokawa et al.* [2009] demonstrated that in the vicinity of highly dense polar cap patches, SuperDARN radars tended to only receive scatter from areas within the patches. If this hypothesis is correct, then large-scale, background estimates of electron density from EISCAT or IRI would not be representative of the actual conditions within the SuperDARN scattering volume. The reason for this can be

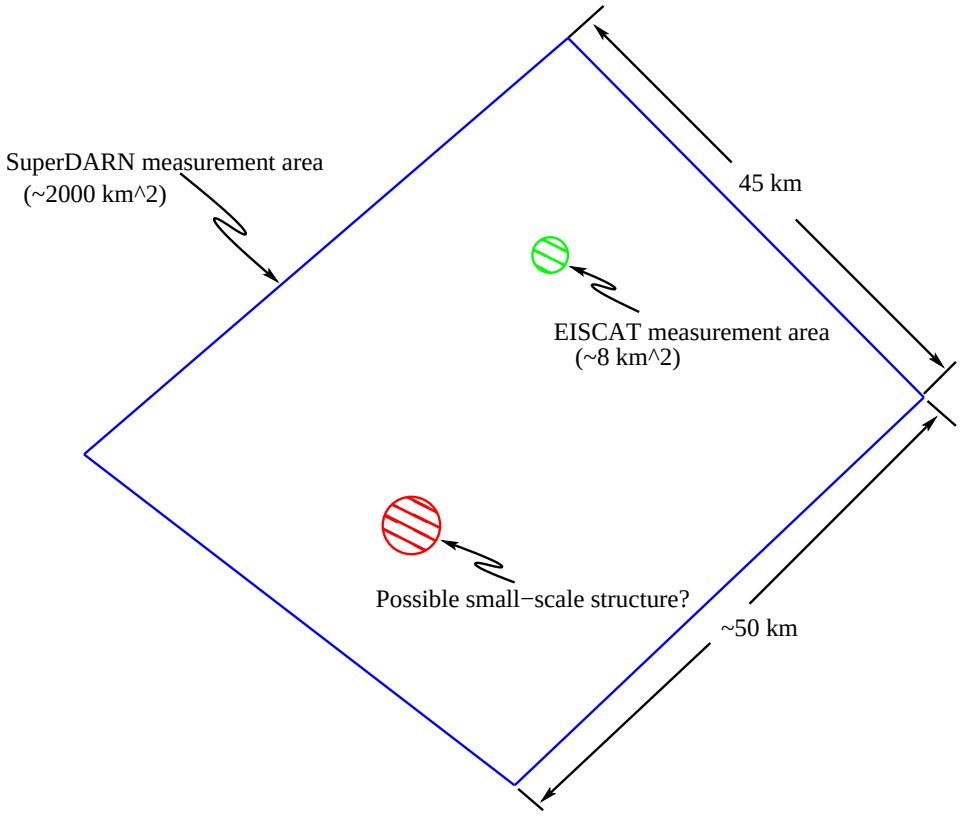

Figure 5.1: The relative sizes of the measurement areas of SuperDARN and EISCAT.

understood by considering the scenario presented in Figure 5.1, which presents the relative sizes of both a SuperDARN range cell and the EISCAT measurement volume (the figure only displays the horizontal measurement areas of the two instruments, not the vertical extent of the volumes). As shown, any small-scale structures within the range cell would likely not be detected by the EISCAT radar; however, SuperDARN coherent scatter would tend to occur predominantly within these structures. This discrepancy would cause the refractive index in the SuperDARN scattering volume to be significantly lower than the refractive index measured by EISCAT (similar arguments can be made in the use of IRI electron densities or SuperDARN elevation angles to determine refractive index).

Unfortunately, it is very difficult to accurately measure the electron density conditions in the scattering volume of SuperDARN radars. Large scale measurements

of electron density from instruments such as incoherent scatter radars and ionosondes will provide only background estimates. Satellite measurements from ePOP, for example, will provide high resolution electron density measurements, which will be able to detect the size and density of these small-scale structures, but they may not determine the exact location at which scatter occurs in a given SuperDARN range cell. The best solution for this problem is to develop a method that will allow measurements of scattering volume electron densities to be made by SuperDARN itself. The development and implementation of a method that allows these measurements to be performed is the topic of the next chapter.

5.3 Published paper

The comparison between ionospheric velocities measured by SuperDARN and EISCAT as discussed in this chapter was published in the *Journal of Geophysical Research* in 2010. Presented immediately below is the paper in the journal format reproduced by permission of American Geophysical Union:

- Gillies, R. G., G. C. Hussey, G. J. Sofko, D. M. Wright, and J. A. Davies. A comparison of EISCAT and SuperDARN F-region measurements with consideration of the refractive index in the scattering volume, *J. Geophys. Res.*, 115, A06319, doi:10.1029/2009JA014694, 2010b. Copyright 2010 American Geophysical Union.

JOURNAL OF GEOPHYSICAL RESEARCH, VOL. 115, A06319, doi:10.1029/2009JA014694, 2010

A comparison of EISCAT and SuperDARN *F*-region measurements with consideration of the refractive index in the scattering volume

R. G. Gillies,[1] G. C. Hussey,[1] G. J. Sofko,[1] D. M. Wright,[2] and J. A. Davies[3]

Received 28 July 2009; revised 11 December 2009; accepted 12 February 2010; published 30 June 2010.

[1] Gillies et al. (2009) proposed the use of interferometric measurements of the angle of arrival as a proxy for the scattering region refractive index n_s needed to estimate the line-of-sight Doppler velocity of the ionospheric plasma from HF [Super Dual Auroral Radar Network (SuperDARN)] radar observations. This study continues this work by comparing measurements of line-of-sight velocities by SuperDARN with tristatic velocity measurements by the EISCAT incoherent scatter radar from 1995 to 1999. From a statistical viewpoint, velocities measured by SuperDARN were lower than velocities measured by EISCAT. This can, at least partially, be explained by the neglect in the SuperDARN analysis of the lower-than-unity refractive index of the scattering structures. The elevation angle measured by SuperDARN was used as a proxy estimate of n_s and this improved the comparison, but the velocities measured by SuperDARN were still lower. Other estimates of n_s using electron densities N_e based on both EISCAT measurements and International Reference Ionosphere model values did not increase the SuperDARN velocities enough to attain the EISCAT values. It is proposed that dense structures that were of comparable size to the SuperDARN scattering volume partially help resolve the low-velocity issue. These dense, localized structures would provide the N_e gradients required for generation of the coherent irregularities from which the SuperDARN radar waves scatter, whereas EISCAT incoherent radar measurements provide only the background N_e and not the density of the small-scale structures. The low-velocity SuperDARN results suggest that small-scale dense structures with refractive indices well below unity must exist within the SuperDARN scattering volume and may contribute greatly to the scattering process.

Citation: Gillies, R. G., G. C. Hussey, G. J. Sofko, D. M. Wright, and J. A. Davies (2010), A comparison of EISCAT and SuperDARN *F*-region measurements with consideration of the refractive index in the scattering volume, *J. Geophys. Res.*, *115*, A06319, doi:10.1029/2009JA014694.

1. Introduction

[2] In the paper by *Gillies et al.* [2009] the concept of using angle-of-arrival measurements as a proxy for refractive index n_s in the local scattering region of a high-frequency (HF) radar was introduced. As outlined below, this allows for a better line-of-sight Doppler velocity estimate to be made by the Super Dual Auroral Radar Network (SuperDARN) [*Greenwald et al.*, 1995] HF radar system. Due to the large field-of-view required for global convection measurements by radar systems such as SuperDARN, the small-scale resolution needed to determine the refractive index n_s at the scattering location is not possible. The detailed electron density measurements needed to determine n_s are not readily available. The result is that estimates of refractive index have been unavailable for use in the Doppler velocity analysis, so a default value of 1.0 is usually used.

[3] Line-of-sight velocities v_s measured by SuperDARN are calculated using the following equation:

$$v_s = \frac{\Delta\omega_D v_p}{2\omega} = \frac{\Delta\omega_D}{2\omega}\frac{c}{n_s}, \quad (1)$$

where $\Delta\omega_D$ is the Doppler shift, v_p is the phase speed of the radar wave in the scattering region, ω is the radar wave frequency [*Baker et al.*, 1995], c is the speed of light in a vacuum, and n_s is the refractive index in the scattering region [*Ginzburg*, 1964]. Recent work by *Gillies et al.* [2009] has demonstrated that n_s will be typically around 0.8 or 0.9, so the default value of 1.0 leads to systematic underestimation of the Doppler velocity.

[4] The determination of the local refractive index for a given SuperDARN echo allows an improved line-of-sight

[1]Institute for Space and Atmospheric Studies, University of Saskatchewan, Saskatoon, Saskatchewan, Canada.
[2]Department of Physics and Astronomy, University of Leicester, Leicester, UK.
[3]Space Science and Technology Department, Rutherford Appleton Laboratory, Didcot, UK.

0148-0227/10/2009JA014694

velocity estimate to be made by application of equation (1). The most direct method to estimate n_s is to use local electron density N_e measurements or estimates and directly calculate the refractive index using the Appleton-Hartree equation [*Budden*, 1961]. This can be done if there is an instrument such as an ionosonde or incoherent scatter radar to measure N_e. Unfortunately, the field of view of a given SuperDARN radar is quite large (~4 million km^2) and it is impossible to have instruments that measure N_e continuously throughout this region. Electron densities can also be estimated using the International Reference Ionosphere (IRI) model [*Bilitza*, 2001], which can provide a mean estimate of N_e at any location. However, these estimates are based on empirical models and do not account for the small-scale structures that are responsible for the majority of SuperDARN scattering.

[5] *Gillies et al.* [2009] proposed a method to determine n_s using elevation angle data from SuperDARN as a proxy for the refractive index in the scattering region. The equation relating n_s to the angle of arrival or elevation angle was:

$$n_s = \frac{R_E}{(R_E + h_s)} \frac{\cos\phi_o}{\sin\psi}, \quad (2)$$

where R_E is the radius of the Earth, h_s is the altitude of the scattering point, ψ is the magnetic dip angle at the scattering point, and ϕ_o is the elevation angle measured by SuperDARN. The benefit of this method is that it does not rely on the existence or reliability of other instruments for an n_s estimate.

[6] Previous studies have consistently demonstrated that, on a statistical basis, SuperDARN measured line-of-sight velocities were lower than velocities derived from other instruments. For example, *F*-region drift velocities as measured by DMSP satellites and SuperDARN were compared by *Drayton et al.* [2005] and *Drayton* [2006]. The *Drayton et al.* [2005] study compared velocities over the period of 1999–2003 and found that the best fit line to the data had a slope of 0.72 (SuperDARN velocities were, on average, lower). A magnetic dipole field-mapping correction of the electric field was then made to this data set in *Drayton* [2006] to account for the fact that DMSP measured velocities at ~840 km and SuperDARN measured velocities at ~250 km. This correction effectively decreased the higher altitude DMSP calculated velocity values and the slope of the best fit line increased to 0.84.

[7] Work by *Gillies et al.* [2009] continued the SuperDARN-DMSP comparison by examining comparison points in which SuperDARN data had an accompanying elevation angle. This reduced the number of comparison points and the best fit slope of this subset was 0.74. It was suggested that the reason for the lower slope value compared to *Drayton* [2006] was that the subset of points with elevation angle information was predominantly situated in the auroral zone where there were typically higher electron densities and more complex structures, while the full data set was significantly weighted with more observations in the polar cap region, where lower electron densities and less complex structures prevail. Nonetheless, when equation (2) was applied to obtain an estimate of n_s, the slope of the best fit line increased to 0.83, about a 12% improvement, indicating that the SuperDARN velocities, although better estimated, were still systematically lower than DMSP velocities.

[8] Studies of comparisons between velocities measured by SuperDARN and velocities measured by incoherent scatter radars have also been performed. Velocities measured by SuperDARN and by the Sondrestrom incoherent scatter radar were compared by *Xu et al.* [2001], resulting in a best fit slope of only 0.42. *Eglitis et al.* [1998] compared tristatic ion drift measurements from the European Incoherent Scatter (EISCAT) UHF radar [*Rishbeth and van Eyken*, 1993] to line-of-sight measurements from the Hankasalmi SuperDARN radar. This study utilized an ionospheric heater [*Robinson*, 1989; *Rietveld et al.*, 1993; *Stubbe*, 1996, and references therein] to generate artificial irregularities that the Hankasalmi SuperDARN detected. It was found that there was very good agreement between velocity values when the heater was on (the best fit line to the data had a slope of 1.02). Using scatter from irregularities that were natural, rather than artificially generated by a heater, a comparison of EISCAT and SuperDARN velocities was performed by *Davies et al.* [1999] over the period of 1995–1997. This study led to a best fit line with a slope of 0.72. The present study expands the above comparison made by *Davies et al.* [1999] to include data from 1998 and 1999, thereby improving the overall statistical database.

2. Experiment Overview

[9] The first of the two instruments used in the present study was the SuperDARN radar located at Hankasalmi, Finland. SuperDARN is a collection of radars that monitor high latitude ionospheric convection in both the Northern and Southern Hemispheres using coherently scattered HF signals in the 8–20 MHz range [*Greenwald et al.*, 1995]. A SuperDARN radar, in its common mode, consists of a main array of 16 antennas that are phased to sample 16 successive beam directions in steps of 3.24°, covering a total of ~52° in azimuth. The radars are routinely configured such that each beam samples 75 different range gates, each with 45 km resolution. In normal operation, each beam is scanned in sequence for 3 s or 7 s, so a full scan of all 16 beams is performed every 1 or 2 min, respectively. An interferometer array of four antennas is also located 100 m behind or in front of the main array at each SuperDARN radar site. The cross-correlation between the signal received by the interferometry array and the main array is used to determine the elevation angle of the returned echo [*Milan et al.*, 1997; *André et al.*, 1998]. The Hankasalmi SuperDARN radar is located at the geographic location 62.3°N, 26.6°E (geomagnetic coordinates: 59.8°N, 105.5°E). The central pointing direction of this radar is 12.0° west of geographic north.

[10] The second instrument used in this study is the EISCAT UHF incoherent scatter radar facility [*Rishbeth and van Eyken*, 1993]. The EISCAT system operates at 931 MHz and consists of three parabolic dish antennas located in Tromsø (Norway), Kiruna (Sweden), and Sodankyla (Finland). The antenna in Tromsø has both transmit and receive capabilities, while the other two antennas operate as passive receivers. The data considered in this study resulted from times when EISCAT was running the common program modes CP-1 and CP-2.

[11] The CP-1 mode consisted of the transmitter at Tromsø oriented to point along a fixed path antiparallel to the local

magnetic field lines (~77° elevation). The antenna beam had a half-power width of 0.6° which corresponds to a width resolution of roughly 7 km at a measurement altitude of 280 km. The Tromsø radar sampled with an altitude resolution of 22 km along the beam from 150 km to 600 km. The two remote sites and the Tromsø antenna received signal from a common intersection volume at an altitude of ~280 km centered at 69.1°N, 19.1°E, which corresponded to beam 5 and range gate 16 of the Hankasalmi SuperDARN radar. The signal received at each EISCAT site was integrated over 5 s, and then these 5 s intervals were post-integrated over 2 min. The result of each integration was a velocity vector for each of the three antennas. The Tromsø velocity vector was along the antenna beam, while the remote receiver velocity vectors were along the bisector between the Tromsø beam and the remote receiver beams. These three velocity vectors allow determination of the full velocity vector within the intersection volume. The component of the full EISCAT velocity vector was then resolved along the Hankasalmi SuperDARN radar line-of-sight direction and the velocity values from the two instruments were directly compared.

[12] The CP-2 mode was nearly identical to the CP-1 mode except that four different intersection volumes were scanned in a period of 6 min so each position had a post-integration time of 90 s. These positions consisted of the Tromsø beam transmitting along the field lines (identical to the position of the CP-1 mode), vertically, and in two different southeastward directions. The geographic locations of each of these positions were as follows: (1) 68.7°N, 21.8°E (Hankasalmi beam 7, range gate 14); (2) 68.4°N, 20.0°E (Hankasalmi beam 5, range gate 14); (3) 69.1°N, 19.1°E (Hankasalmi beam 5, range gate 16); and (4) 69.6°N, 19.2°E (Hankasalmi beam 5, range gate 17). Note that the four CP-2 positions were relatively close to each other and only extended from Hankasalmi range gates 14 to 17.

3. Statistical Velocity Comparisons

3.1. Initial Comparison

[13] All the CP-1 and CP-2 velocity measurements from 1995 to 1999 during periods with simultaneous Hankasalmi SuperDARN velocity data have been compared. Both in order to filter out SuperDARN *E*-region velocities and, more importantly, to improve the SuperDARN measurements by taking the index of refraction into account, only SuperDARN echoes with available elevation angle information were used. SuperDARN velocities that were less than 50 m/s or that had a signal-to-noise ratio less than 3 dB were discarded. Typically, the SuperDARN radar performed 2 min scans so the 2 min EISCAT integration time of the CP-1 mode was coincident with the SuperDARN scan time. On some occasions, SuperDARN was operating in a special mode with shorter scans or in the 1 min scan mode. In these cases, any SuperDARN values that were within the EISCAT scan time were averaged. For the CP-2 mode, EISCAT integrated at each position for 90 s and the data observations were compared when any part of the SuperDARN scan overlapped with any part of the EISCAT integration and, as such, temporal alignment was not often ideal.

[14] From 1995 to 1999 there were 11 CP-1 experiments that varied in length between 2 and 5 days and 10 such experiments in the CP-2 mode. In total, over 1300 velocity comparisons were performed using the criteria discussed above, and these were split roughly equally between CP-1 and CP-2 types (658 and 668, respectively). This velocity comparison between EISCAT and SuperDARN is presented as Figure 1. EISCAT velocities are plotted along the horizontal axis and SuperDARN velocities are plotted along the vertical axis. The best fit line to the data is also plotted as the solid line. The immediate issue with this comparison is the low correlation coefficient $r = 0.39$. This is due to the large collection of points along the vertical axis, which correspond to very low EISCAT velocities and a large range of SuperDARN velocities.

3.2. Removal of *E*-Region and Noisy Data

[15] In order to check the reliability of the SuperDARN data in a given range cell, the surrounding eight cells in a 3×3 grid were examined. Points were discarded if more than four of these cells did not record data or the standard deviation of velocity in all considered cells (up to a maximum of nine cells) was greater than 50% of the velocity average of the cells. Note that the single SuperDARN velocity value of the cell under consideration (not the average velocity of the nine cells) was the value used for comparison with the EISCAT velocity value. The results of this filtering are presented in Figure 2 and it is apparent that most of the anomalous data has been removed. Some 40% of the original points have been discarded. The correlation coefficient has risen to 0.91 and the slope of the best fit line has risen from 0.66 to 0.78.

[16] The next step in the comparison was to filter out any SuperDARN echoes that may be *E*-region scatter. In contrast to the *F* region, convection in the *E* region is limited to the ion-acoustic velocity (400–600 m/s) [*Haldoupis and Schlegel*, 1990] and thus *E*-region SuperDARN velocities would not agree with *F*-region EISCAT velocities. To distinguish *E*-region velocities from *F*-region velocities, the distribution of elevation angles was examined as presented in Figure 3. The majority of the elevation angles that were observed in this study clustered around 25° with a much smaller cluster between 10° and 15°. The latter cluster is expected to be due to *E*-region backscatter. The SuperDARN echoes examined in this study all came from essentially the same range (from gates 14 to 17, inclusive). At this range, elevation angles of ~25° were appropriate for half-hop *F*-region scatter and elevation angles below ~15° were appropriate for *E*-region scatter. Therefore, echoes with elevation angles below 15° were considered to be from *E*-region altitudes and were discarded. This removed an additional 64 comparison points; however, the slope of the best fit line and the correlation coefficient did not change in the EISCAT-SuperDARN comparison (figure not shown).

[17] A further analysis of possible *E*-region contamination in the SuperDARN data set was performed by examining various SuperDARN low-velocity cutoff values. It was found that discarding SuperDARN velocities that were below various arbitrary cutoff values did not appreciably change the slope of the best fit line. The slope of the best fit line was examined for several low velocity cutoffs from 50 m/s to 600 m/s in 25 m/s increments and it was found that the best result was obtained when velocities which were less than 125 m/s were removed. Using this cutoff,

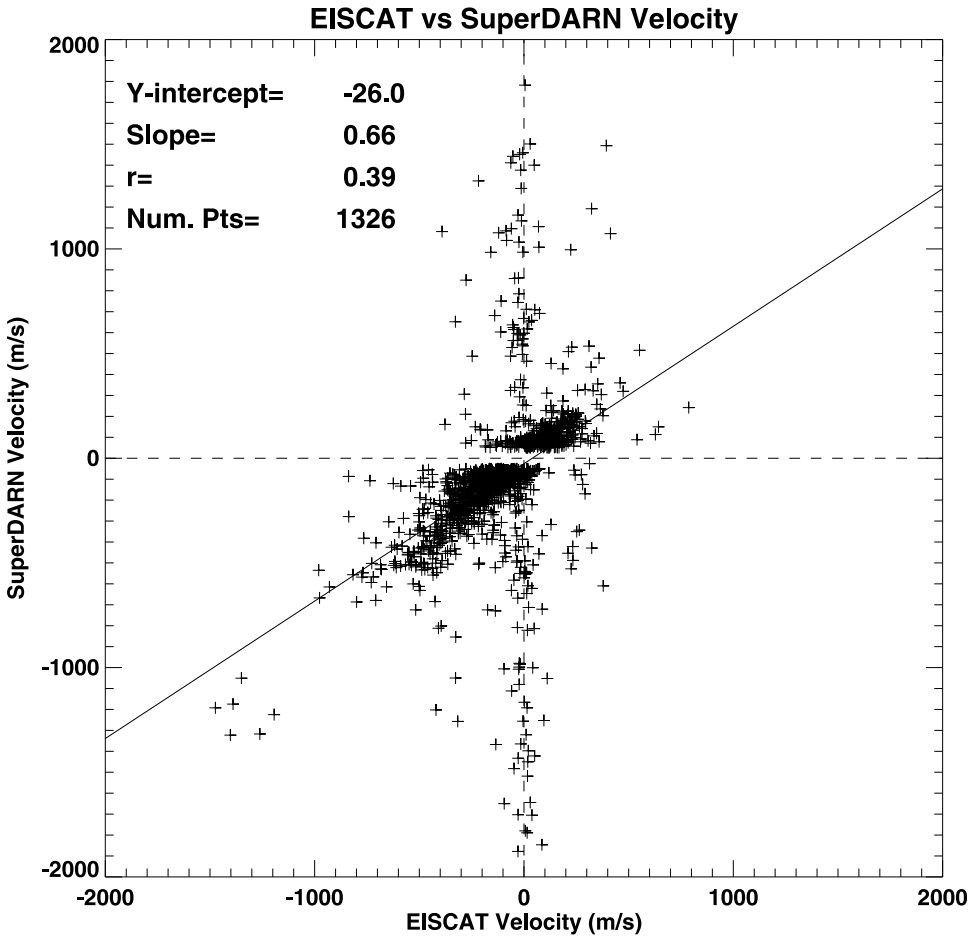

Figure 1. SuperDARN and EISCAT velocity comparison for EISCAT CP-1 and CP-2 modes from 1995 to 1999.

391 points were removed and the best fit slope increased from 0.78 to 0.81. However, since there is no basis for removing points with velocities below this arbitrary threshold (and the removal had little effect on the best fit slope), it was determined that the most accurate representation of F-region scatter was obtained using the elevation angle cutoff criteria which was discussed above.

3.3. Accounting for n_s in the SuperDARN Scattering Volume

[18] The slope of the best fit line when comparing the SuperDARN velocities to EISCAT velocities as presented in Figure 2 is 0.78 from 832 points (note that there were 768 points after the probable *E*-region echoes were removed). SuperDARN, on average, underestimated the ionospheric scatterer velocities; however, the measured velocities still need to be adjusted to account for the refractive index in the scattering region, n_s. Three different methods have been employed to determine an estimate of n_s for each comparison point.

[19] The first method is based on the electron density N_e values that the EISCAT Tromsø radar measured. In order to estimate n_s for SuperDARN, the maximum N_e measured along the Tromsø EISCAT beam was selected to represent the electron density in the local scattering volume. The Appleton-Hartree equation [*Budden*, 1961] was used to determine n_s from this N_e value. With this estimate for n_s, equation (1) was applied to determine SuperDARN velocities. The slope of the best fit line increased from 0.78 to 0.84, an increase of ~8%. It should be noted that in order for this method to deliver accurate results, a significant assumption has been made: the SuperDARN scatter came from the same location at which EISCAT measured the peak N_e. If the SuperDARN scatter location was offset in altitude from the peak electron density and/or the distribution of SuperDARN scatter within the range cell predominantly occurred in a different location than where EISCAT measured within the range cell, the estimate for n_s from this method will not accurately reflect the electron density at the scattering location. This altitude ambiguity and difference in the instrument scattering volumes will be discussed in more detail in section 4.

[20] The second method is also based on using electron density values to obtain an estimate for n_s. For this method, the IRI model was used to determine the peak N_e estimate at the time and location of the velocity measurement. Applying equation (1) to determine the SuperDARN velocity values with this approximation for n_s resulted in the slope of the best fit line increasing from 0.78 to 0.87, an increase of ~12%. Again, in the application of this method, the assumption was made that SuperDARN scatter occurred at the

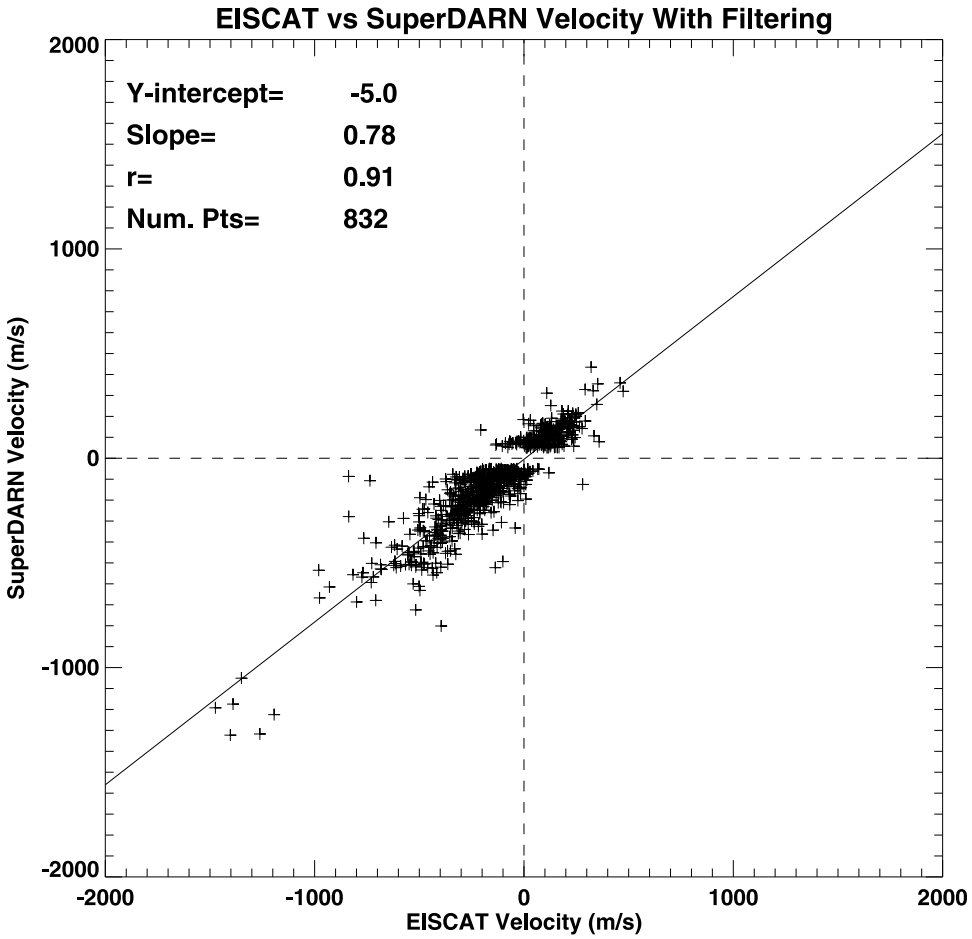

Figure 2. SuperDARN and EISCAT velocity comparison for EISCAT CP-1 and CP-2 modes from 1995 to 1999. SuperDARN points that showed either high standard deviation or little data in the surrounding cells were discarded.

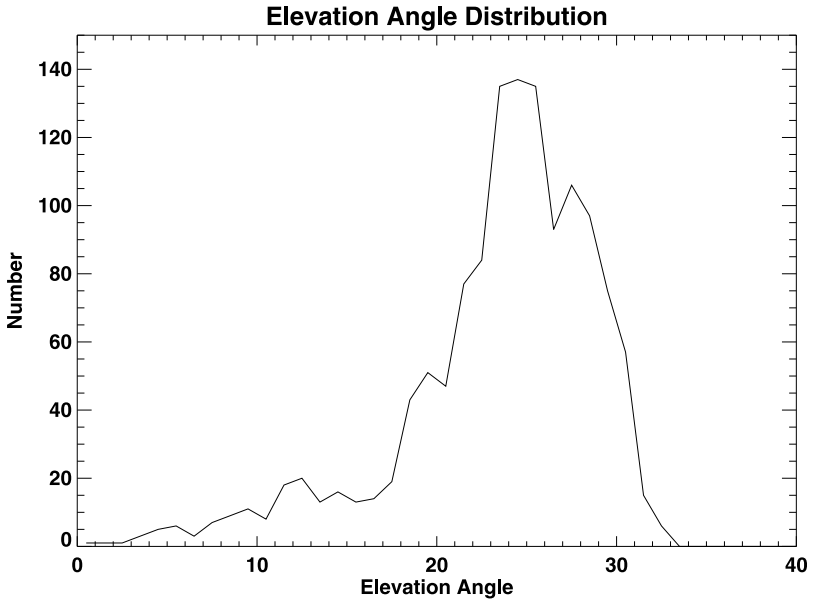

Figure 3. The number of data points with a given elevation angle.

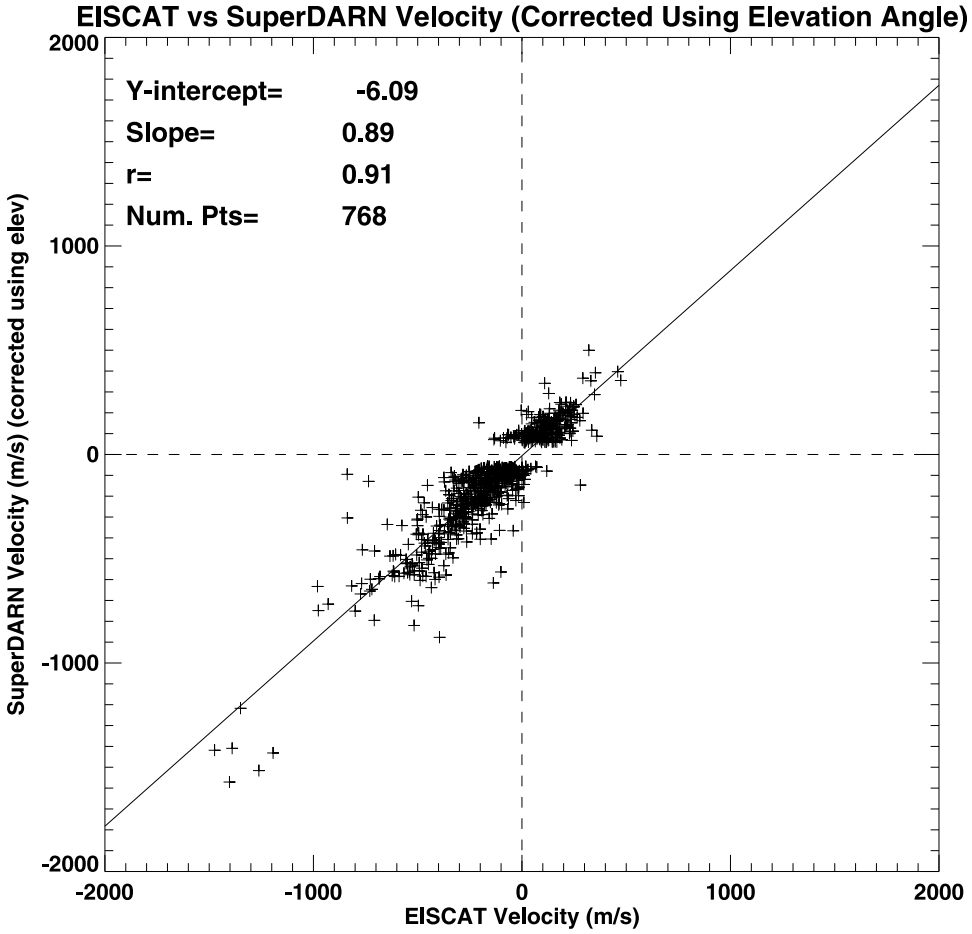

Figure 4. SuperDARN and EISCAT velocity comparison for EISCAT CP-1 and CP-2 modes from 1995 to 1999. SuperDARN points that showed either high standard deviation or little data in the surrounding cells were discarded. Also discarded were SuperDARN velocities that had elevation angles below 15° to remove *E*-region scatter. Finally, n_s was estimated and used to improve the SuperDARN velocities using equations (1) and (2).

F-region peak altitude. Further, the IRI uses empirical models and gives only a large-scale estimate of N_e so that any small-scale structures, which may be very important in the generation of field-aligned irregularities, will not be taken into account.

[21] The final method to determine an estimate for n_s exploits equation (2) and the elevation angle ϕ_o that SuperDARN was capable of measuring for each echo. Again, the estimate for n_s was used with equation (1) to improve each SuperDARN velocity measurement. The comparison between EISCAT and SuperDARN velocity values using the elevation angle as a proxy for n_s is presented as Figure 4. The result was an increase of the best fit slope from 0.78 to 0.89, an improvement of ~14%. The important assumption made with this approximation for n_s was that there were no horizontal gradients in N_e along the radar wave path. This was most likely not the case; nonetheless, a reasonable estimate of n_s is possible with this method (it is the best of the three presented here) and this method had the added benefit that the elevation angle was directly linked to the scattering location of SuperDARN and not of any other instrument whose target region may be displaced spatially and temporally from that of SuperDARN.

3.4. Comparison of n_s Values From Different Methods

[22] It is useful to compare directly the n_s values obtained from each different method. These methods measure the same parameter in the ionosphere, so in principle, they should provide the same average refractive index value and there should be high correlation between individual data points measured from each method. The mean refractive index predicted using the elevation angle proxy was 0.88 with a standard deviation of 0.02. Using EISCAT measurements of electron density provided a mean refractive index value of 0.92 with a standard deviation of 0.03. Finally, IRI estimates of electron density provided a mean refractive index value of 0.91 with a standard deviation of 0.05. These numbers indicate that, on average, use of any of the three presented methods to predict refractive index in the SuperDARN scattering region will provide results similar to the other two methods. A point-by-point comparison revealed that the correlation between the different measures

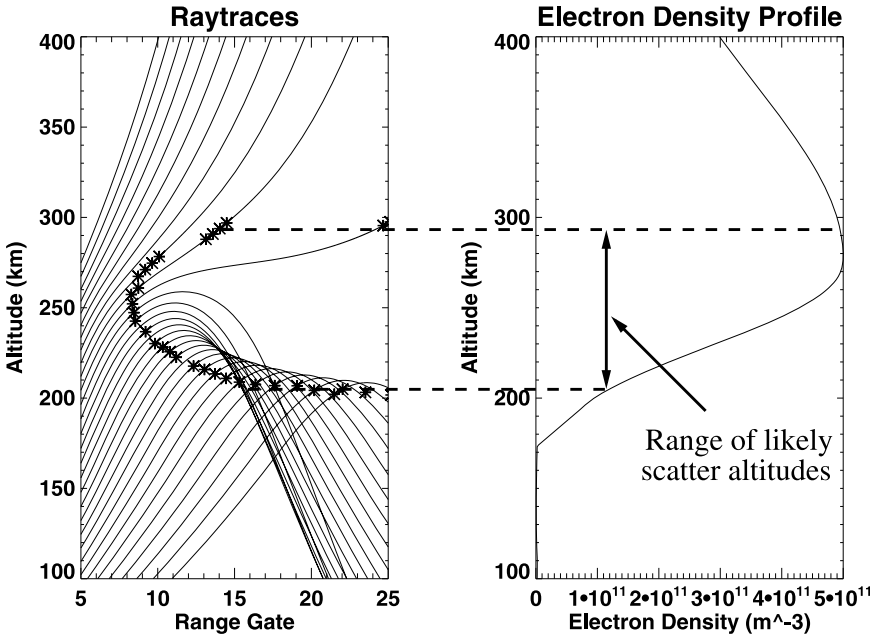

Figure 5. On the left are the raypaths from SuperDARN through the profile displayed on the right. The operating frequency was 12.5 MHz.

of n_s was low (e.g., estimates of n_s as derived from EISCAT N_e measurements and the elevation angle proxy estimate, when compared on a point-to-point basis, resulted in a correlation coefficient of 0.21). Comparisons between IRI and elevation angle estimates of n_s and between IRI and EISCAT estimates of n_s were lower. Possible explanations for this lack of correlation are discussed in the following section.

4. Discussion

4.1. Comparison Results

[23] Three different methods have been applied to account for refractive index in the SuperDARN velocity determinations. These methods increased the best fit slope between SuperDARN and EISCAT velocity measurements between 8% and 14%, but the results still indicate that SuperDARN velocities are on average lower than velocities measured by EISCAT. Comparisons with other instruments (such as the DMSP satellites) have also demonstrated lower SuperDARN velocities even after accounting for refractive index using the elevation angle proxy [*Gillies et al.*, 2009]. This would suggest that, although an estimate for the local scattering volume refractive index can significantly improve the SuperDARN velocity determination, a refinement of the technique or some further physical reasoning is needed to fully explain the systematic underestimate by SuperDARN of line-of-sight velocities.

[24] Another intriguing result from this study was the low correlation between n_s values obtained using the different methods. As discussed in the previous section, there is little correlation between n_s estimates from the different methods. An explanation for this lack of correlation is required as one may expect that they should deliver similar results.

4.2. Altitude Ambiguities

[25] A plausible explanation for the lack of correlation between n_s values could arise from the lack of precise knowledge about the altitude of SuperDARN scatter [*Chisham et al.*, 2008]. Slight variations in the scatter altitude would reduce the correlation between n_s values measured by EISCAT and those from the SuperDARN elevation angle. Since the elevation angle measurement is directly tied to the scattering location, estimates of n_s using elevation angle would differ from estimates using N_e measurements of the F-region peak if the scatter did not occur at the peak.

[26] The vertical gradient in N_e in the F region can be quite steep. To demonstrate the variation in scattering altitudes that is possible with SuperDARN, raytracing simulations through a model ionosphere have been performed. Figure 5 presents raypaths through a typical electron density profile that is presented beside the raypaths. The horizontal axis in Figure 5 represents an estimate of SuperDARN range gate and the vertical axis is altitude. Crosses on the raypaths represent points where the ray was within 1° of perpendicularity to the magnetic field lines, since coherent scattering requires high magnetic aspect sensitivity. At the ranges applicable for this study, the altitude at which scatter is possible can vary by up to ~100 km. Examination of the plot of N_e versus altitude (Figure 5, right) demonstrates that the electron density in the scattering region could range from $<2 \times 10^{11}$ m^{-3} (the density at ~200 km) to ~5×10^{11} m^{-3} (the density at ~280 km). At 12.5 MHz, this range of possible N_e values would result in n_s values of 0.95 and 0.85, respectively. This demonstrates that, under these conditions, using the peak density provided by IRI or EISCAT would result in a value of 0.85, although the actual value could be as high as 0.95. This would explain at least some of the lack of correlation between n_s predictions from the different methods. Note that although

the density profile used to produce Figure 5 is typical, the actual conditions can vary substantially and the locations of possible scatter would be different for different profiles. Figure 5 is simply meant to demonstrate the variability in scattering altitude that could occur under typical conditions.

4.3. Measurement Area Discrepancies

[27] Another plausible explanation for both the lack of agreement between the different methods to estimate n_s and the systematically lower SuperDARN velocities (even after attempts were made to account for n_s) involves the difference in measurement volumes between the two instruments. The electron density measurements from EISCAT occurred at a fixed location within the large SuperDARN range cell scattering volume. The beam width of EISCAT was 0.6°, which resulted in a scattering area of ~8 km^2 at an altitude of 280 km. The SuperDARN cell was 45 km in range and roughly 50 km wide at the range gates considered in this study. This results in a possible scattering area of more than 2000 km^2. Therefore the EISCAT measurement area was more than two orders of magnitude smaller than the SuperDARN measurement area.

[28] Not only did the size of the measurement areas differ, but the measurement techniques also differed. SuperDARN measured ionospheric velocities using coherent scattering from field-aligned irregularities. Therefore, SuperDARN scatter could occur in localized regions within the larger SuperDARN measurement volume. For example, it is possible that scatter occurred only in a small fraction of the SuperDARN cell in which conditions for scattering were appropriate. The main driver of field-aligned irregularities in the *F* region is the gradient drift instability that occurs in regions with electron density gradients. It is reasonable to assume that, compared to the well-behaved background electron density, localized structures with densities higher than background would produce stronger irregularities. In fact, a study of SuperDARN echoes in relation to polar cap patches has found that scatter tends to occur predominantly in regions with higher electron density [*Hosokawa et al.*, 2009]. These two behaviors indicate that coherent scatter from SuperDARN will be localized in regions with high electron densities and high gradients. Conversely, EISCAT measured the average electron density at a fixed location within the much larger SuperDARN cell. Therefore, on average, the EISCAT measurements of electron density would have delivered the average electron density in a SuperDARN cell, while SuperDARN measurements would have been biased to areas of the cell with high gradients and/or densities.

[29] The electron density in the auroral and polar regions of the *F*-region ionosphere can be quite structured. Small-scale structures with high gradients can form in the auroral region from processes such as particle precipitation and may be as small as hundreds of meters [e.g., *Noël et al.*, 2000, 2005; *Sofko et al.*, 2007]. In fact, any structure with scale sizes smaller than the 2000 km^2 size of a SuperDARN range cell would be important. On the dayside and over the polar cap, polar patches exist with regions of enhanced electron densities greater than 100% of the background level and scale sizes on the order of a few hundred kilometers. Although this scale is quite large, smaller structures are expected to develop within these patches [*Hosokawa et al.*, 2009]. Structure also exists in the region of the high-latitude ionospheric trough that, at least on the dayside, can be located poleward of the Hankasalmi SuperDARN radar location [e.g., *Sojka et al.*, 1990; *Pryse et al.*, 2005]. The poleward edge of the trough can produce an increase in electron density by an order of magnitude in a few tens of kilometers [e.g., *Mitchell et al.*, 1995]. Also of importance are traveling ionospheric disturbances (TIDs), which are wavelike structures in the ionosphere that also have scales of a few tens of kilometers and electron density enhancements of roughly 50%–100% [e.g., *Pryse et al.*, 1995].

[30] If SuperDARN scatter occurred in localized regions that had electron densities that were enhanced compared to the background values, then the actual value for N_e would be higher than the value predicted by the EISCAT measurement of N_e. Since a higher N_e value results in a lower n_s value, an enhanced N_e in the local scattering region will result in n_s values that are lower than those predicted using EISCAT. By equation (1) this would result in an underestimation of SuperDARN velocities compared to EISCAT velocities. If the electron density in the local SuperDARN scattering volume was systematically 50%–100% larger than the electron density predicted using EISCAT measurements, then the best fit slope line of Figure 4 would rise to unity and SuperDARN velocities would no longer be underestimated compared to EISCAT velocities. Although electron density perturbations of this magnitude on scale sizes comparable to a SuperDARN cell are possible (as discussed above), it may not be reasonable to expect that such structures existed for a large portion of the data points examined in this study. However, this effect at least partially explains the underestimation of SuperDARN velocities compared to EISCAT velocities even when attempts to account for n_s are made. Further, the fact that the two measurement volumes were of different sizes is one explanation for the lack of correlation between the different methods to estimate n_s because the EISCAT N_e measurement was essentially independent of the electron density in the effective SuperDARN scattering region. It should be noted that the preceeding argument dealt only with the N_e measurement by EISCAT and not the velocity measurement. It was assumed that even if electron density structures existed, the background velocity field was quite uniform throughout the range cell. This is the reason that the velocity comparisons had good correlation, but the n_s comparisons did not.

4.4. Horizontal Gradients

[31] The previous two suggestions for the lack of correlation between n_s estimates addressed problems that arose from using peak electron density measurements to determine n_s. It needs to be reiterated that using the elevation angle to determine n_s is only a proxy and therefore may not completely describe the situation. The estimate for n_s from the elevation angle as derived by *Gillies et al.* [2009] assumes that there were no horizontal gradients in electron density along the radar wave path. Clearly this assumption does not hold in all cases as the ionosphere is very dynamic and changes with latitude and longitude due to spatially dependent processes such as particle precipitation on the nightside and photoionization on the dayside. As a result, horizontal gradients may be important. *Gillies et al.* [2009]

used raypath simulations to demonstrate that, for even quite extreme large-scale (on the order of hundreds of kilometers) horizontal gradients, the elevation angle recorded by SuperDARN provides a reasonable estimate for n_s. Nevertheless, any deviation from the expected $\phi_o - n_s$ relationship due to horizontal gradients would also lower the correlation between n_s values estimated from elevation angle as compared to the other n_s estimations. *Gillies et al.* [2009] did not consider the effect of small-scale gradients, which, as discussed above, may be important.

4.5. Time Discrepancies Between Instruments

[32] The discrepancy between the integration times of the two instruments used in this study may also negatively impact the correlation. Recall that roughly 40% of the original comparison points were removed because there was high variability in the SuperDARN velocity values as compared to the surrounding SuperDARN cells. The comparison between EISCAT data integrated at 2-min intervals and SuperDARN single-beam data integrated for 3 or 7 s improved greatly when this removal was performed. The SuperDARN beams were sampled sequentially so that fast variations in velocities would have been apparent between neighboring beams. Such fast variations of velocity did occur for a large number of points, indicating that velocity changes on a timescale of just a few seconds were quite common in the SuperDARN scattering region.

[33] As the integration time of SuperDARN was under ~10 s and EISCAT had an integration time more than an order of magnitude longer at ~100 s, any velocity changes on a timescale shorter than the EISCAT integration time could result in a lack of correlation between SuperDARN and EISCAT measured velocity values. Therefore, at some times the instruments could conceivably measure different conditions in the ionosphere.

4.6. Ionospheric Heating Effects

[34] It is useful to note that in a study performed by *Eglitis et al.* [1998], use of the ionospheric heater at Tromsø resulted in good agreement between SuperDARN and EISCAT velocities with a slope value of 1.02 obtained. When the ionospheric heater was used, artificial irregularities were generated and detected by SuperDARN. These are expected to be more uniformly structured than natural auroral scattering regions. The SuperDARN radar would not have needed to rely on scatter from highly dense, presumably small-scale, spatially localized structures as the heater created irregularities throughout the scattering region from which the SuperDARN waves could scatter.

[35] Another effect of heating is the modification of the ambient electron density. At certain *F*-region altitudes it is expected that the electron density would decrease due to ionospheric heating increasing the recombination rate [e.g., *Rietveld et al.*, 1993]. A decrease in electron density would have brought the index of refraction closer to unity and caused less velocity underestimation by SuperDARN. Several studies have demonstrated an electron density depletion of 25%–50% created by lower latitude heating experiments at Arecibo [e.g., *Duncan et al.*, 1988; *Bernhardt et al.*, 1989; *Hansen et al.*, 1990; *Hansen et al.*, 1992]. A study by *Wright et al.* [1988] reported a density decrease of 15% due to heating at the higher latitude Tromsø facility. Conversely, *Stocker et al.* [1992] predicted and measured both increases and decreases of the electron density depending on several factors such as background electron density, heater frequency, and time of day. Further, the actual amount of electron density increase or decrease in the *Stocker et al.* [1992] study was quite low (less than 10%) which indicates that the refractive index was probably not affected greatly by this behavior. It would be beneficial to perform a more in-depth study of velocities measured by SuperDARN and EISCAT when the ionospheric heater is used.

5. Conclusions

[36] As a continuation of the work by *Gillies et al.* [2009], a comparison between SuperDARN line-of-sight velocities and EISCAT tristatic velocities has been performed. There was good correlation between the two data sets, but the velocities measured by SuperDARN tended to be lower than the corresponding velocities measured by EISCAT. This underestimation of velocities by SuperDARN was consistent with previous results [e.g., *Davies et al.*, 1999; *Drayton et al.*, 2005; *Drayton*, 2006]. This underestimate of line-of-sight velocities by SuperDARN was at least partially caused by the use of too high a value of the refractive index n_s in the scattering region. By using elevation angle measurements made by SuperDARN as a proxy for n_s, as proposed by *Gillies et al.* [2009], the best fit slope between SuperDARN and EISCAT velocities increased from 0.78 to 0.89 (an increase of 14%).

[37] One significant drawback to use of the elevation angle as a proxy for n_s is that these measurements are not always available. Therefore, other methods to estimate n_s were also considered. Electron density measurements by EISCAT and estimates from the IRI model were used to predict n_s, but these methods also have significant limitations. The EISCAT measurement of N_e was localized to a small area within one SuperDARN range cell and thus will typically not be of use to determine n_s in other parts of that range cell or for other range cells. The electron density value from IRI relied on large-scale mean estimates of N_e, thereby neglecting the higher densities expected in localized smaller-scale structures which cause coherent scatter.

[38] The two main issues raised from this comparison were the underestimation of velocities by SuperDARN even after elevation angle was used to estimate n_s and the lack of correlation between the different methods to estimate n_s. It is speculated that small-scale, highly dense structures in the SuperDARN scattering region partially explain both of these issues. These small-scale structures are important when they are of comparable size to the SuperDARN scattering volume. The small-scale structures cause strong irregularities from which the SuperDARN coherent radar waves scatter, while EISCAT incoherent radar measurements and IRI estimates of N_e provide only the background electron density and not the density of the small-scale structures, which are expected to be important in the coherent scattering process. Further, the altitude from which SuperDARN scattering occurs is known only approximately so it was difficult to select an appropriate value for N_e from either EISCAT or IRI. The angle-of-arrival proxy better accounts for both structures and the altitude ambiguity because the elevation angle measurements are directly linked

to the scattering region measurements. From this work, it can be inferred that SuperDARN scatter primarily occurs in localized regions with high electron density. It is also apparent that the modification of SuperDARN measured velocities due to the refractive index is larger than that based on the higher n_s values inferred from either the angle-of-arrival method or available electron density measurements.

[39] **Acknowledgments.** During this work RGG was supported by the Canadian Space Agency and the Natural Sciences and Engineering Research Council (NSERC) to the Canadian component of the SuperDARN ground based radar system and the CASSIOPE/ePOP project and by the EU Marie Curie Early Stage Training in Space, Planetary and Astrophysical Sciences (SPARTAN) Programme. The CUTLASS (Co-operative UK Twin Located Auroral Sounding System) radars form part of the SuperDARN (Dual Auroral Radar Network) HF project and consist of radars at Hankasalmi (Finland) and Pykkvibaer (Iceland). They are operated by the Radio and Space Plasma Physics Group at the University of Leicester with support from the Particle Physics and Astronomy Council and additional support from the Finnish Meteorological Institute and the Swedish Meteorological Institute. We are indebted to the Director and staff of EISCAT for operating the facility and supplying the data. EISCAT is an International Association supported by Finland (SA), France (CNRS), Germany (MPG), Japan (NIPR), Norway (NFR), Sweden (VR), and the United Kingdom (PPARC). During this work DMW was supported by the UK Science and Technology Facilities Council (Grant Number: PP/E000983).

[40] Zuyin Pu thanks William Bristow and another reviewer for their assistance in evaluating this paper.

References

André, D., G. Sofko, K. Baker, and J. MacDougall (1998), SuperDARN interferometry: Meteor echoes and electron densities from groundscatter, *J. Geophys. Res.*, *103*, 7003–7015.

Baker, K. B., J. R. Dudeney, R. A. Greenwald, M. Pinnick, P. T. Newell, A. S. Rodger, N. Mattin, and C.-I. Meng (1995), HF radar signatures of the cusp and low-latitude boundary layer, *J. Geophys. Res.*, *100*, 7671–7695.

Bernhardt, P. A., C. A. Teply, and L. M. Duncan (1989), Airglow enhancements associated with plasma cavities formed during ionospheric heating experiments, *J. Geophys. Res.*, *94*, 9071–9092.

Bilitza, D. (2001), International Reference Ionosphere 2000, *Radio Sci.*, Vol. 36, 261–275.

Budden, K. G. (1961), *Radio Waves in the Ionosphere*, Cambridge University Press, Cambridge, U. K.

Chisham, G., T. K. Yeoman, and G. J. Sofko (2008), Mapping ionospheric backscatter measured by the SuperDARN HF radars. Part 1: A new empirical virtual height model, *Ann. Geophys.*, *26*, 823–841.

Davies, J. A., M. Lester, S. E. Milan, and T. K. Yeoman (1999), A comparison of velocity measurements from the CUTLASS Finland radar and the EISCAT UHF system, *Ann. Geophys.*, *17*, 892–902.

Drayton, R. A. (2006), Study of SAPS-like flows with the King Salmon SuperDARN radar, M.Sc. thesis, Institute of Space and Atmospheric Studies, Univ. of Saskatchewan, Saskatchewan.

Drayton, R. A., A. V. Koustov, M. R. Hairston, and J.-P. Villian (2005), Comparison of DMSP cross-track ion drifts and SuperDARN line-of-sight velocities, *Ann. Geophys.*, *23*, 2479–2489.

Duncan, L. M., J. P. Sheerin, and R. A. Behnke (1988), Observations of ionospheric cavities generated by high-power radio waves, *Phys. Rev. Lett.*, *61*, 239–242, 1988.

Eglitis, P., T. R. Robinson, M. T. Rietveld, D. M. Wright, and G. E. Bond (1998), The phase speed of artificial field-aligned irregularities observed by CUTLASS during HF modification of the auroral ionosphere, *J. Geophys. Res.*, *103*, 2253–2259.

Gillies, R. G., G. C. Hussey, G. J. Sofko, K. A. McWilliams, R. A. D. Fiori, P. Ponomarenko, and J.-P. St. Maurice (2009), Improvement of SuperDARN velocity measurements by estimating the index of refraction in the scattering region using interferometry, *J. Geophys. Res.*, *114*, A07305, doi:10.1029/2008JA013967.

Ginzburg, V. L. (1964), *The Propagation of Electromagnetic Waves in Plasmas*, Pergamon Press, New York.

Greenwald, R. A., et al. (1995), DARN/SuperDARN: A global view of the dynamics of high-latitude convection, *Space Sci. Rev.*, *71*, 761–796.

Haldoupis, C., and K. Schlegel (1990), Direct comparison of 1-m irregularity phase velocities and ion acoustic speeds in the auroral *E*-region ionosphere, *J. Geophys. Res.*, *95*, 989–1000.

Hansen, J. D., G. J. Morales, L. M. Duncan, J. E. Maggs, and G. Dimonte (1990), Large-scale ionospheric modifications produced by nonlinear refractions of an hf wave, *Phys. Rev. Lett.*, *65*, 3285–3288.

Hansen, J. D., G. J. Morales, L. M. Duncan, and G. Dimonte (1992), Large-scale HF-induced ionospheric modifications: experiments, *J. Geophys. Res.*, *97*, 113–122.

Hosokawa, K., K. Shiokawa, Y. Otsuka, T. Ogawa, J.-P. St-Maurice, G. J. Sofko, and D. A. Andre (2009), Relationship between polar cap patches and field-aligned irregularities as observed with an all-sky airglow imager at Resolute Bay and the PolarDARN radar at Rankin Inlet, *J. Geophys. Res.*, *114*, A03306, doi:10.1029/2008JA013707.

Mitchell, C. N., D. G. Jones, L. Kersley, S. E. Pryse, and I. K. Walker (1995), Imaging of field-aligned structures in the auroral ionopshere, *Ann. Geophys.*, *13*, 1311–1319.

Milan, S. E., T. B. Jones, T. R. Robinson, E. C. Thomas, and T. K. Yeoman (1997), Interferometric evidence for the observation of ground backscatter originating behind the CUTLASS coherent radars, *Ann. Geophys.*, *15*, 29–39.

Noël, J.-M. A., J.-P. St. Maurice, and P.-L. Blelly (2000), Nonlinear model of short-scale electrodynamics in the auroral ionosphere, *Ann. Geophys.*, *18*, 1128–1144.

Noël, J.-M. A., J.-P. St. Maurice, and P.-L. Blelly (2005), The effect of *E*-region wave heating on electrodynamical structures, *Ann. Geophys.*, *23*, 2081–2094.

Pryse, S. E., C. N. Mitchell, J. A. Heaton, and L. Kersley (1995), Travelling ionospheric disturbances imaged by tomographic techniques, *Ann. Geophys.*, *13*, 1325–1330.

Pryse, S. E., K. L. Dewis, R. L. Balthazor, H. R. Middleton, and M. H. Denton (2005), The dayside high-latitude trough under quiet geomagnetic conditions: Radio tomography and the CTIP model, *Ann. Geophys.*, *23*, 1199–1206, 2005.

Rietveld, M. T., H. Kohl, H. Kopka, and P. Stubbe (1993), Introduction to ionospheric heating at Tromsø. I. Experimental overview, *J. Atmos. Terr. Phys.*, *55*, 577–599.

Rishbeth, H., and A. P. van Eyken (1993), EISCAT: Early history and the first ten years of operation, *J. Atmos. Terr. Phys.*, *55*, 525–542.

Robinson, T. R. (1989), The heating of the high latitude ionosphere by high power radio waves, *Phys. Rep.*, *179*, 79–209.

Sofko, G., R. Schwab, M. Watanabe, C. Huang, J. Foster, and K. McWilliams (2007), Auroral post-secondary ions from the nightside ionosphere in the inner magnetosphere, *J. Atmos. Sol. Terr. Phys.*, *69*, 1213–1232.

Sojka, J. J., R. W. Schunk, and J. A. Whalen (1990), The longitude dependence of the dayside *F* region trough: A detailed model-observation comparison, *J. Geophys. Res.*, *95*, 15,275–15,280.

Stocker, A. J., F. Honary, T. R. Robinson, T. B. Jones, P. Stubbe, and H. Kopka (1992), EISCAT observations of large scale electron temperature and electron density perturbations caused by high power HF radio waves, *J. Atmos. Terr. Phys.*, *54*, 1555–1572.

Stubbe, P. (1996), Review of ionospheric modification experiments at Tromsø, *J. Atmos. Terr. Phys.*, *58*, 349–368.

Wright, J. W., H. Kopka, and P. Stubbe (1988), A large-scale ionospheric depletion by intense radio wave heating, *Geophys. Res. Lett.*, *15*, 1531–1533.

Xu, L., A. V. Koustov, J. Thayer, and M. A. McCready (2001), SuperDARN convection and Sondrestrom plasma drift, *Ann. Geophys.*, *19*, 749–759.

J. A. Davies, Space Science and Technology Department, Rutherford Appleton Laboratory, Harwell Science and Innovation Campus, Didcot OX11 0QX, UK.

R. G. Gillies, G. C. Hussey, and G. J. Sofko, Institute of Space and Atmospheric Science, University of Saskatchewan, 116 Science Pl., Saskatoon, SK S7N 5E2, Canada. (Rob.Gillies@usask.ca)

D. M. Wright, Department of Physics and Astronomy, University of Leicester, University Road, Leicester LE1 7RH, UK.

Chapter 6

Refractive index estimates from frequency shifting

6.1 Introduction

The research presented in this chapter is based on the following manuscript:

- Gillies, R. G., G. C. Hussey, G. J. Sofko, P. V. Ponomarenko, and K. A. McWilliams. Improvement of HF coherent radar line-of-sight velocities by estimating the refractive index in the scattering volume using radar frequency shifting, Submitted to *J. Geophys. Res.*, Accepted 5 November 2010.

This study introduces a method to measure the electron density and refractive index in the scattering volume of SuperDARN radars using routine shifts in radar operating frequency. The analysis of these frequency shifts found that electron density values in the scattering volume of HF coherent radars are significantly higher than background estimates.

6.2 Results

As discussed in Section 1.7, the highly variable electron density in the ionosphere greatly affects the propagation paths of HF radio waves. Fortunately, the SuperDARN radars have the ability to transmit HF waves at various frequencies from 8 MHz to 20 MHz, to minimize the effect of changing propagation conditions due to

changes in electron density, in order to maximize scattering. Since higher ionospheric electron densities are expected on the dayside of the Earth than on the nightside, until ∼2002 the SuperDARN radars operated by using a fixed higher frequency during daytime and a fixed lower frequency during nighttime. After ∼2002, most radars operated by automatically choosing the best transmitting frequency to optimize the number of ionospheric echoes they received. The result of this automatic frequency changing is that most radars transmit several different frequencies during a given day. Fortunately, these frequency shifts by the radars offer a unique opportunity to measure the refractive index in the scattering volume of the SuperDARN radars.

The velocity measured by the SuperDARN radars is lower than the actual plasma velocity by a factor equal to the refractive index. As discussed in Section 1.7, the refractive index depends on wave frequency. If all other factors are constant, higher wave frequencies will result in higher refractive indices and lower wave frequencies will result in lower refractive indices. If it is assumed that the electron density and plasma velocity in the scattering volume are relatively constant during a shift in operating frequency, the velocity that is measured by SuperDARN should change when the frequency is changed. This change in measured velocity can be used to measure the electron density in the scattering volume. The details of this frequency shifting analysis are presented in the *Gillies et al.* [2010a] manuscript associated with this chapter.

The analysis of the velocities measured before and after frequency shifts involved all SuperDARN radars over the last 20 years. This analysis identified that the electron density in the scattering volume is significantly higher than the background electron density, confirming the hypothesis discussed in Chapter 5. The electron density and refractive index values determined from the frequency shifting technique was applied to a comparison between velocities measured by SuperDARN and velocities measured by the DMSP satellites and the EISCAT incoherent scatter radar. Figure 6.1 presents the comparison without accounting for refractive index and it is apparent that velocities measured by SuperDARN were statistically lower than velocities measured by the other instruments (a best fit slope of 0.81 was found).

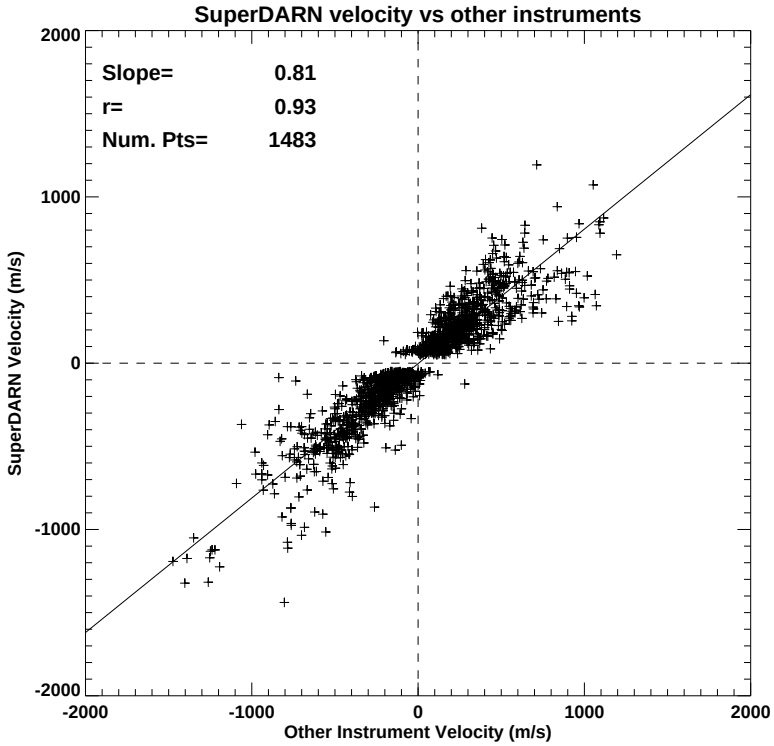

Figure 6.1: A comparison of velocities measured by the SuperDARN radars and by other instruments.

Figure 6.2 is the same comparison; however, velocities measured by SuperDARN now took into account the refractive index estimated from the frequency shifting method. In this comparison, velocities measured by SuperDARN are not statistically lower than velocities measured by other instruments. In fact, as the best fit slope is 1.05, SuperDARN actually slightly overestimates velocities in this case.

This frequency shifting study has found that coherent scatter of SuperDARN radar waves occurs in the most disturbed and highly dense regions of the ionosphere. It was found that the average electron density in the scattering volume of SuperDARN was nearly double the background electron density. Future studies that have access to a more uniform set of frequency shifting statistics will examine this issue further. As will be discussed in more detail in the concluding chapter, future work in this area will involve designated experiments in which the operating frequency of a SuperDARN radar is continuously changed to allow electron density measurements.

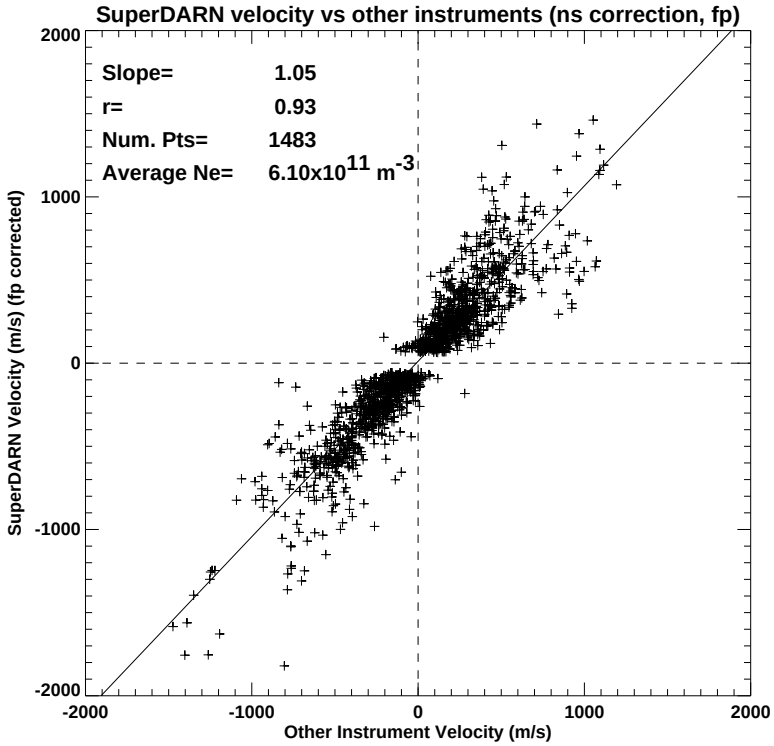

Figure 6.2: A comparison of velocities measured by the SuperDARN radars and by other instruments. Velocities measured by SuperDARN have been modified to account for the refractive index in the scattering volume.

Also, Stereo mode data from the CUTLASS SuperDARN radars [*Lester et al.*, 2004], in which coherent scatter data from two frequencies is simultaneously recorded, will be examined.

6.3 Accepted paper

The manuscript describing the development and testing of the frequency shifting technique to measure electron density in the SuperDARN scattering volume was accepted by the *Journal of Geophysical Research* in November 2010. Immediately following is the paper in manuscript format (figures appear at the end of manuscript as per AGU requirements) reproduced by permission of American Geophysical Union:

- Gillies, R. G., G. C. Hussey, G. J. Sofko, P. V. Ponomarenko, and K. A. McWilliams.

Improvement of HF coherent radar line-of-sight velocities by estimating the refractive index in the scattering volume using radar frequency shifting, Submitted to *J. Geophys. Res.*, Accepted 5 November 2010.

Improvement of HF coherent radar line-of-sight velocities by estimating the refractive index in the scattering volume using radar frequency shifting

R. G. Gillies[1], G. C. Hussey[1], G. J. Sofko[1], P. V. Ponomarenko[1], and

K. A. McWilliams[1]

R. G. Gillies, Institute of Space and Atmospheric Science, University of Saskatchewan, 116 Science Place, Saskatoon, SK, Canada (Rob.Gillies@usask.ca)

[1]Institute for Space and Atmospheric

Studies, University of Saskatchewan,

Saskatoon, Saskatchewan, Canada

Abstract. Measurements of ionospheric drift velocities using HF coherent scatter radars, such as SuperDARN, are generally underestimated because the refractive index in the scattering volume has not been taken into account. Refractive index values evaluated from electron density measurements, IRI predictions, or elevation angle measurements have been applied to SuperDARN velocities in past studies. However the SuperDARN velocities so obtained were, on average, statistically lower than velocities measured by other instruments. One possible explanation for this underestimation is that HF coherent scatter preferentially occurs in regions of the ionosphere where the scattering cross-section is largest, and such regions are characterized by small-scale structures which have higher-than-average electron densities. This was not accounted for in past studies because the refractive index estimates used were from large-scale and therefore smoothed estimates of electron density. In this paper, a new method of estimating the actual electron density (or plasma frequency) at the location of SuperDARN scatter (instead of the larger-scale background electron density) is presented. This method takes advantage of the frequency shifts which occur in normal SuperDARN operations. If it is assumed that, on average, the actual ionospheric drift velocity and plasma frequency are roughly constant before and after a shift in frequency, any change in measured velocity as SuperDARN changes frequency is due to a change in refractive index. An analysis of the change in the measured velocity resulting from each shift in frequency gives an experimentally-based estimate of the electron density in the scattering volume. A statisti-

cal analysis of essentially all frequency shifts by SuperDARN and the estimated electron densities in the scattering volume has been performed. The resulting electron densities are appreciably higher than previous methods to estimate electron density predict. Application of this new method to velocity comparisons between SuperDARN and other instruments results in agreement between the HF radar and non-HF radar velocities for the first time. This new method allows for the first direct measurements of electron densities in the exact locations where the cross-section for SuperDARN scatter maximizes.

1. Introduction

The Super Dual Auroral Radar Network (SuperDARN) of High Frequency (HF) radars has continuously monitored high-latitude ionospheric plasma convection velocities for more than 15 years [*Greenwald et al.*, 1995]. Refraction of the transmitted signal from SuperDARN is necessary to bend the waves to perpendicularity with the local geomagnetic field in the scattering volume so that coherent scatter from field-aligned ionospheric plasma irregularities can occur. The line-of-sight velocity of these scatterers is then inferred from the Doppler shift of the returned wave. Every one or two minutes, line-of-sight (LOS) velocities are measured by over twenty radars in the northern and southern hemispheres, each with over 700 range cells. By assuming that the F-region plasma moves with the $\mathbf{E} \times \mathbf{B}$ drift, these velocities are used to infer ionospheric electric fields which are then used to create high latitude electric potential contour maps [*Ruohoniemi and Baker*, 1998].

One important aspect of HF ionospheric scatter which has, until recently, been neglected in the calculation of LOS velocities measured by SuperDARN is the refractive index in the scattering volume n_s [*Gillies et al.*, 2009]. The refractive index in the scattering volume directly affects the LOS velocity measured by SuperDARN, v_m, compared to the actual LOS velocity of the ionospheric scatterer, v_s, according to:

$$v_m = v_s n_s. \tag{1}$$

Since the refractive index is typically less than one, neglecting its value has led to SuperDARN velocities that systematically underestimate the actual ionospheric drift velocities. Indeed, several past comparisons of SuperDARN velocity measurements to those

performed by other instruments have found that SuperDARN values were, on average, consistently lower [e.g., *Davies et al.*, 1999; *Xu et al.*, 2001; *Drayton et al.*, 2005]. These studies indicated that accurate estimates of refractive index in the SuperDARN scattering volume were needed for improving velocity estimates.

One method to estimate refractive index using SuperDARN elevation angle measurements was proposed by *Gillies et al.* [2009]. This method applied Snell's law in spherical coordinates to allow the elevation angle measured by SuperDARN radars to be used as a proxy for refractive index. Two assumptions that were made to apply this method were that the ionosphere was spherically stratified and that SuperDARN radars always measure and record accurate elevation angle data. This method was limited as these assumptions do not always hold, nevertheless, the elevation angle proxy was a first step in estimating the refractive index.

The next method proposed to estimate refractive index was to simply apply the International Reference Ionosphere (IRI) model [*Bilitza*, 2001] to infer electron density (and thus refractive index) at the time and location of a given SuperDARN velocity measurement [*Ponomarenko et al.*, 2009]. This method had the benefit of always providing a value for refractive index. However, the method provided only the large-scale background electron density and was not able to take into account small-scale structures that may be very important for SuperDARN scatter. Application of elevation angle measurements [*Gillies et al.*, 2009] or IRI electron densities [*Ponomarenko et al.*, 2009] for refractive index estimates improved comparisons between SuperDARN velocities and DMSP satellite velocities by ∼12–15%, however the improved velocities measured by SuperDARN, v_{mi}, were still, on average, lower.

Another comparison of SuperDARN velocities with velocities measured by the European Incoherent SCATter (EISCAT) radar was performed by *Gillies et al.* [2010a]. This study compared velocities measured by the Hankasalmi SuperDARN and tristatic velocities measured by EISCAT from 1995–1999. It was found that unmodified SuperDARN velocities were about 20% lower than EISCAT velocities. Estimates of refractive index in the SuperDARN scattering volume were made using the elevation angle proxy, IRI estimates of electron density, and electron densities from EISCAT. Each of these methods improved the comparison but the improved velocities measured by SuperDARN were still about 10% lower than EISCAT velocities.

It was suggested by *Gillies et al.* [2010a] that the reason for lower SuperDARN velocities (even after attempting to account for refractive index) was that SuperDARN scatter would tend to occur most strongly in the regions of highest electron density. It is reasonable to assume that, although scatter will occur throughout a SuperDARN range cell (which is 45 km in range, ∼50 km in width, and up to several hundred kilometers in altitude), the strongest scatter occurs in only small regions (∼hundreds of meters) of the cell. These smaller regions have larger electron densities which produce larger radar cross sections [*Booker*, 1956] and result in higher backscatter power. A study of echo occurrence in relation to polar cap patches has found that the majority of SuperDARN backscatter does tend to occur in regions with the highest electron density [*Hosokawa et al.*, 2009]. Since the methods used to estimate n_s have relied on relatively large-scale (background) measurements of refractive index, they would not account for these small-scale structures of high scattering cross-section and lower-than-average refractive indices which, if neglected, would lead to velocity underestimation by SuperDARN.

In this paper, we propose a new method to estimate refractive index in the SuperDARN scattering volume that takes advantage of changes in the SuperDARN transmitting frequency. Many SuperDARN radars employ a 'sounding mode' which routinely changes frequencies to accommodate for the ionospheric propagation conditions in order to maximize ionospheric scatter. Since refractive index n_s is dependent on radar frequency and the Doppler velocity measured by an HF radar v_m is dependent on n_s (Equation 1), different values of v_m will be measured before and after a shift in radar frequency. This shift in v_m can then be used to experimentally estimate refractive index. Unlike the previous methods, this new frequency shifting technique provides a direct in-situ scattering volume measurement of refractive index which will allow calculation of improved measured velocity v_{mi} values. This method could also provide information about the characteristics of small-scale ionospheric structures in the scattering volume of SuperDARN radars.

2. Theory

2.1. Scattering volume plasma frequency from frequency shifts

A lower than expected index of refraction in the SuperDARN scattering volume causes an underestimation of the velocity measurements made by SuperDARN. Previous attempts to model the refractive index using electron density estimates or elevation angle measurements have showed significant improvement, but have not been completely successful. It was proposed by *Gillies et al.* [2010a] that small-scale, dense structures are dominant in the scattering process. In turn, these structures with enhanced electron densities cause the refractive index in the scattering volume to be much lower than the current estimates predict. For this reason, a method which uses SuperDARN frequency

shifts to directly determine the refractive index in the SuperDARN scattering volume has been developed.

The index of refraction n in a magnetoionic medium for quasi-transverse (QT) wave propagation (i.e., propagation which is nearly perpendicular to the magnetic field lines, as is the case for coherent SuperDARN scatter) is given by the Appleton-Hartree equation [*Budden*, 1961] as:

$$n^2 = 1 - \frac{f_p^2/f^2}{1 - f_c^2/2(f^2 - f_p^2) \pm f_c^2/2(f^2 - f_p^2)} \tag{2}$$

where f_c is the gyrofrequency or cyclotron frequency, f_p is the plasma frequency, and f is the radar wave frequency. Inspection of Equation 2 indicates that there are two possible modes of propagation: the positive sign corresponds to the ordinary (O) mode and the negative sign corresponds to the extraordinary (X) mode. For typical QT propagation conditions, the refractive indices of the two modes are quite similar. For example, with an f_p value of 7.5 MHz, an f_c value of 1.5 MHz, and an f value of 12.5 MHz (which are typical values for SuperDARN scatter in the high latitude ionosphere), the refractive indices of the O- and X-modes are 0.800 and 0.795, respectively. Due to this similarity, use of the analytically simpler O-mode equation is an appropriate approximation for describing the refractive index in the SuperDARN scattering volume (although it should be noted that *Gillies et al.* [2010b] predicted that it is the X-mode which primarily participates in SuperDARN scatter).

The index of refraction n_s in the SuperDARN scattering volume of the O-mode for QT propagation is found by taking the positive sign in the denominator of Equation 2:

$$n_s = \sqrt{1 - f_p^2/f^2}. \tag{3}$$

Note that this expression does not contain any term relating to the magnetic field so that when propagation is perpendicular to the magnetic field lines, the O-mode is not affected by the magnetic field. At the next step we substitute Equation 3 into Equation 1:

$$v_m = v_s\sqrt{1 - f_p^2/f^2}. \tag{4}$$

As the plasma frequency is dependent on the variable electron density in the scattering volume, there are two unknowns in this Equation, f_p and v_s. If it is assumed that f_p and v_s are relatively constant from one SuperDARN scan to the next (a time scale of one or two minutes), a change in transmitted frequency will modify the measured velocity v_m. Using Equation 4 and observing v_m immediately before (v_{m1}) and after (v_{m2}) a frequency shift from frequency f_1 to frequency f_2 will provide a direct measure of both f_p and v_s in the scattering volume. Solutions for f_p and v_s are:

$$f_p^2 = \frac{f_1^2(1 - v_{m1}^2/v_{m2}^2)}{(1 - v_{m1}^2 f_1^2/v_{m2}^2 f_2^2)} \tag{5}$$

and

$$v_s^2 = \frac{f_2^2 v_{m2}^2 - f_1^2 v_{m1}^2}{f_2^2 - f_1^2}. \tag{6}$$

Since SuperDARN radars routinely change transmitting frequencies to optimize the amount of ionospheric scatter, there are numerous opportunities to measure the plasma frequency in the scattering volumes. Once a measure of f_p is made, Equation 3 can be applied to find an estimate for refractive index in the scattering volume, which can then be used with Equation 1 to improve the line-of-sight velocities which are measured by SuperDARN.

2.2. Change in scattering location from shift in frequency

A change in transmitted frequency will change the propagation characteristics of the HF waves and scatter will occur in slightly different locations for two different frequencies. In order to estimate plasma frequency in the SuperDARN scattering volume using instances of shifts in transmitting frequency, it is important to ensure that the ionospheric location at which the scatter occurs does not change significantly so that it can be assumed that any changes in measured velocity from one frequency to the next is indeed due to a change in the refractive index. In this section, we examine the variability of possible scattering locations for different frequencies and, more importantly, determine whether different frequencies tend to systematically propagate to regions of the ionosphere with higher or lower drift velocities.

Possible ionospheric scatter locations for various transmitter frequencies have been determined using raytracing. A one-dimensional electron density profile generated by IRI was used with a peak F-region electron density of 5×10^{11} m^{-3} occurring at 280 km altitude. This profile is typical of ionospheric conditions at SuperDARN latitudes. Ray paths for radar frequencies of 10 MHz, 12 MHz, 14 MHz, and 16 MHz were calculated using equations developed by *Haselgrove* [1963] for northward propagation from the Saskatoon SuperDARN radar at elevation angles ranging from 0.1° to 90.0° in 0.1° steps. On the ray paths, points at which the wave propagation direction and the magnetic field of the Earth were perpendicular to one another to within 1° were recorded as possible coherent scatter locations. Figure 1 plots the movement of SuperDARN range cells as the transmitting frequency is increased from 10 MHz to 12 MHz (small arrowheads), from 12 MHz to 14 MHz (medium arrowheads), and from 14 MHz to 16 MHz (large arrowheads). The horizontal dashed line in the figure gives the F-region peak altitude and the electron density profile

is presented on the left side of the figure. For latitudes between 55° and 65° there exists two distinct branches at which scatter occurs, a lower branch between ∼190–250 km and an upper branch between ∼265–305 km. It is likely that the majority of coherent scatter will occur in the upper branch of scatter locations as this is the altitude with the highest electron densities [*Ponomarenko et al.*, 2009]. Therefore, in the following discussions, we will only consider this upper branch. It is apparent that, in general, as frequency is increased the scatter locations tend to move in altitude towards the electron density peak and slightly poleward in latitude. It should be noted that a study by *André et al.* [1997] also found that scatter locations for HF radars tended to move both poleward and towards the F-region peak altitude by ∼50 km when operating frequencies were increased by ∼3 MHz.

This raytracing analysis has shown that the movement of the scatter volume when frequency is shifted is small and mostly in the vertical direction so the drift velocities in the scattering volumes should be roughly the same before and after a frequency shift. Although, one systematic effect of movement of the scatter locations towards the peak electron density would be an increase in electron density (and therefore plasma frequency) at the scattering location. Conversely, since the overall electron density tends to decrease with increasing latitude, movement of the scattering location poleward would tend to cause scatter to occur in regions with lower plasma frequencies. Equation 4 predicts, and the results presented in the next section confirm, an increase in measured velocity from an increase in transmitter frequency. However, since the motion of the scattering locations in Figure 1 appears to be mostly vertical, the net effect is probably a small increase in f_p corresponding to an increase in transmitted frequency. Inspection of the

upper scattering branch in Figure 1 reveals that the change in electron density in the scattering volumes from the change in frequency is less than 5% (resulting in a change in f_p of ∼2%). This behaviour will slightly counteract the predicted increase in measured velocity from Equation 4. In other words, the plasma frequencies derived in the next section from this method may be slightly too low.

3. Results

3.1. Typical scan-to-scan variation of velocity measured by SuperDARN

Equations 5 and 6 allow the calculation of plasma frequency in the SuperDARN scattering volume and the actual ionospheric drift velocity given a shift in radar frequency. The main assumption in the derivation of both these equations was that both plasma frequency f_p and actual scatterer velocity v_s were constant from one SuperDARN scan to the next. Unfortunately, the natural variation of velocities measured by SuperDARN from one scan to the next is higher than the shift in velocity which is expected from Equation 4. For example, Figure 2 plots the velocity measured by the Saskatoon SuperDARN for 20 minutes over a randomly chosen frequency shift occurrence from 13 to 15 MHz in beam 8, range gate 24, on October 2, 2000. Notice that the change in velocity near the radar frequency increase (from above 600 m/s to below 500 m/s) is no more significant than the variations in velocity at other times in the scan (for example, seven minutes before the shift there is a change in velocity from nearly 800 m/s to ∼400 m/s). For a scattering volume plasma frequency of 7.5 MHz, the expected shift in measured velocity from this shift in operating frequency would be only 6%. Clearly, the random variations of velocity measured by SuperDARN are much larger than the effect which is expected from shifting frequency. Therefore, it is not possible with the dataset used in this study to determine

the plasma frequency for every individual SuperDARN frequency shift, so a statistical analysis of velocities before and after frequency changes was performed instead. In future studies, analysis of SuperDARN stereo [*Lester et al.*, 2004] or sounding [*Hughes et al.*, 2002] operation modes may allow real-time analysis of refractive index and SuperDARN velocity improvements.

3.2. Superposed epoch analysis of velocity measured at radar frequency shifts

An analysis of all the common-mode operation data (one- and two-minute scans) from each SuperDARN radar has been performed. From the start of operation in 1993 to about 2002, most radars routinely performed two frequency shifts per day (one in the morning at ∼6 LT and one in the evening at ∼18 LT). Since then, radars commonly operate in a sounding mode which automatically determines the appropriate transmitting frequency required to maximize ionospheric scatter occurrence. The use of the sounding mode typically resulted in several frequency shifts per day for every radar. Every frequency shift which was more than 0.5 MHz and for which the frequency was constant for ten scans before and after the shift has been analyzed. Each range cell was examined and if velocities with absolute values of more than 50 m/s were recorded for at least half the scans before the shift and half the scans after the shift, the time sequence of velocities for the given range cell was recorded. The 50-m/s velocity cut-off was included to ensure that the echoes were not ground scatter although echoes actually flagged as ground scatter were also not included. Each velocity time sequence was normalized by dividing each individual velocity in the sequence by the average velocity of the entire sequence. This normalization was performed to prevent biasing from time sequences which had larger overall velocities since the important aspect of this study is the ratio of velocities at two

frequencies, not the actual velocities. In total, $\sim 1.3 \times 10^6$ normalized velocity sequences from all the radars were recorded. It is important that scatter for both frequencies occurs in the same ionospheric layer (in this study we considered F-region data). Therefore, only range gates 20 through 35 ($\sim$1100 km to 1600 km in range) were considered for this analysis to remove any possible E-region contamination, and this reduced the number of sequences to $\sim 4 \times 10^5$.

The normalized velocity sequences were combined by averaging each velocity at a given time in the sequence (i.e., all velocities two minutes before the shift were averaged together, all velocities two minutes after the shift were averaged together, etc.). Scans which occurred with one minute resolution were averaged to give velocity values every two minutes regardless of scan time. A superposed epoch analysis of the normalized velocity sequences is presented as Figure 3. Note that Figure 3 shows a frequency change from lower to higher frequency but changes obviously occur in the opposite direction as well. The time axis was inverted in any sequences for which the frequency decreased so that the lower frequency was always placed before the higher frequency. The average low frequency at a shift was 12 MHz and the average high frequency at a shift was 14 MHz. It is immediately apparent that an increase in velocity occurs at the same time as the increase in radar frequency, as expected when Equation 4 is considered. Use of Equation 5 and the normalized velocities immediately before and after the shift in radar frequency, v_{m1} and v_{m2}, provides a f_p value of 7.8 MHz (which corresponds to an electron density of 7.2×10^{11} m^{-3}). For comparison, the average f_p predicted by the IRI model at the times and locations used to generate Figure 3 was only 5.9 MHz (which corresponds to an electron density of 4.2×10^{11} m^{-3}). Applying the value of 7.8 MHz for plasma frequency

to Equation 3 results in refractive indices of 0.76 and 0.83 for before and after the shift in frequency. Also apparent in Figure 3 is a slight negative slope in the measured velocity as time increases. Possible reasons for this will be discussed in Section 4.1.

The uncertainty of the plasma frequency inferred from Figure 3 was also estimated. The standard error of the average normalized velocities before v_{m1} and after v_{m2} the shift were found to provide minimum and maximum values for each. A minimum/maximum value of f_p was determined by substituting into Equation 5 the maximum/minimum possible value of v_{m1} and the minimum/maximum value of v_{m2}. This procedure resulted a possible error in the 7.8-MHz average value for f_p of less than 0.1 MHz. This procedure to estimate uncertainty was used throughout this study to provide error bars on the plots presented in the next section.

3.3. Dependence of plasma frequency on various parameters

The analysis performed in Section 3.2 considered velocities from all magnetic latitudes, local times, radars, and years. The average plasma frequency of 7.8 MHz found in Figure 3 may be biased by the parameters (for example, magnetic latitude, time of day, solar cycle period, etc.) that had the most frequency shifting events. Since variations in electron density may occur for all these parameters, it is important to examine the effect on measured f_p as each is varied. The goal of this section is to provide estimations of refractive index in the SuperDARN scattering volume for any given time and location.

3.3.1. Plasma frequency from different radars

The average plasma frequency in SuperDARN scattering volumes was determined in Section 3.2 from radar operating frequency shifts. Due to different operating procedures and lifespan of radars, a different number of radar frequency shifts occurred for each

radar. It is important to examine each radar individually to determine if there is any bias in the results presented in Figure 3. Table 1 lists each SuperDARN radar examined in this study, the number of velocity sequences the radar provided for averaging in Figure 3, and the average f_p in the scattering volume of the radar determined by the radar frequency shifts. Also provided in Table 1 is the average value for f_p provided by IRI for each radar. Considering only radars which provided a significant number of frequency shift events (more than 10,000), all radars with the exception of Rankin Inlet and Inuvik have average plasma frequencies within 1 MHz of the 7.8-MHz average for all radars. Nearly all the radars considered in this study were auroral radars except Rankin Inlet and Inuvik (the PolarDARN radars) which are polar cap radars (mid-latitude radars such as Blackstone, Hokkaido, and Wallops Island were examined, however very few radar frequency shifting events were found for these). Since the PolarDARN radars are located at higher magnetic latitudes than the other radars, it can be expected that the background electron density and plasma frequency for these radars would be lower.

The Kodiak radar contributes nearly half the total number frequency shifts used in this study so it is important to examine separately the effect of this radar to ensure that it does not significantly bias the overall results. Performing an analysis nearly identical to that presented in Section 3.2, without the Kodiak radar data, provides a total of 2.2×10^5 frequency shifting events (compared to 4×10^5 with Kodiak included), which result in an average plasma frequency of 7.4 MHz (compared to 7.8 MHz with Kodiak included). This 0.4 MHz increase in f_p, when the Kodiak radar observations are included, is not significant compared to the variations of plasma frequency with respect to magnetic latitude and solar cycle presented in the next sections. This analysis indicates that although the Kodiak

radar provides a significant fraction of the statistics used in generating Figure 3, it does not significantly bias the overall average plasma frequency result.

3.3.2. Magnetic latitude

The analysis performed in Section 3.2 considered velocities from all magnetic latitudes. Since the electron density in the ionosphere is highly dependent on latitude, it is essential to examine the change in predicted plasma frequency for different latitudes. An analysis similar to that described in Section 3.2 was performed for specific magnetic latitudes. The solid curve in Figure 4 is the derived plasma frequency as a function of magnetic latitude. The value for f_p in the SuperDARN scattering volume appears to reach a maximum between latitudes 68° and 76°. This behaviour is expected because the auroral oval, which has higher electron density values, is usually located near this latitude interval. The dashed curve represents the peak f_p that is predicted by the IRI model at each latitude and will be discussed in Section 4.3.

3.3.3. Solar cycle dependence on plasma frequency

Like the dependence on magnetic latitude, the period in the solar cycle will directly impact the plasma frequency and electron density. Again, since the analysis performed in Section 3.2 considered all years of SuperDARN operation, it is important to also examine the change in measured f_p with respect to year. Figure 5 presents the derived plasma frequency in the SuperDARN scattering volume for the years 1994 to 2009. A peak in f_p is found in the year 2002, which roughly corresponds to the maximum in the solar cycle. The 2000 to 2005 interval of solar cycle 23 maximum conditions is characterized by higher plasma frequencies. The plasma frequency since 2002 decreased with decreasing solar activity until about 2007. From 2007 to the present f_p has begun to increase slightly.

Again, the dashed curve represents the peak f_p that is predicted by the IRI model for each year and will be discussed in Section 4.3.

3.3.4. Diurnal dependence on plasma frequency

For several years, many radars operated in a mode in which they shifted radar frequencies twice during the day. These shifts occurred once in the evening and once in the morning. The result of this behaviour is that the derived f_p is biased towards local times around 6 and 18 LT. An analysis of local time dependence on f_p has been performed. Figure 6 presents the derived plasma frequency as a function of local time at the location of scatter. The derived plasma frequency peaks slightly near noon and reaches a minimum near midnight. There are larger error bars on the data for daytime due to fewer frequency shifting events. Again, f_p predicted by the IRI model is presented as the dashed curve in the figure. In this case, the IRI predictions of f_p do not follow the same trends as the f_p values predicted from the radar frequency shifting technique. Possible reasons for this disagreement will be discussed in Section 4.3.

3.3.5. Annual dependence on plasma frequency

The final parameter to examine is the month-to-month variation of the plasma frequency. Like the previous sections, f_p as a function of month has been plotted in Figure 7. There is very little variation of derived plasma frequency with respect to time of year. The only feature of note is that the month of February seems to show a slightly higher plasma frequency than the other months. The dashed curve again shows the values of f_p predicted by IRI for each month. Again, the IRI predicted f_p values do not follow the same trend as the values predicted from the radar frequency shifting technique and this will be discussed in Section 4.3.

4. Discussion

4.1. Slope of superposed epoch plot

As anticipated, statistically Figure 3 shows a clear increase in velocity measured by SuperDARN v_m as a consequence of an increase in transmitting frequency. Also observed in this figure is a slight continuous decrease in v_m as time progresses both before and after the increase in frequency. For the most part, the SuperDARN radars shift to a higher operating frequency when the ionosphere has changed and the propagation conditions at a higher frequency are better for receiving scatter than at the lower frequency. This generally occurs when the electron density in the ionosphere increases and the rays at the lower frequency used before the frequency shift over-refract and do not reach the scatter locations. Therefore, in general, a shift upwards in frequency is a consequence of an increasing electron density in the ionosphere (of course, a shift down in frequency is a consequence of a decreasing electron density in the ionosphere). In other words, to provide backscatter from the same range while f_p is increasing, it is necessary to increase radar frequency. Equation 3 indicates that an increasing electron density (or plasma frequency) will cause a decreasing refractive index. By Equation 1, a decreasing refractive index will decrease the velocity measured by SuperDARN. Since statistically $v_m \propto n_s$ Figure 3 is essentially a plot of the behaviour of n_s with time. As the electron density in the ionosphere increases, n_s (and therefore v_m) decreases and when the radar frequency suddenly increases, n_s (and therefore v_m) also suddenly increases. Therefore, the cause of the slight negative slope in Figure 3 is probably the increase in background electron density with time which causes the shift in frequency to occur.

4.2. Effect of range gate selection

It is possible that the selection of only range gates 20-35 for analysis may have biased the results to a certain electron density. Since the condition for scatter is that the radar wave vector and the magnetic field are perpendicular, scatter will only be received from a certain number of range gates for a given density profile (as can be observed in Figure 1). An analysis of whether the range selection biased the resulting scatter to conditions with higher average electron densities has been undertaken.

Raytracings of wave propagation paths at radar frequencies of 12 MHz and 14 MHz have been performed for a variety of one dimensional electron density profiles for both the Saskatoon and Rankin Inlet radars. The locations on these ray paths at which the wave vector and the external magnetic field were perpendicular to within 1° have been chosen as possible scatter locations. In Figure 8 the range gates which received scatter at both frequencies as a function of peak plasma frequency are plotted. Note that some scatter will occur between range gates 20-35 when the peak plasma frequency is between ∼4.5 MHz and 7.0 MHz. If the peak ionospheric plasma frequency is less than ∼4.5 MHz, there is not sufficient refraction to receive scatter at any ranges. When the peak plasma frequency is above ∼7.0 MHz, the waves over-refract and 1/2-hop scatter (direct scatter) is received at closer ranges (1 1/2-hop scatter is received at farther ranges). This implies that the range selection criteria did not bias the results to instances of higher background electron densities. It can also be noted that the results for the Saskatoon radar and the Rankin Inlet radar are similar. This raytracing analysis has confirmed that the electron densities measured using the frequency shifting technique are higher than background electron densities.

4.3. Comparisons to IRI

The study by *Gillies et al.* [2010a] attributed lower than average SuperDARN velocities to the existence of small-scale, highly dense structures in the SuperDARN scattering volume. It is reasonable to expect that coherent backscatter which is detected by SuperDARN only occurs in relatively small portions of a larger SuperDARN range cell. These small volumes could contain larger-than-average electron densities which would cause the backscatter power to be higher. In this way, SuperDARN would systematically scatter from regions of the ionosphere with higher electron densities. The direct estimate of plasma frequency (or electron density) by the new frequency shifting technique has provided further support to this hypothesis. The average f_p in the SuperDARN scattering volume has been measured to be ∼7.8 MHz. Previous estimates of f_p have used IRI values which tend to predict much lower average values. For example, over the time period of this study, the average peak f_p in the F-region ionosphere from IRI is 5.9 MHz. This indicates that on average, SuperDARN coherent scatter occurs in regions of the ionosphere which have plasma frequencies ∼32% higher than the background ionosphere (this corresponds to electron densities ∼75% higher in the scattering volume than the background ionosphere).

Small-scale electron density structures can often exist in the F-region of the auroral and polar ionosphere. These structures may form from processes such as particle precipitation on the nightside [e.g., *Noël et al.*, 2000; *Noël et al.*, 2005; *Sofko et al.*, 2007] and photonization creating polar cap patches on the dayside [*Weber et al.*, 1984]. Other structures which may provide locations for HF coherent radar scatter are the mid-latitude trough [*Moffet and Quegan*, 1983] and travelling ionospheric disturbances (TIDs) [e.g., *Pryse et*

al., 1995]. A more detailed description of these possible small-scale structures and their importance to SuperDARN coherent scatter may be found in *Gillies et al.* [2010a].

Comparisons between plasma frequencies estimated by the radar frequency shifting technique and predicted by IRI show similar trends. Figure 4 demonstrates that there is agreement between IRI and the frequency shifting technique from latitudes ∼55° to 65°. At higher latitudes, the frequency shifting technique provides higher plasma frequencies than predicted by IRI. This could be due to the auroral and polar regions having more active small-scale structures which cause the bulk of the SuperDARN coherent scatter, while the IRI model only provides background smoothed values for f_p.

Figure 5 presents the plasma frequency measured by the radar frequency shifting technique and predicted by IRI from 1994 to 2009. It can be observed that the two techniques provide values that follow the same solar cycle trend. However, plasma frequencies predicted by IRI are considerably lower than those estimated by the frequency shifting technique. During solar minimum conditions (∼1995–1998 and ∼2006–2009), the radar frequency shifting technique f_p values are roughly double the f_p values predicted by IRI. Conversely, near solar maximum (∼1999–2004) the radar frequency shifting technique estimates plasma frequencies which are only ∼10–30% higher than those predicted by IRI. During solar maximum conditions it is possible that the background electron density is often high enough to provide large HF backscatter cross-sections, which lowers the importance of small-scale structures in these conditions. This would explain why the f_p estimates from the frequency shifting technique are only slightly higher than f_p predictions from IRI during solar maximum conditions.

The results of Figure 6 shows the diurnal variation of f_p and the results indicate that plasma frequencies measured by the radar frequency shifting technique are significantly higher than those predicted by the IRI model. Interestingly, this figure shows that IRI plasma frequencies do vary diurnally, but the radar frequency shifting technique does not follow this trend. Figure 6 indicates that f_p provided by the radar frequency shifting technique peaks near noon and is lower near midnight. The values for f_p predicted by IRI follow the opposite trend, f_p peaks near midnight and is lower during the daytime. This behaviour is probably a consequence of variations in parameters other than local time. For example, the majority of velocity sequences which were averaged to obtain f_p values for local times between 10 to 15 LT were from the years 2003 to 2009 (the sounding mode for SuperDARN operation was in use for these years, resulting in frequency shifts throughout a given day). Figure 5 clearly shows that IRI predicted f_p values were much lower than f_p values given by the radar frequency shifting method for these years. Therefore, the decrease in IRI f_p values in Figure 6 from 10–15 LT may be due to the decrease in IRI f_p values in Figure 5 from 2003–2009. This issue can be further examined in future studies with more frequency shifting statistics so that the variation of f_p as a function of one given parameter can be analyzed with all other parameters held constant.

Finally, Figure 7 presents f_p values from both IRI and the radar frequency shifting technique as functions of time of year. The main result to note from this figure is that the plasma frequencies estimated by the radar frequency shifting technique are, as with the previous comparisons, significantly higher than those predicted by the IRI model. There is little variation in f_p from the radar frequency shifting technique throughout the year.

IRI values for f_p show slightly higher values in wintertime which is probably a consequence of the seasonal anomaly [*Davies*, 1966].

It is clear that IRI estimates of electron density are lower than those measured by SuperDARN using the new frequency shifting technique. It is also beneficial to consider electron densities measured by other instruments. In fact, it can be inferred from the previous study by *Gillies et al.* [2010a], that electron density measurements made by EISCAT from 1995 to 1999 are also lower than those determined from the frequency shifting technique. This previous study compared refractive indices (or electron densities) from IRI, EISCAT and SuperDARN elevation angle measurements. The study found that the background electron densities measured by EISCAT were lower than electron densities estimated by both IRI and the elevation angle method and; therefore, would also be lower than those measured using the frequency shifting technique.

4.4. Velocity comparisons of SuperDARN to other instruments

A comparison in which IRI predictions of refractive index were used to improve SuperDARN velocities, of ∼700 measurements by SuperDARN radars and DMSP satellites was performed by *Ponomarenko et al.* [2009]. Another comparison of ∼800 velocities measured by both the EISCAT incoherent scatter radar and the Hankasalmi SuperDARN radar was performed by *Gillies et al.* [2010a]. Both of these comparisons showed that the original velocities measured by SuperDARN v_m were ∼20% lower than velocities measured by the other instrument. IRI predictions of electron density (and thus f_p and n_s) were applied to improve the SuperDARN velocity measurements and in each case an average refractive index of ∼0.9 was found, which resulted in improved velocities v_{mi} which were, on average, 10% higher than the original v_m values. It should be noted that for the

EISCAT comparison, elevation angle data from SuperDARN and EISCAT measurements of electron density were also used and similar improvements to the comparison were obtained. Elevation angle data and incoherent scatter measurements are not continuously available so only the IRI model was considered for this present study.

Results presented in Figures 3 to 7 show that IRI estimates of f_p are, on average, $\sim$40% lower than the actual f_p in the SuperDARN scattering volume. Using as a basis the studies by *Ponomarenko et al.* [2009] and *Gillies et al.* [2010a], in which average values for v_m were $\sim$20% lower than average velocities measured by other instruments, a rough estimate of the effect of this increase in f_p can be made in a straight-forward manner. From Equation 3, the average value of 0.9 for refractive index in the SuperDARN scattering volume predicted by IRI in these studies corresponds to a plasma frequency of $\sim$5.4 MHz if the transmitting frequency is 12.5 MHz (a typical operating frequency for SuperDARN). Increasing this IRI plasma frequency by 40% results in an actual scattering volume plasma frequency of 7.6 MHz. A transmitting frequency of 12.5 MHz and plasma frequency of 7.6 MHz results in a refractive index value of $\sim$0.8. Finally, dividing the original v_m values by the refractive index of 0.8 will provide average v_{mi} values which are 20% higher, accounting for all the underestimation of velocity by SuperDARN. This is further evidence that the direct measurement of refractive index by SuperDARN presented here provides a more accurate description of the SuperDARN scattering volume than large scale predictions based upon the IRI model.

5. Conclusions

The SuperDARN network routinely underestimates ionospheric line-of-sight drift velocities because the refractive index in the scattering volume is not taken into account.

Previous attempts to account for this effect based on refractive index estimates from the IRI model, incoherent scatter measurements of electron density, or SuperDARN elevation angle measurements have increased SuperDARN velocities by ∼10%. However, the modified velocities were still ∼10% lower than those measured by other instruments [*Gillies et al.*, 2009; *Ponomarenko et al.*, 2009; *Gillies et al.*, 2010a]. The main issue with using electron density predictions from, for example, IRI was that they provided background values that may not have been appropriate for SuperDARN scatter. SuperDARN scatter probably occurs in regions of the ionosphere with small-scale, highly dense structures that are not accounted for by large-scale background predictions like those based upon the IRI model. These structures would have lower refractive index values and the velocities measured by SuperDARN would be underestimated to a greater extent than previous studies predicted if not taken into account. To address this issue, a new method to measure plasma frequency (or refractive index) at the exact scattering location using SuperDARN radar frequency shifts has been developed.

The velocity measured by SuperDARN is proportional to the refractive index, which is dependent to the radar wave frequency. SuperDARN radars routinely shift operating frequencies to maximize ionospheric scatter. An analysis of measured velocities before and after these shifts has provided the first direct measurement of plasma frequency within the SuperDARN scattering volume. It has been found that, on average, plasma frequencies within the scattering volumes are ∼40% higher than the background plasma frequency predicted by the IRI model. The application of the refractive indices determined by the radar frequency shifting method would account for all the underestimation of SuperDARN velocities compared to DMSP satellites and the EISCAT incoherent scatter radar reported

previously [e.g., *Ponomarenko et al.*, 2009; *Gillies et al.*, 2010a]. Refinements to this method could be made in the future if SuperDARN radars would routinely shift frequencies to improve the statistics presented here. Another possibility to improve this procedure, and perhaps determine plasma frequencies on a real-time basis, is to analyze data during stereo mode operations. The stereo mode would allow measurements of velocity at two frequencies to be made simultaneously for each SuperDARN scan. This would negate the temporal disparity between two frequency scans in the present study and provide a much larger statistical data set to analyze. Nevertheless, this study represents the first direct measurement of the average electron density (or plasma frequency) at the locations where SuperDARN scatter occurs, and the results are consistent with the hypothesis that the scatter does in fact arise in regions of the ionosphere with highly dense, small-scale, structures.

Acknowledgments. We acknowledge the support of the Canadian Space Agency (CSA) and the Natural Sciences and Engineering Research Council (NSERC) to the Canadian component of the SuperDARN ground based radar system and the CASSIOPE/ePOP project for our research. International Reference Ionosphere (IRI) electron density profiles have been provided by the Space Physics Data Facility (SPDF).

References

André, R., C. Hanuise, J.-P. Villain, and J.-C. Cerisier. HF radars: Multifrequency study of refraction effects and localization of scattering, *Radio Sci.*, 32, 153–168, 1997.

Bilitza, D. International Reference Ionosphere 2000, *Radio Sci.*, Vol. 36, 261–275, 2001.

Booker, H. G. A theory of scattering by nonisotropic irregularities with application to radar reflections from the aurora, *J. Atmos. Terr. Phys.*, 8, 204–221, 1956.

Budden, K.G. *Radio Waves in the Ionosphere*, Cambridge University Press, Cambridge, U. K., 1961.

Davies, K. *Ionospheric Radio Propagation*, General Publishing Company Ltd., Toronto, 1966.

Davies, J. A., M. Lester, S. E. Milan, and T. K. Yeoman. A comparison of velocity measurements from the CUTLASS Finland radar and the EISCAT UHF system, *Ann. Geophys.*, 17, 892–902, 1999.

Drayton, R. A., A. V. Koustov, M. R. Hairston, and J. -P. Villian. Comparison of DMSP cross-track ion drifts and SuperDARN line-of-sight velocities, *Ann. Geophys.*, 23, 2479–2489, 2005.

Gillies, R. G., G. C. Hussey, G. J. Sofko, K. A. McWilliams, R. A. D. Fiori, P. Ponomarenko, and J.-P. St.-Maurice. Improvement of SuperDARN velocity measurements by estimating the index of refraction in the scattering region using interferometry, *J. Geophys. Res.*, 114, A07305, doi:10.1029/2008JA013967, 2009.

Gillies, R. G., G. C. Hussey, G. J. Sofko, D. M. Wright, and J. A. Davies. A comparison of EISCAT and SuperDARN F-region measurements with consideration of the refractive index in the scattering volume, *J. Geophys. Res.*, 115, A06319, doi:10.1029/2009JA014694, 2010a.

Gillies, R. G., G. C. Hussey, G. J. Sofko, and H. G. James. Relative O-and X-mode transmitted power from SuperDARN as it relates to the RRI instrument on ePOP, *Ann. Geophys.*, 28, 861-871, 2010b.

Greenwald, R. A., K. B. Baker, J. R. Dudeney, M. Pinnock, T. B. Jones, E. C. Thomas, J. -P. Villain, J. -C. Cerisier, C. Senior, C. Hanuise, R. D. Hunsucker, G. Sofko, J. Koehler, E. Nielsen, R. Pellinen, A. D. M. Walker, N. Sato, and H. Yamagishi. DARN/SuperDARN: A Global View of the Dynamics of High-Latitude Convection, *Space Sci. Rev.*, 71, 761–796, 1995.

Haselgrove, J. The Hamiltonian ray path equations, *J. Atmos. Terr. Phys.*, 25, 397–399, 1963.

Hosokawa, K., K. Shiokawa, Y. Otsuka, T. Ogawa, J.-P. St-Maurice, G. J. Sofko, and D. A. André. Relationship between polar cap patches and field-aligned irregularities as observed with an all-sky airglow imager at Resolute Bay and the PolarDARN radar at Rankin Inlet, *J. Geophys. Res.*, 114, A03306, doi:10.1029/2008JA013707, 2009.

Hughes, J. M., W. A. Bristow, R. A. Greenwald, and R. J. Barnes. Determining characteristics of HF communications links using SuperDARN, *Ann. Geophys.*, 20, 1023–1030, 2002.

Lester, M., P. J. Chapman, S. W. H. Cowley, S. J. Crooks, J. A. Davies, P. Hamadyk, K. A. McWilliams, S. E. Milan, M. J. Parsons, D. B. Payne, E. C. Thomas, J. D. Thornhill, N. M. Wade, T. K. Yeoman, and R. J. Barnes. Stereo CUTLASS – A new capability for the SuperDARN HF radars, *Ann. Geophys.*, 22, 459–473, 2004.

Noël, J.-M. A., J.-P. St.-Maurice, and P.-L. Blelly. Nonlinear model of short-scale electrodynamics in the auroral ionosphere, *Ann. Geophys.*, 18, 1128–1144, 2000.

Noël, J.-M. A., J.-P. St.-Maurice, and P.-L. Blelly. The effect of E-region wave heating on electrodynamical structures, *Ann. Geophys.*, 23, 2081–2094, 2005.

Ponomarenko, P., J.-P. St.-Maurice, C. L. Waters, R. G. Gillies, and A. V. Koustov. Refractive index effects on formation and velocity estimates of ionospheric HF backscatter echoes, *Ann. Geophys.*, 27, 4207–4219, 2009.

Pryse, S. E., C. N. Mitchell, J. A. Heaton, and L. Kersley. Travelling ionospheric disturbances imaged by tomographic techniques, *Ann. Geophys.*, 13, 1325–1330, 1995.

Ruohoniemi, J.M. and K.B. Baker. Large-scale imaging of the high-latitude convection with Super Dual Auroral Radar Network HF radar observations, *J. Geophys. Res.*, 103, 20797–20811, 1998.

Sofko, G., R. Schwab, M. Watanabe, C. Huang, J. Foster, K. McWilliams. Auroral post-secondary ions from the nightside ionosphere in the inner magnetosphere, *J. Atmos. Sol. Terr. Phys.*, 69, 1213–1232, 2007.

Weber, E. J., J. Buchau, J. G. Moore, J. R. Sharber, R. C. Liningston, J. D. Winningham, B. W. Reinisch. F-layer ionization patches in the polar cap, *J. Geophys. Res.*, 89, 1683–1694, 1984.

Xu, L., A. V. Koustov, J. Thayer, and M. A. McCready. SuperDARN convection and Sondrestrom plasma drift, *Ann. Geophys.*, 19, 749–759, 2001.

Table 1. Results from various SuperDARN radars

Radar	Number of shifts	Measured f_p (MHz)	IRI f_p (MHz)
Goose Bay	14856	8.4	5.1
Halley	8723	5.7	4.0
Hankasalmi	9608	7.1	4.5
Inuvik	11974	6.6	3.0
Kapuskasing	23270	8.4	6.1
Kerguelen	1264	4.6	3.9
King Salmon	9005	6.9	6.5
Kodiak	178640	8.2	7.1
Prince George	59476	7.6	5.5
Rankin Inlet	23246	5.3	3.0
Saskatoon	31910	8.1	4.7
Stokkseyri	12245	7.1	4.3
Syowa East	3368	5.8	3.4
Syowa South	480	8.7	5.2
Tiger	11826	7.3	7.2
Tiger Unwin	132	6.7	5.1
All	400497	7.8	5.9

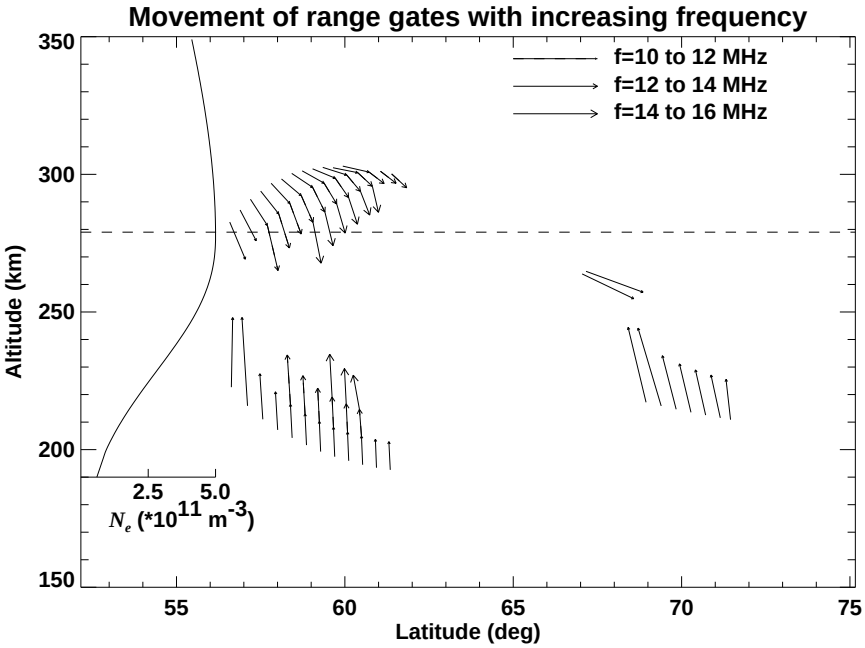

Figure 1. The movement of SuperDARN range gates as transmitting frequency is increased from 10 MHz to 12 MHz, 12 MHz to 14 MHz, and 14 MHz to 16 MHz. The dashed line shows the altitude of the F-region peak density of 5×10^{11} m^{-3} and the curve on the left shows the electron density profile.

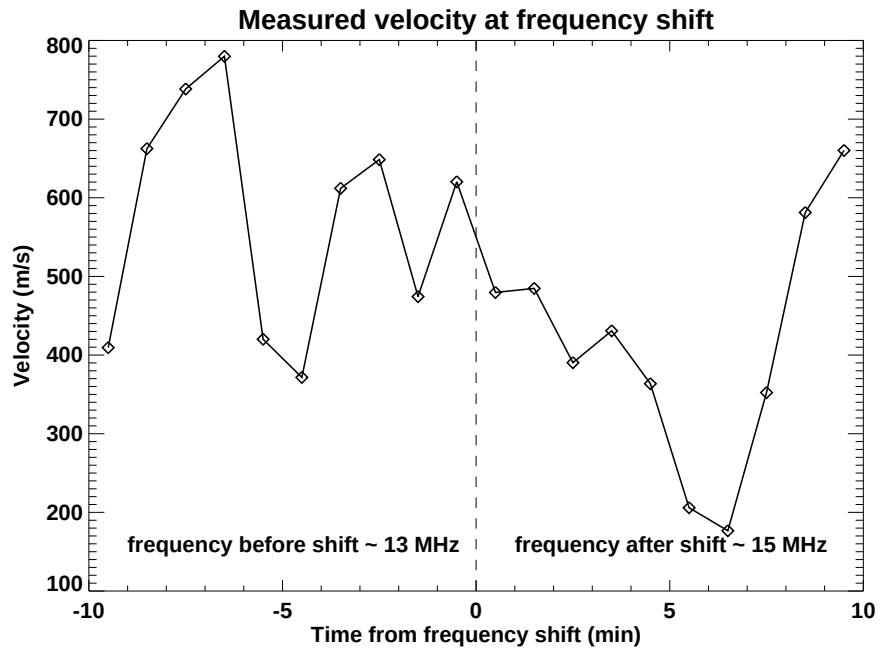

Figure 2. Plot of velocity at a single radar frequency shift. The dashed vertical line represents the time of the shift in frequency.

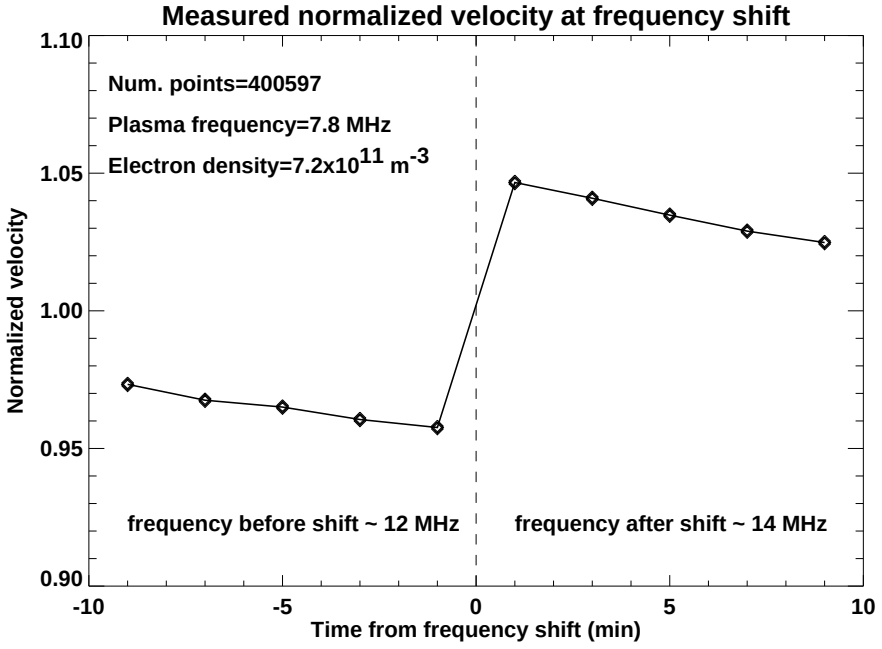

Figure 3. Superposed epoch plot of velocity at a radar frequency shift for range gates 20-35.

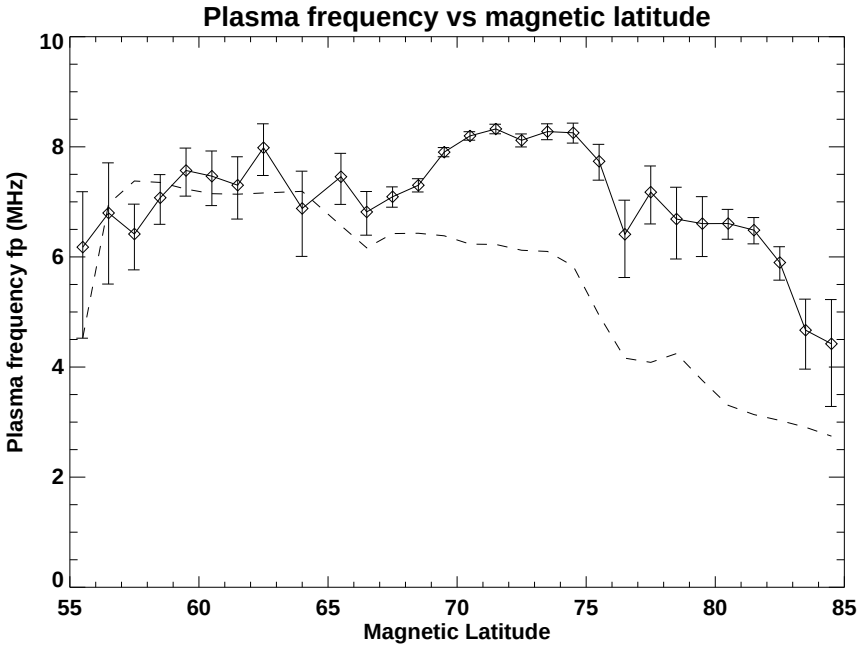

Figure 4. The solid curve is the plasma frequency derived from the radar frequency shifting technique. The dashed curve is the average peak plasma frequency predicted by IRI.

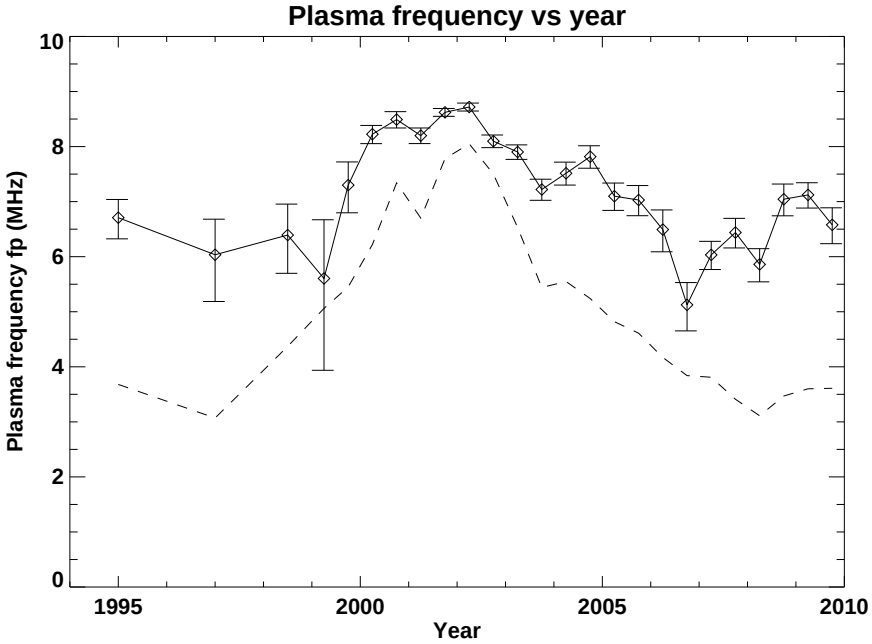

Figure 5. The solid curve is the plasma frequency derived from the radar frequency shifting technique. The dashed curve is the average peak plasma frequency predicted by IRI.

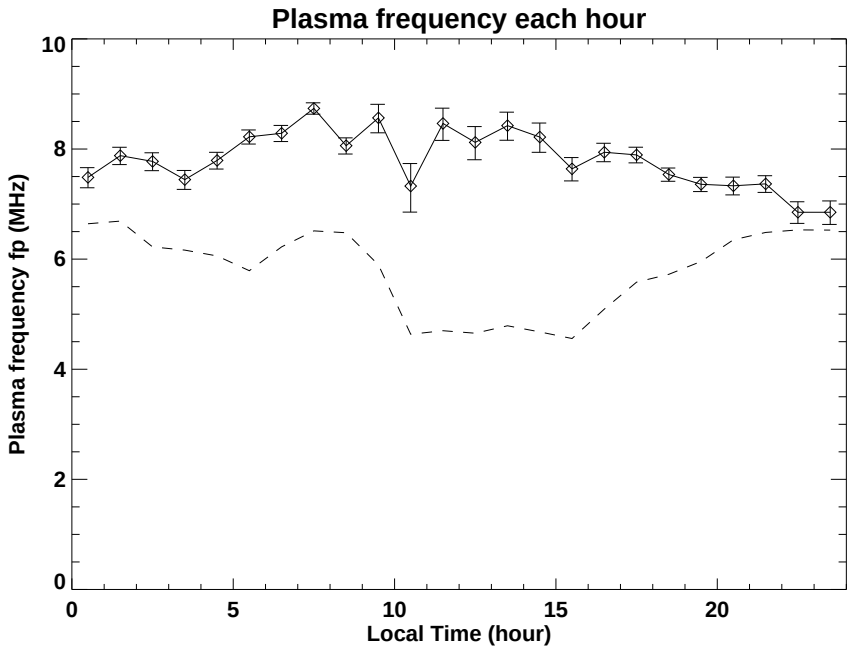

Figure 6. The solid curve is the plasma frequency derived from the radar frequency shifting technique as a function of local time. The dashed curve is the average peak plasma frequency predicted by IRI.

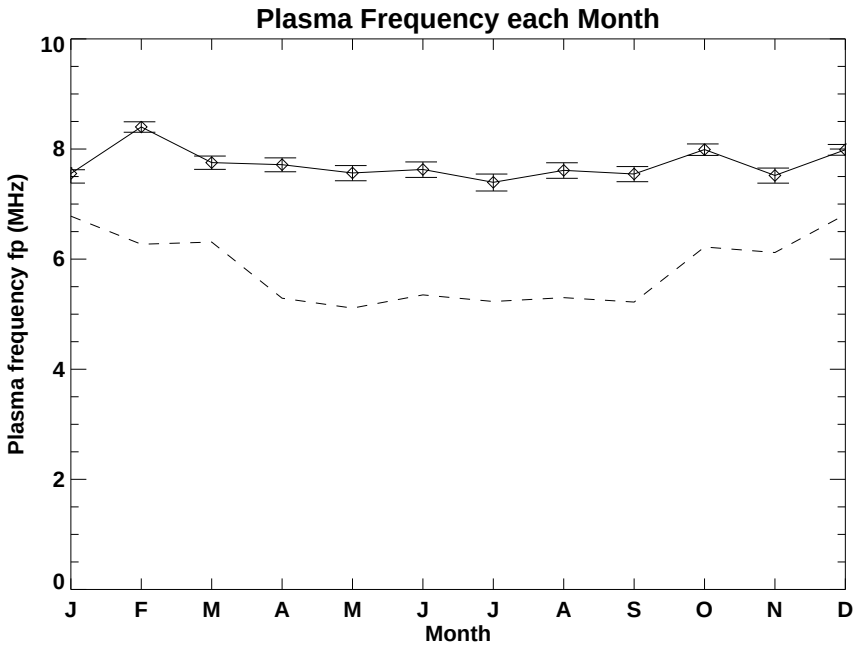

Figure 7. The solid curve is the plasma frequency derived from the radar frequency shifting technique as a function of time of year. The dashed curve is the average peak plasma frequency predicted by IRI.

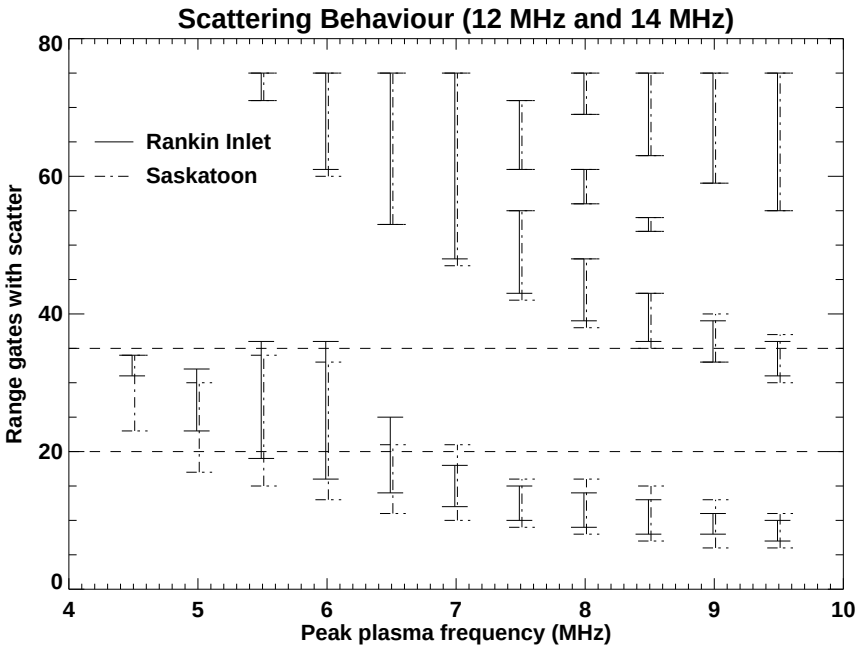

Figure 8. The range gates which provide scatter for various peak ionospheric plasma frequencies at transmitter frequencies of both 12 MHz and 14 MHz determined through raytracing. The solid lines represent results for the Rankin Inlet radar and the dashed lines represent results for the Saskatoon radar.

Chapter 7

Conclusions

The goal of this thesis has been to study transionospheric propagation of HF radio waves. This research goal has been accomplished by examining two related areas of study. The first was modelling the behaviour of radio waves as they propagate through the ionosphere. This modelling was for preparation of the upcoming ePOP-SuperDARN experiment. The second was a study of the cause and development of a solution to the systematic underestimation of ionospheric velocities measured by SuperDARN. This examination of velocities also provided insight into the physics and nature of coherent radio scatter in the ionosphere.

7.1 Transionospheric modelling for ePOP

7.1.1 Transionospheric modelling results

As the ePOP satellite has not yet been launched, the research performed to date has consisted of theoretical modelling work and analysis of a past transionospheric experiment. Analysis and interpretation of a 1978 transionospheric experiment, where radio signals were received by the Canadian ISIS 2 satellite from a ground-based transmitter located in Ottawa, demonstrated some of the various properties that will be measurable by the RRI instrument on ePOP [*James*, 2006; *James et al.*, 2006; *Gillies*, 2006; *Gillies et al.*, 2007]. Ray path modelling performed by *Gillies et al.* [2007], as part of this thesis research presented in Chapter 2, verified that large-scale measurements (∼300 km horizontal resolution) of the F-region peak density by the topside sounder on the ISIS 2 satellite, supplied sufficient information to

the model to reproduce signal parameters measured by the transionospheric experiment on ISIS 2. This showed that the ray tracing model can accurately reproduce actual transionospheric experimental results. Using this modelling work as a basis for when ePOP is operational, a similar analysis of the RRI observations will provide large-scale measurements of the electron density in the ionosphere.

The ISIS 2 satellite had only a single dipole antenna for measurement of HF radio waves. Use of a single dipole does not allow measurement of the full wave polarization state. The behaviour of the received signal as the ISIS 2 satellite passed over the Ottawa transmitter could not be fully explained as information about the polarization state of the wave was lacking. Fortunately, the RRI on ePOP will contain two crossed dipole antennas which are necessary for full polarization measurements. When the ePOP satellite is at an orbit location where the RRI can detect signal from a SuperDARN radar, the satellite will be positioned so that the two dipole antennas will allow the RRI to make full polarization measurements of the wave. Analysis of the full polarization state will provide insight into the propagation conditions and the nature of transionospheric HF radio wave propagation. Modelling of the full polarization state of the received waves for various ionospheric conditions has been undertaken in preparation for the ePOP mission, as presented in Chapter 3 and *Gillies et al.* [2010c].

7.1.2 Future work in transionospheric studies

The analysis of ISIS 2 transionospheric data and the propagation and polarization modelling performed in preparation for the ePOP-SuperDARN experiment, Chapters 2 and 3 of this thesis, has divulged the characteristics of the transionospheric signal that will be detected by the RRI instrument. Using this research as a basis, interpretation of the signal received by the RRI will allow identification and measurement of ionospheric structures. Also of significant interest will be the analysis of situations when SuperDARN receives backscatter and the RRI receives forward scatter. Measurement of the angle-of-arrival of the received wave by the RRI and the elevation angle of the backscattered echo by SuperDARN will allow for a determination

of the scattering location to be made. Another experiment that can be performed will involve the measurement by the RRI of the Doppler shift of SuperDARN waves scattered by ionospheric irregularities. From the Doppler shift information, velocity measurements can be made by the RRI to compare to SuperDARN measurements of velocity. Further, the data provided by the other instruments on ePOP, discussed in Section 1.6.2, will complement the data from the RRI-SuperDARN experiment. The two other radio instruments, the GAP and CER instruments, will provide measurements of electron density which can be compared to values inferred from the signal received by the RRI. The particle detector instruments, specifically the IRM and SEI instruments, will provide high resolution measurements of the plasma density and velocity near the satellite.

7.2 Improvement of SuperDARN velocity measurements

7.2.1 Refractive index effect

Another main objective of the ePOP mission will be to provide high resolution measurements in the same region of the ionosphere from which SuperDARN receives coherent backscatter. This is the other main research theme and objective of this thesis. In particular, accurate measurements of the refractive index in this region is an important aspect for general SuperDARN operations. Radar waves at SuperDARN operating frequencies are refracted by the ionosphere to be perpendicular to the nearly vertical magnetic field lines in the auroral and polar regions of the Earth. This refraction is important as electrostatic plasma wave irregularities in the ionospheric plasma are aligned with respect to the magnetic field (their wave vectors perpendicular to the magnetic field lines). When a SuperDARN wave encounters these irregularities, it can be coherently scattered back to the radar location through Bragg scattering if the irregularity has a wavelength half that of the SuperDARN radar wavelength. Measurement of the Doppler shift of the scattered SuperDARN

radar wave gives a measure of the drift velocity of the plasma in the F-region ionosphere. By combining data from all the SuperDARN radars a map of the convection pattern of the ionosphere at high latitudes is available every one or two minutes [*Ruohoniemi and Baker*, 1998]. The ionospheric convection patterns measured by SuperDARN are driven by solar activity and provide valuable information about the dynamics of the near-Earth space environment. One issue with the SuperDARN measurement technique is that the refractive index at the location of backscatter directly affects the velocity that is measured as presented in Chapter 4 and *Gillies et al.* [2009]. Since refraction is necessary for the operation of the radars, the refractive index is typically significantly less than unity in the scattering volume (between $\sim$0.75 and 0.90). Unfortunately, the refractive index can be quite variable and is not directly measured by the SuperDARN radars so it has been neglected in past studies. Direct measurements of SuperDARN scattering volumes by the ePOP satellite experiment will provide measurements of the refractive index, which can be used to improve the velocities measured by SuperDARN.

7.2.2 Determination of refractive index

In addition to future ePOP measurements, various other methods to estimate or measure refractive index in the SuperDARN scattering volume have been developed and tested in this thesis in Chapters 4 through 6, *Gillies et al.* [2009], *Gillies et al.* [2010b], and *Gillies et al.* [2010a].

SuperDARN radars have an interferometry array which can measure the elevation angle at which scattered waves are received [*Milan et al.*, 1997; André et al., 1998]. As coherent backscatter only occurs for certain radar wave propagation directions (which are relatively well-known and constant), the elevation angle recorded by SuperDARN for a given ionospheric echo can be used as a proxy for refractive index. This research was presented in Chapter 4 and *Gillies et al.* [2009].

Another method to determine refractive index is to use an estimate of electron density in the scattering region from a model such as the International Reference Ionosphere (IRI) [*Bilitza*, 2001]. The IRI model can provide an estimate of elec-

tron density (and thus refractive index) for any time and location in the ionosphere based on empirical models. Both the elevation angle technique and IRI estimates of refractive index give large-scale, background values which then may be used to improve SuperDARN velocity estimates. These approaches were used in the analysis presented in Chapter 5, *Ponomarenko et al.* [2009], and *Gillies et al.* [2010b]. A comparison between incoherent scatter radar data from the EISCAT radar and SuperDARN was performed. In this comparison, elevation angle, IRI, and EISCAT estimates of refractive index were used to improve SuperDARN velocities. It was found that each method improved the comparison; however, the velocity measurements by SuperDARN were still significantly lower than those measured by EISCAT. One possible explanation for the underestimation of velocities measured by SuperDARN is due to the nature of coherent backscatter. Coherent backscatter results from the strongest scattering cross sections, which are highest in regions of the ionosphere with the highest electron densities [*Booker*, 1956]. This suggests that, while the use of background estimates of refractive index significantly improved SuperDARN velocities, a more accurate method to take into account the importance of small-scale, highly dense structures expected in the coherent scattering process, needed to be developed.

A technique to directly measure electron density and refractive index in the SuperDARN scattering volume was developed, which took advantage of routine shifts in the frequency transmitted by the radars. This research was presented in Chapter 6 and *Gillies et al.*, 2010a. Since refractive index is dependent on radar wave frequency, a shift of frequency causes a shift of refractive index and measured velocity. If it is assumed that the electron density and actual ionospheric drift velocity are constant for the time it takes the radar to shift frequencies (on the order of a few minutes), the shift in measured velocity can provide a direct measurement of refractive index and electron density in the SuperDARN scattering volume – the portion of the scattering volume where the coherent scattering originates. This technique was used to find that, as suspected from the previous research [*Gillies et al.*, 2009; *Gillies et al.*, 2010b], electron densities within the SuperDARN scattering volumes tended

to be significantly higher than background values. When the new higher values for electron density were applied to determine refractive index and improve SuperDARN velocities, the SuperDARN measurements agreed with velocities measured by other instruments, such as the DMSP satellites and the EISCAT radar system. This study was very important because it not only suggested a method to retroactively improve nearly twenty years of HF coherent radar data, but also granted insight into the conditions within the scattering volume and the physics and nature of coherent scattering.

Several conclusions may be drawn from the studies of line-of-sight velocities measured by SuperDARN presented in Chapters 4, 5, and 6, and *Gillies et al.* [2009], *Gillies et al.* [2010b] and *Gillies et al.* [2010a]. It is evident that velocities measured by SuperDARN have been significantly underestimated because no account for the refractive index in the scattering volume has been made. On a statistical basis, this neglect of the refractive index value caused velocities measured by SuperDARN to be roughly 20% lower than velocities measured by other instruments. The methods presented in this thesis to measure the refractive index in the scattering volume have found that coherent scatter tends to occur most strongly in the regions of the ionosphere with the highest electron densities. It was found that, on average, the electron density at the location of scatter is nearly double the background electron density.

7.2.3 Future work for improvement of velocity measurements

As discussed in Chapters 4, 5, and 6, various methods to infer the refractive index in the SuperDARN scattering volume have been developed to improve the velocities measured by SuperDARN. The latest technique developed to measure refractive index used instances of shifts in the transmitted frequency by SuperDARN as presented in Chapter 6 and *Gillies et al.* [2010a]. This method provided important results; however, improvements can be made in the future by analyzing data from dedicated SuperDARN frequency shifting experiments to provide a more uniform set of refractive index statistics. Several SuperDARN radars operate a Stereo mode in

which two frequencies can be transmitted and received simultaneously [*Lester et al.*, 2004]. Another experiment mode that could be run by SuperDARN radars is one in which the frequency is switched every scan. Analysis of velocity data from these modes will be very useful for developing a better model for predicting the refractive index in the scattering volume. Both the Stereo and constant frequency switching modes will provide a much greater quantity of electron density and refractive index data than was used in the *Gillies et al.* [2010a] study reported in this thesis. The variation of the electron density in the scattering volume as a function of location, time of day, time of year, and solar cycle period will be much better characterized by analysis of these modes. The ultimate goal for improving the measurements of velocity in real-time would be accomplished if the radars continuously operate in a mode that consists of constant frequency shifting. Although, even if no further refinements are made to improve the measured velocities on a real-time basis, a rough estimate of the effect of the refractive index can be made by assuming that all ionospheric velocities measured by HF coherent radars are $\sim$20% too low and the velocities and any parameters derived from them, such as the cross polar cap potential, could be made more accurate accordingly.

7.3 Summary

In summary, the research involved in this thesis accomplished two goals: 1) the reason for the systematic underestimation of velocities measured by SuperDARN was determined and solutions to improve the measurements were developed; and 2) transionospheric HF radio wave propagation modelling in preparation for the ePOP satellite mission was performed. The analysis and transionospheric propagation modelling performed for the RRI-SuperDARN mission will be used as the basis for interpreting the results of the satellite experiment when it is launched and operational. The ePOP mission will provide an excellent opportunity to study the F-region ionosphere, and in particular, the characteristics of the coherent scattering processes for HF radars such as SuperDARN.

References

André, D., G. J. Sofko, K. Baker, and J. MacDougall, SuperDARN interferometry: Meteor echoes and electron densities from groundscatter, *J. Geophys. Res.*, 103, 7003–7015, 1998.

André, R., C. Hanuise, J.-P. Villian, and J.-C. Cerisier, HF radars: Multifrequency study of refraction effects and localization of scattering, *Radio Sci.*, 32, 153–168, 1997.

Anderson, D. N., J. Buchau, and R. A. Heelis, Origin of density enhancements in the winter polar cap ionosphere, *Radio Sci.*, 23, 513–519, doi:10.1029/RS023i004p00513, 1988.

Angelopoulos, V., The THEMIS Mission, *Space Sci. Rev.*, 141, 5–34, 2008.

Appleton, E. V. and G. Builder, The ionosphere as a doubly refracting medium, *Proc. Phys. Soc.*, 45, 208, 1933.

Arnold, N. F., T. R. Robinson, M. Lester, P. B. Byrne, and P. J. Chapman, Super Dual Auroral Radar Network observations of fluctuations in the spectral distribution of near range meteor echoes in the upper mesosphere and lower thermosphere, *Ann. Geophys.*, 19, 425–434, 2001.

Bahcivan, H., R. Tsunoda, M. Nicolls, and C. Heinselman, Initial ionospheric observations made by the new Resolute incoherent scatter radar and comparison to solar wind IMF, *Geophys. Res. Lett.*, 37, L15103, doi:10.1029/2010GL043632, 2010.

Baker, K. B., J. R. Dudeney, R. A. Greenwald, M. Pinnock, P. T. Newell, A. S. Rodger, N. Mattin, and C.-I. Meng, HF radar signatures of the cusp and low-latitude boundary layer, *J. Geophys. Res.*, 100, 7671–7695, 1995.

Balogh, A., C. M. Carr, M. H. Acuna, M. W. Dunlop, T. J. Beek, P. Brown, K.-H. Fornacon, E. Georgescu, K.-H. Glassmeier, J. Harris, G. Musmann, T. Oddy, and K. Schwingenschuh, The Cluster Magnetic Field Investigation: overview of in-flight performance and initial results, *Ann. Geophys.*, 19, 1207-1217, 2001.

Baumjohann, W., R. A. Treumann, *Basic Space Plasma Physics*, Imperial College Press, UK, 1997.

Bernhardt, P. A., R. P. McCoy, K. F. Dymond, J. M. Picone, R. R. Meier, F. Kamalabadi, D. M. Cotton, S. Charkrabarti, T. A. Cook, J. S. Vickers, A. W. Stephan, L. Kersley, S. E. Pryse, I. K. Walker, C. N. Mitchell, P. R. Straus, H. Na, C. Biswas, G. S. Bust, G. R. Kronschnabl, and T. D. Raymund, Two-dimensional mapping of the plasma density in the upper atmosphere with computerized ionospheric tomography (CIT), *Phys. Plasmas*, 5, 2010–2021, 1998.

Bernhardt, P. A., C. A. Teply, and L. M. Duncan, Airglow enhancements associated with plasma cavities formed during ionospheric heating experiments, *J. Geophys. Res.*, 94, 9071–9092, 1989.

Bhuyan, P. K, M. Chamua, K. Bhuyan, P. Subrahmanyam, and S. C. Garg, Diurnal, seasonal and latitudinal variation of the electron density in the topside F-region of the Indian zone ionosphere at solar minimum and comparison with the IRI, *J. Atmos. Sol. Terr. Phys.*, 65, 359-368, 2003.

Bibl, K., and B. W. Reinisch, The universal digital ionosonde, *Radio Sci.*, 13, 519530, doi:10.1029/RS013i003p00519, 1978.

Bilitza, D., X. Huang, B. W. Reinisch, R. F. Benson, H. K. Hills, and W. B. Schar, Topside Ionogram Scaler With True Height Algorithm (TOPIST): Automated processing of ISIS topside ionograms *Radio Sci.*, 39, RS1S27, doi:10.1029/2002RS002840, 2004.

Bilitza, D., International Reference Ionosphere 2000, *Radio Sci.*, 36, 261–275, 2001.

Booker, H. G., A theory of scattering by nonisotropic irregularities with application to radar reflections from the aurora, *J. Atmos. Terr. Phys.*, 8, 204–221, 1956.

Born, M., and E. Wolf, *Principles of Optics: Electromagnetic Theory of Propagation Interference and Diffraction of Light, Sixth Edition*, Pergamon Press Canada Ltd., Toronto, 1980.

Bowles, K. L., Observation of Vertical-Incidence Scatter from the Ionosphere at 41 Mc/sec, *Phys. Rev. Lett.*, 1, 454-455, 1958.

Budden, K. G., *The propagation of radio waves: The theory of radio waves of low power in the ionosphere and magnetosphere*, Cambridge University Press, UK, 1985.

Budden, K. G., *Radio Waves in the Ionosphere: the mathematical theory of the reflection of radio waves from stratified ionised layers*, Cambridge University Press, UK, 1961.

Chappell, C. R., T. E. Moore, and J. H. Waite Jr., The ionosphere as a fully adequate source of plasma for the Earth's magnetosphere, *J. Geophys. Res.*, 92, 5896–5910, 1987.

Chisham, G., T. K. Yeoman, and G. J. Sofko, Mapping ionospheric backscatter measured by the SuperDARN HF radars. Part 1: A new empirical virtual height model, *Ann. Geophys.*, 26, 823–841, 2008.

Chisham, G., M. Lester, S. E. Milan, M. P. Freeman, W. A. Bristow, A. Grocott, K. A. McWilliams, J. M. Ruohoniemi, T. K. Yeoman, P. L. Dyson, R. A. Greenwald, T. Kikuchi, M. Pinnock, J. P. S. Rash, N. Sato, G. J. Sofko, J.-P. Villain,

A. D. M. Walker, A decade of the Super Dual Auroral Radar Network (SuperDARN): scientific achievements, new techniques, and future directions, *Surv. Geophys.*, 28, 33–109, 2007.

Daniels, F., ISIS-II Spacecraft, CRC Report No. 1218, Communications Research Centre, Ottawa, 1971.

Davies, J. A., M. Lester, S. E. Milan, and T. K. Yeoman, A comparison of velocity measurements from the CUTLASS Finland radar and the EISCAT UHF system, *Ann. Geophys.*, 17, 892–903, 1999.

Davies, K., *Ionospheric Radio Propagation* General Publishing Company, Ltd. Toronto, 1966.

Drayton, R. A., *Study of SAPS-like flows with the King Salmon SuperDARN radar*, M.Sc. Thesis, University of Saskatchewan, 2006.

Drayton, R .A., A. V. Koustov, M. R. Hairston, and J.-P. Villian, Comparison of DMSP cross-track ion drifts and SuperDARN line-of-sight velocities, *Ann. Geophys.*, 23, 2479–2489, 2005.

Duncan, L. M., J. P. Sheerin, and R. A. Behnke, Observations of ionospheric cavities generated by high-power radio waves, *Phys. Rev. Lett.*, 61, 239–242, 1988.

Eglitis, P., T. R. Robinson, M. T. Rietveld, D. M. Wright, and G. E. Bond, The phase speed of artificial field-aligned irregularities observed by CUTLASS during HF modification of the auroral ionosphere, *J. Geophys. Res.*, 103, 2253–2259, 1998.

Fejer, B. G., and M. C. Kelley, Ionospheric irregularities, *Reviews of Geophysics and Space Physics*, 18, 401–454, doi:10.1029/RG018i002p00401 , 1980.

Foster, J. C., A. J. Coster, P. J. Erickson, J. M. Holt, F. D. Lind, W. Rideout, M. McCready, A. van Eyken, R. J. Barnes, R. A. Greenwald, and F. J. Rich, Multiradar observations of the polar tongue of ionization, *J. Geophys. Res.*, 110, A09S31, doi:10.1029/2004JA010928, 2005.

Franklin, C. A. and M. A. Maclean, The design of swept-frequency topside sounders, *Proc. of the IEEE*, 57(6), 897–929, 1969.

Gillies, R. G., G. C. Hussey, G. J. Sofko, P. V. Ponomarenko, and K. A. McWilliams, Improvement of HF coherent radar line-of-sight velocities by estimating the refractive index in the scattering volume using radar frequency shifting, Submitted to *J. Geophys. Res.*, Accepted November 2010a.

Gillies, R. G., G. C. Hussey, G. J. Sofko, D. M. Wright, and J. A. Davies, A comparison of EISCAT and SuperDARN F-region measurements with consideration of the refractive index in the scattering volume, *J. Geophys. Res.*, 115, A06319, doi:10.1029/2009JA014694, 2010b.

Gillies, R. G., G. C. Hussey, G. J. Sofko, and H. G. James, Relative O- and X-mode transmitted power from SuperDARN as it relates to the RRI instrument on ePOP, *Ann. Geophys.*, 28, 861–871, 2010c.

Gillies, R. G., G. C. Hussey, G. J. Sofko, K. A. McWilliams, R. A. D. Fiori, P. V. Ponomarenko, and J.-P. St.-Maurice, Improvement of SuperDARN velocity measurements by estimating the index of refraction in the scattering region using interferometry, *J. Geophys. Res.*, 114, A07305, doi:10.1029/2008JA013967, 2009.

Gillies, R. G., G. C. Hussey, H. G. James, G. J. Sofko, and D. André, Modelling and observation of transionospheric propagation results from ISIS II in preparation for ePOP, *Ann. Geophys.*, 25, 87–97, 2007.

Gillies, R. G., *Modelling of transionospheric HF radio wave propagation for the ISIS II and ePOP satellites*, M.Sc. Thesis, Institute of Space and Atmospheric Studies, University of Saskatchewan, 2006.

Ginzburg, V. L., *The Propagation of Electromagnetic Waves in Plasmas*, Pergamon Press, New York, 1964.

Gordon, W. E., Incoherent Scattering of Radio Waves by Free Electrons with Applications to Space Exploration by Radar, *Proc. IRE*, 46, 1824–1829, 1958.

Grant, I. F., J. W. MacDougall, J. M. Ruohoniemi, W. A. Bristow, G. J. Sofko, J. A. Koehler, D. Danskin, and D. André, Comparison of plasma flow velocities determined by the ionosonde Doppler drift technique, SuperDARN radars, and patch motion, *Radio Sci.*, 30, 1537–1549, 1995.

Greenwald, R. A., K. B. Baker, J. R. Dudeney, M. Pinnock, T. B. Jones, E. C. Thomas, J.-P. Villain, J.-C. Cerisier, C. Senior, C. Hanuise, R. D. Hunsucker, G. Sofko, J. Koehler, E. Nielsen, R. Pellinen, A. D. M. Walker, N. Sato, and H. Yamagishi, DARN/SuperDARN: A Global View of the Dynamics of High-Latitude Convection, *Space Sci. Rev.*, 71, 761-796, 1995.

Haldoupis, C., and K. Schlegel, Direct comparison of 1-m irregularity phase velocities and ion acoustic speeds in the auroral E-region ionosphere, *J. Geophys. Res.*, 95, 989–1000, 1990.

Hansen, J. D., G. J. Morales, L. M. Duncan, and G. Dimonte, Large-scale HF-induced ionospheric modifications: experiments, *J. Geophys. Res.*, 97, 113–122, 1992.

Hansen, J. D., G. J. Morales, L. M. Duncan, J. E. Maggs, and G. Dimonte, Large-scale ionospheric modifications produced by nonlinear refractions of an HF wave, *Phys. Rev. Lett.*, 65, 3285–3288, 1990.

Hargreaves, J. K. and R. D. Sharp, Electron precipitation and ionospheric radio absorption in the auroral zones, *Planetary and Space Sci.*, 13, 1171–1183, 1965.

Hartz, T. R., Observations of the Galactic Radio Emission Between 1.5 and 10 MHz From the Alouette Satellite, *Annales D'Astrophysique*, 27, 823-830, 1964.

Hartree, D. R., The propagation of electromagnetic waves in a stratified medium, *Proc. Camb. Phil. Soc.*, 25, 97, 1929.

Haselgrove, J., The Hamiltonian ray path equations, *J. Atmos. Terr. Phys.*, 25, 397–399, 1963.

Hosokawa, K., K. Shiokawa, Y. Otsuka, T. Ogawa, J.-P. St.-Maurice, G. J. Sofko, and D. A. André, Relationship between polar cap patches and field-aligned irregularities as observed with an all-sky airglow imager at Resolute Bay and the PolarDARN radar at Rankin Inlet, *J. Geophys. Res.*, 114, A03306, doi:10.1029/2008JA013707, 2009.

Hughes, J. M., W. A. Bristow, R. A. Greenwald, and R. J. Barnes, Determining characteristics of HF communications links using SuperDARN, *Ann. Geophys.*, 20, 1023–1030, 2002.

Hunsucker, R. D., *Radio Techniques for Probing the Terrestrial Ionosphere*, Springer-Verlag Berlin Heidelberg, 1991.

Hunsucker, R.D., and J.K. Hargreaves, *The High-Latitude Ionosphere and its Effects on Radio Propagation* Cambridge University Press, UK, 2003.

James, H. G., R. G. Gillies, G. C. Hussey, and P. Prikryl, HF fades caused by multiple wave fronts detected by a dipole antenna in the ionosphere, *Radio Sci.*, 41, RS4018, doi:10.1029/2005RS003385, 2006.

James, H. G. and W. H. H. J. Lunscher, A digital radio receiver for ionospheric research, NATO Specialist Meeting IST-056, "Characterizing the Ionosphere", Paper 23, Fairbanks, AK, USA, 12–16 June 2006.

James, H. G., Effects on transionospheric HF propagation observed by ISIS at middle and auroral latitudes, *Adv. Space Res.*, 38(11), 2303–2312, 2006.

James, H. G., High-frequency direction finding in space, *Review of Scientific Instruments*, 74(7), 3478–3486, 2003.

Jayachandran, P. T., R. B. Langley, J. W. MacDougall, S. C. Mushini, D. Pokhotelov, A. M. Hamza, I. R. Mann, D. K. Millin, Z. C. Kale, R. Chadwick, T. Kelly, D. W. Danskin, and C. S. Carrano, Canadian High Arctic Ionospheric Network (CHAIN), *Radio Sci.*, 44, RS0A03, doi:10.1029/2008RS004046, 2009.

Kelley, M. C., *The Earth's Ionosphere: Plasma Physics and Electrodynamics, Second Edition*, Elsevier Inc., San Diego, 2009.

Kersley, L., S. E. Pryse, I. K. Walker, J. A. T. Heaton, C. N. Mitchell, M. J. Williams, and C. A. Willson, Imaging of electron density troughs by tomographic techniques, *Radio Sci.*, 32(4), 1607–1621, 1997.

Kivelson, M. G., and C. T. Russell, *Introduction to Space Physics*, Cambridge University Press, UK, 1995.

Knecht, R. W., T. E. van Zandt, and S. Russell, First pulsed radio soundings of the topside of the ionosphere, *J. Geophys. Res.*, 66, 3078–3081, 1961.

Lester, M., P. J. Chapman, S. W. H. Cowley, S. J. Crooks, J. A. Davies, P. Hamadyk, K. A. McWilliams, S. E. Milan, M. J. Parsons, D. B. Payne, E. C. Thomas, J. D. Thornhill, N. M. Wade, T. K. Yeoman, and R. J. Barnes, Stereo CUTLASS – A new capability for the SuperDARN HF radars, *Ann. Geophys.*, 22, 459–473, 2004.

Little, C. G. and H. Leinbach, The Riometer – A Device for the Continuous Measurement of Ionospheric Absorption, *Proc. of the IRE*, 47, 315–320, 1959.

MacDougall, J. W., I. F. Grant and X. Shen, The Canadian Advanced Digital Ionosonde: Design and Results, Rep. UAG-104, Ionosondes and Ionosonde Networks, 21–27, World Data Center A, Boulder, 1995.

Maus, S., S. Macmillan, T. Chernova, S. Choi, D. Dater, V. Golovkov, V. Lesur, F. Lowes, H. Luhr, W. Mai, S. McLean, N. Olsen, M. Rother, T. Sabaka, A. Thomson and T. Zvereva, The 10th generation international geomagnetic reference field, *Phys. Earth Planet. Inter.*, 151, 320–322, 2005.

Milan, S. E., T. B. Jones, T. R. Robinson, E. C. Thomas, and T. K. Yeoman, Interferometric evidence for the observation of ground backscatter originating behind the CUTLASS coherent radars, *Ann. Geophys.*, 15, 29–39, 1997.

Mitchell, C. N., D. G. Jones, L. Kersley, S. E. Pryse, and I. K. Walker, Imaging of field-aligned structures in the auroral ionosphere, *Ann. Geophys.*, 13, 1311–1319, 1995.

Moffett, R. J. and S. Quegan, The mid-latitude trough in the electron concentration of the ionospheric F-layer: a review of observations and modelling, *J. Atmos. Terr. Phys.*, 45, 5, 315–343, 1983.

Montenbruck, O., and E. Gill, *Satellite Orbits: models, methods, applications*, Springer-Verlag Berlin Heidelberg, 2000.

Noël, J.-M. A., J.-P. St.-Maurice, and P.-L. Blelly, The effect of E-region wave heating on electrodynamical structures, *Ann. Geophys.*, 23, 2081–2094, 2005.

Noël, J.-M. A., J.-P. St.-Maurice, and P.-L. Blelly, Nonlinear model of short-scale electrodynamics in the auroral ionosphere, *Ann. Geophys.*, 18, 1128–1144, 2000.

Parker, E. N., Dynamics of the interplanetary gas and magnetic fields, *Astrophys. J.*, 128, 664–676, 1958.

Pfotzer, G., History of the Use of Balloons in Scientific Experiments, *Space Sci. Rev.*, 13, 199–242, 1972.

Ponomarenko, P. V., J.-P. St.-Maurice, C. L. Waters, R. G. Gillies, and A. V. Koustov, Refractive index effects on formation and velocity estimates of ionospheric HF backscatter echoes, *Ann. Geophys.*, 27, 4207–4219, 2009.

Pryse, S. E., K. L. Dewis, R. L. Balthazor, H. R. Middleton, and M. H. Denton, The dayside high-latitude trough under quiet geomagnetic conditions: Radio tomography and the CTIP model, *Ann. Geophys.*, 23, 1199–1206, 2005.

Pryse, S. E., C. N. Mitchell, J. A. Heaton, and L. Kersley, Travelling ionospheric disturbances imaged by tomographic techniques, *Ann. Geophys.*, 13, 1325–1330, 1995.

Reinisch, B. W., J. L. Scali, D. L. Haines, Ionospheric drift measurements with ionosondes, *Ann. Geophys.*, 41, 695–702, 1998.

Rietveld, M. T., H. Kohl, H. Kopka, and P. Stubbe, Introduction to ionospheric heating at Tromsø. I. Experimental overview, *J. Atmos. Terr. Phys.*, 55, 577–599, 1993.

Rishbeth, H., and A. P. van Eyken, EISCAT: Early history and the first ten years of operation, *J. Atmos. Terr. Phys.*, 55, 525–542, 1993.

Robinson, T. R., The heating of the high latitude ionosphere by high power radio waves, *Phys. Rep.*, 28, 79–209, 1989.

Rodger, A. S., R. J. Moffett, and S. Quegan, The role of ion drift in the formation of ionisation troughs in the mid- and high-latitude ionosphere–a review, *J. Atmos. Terr. Phys.*, 54, 1–30, 1992.

Rostoker, G., J. C. Samson, F. Creutzberg, T. J. Hughes, D. R. McDiarmid, A. G. McNamara, A. Vallance Jones, D. D. Wallis and L. L. Cogger, Canopus A ground-based instrument array for remote sensing the high latitude ionosphere during the ISTP/GGS program, *Space Sci. Rev.*, 71, 743–760, 1993.

Ruohoniemi, J. M., and K. B. Baker, Large-scale imaging of the high-latitude convection with Super Dual Auroral Radar Network HF radar observations, *J. Geophys. Res.*, 103, 20797–20811, 1998.

Schunk, R. W., and A. F. Nagy, *Ionospheres: Physics, Plasma Physics, and Chemistry*, Cambridge University Press, UK, 2000.

Simon, A., Instability of a partially ionized plasma in crossed electric and magnetic fields, *Physics of Fluids*, 6, 382–388, 1963.

Sofko, G., R. Schwab, M. Watanabe, C. Huang, J. Foster, and K. McWilliams, Auroral post-secondary ions from the nightside ionosphere in the inner magnetosphere, *J. Atmos. Sol. Terr. Phys.*, 69, 1213–1232, 2007.

Sojka, J. J., M. D. Bowline, R. W. Schunk, D. T. Decker, C. E. Valladares, R. Sheehan, D. N. Anderson, R. A. Heelis, Modeling polar cap Fregion patches using time varying convection, *Geophys. Res. Lett.*, 20, 1783–1786, doi:10.1029/93GL01347, 1993.

Sojka, J. J., R. W. Schunk, and J. A. Whalen, The longitude dependence of the dayside F region trough: A detailed model-observation comparison, *J. Geophys. Res.*, 95, 15275–15280, 1990.

Stocker, A. J., F. Honary, T. R. Robinson, T. B. Jones, P. Stubbe, and H. Kopka, EISCAT observations of large scale electron temperature and electron density perturbations caused by high power HF radio waves, *J. Atmos. Terr. Phys.*, 54, 1555–1572, 1992.

Stone, E. C., A. M. Frandsen, R. A. Mewaldt, E. R. Christion, D. Margolies, J. F. Ormes, and F. Snow, The Advanced Composition Explorer, *Space Sci. Rev.*, 86, 1–22, 1998.

Stubbe, P., Review of ionospheric modification experiments at Tromsø, *J. Atmos. Terr. Phys.*, 58, 349–368, 1996.

Tepley, C. A., Current developments at Arecibo for research in the atmospheric sciences at low latitudes, *J. Atmos. Sol. Terr. Phys.*, 59, 1679–1686, 1997.

Titheridge, J. E., Ionogram analysis with the generalised program POLAN, Rep. UAG-93, World Data Cen. A for Sol. Terr. Phys., Boulder, 1985.

Treumann, R. A., and W. Baumjohann, *Advanced Space Plasma Physics*, Imperial College Press, UK, 1997.

Troshichev, O., H. Hayakawa, A. Matsuoka, T. Mukai, and K. Tsuruda, Cross polar cap diameter and voltage as a function of PC index and interplanetary quantities, *J. Geophys. Res.*, 101, 13,42913,435, doi:10.1029/95JA03672, 1996.

Villain, J.-P., C. Hanuise, and G. Caudal, A SAFARI-EISCAT comparison between the velocity of F region small-scale irregularities and the ion drift, *J. Geophys. Res.*, 90, 8433–8443, 1985.

Wang, L., J. W. MacDougall, and H. G. James, Ionospheric structure effects on HF radio wave propagation for the Enhanced Polar Outflow Probe (e-POP) satellite mission, *Radio Sci.*, 39, RS2019, doi:10.1029/2003RS002975, 2004.

Weber, E. J., J. Buchau, J. G. Moore, J. R. Sharber, R. C. Liningston, J. D. Winningham, B. W. Reinisch, F-layer ionization patches in the polar cap, *J. Geophys. Res.*, 89, 1683–1694, 1984.

Wright, J. W., H. Kopka, and P. Stubbe, A large-scale ionospheric depletion by intense radio wave heating, *Geophys. Res. Lett.*, 15, 1531–1533, 1988.

Xu, L., *SuperDARN-derived Plasma Convection Comparison with Other Data and Application to Field-aligned Current Measurements*, Ph.D. Thesis, University of Saskatchewan, 2003.

Xu, L., A. V. Koustov, J. Thayer, and M. A. McCready, SuperDARN convection and Sondrestrom plasma drift, *Ann. Geophys.*, 19, 749–759, 2001.

Yau, A. W, , H. G. James, and W. Lui, The Canadian Enhanced Polar Outflow Probe (ePOP) mission in ILWS, *Adv. Space Res.*, 38(8), 1870–1877, 2006.

Yau, A. W., L. L. Cogger, E. P. King, D. J. Knudsen, J. S. Murphree, T. S. Trondsen, K. Tsuruda, H. G. James, and I. Walkty, The Polar Outflow Probe (POP): Science Objectives and Instrument Development, *Canadian Aeronautics and Space Journal*, 48(1), 39–49, 2002.

Appendix A

Copyright Agreements

A.1 European Geosciences Union (pre-2009)

Copernicus.org
Meetings & Open Access Publications
Serving Sciences since 1988

Copernicus Gesellschaft mbH
Bahnhofsallee 1e ▪ 37081 Göttingen ▪ Germany

Robert Gillies
(rgg646@mail.usask.ca)

Your Contact:

Nadine Deisel
Head of Publication Production & Promotion

Phone +49-551-900339-50
Fax +49-551-900339-70

nadine.deisel@copernicus.org
www.copernicus.org

Granting of Reproduction Request

Copernicus Publications on behalf of the European Geosciences Union grants the permission to reproduce the requested item(s) and expect that the moral right of the original author(s) is asserted by identifying the author(s) of the reproduced item(s).

Request granted to: Robert Gillies

Journal: Ann. Geophys., 25, 87-97, 2007
Article Title: Modelling and observation of transionospheric propagation results from ISIS II in preparation for ePOP
Authors: Gillies, R. G., Hussey, G. C., James, H. G., Sofko, G. J., and André, D.
Item: entire article

For reproduction in: Doctoral thesis at the University of Saskatchewan

With kind regards,

Nadine Deisel

Nadine Deisel
Head of Publication Production & Promotion

A.2 European Geosciences Union (post-2009)

License and Copyright Agreement

The following License and Copyright Agreement is valid for any article published by Copernicus Publications on behalf of the European Geosciences Union (EGU) in the journal Annales Geophysicae whose original manuscript was received from **01 January 2009** on. The License and Copyright Agreement for articles based on manuscripts received before 01 January 2009 can be found here.

Author's Certification

In submitting the manuscript, the authors certify that:

- They are authorized by their co-authors to enter into these arrangements.
- The work described has not been published before (except in the form of an abstract or proceedings-type publication – including discussion papers – or as part of a published lecture or thesis), that it is not under consideration for publication elsewhere, that its publication has been approved by all the author(s) and by the responsible authorities – tacitly or explicitly – of the institutes where the work has been carried out.
- They secure the right to reproduce any material that has already been published or copyrighted elsewhere.
- They agree to the following license and copyright agreement:

Copyright

- Copyright on any article is retained by the author(s).
- Authors grant Copernicus Publications a license to publish the article and identify itself as the original publisher.
- Authors grant Copernicus Publications commercial rights to produce hardcopy volumes of the journal for sale to libraries and individuals.
- Authors grant any third party the right to use the article freely as long as its original authors and citation details are identified.
- The article and any associated published material is distributed under the Creative Commons Attribution 3.0 License:

Creative Commons Attribution 3.0 License

Anyone is free:

to Share — to copy, distribute and transmit the work

to Remix — to adapt the work

Under the following conditions:

Attribution. The original authors must be given credit.

- For any reuse or distribution, it must be made clear to others what the license terms of this work are.
- Any of these conditions can be waived if the copyright holders give permission.
- Nothing in this license impairs or restricts the author's moral rights.

The full legal code of this license.

A.3 American Geophysical Union

Date: **Mon, 01 Nov 2010 13:55:05 -0400**
From: "Michael Connolly" <MConnolly@agu.org> **Block Address**
To: "rgg646@mail.usask.ca" <rgg646@mail.usask.ca>
Subject: **permission**

Reply | Reply All | Forward | Print | Delete

We are pleased to grant permission for the use of the material requested for inclusion in your thesis. The following non-exclusive rights are granted to AGU authors:

- All proprietary rights other than copyright (such as patent rights).
- The right to present the material orally.
- The right to reproduce figures, tables, and extracts, appropriately cited.
- The right to make hard paper copies of all or part of the paper for classroom use.
- The right to deny subsequent commercial use of the paper.

Further reproduction or distribution is not permitted beyond that stipulated. The copyright credit line should appear on the first page of the article or book chapter. The following must also be included, "Reproduced by permission of American Geophysical Union." To ensure that credit is given to the original source(s) and that authors receive full credit through appropriate citation to their papers,

we recommend that the full bibliographic reference be cited in the reference list. The standard credit line for journal articles is: "Author(s), title of work, publication title, volume number, issue number, citation number (or page number(s) prior to 2002), year. Copyright [year] American Geophysical Union."

If an article was placed in the public domain, in which case the words "Not subject to U.S. copyright" appear on the bottom of the first page or screen of the article, please substitute "published" for the word "copyright" in the credit line mentioned above.

Copyright information is provided on the inside cover of our journals. For permission for any other use, please contact the AGU Publications Office at AGU, 2000 Florida Ave., N.W., Washington, DC 20009.

Michael Connolly

American Geophysical Union

2000 Florida Avenue, NW

Washington, DC 20009

202-777-7365

mconnolly@agu.org

Reply | Reply All | Forward | Print | Delete